TAMPEREEN TEKNILLINEN YLIOPISTO
TAMPERE UNIVERSITY OF TECHNOLOGY

Antti-Juhana Mäki

Modeling and Control of Microscale Cell Culture Environments

Julkaisu 1557• Publication 1557

Tampere 2018

Tampereen teknillinen yliopisto. Julkaisu 1557
Tampere University of Technology. Publication 1557

Antti-Juhana Mäki

Modeling and Control of Microscale Cell Culture Environments

Thesis for the degree of Doctor of Science in Technology to be presented with due permission for public examination and criticism in Festia Building, Auditorium Pieni Sali 1, at Tampere University of Technology, on the 16th of August 2018, at 12 noon.

Tampereen teknillinen yliopisto - Tampere University of Technology
Tampere 2018

Doctoral candidate: Antti-Juhana Mäki
Micro- and Nanosystems Research Group
Faculty of Biomedical Sciences and Engineering
Tampere University of Technology
Finland

Supervisor: Pasi Kallio, Professor
Micro- and Nanosystems Research Group
Faculty of Biomedical Sciences and Engineering
Tampere University of Technology
Finland

Pre-examiners: Edmund W. K. Young, Assistant Professor
Department of Mechanical & Industrial Engineering
University of Toronto
Canada

Hongsoo Choi, Associate Professor (Tenured)
Department of Robotics Engineering
Daegu Gyeongbuk Institute of Science & Technology
Republic of Korea

Opponents: Andreas Dietzel, Professor
Institute of Microtechnology
Technical University of Braunschweig
Germany

Edmund W. K. Young, Assistant Professor
Department of Mechanical & Industrial Engineering
University of Toronto
Canada

ISBN 978-952-15-4168-1 (printed)
ISBN 978-952-15-4174-2 (PDF)
ISSN 1459-2045

Abstract

Culturing cells *in vitro* is one of the core techniques used in a wide range of biomedical engineering areas. Special care is required to successfully grow cells in an artificial environment. It is essential to ensure that the culture environment is cell-friendly and sterile, supplies important products such as nutrients and growth factors, and provides a proper physiological microenvironment. To optimize long-term cell culturing, parameters such as pH, oxygen concentration, and temperature, should be precisely maintained at the desired levels. Furthermore, it is sometimes desirable to change environmental parameter(s) in a controlled way to study the cell response.

Bioreactors are typically used for cell culture *in vitro*. However, precise control of each cell culture's microenvironment is difficult, leading to uneven culture conditions that can affect cell behavior. Furthermore, studying how certain environmental parameter affect the cultures is challenging, as it is difficult, or even impossible, to vary certain parameters in a controlled manner between each culture.

Microscale cell culture systems, known as microbioreactors, have recently been extensively studied to enhance control and improve long-term cell culturing by better mimicking cells' microenvironments. Microbioreactors provide better environment control, thereby enhancing long-term cell cultivation. Unfortunately, integrating microbioreactors with the required sensors, actuators, electronics and other required devices can be challenging. Implementing sensors near the cell culture can also disturb them or prevent other measurements, such as optical microscopy. Certain measurements, such as direct long-term pH measurement, can be impossible, as there are no suitable microscale sensors available.

For these reasons, there is a huge demand for methods that can be used to study and develop proper microbioreactors. This thesis includes several studies in which modeling was used as design tools to improve and control culture environments. First, an analytical model to study gravity-driven flows in microfluidic devices is developed. Next, developed finite element method (FEM) computer models are used to study fluid flow profiles, drug distributions, shear stress levels on cells, and sensitivity of a calorimetric flow measurement system. A FEM model of carbon dioxide transport and liquid pH is also created. Additionally, the thesis proposes a novel method to indirectly control the cell culture temperature. Using system identification techniques, a developed estimation model can precisely control temperature with a sensor that does not disturb cells or other measurements. Although this thesis only demonstrates temperature control in the cell culture, the method can potentially be used to control other environment parameters as well. Lastly, this thesis considers the limitations of the presented models and control methods, and provides recommendations for future studies.

Preface

The work presented in this thesis was carried out at BioMediTech and the Faculty of Biomedical Sciences and Engineering, and its predecessor Department of Automation Science and Engineering, at Tampere University of Technology during the years 2011–2018. My gratitude goes to the Doctoral Programme of the President of the Tampere University of Technology where I received most of my personal funding. I would also like to thank the Business Finland (former TEKES), for funding the Human Spare Parts 1 and 2 projects I have worked in, the Faculty of Biomedical Sciences and Engineering for the support to finish the thesis, and the Finnish Society of Automation for traveling grants.

I would like to express my deepest gratitude to my supervisor, Professor Pasi Kallio, for his invaluable support during these years. It has been my absolute privilege to prepare this thesis under your supervision. I am also deeply grateful to the pre-examiners of this thesis, Professors Edmund W.K. Young from University of Toronto and Hongsoo Choi from Daegu Gyeongbuk Institute of Science & Technology. Their comments and suggestions were valuable for me to improve the thesis. I want also thank Professors Young and Andreas Dietzel from Technical University of Braunschweig for accepting the request to act as opponents in the public examination of my thesis.

I am deeply grateful to all the co-authors of my publications for your help with the experiments and the writing processes. I am very thankful to the present and past colleagues at the university and especially at MST-group, particularly MSc Joose Kreutzer and PhD Juha Hirvonen. It has indeed been a great place to work and waiting for the Viikonloppu song! I also appreciate very helpful discussions with PhD Terho Jussila and Professor Matti Vilkko related to control systems and system identification techniques, and LaTeX guru PhD Ville Rantanen; this book certainly would look different without your help!

I am profoundly grateful to my a lifelong support team; my parents Eevaliisa and Seppo and sister Anniina. Your encouragement has been essential for me during this long process. I want also thank all my friends, especially Lakeuden Komiat and the Good-Looking Guys; your company have provided me a vital counterbalance to my thesis work.

Above all, my warmest thanks go to my wife Mari and our charming children. Your love and support have kept me going. I am so thankful to share my life with you now and in the future!

Tampere, May 2018

Antti-Juhana Mäki

Contents

Abstract i

Preface iii

Glossaries vii

List of Publications xv

1 Introduction 1
- 1.1 Motivation . . . 1
- 1.2 Objectives and Research Questions . . . 2
- 1.3 Main Results . . . 3
- 1.4 Outline . . . 4

2 Background 5
- 2.1 Introduction . . . 5
- 2.2 Microbioreactors . . . 6
- 2.3 Cell Culture Environment . . . 8
- 2.4 Modeling and Control . . . 10
- 2.5 Current Challenges . . . 13

3 Theoretical Background 15
- 3.1 Microfluidic Perfusion Culture, Gravity-Driven Flow, and Drug Delivery . 15
- 3.2 Gas Contents and Liquid pH . . . 19
- 3.3 Identification . . . 22
- 3.4 Closed-Loop Control System . . . 22

4 Modeling the Microscale Cell Culture Environment 25
- 4.1 Gravity-Driven Flow Model . . . 25
- 4.2 Drug Delivery Model in Microfluidic Devices Using Gravity-Driven Flow . 28
- 4.3 Flow Sensor Model in Gravity-Driven Microfluidic Devices . . . 32
- 4.4 CO_2 Transport and Liquid pH in PDMS-Based Devices . . . 37

5 Indirect Cell Culture Temperature Measurement and Control 43
- 5.1 Indirect Temperature Measurement . . . 44
- 5.2 Indirect Temperature Control . . . 49

6 Conclusions 57
- 6.1 Summary of the Results . . . 57
- 6.2 Answering the Research Questions . . . 58

6.3 Limitations of the Study 59
6.4 Discussion and Future Outlook 59

Bibliography **61**

Publications **75**

Glossaries

Abbreviations

3D
three-dimensional

BPM
beats per minute

DI
deionized

FEM
finite element method

GDF
gravity-driven flow

ITO
indium tin oxide

PDMS
polydimethylsiloxane

PI
proportional-integral

PID
proportional-integral-derivative

pKa
negative common logarithm of the acid dissociation constant of $NaHCO_3$

TSP
temperature sensor plate

Symbols

A

area

D_x

diffusion coefficient of x

Fl_{xy}

mass transport flux between two phases x and y

Fv_{CO2}

volume fraction of CO_2

G_i, Gk

geometry, $i = 1...4$, $k = 1...2$

H

a constant used to calculate temperature-dependent, Henry's law constant (in K)

K_c

thermodynamic constant

K_{hyd}

hydration equilibrium constant

K_p, K_i, K_d

non-negative coefficients of proportional, integral, and derivative terms, respectively, of PID controller

K_w

ion product of water

Kp_{xy}

a dimensionless partition coefficient ratio between two phases x and y

L

characteristic length

L_c

channel length

P

permeability coefficient

P_{wet}

wetted perimeter

Q

flow rate

Q_{min}
: minimum flow rate

R
: ideal gas constant

$R(T)$
: resistance at temperature T

R_{hyd_rec}
: hydraulic resistance of a channel with a rectangular cross-section

R_{hyd}
: hydraulic resistance

Re
: Reynolds number

S_{TQ}
: sensitivity

S_{inf}
: infinite dilution solubility

S_x
: solubility of x

T
: temperature

T_Ri
: inside temperature

T_Ro
: outside temperature

T_heater
: heater temperature

T_0
: reference temperature

T_{ITO}
: ITO plate temperature

T_{SATP}
: standard ambient temperature (298.15 K)

T_{TSP}
: temperature sensor plate temperature

$T_{cell-est}$
: estimated cell culture temperature

T_{cell}
: cell culture temperature

T_{down}
: downstream temperature

$T_{outside}$
: outside temperature

T_{room}
: ambient room temperature

T_{set}
: set-point temperature

T_{up}
: upstream temperature

V
: volume

ΔQ
: flow rate difference

ΔT
: temperature difference

ΔT_{min}
: minimum detectable temperature difference

Δh
: height difference

Δp
: pressure difference

Δp_{cap}
: capillary pressure drop

α
: temperature coefficient of resistance

$\bar{y}$
: mean of measured output

η
: dynamic viscosity of liquid

$\hat{y}$
: estimated output

ρ
: density

σ_{lg}
: surface tension between liquid-gas interface

θ_a
: advancing contact angle

θ_r
: receding contact angle

$\boldsymbol{A}$
: state matrix

$\boldsymbol{B}$
: input-to-state matrix

$\boldsymbol{C}$
: state-to-output matrix

$\boldsymbol{D}$
: feedthrough matrix

$\boldsymbol{I}$
: identity matrix

$\boldsymbol{N}$
: flux expression

$\boldsymbol{u}$
: input vector

$\boldsymbol{v}$
: velocity field

$\boldsymbol{x}$
: state vector

$\boldsymbol{y}$
: output vector

a_{11}, a_{12}, b_1, c_1, c_2, c_3
: constants in matrices $\boldsymbol{A}$, $\boldsymbol{B}$, and $\boldsymbol{C}$

c_{avg}
: average concentration

c_{in}
: inlet concentration

c_{max}
: maximum concentration

c_{xsat}
: saturated concentration of x

c_x
: concentration of x

d_{cc}
: center-to-center distance

e
: error signal

g
: gravitational acceleration

h_1
: height difference between the bottom of the channel and the cell area

h_2
: height difference between the top of the channel and the outlet

h_c
: channel height

h_s
: sensor height

k_{xy}
: mass transport coefficient at the specific surface from x phase to y phase

$kh_{H(0)}$
: Henry's law constant at standard ambient temperature

$kh_{H(T)}$
: Henry's law constant at temperature T

n
: amount of substance

n_p
: pressure dependence of solubility

p
: pressure

p_{CO2}
: partial pressure of CO_2 gas component

p_{ch}
: total chamber pressure

p_{hyd}
: hydrostatic pressure

p_i
: constants to calculate K_w, $i = 1...3$

r
: set-point value

r_{ha}
: hydraulic radius at the point where the advancing liquid-gas interface is located

r_{hr}
: hydraulic radius at the point where the receding liquid-gas interface is located

r_h
: hydraulic radius

s
: calculated integral value of the error using trapezoidal approximation

t_r
: rise time, time required for the output to rise to 90 percent of the final value

t_s
: sample time

u
: control variable

v
: velocity

w_c
: channel width

y
: output

y_m
: measured output

Chemical Symbols and Formulas

CO_3^{2-}
: carbonate ion

$CO_{2(aq)}$
: carbon dioxide in the liquid phase

$CO_{2(gas)}$
: carbon dioxide in the gas phase

CO_2
: carbon dioxide

H_2CO_3
: carbonic acid

H_2O
: water

H^+
: hydrogen ion

HCO_3^-
: bicarbonate ion

Na_2CO_3
: sodium carbonate

Na^+
: sodium ion

$NaHCO_3$
: sodium bicarbonate

O_2
: oxygen

OH^-
: hydroxide ion

List of Publications

This thesis is based on the following original publications, which are referenced in the text as Publications I-VI. Publications I-V are reproduced with permission from the publishers. This thesis also includes an unpublished manuscript, referenced as Publication VI.

I Mäki, A.-J., Hemmilä, S., Hirvonen, J., Girish, N.N., Kreutzer, J., Hyttinen, J., and Kallio, P., "Modeling and Experimental Characterization of Pressure Drop in Gravity-Driven Microfluidic Systems," *Journal of Fluids Engineering*, vol. 137, no. 2, art. no. 021105, 2015.

II Mäki, A.-J., Kreutzer, J., and Kallio, P., "Modeling Drug Delivery in Gravity-Driven Microfluidic System," in *Proceedings of the ASME 2014 12th International Conference on Nanochannels, Microchannels, and Minichannels (ICNMM2014)*, paper no. ICNMM2014-21183, p. V001T02A003, Aug. 2014.

III Mäki, A.-J., Kontunen, A., Ryynänen, T., Verho, J., Kreutzer, J., Lekkala, J., and Kallio, P., "Design and Simulation of a Thermal Flow Sensor for Gravity-Driven Microfluidic Applications", in *Proceedings of the 11th IEEE Annual International Conference on Nano/Micro Engineered and Molecular Systems (NEMS)*, pp. 125 – 129, Apr. 2016.

IV Mäki, A.-J., Peltokangas, M., Kreutzer, J., Auvinen, S., and Kallio, P., "Modeling carbon dioxide transport in PDMS-based microfluidic cell culture devices," *Chemical Engineering Science*, vol. 137, pp. 515 – 524, 2015.

V Mäki, A.-J., Ryynänen, T., Verho, J., Kreutzer, J., Lekkala, J., and Kallio, P., "Indirect Temperature Measurement and Control Method for Cell Culture Devices," *IEEE Transactions on Automation Science and Engineering*, vol. 15, no. 2, pp. 420 – 429, 2018.

Unpublished manuscripts

VI Mäki, A.-J., Verho, J., Kreutzer, J., Ryynänen, T., Rajan, D., Pekkanen-Mattila, M., Ahola, A., Hyttinen, J., Aalto-Setälä, K., Lekkala, J., and Kallio, P., "A Portable Microscale Cell Culture System with Indirect Temperature Control."

A peer-reviewed version of the unpublished manuscript has been published online in *SLAS TECHNOLOGY: Translating Life Sciences Innovation* on 3.5.2018.

- Mäki, A.-J., Verho, J., Kreutzer, J., Ryynänen, T., Rajan, D., Pekkanen-Mattila, M.,Ahola, A., Hyttinen, J., Aalto-Setälä, K., Lekkala, J., and Kallio, P., "A Portable Microscale Cell Culture System with Indirect Temperature Control," *SLAS TECHNOLOGY: Translating Life Sciences Innovation*, May 3, 2018, DOI: 10.1177/2472630318768710.

The author of this thesis was the main author in all the listed publications. Furthermore, the author analyzed the data and calculated most of the results in all the publications. The author also wrote major parts of each publication. The author's own contributions in each publication are described below in more detail.

In Publication I, the author summarized all measurement data, designed and implemented the developed models, and compared the measurement and simulation results. Samu Hemmilä fabricated the used microchannels and performed the experimental work together with Joose Kreutzer, Nathaniel Narra Girish imaged the channels using micro-computing tomography, and Juha Hirvonen developed image-based analysis softwares. The manuscript was revised and improved with the co-authors.

The author developed and simulated the models used in Publication II. The author also studied different geometries using simulation, in order to improve drug delivery. Joose Kreutzer and Pasi Kallio provided the assistance and helped finalize the paper.

In Publication III, the author analyzed the validation data, developed numerical models used in the study, compared simulation and measurement data, and provided structure improvement using the developed model. Anton Kontunen, Tomi Ryynänen, Jarmo Verho, and Joose Kreutzer fabricated the experimental setup and performed the model validation work. All co-authors helped finalize the manuscript.

For Publication IV, the author designed and closely supervised the model development and validation experiments, developed numerical models, performed simulations, and analyzed the measurement and simulation data. The author also provided model-based geometry improvement. Mikko Peltokangas and Joose Kreutzer performed model development and validation experiments and Sanna Auvinen carrried out permeability measurements. The manuscript was revised with the co-authors.

The author designed the required measurement system, designed and executed the experiments, and analyzed experimental data for Publication V. The author also developed indirect temperature estimation models using system identification techniques, compared measurements and modeled data, and provided model-based, control system studies and controller tuning. Tomi Ryynänen, Jarmo Verho, and Joose Kreutzer provided materials and equipments for the measurement system. All co-authors helped finalize the paper.

For Publication VI, the author partly designed the required control system, executed all the experiments without cells, gathered and analyzed experimental data, developed temperature estimation models using system identification techniques, compared measurements and modeled data, and developed the temperature control system method. The author also designed, experimented, and analyzed cell culture studies together with Joose Kreutzer, Dhanesh Rajan, Mari Pekkanen-Mattila, and Antti Ahola. Jarmo Verho provided the control system and electronic circuits and Tomi Ryynänen fabricated the measurement plate. Dhanesh Rajan developed the used optical system. All co-authors revised the manuscript.

Chapter 1

Introduction

1.1 Motivation

Culturing cells *in vitro*, outside their normal biological surroundings, is one of the most common techniques used in many biomedical and biochemical engineering fields, and in basic research of human development. For example, cultured cells are used in tissue engineering as a product to repair, enhance, or replace biological tissues. On the other hand, cultured cells are also used to make various products, such as viral vaccines, proteins, and antibodies. In cytotoxicity tests, cell cultures are used to develop physiological disease models to replace animal testing for drug screening, validating certain compounds (such as cosmetic products), and determining the appropriate dosage of drugs and other compounds.

Successful cell culturing *in vitro* requires that the culture environment is highly controllable to provide desired culture conditions, such as proper temperature, O_2 level, and pH. In addition, the capability to change the culture environment in a controlled way is advantageous for some cell studies. A biocompatible, sterile, and contamination-free system is also required. It should provide nutrients (such as glucose, vitamins, amino acids, and hormones) for cells, remove waste products, and be user-friendly. If needed, the system should also provide a method to stimulate cells.

As the focus of this thesis is on the surrounding cell culture microenvironment, issues related to intracellular phenomenon or functions, such as cell-to-cell interactions, are not considered. Furthermore, this thesis does not cover stimulation of cells by chemical, mechanical, optical, and electrical factors. Based on these restrictions, Figure 1.1 shows a simplified presentation of the *in vitro* cell culture microenvironment.

One of the main goals with *in vitro* human cell cultures is to develop models that mimic better cellular behavior or drug response in humans compared to *in vivo* animal models. A major problem with traditional *in vitro* cell culture methods, in which culture plates are placed in an incubator, is providing uniform environmental conditions for each culture inside the incubator. Recent developments in microsystems, microfluidic-based devices, and tissue engineering have provided solutions to tackle these problems by using microbioreactors. These miniaturized devices have dimensions closer to the natural cell environment, so it is possible to maintain cell culture conditions much more precisely. This can enhance successful, long-term cell culturing. Microbioreactors are also cheaper to fabricate than incubators and require less time, power, and reagents. With reduced reaction volumes, smaller volumes of expensive reagents are required.

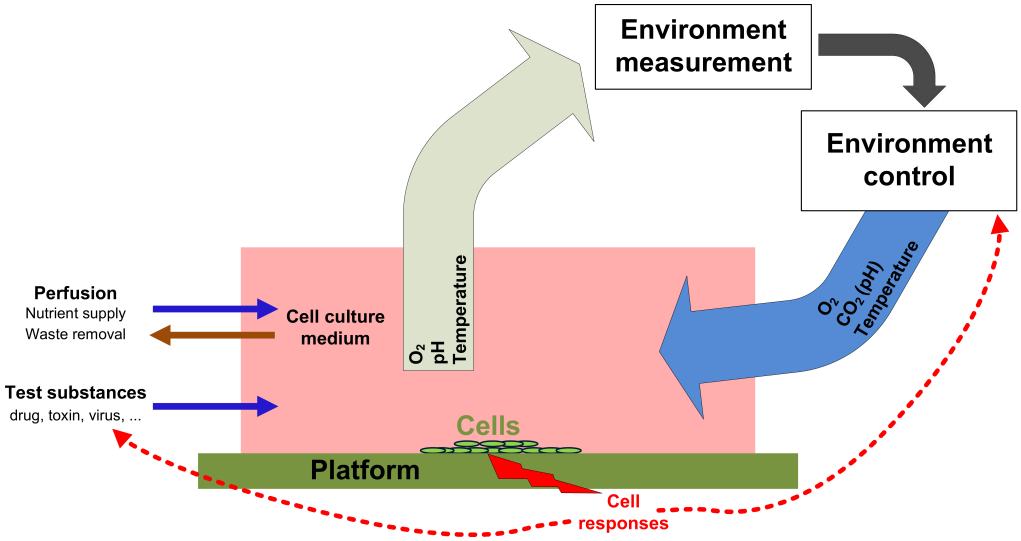

Figure 1.1: Simplified presentation of *in vitro*, monolayer cell culture microenvironment.

As a result, drug development costs could be lowered. In addition, microfabrication provides the possibilities for designing and manufacturing geometries that are relevant for the cells. Also, as accurate flow control is typically possible in the microbioreactor due to laminar flow, microfluidics is beneficial for processes such as nutrient transport, sample handling, reagent mixing, and cell differentiation, separation, and detection. Furthermore, microbioreactors can image, track, and manipulate cells online, which is not typically possible with conventional culturing methods without costly, specialized arrangements. (Christen and Andreou, 2007; Davis, 1994; Jiang et al., 2014; Nelson et al., 2010; Pasirayi et al., 2011; Petronis et al., 2006; Yum et al., 2014)

Microbioreactors, even with their high potential, are still in the development phase without standardized techniques. There are still many research questions and problems to study and solve. One task is to integrate these devices with widely used laboratory equipment, such as pumps and gas supply. Another question is how to measure and control environmental parameters, as implementing the sensors and actuators can be challenging in microscale devices. Modeling tools are often the only way to study certain issues in these microbioreactors, so they have been widely used in the design process. In this thesis, several mathematical models have been developed to study fluid flow and drug delivery, CO_2 transport and medium pH, and temperature in microscale cell culture devices. In addition, a novel, non-invasive temperature control method is implemented.

1.2 Objectives and Research Questions

The fundamental objective of this thesis is to determine if modeling and indirect control methods enhance the performance of microscale *in vitro* cell cultures by improving the surrounding environment. More precisely, this thesis has two main objectives. The first is to develop mathematical models for a deeper understanding of the cell culture microenvironment and using these models as design tools to enhance cell culturing in microsystems. The second goal is to see if the cell culture microenvironment could be indirectly controlled and what advantages this may have. This thesis demonstrates this

objective by integrating an indirect temperature control system to a developed microscale cell culture device. To summarize, the specific research questions in this work are:

- Can numerical modeling tools be used to study gravity-driven flow and drug concentration profiles in microscale systems, without the need for extensive computation time?
- Can CO_2 transport and medium pH be estimated using numerical methods in silicone-based microscale cell culture devices, as only O_2 transport models in these devices have been reported?
- Is an indirect temperature measurement method acceptably accurate to successfully monitor and control temperature for long-term cell culturing purposes?

1.3 Main Results

The main scientific contributions of this thesis are listed below.

- A model for studying, designing, and optimizing gravity-driven flow (GDF) in microfluidic devices.
- A method that integrates GDF and a finite element method (FEM) model to estimate drug delivery and concentration gradients in these devices, without the need for computation-intensive calculations.
- An analysis tool to optimize flow measurement in microfluidic devices using GDF.
- A mathematical model to study transient CO_2 transport and pH of the liquid in silicone-based microfluidic devices.
- A method to precisely measure and control cell culture temperature using indirect measurement and system identification.

To clarify, Figure 1.2 shows the main contributions of each publication and their relationships.

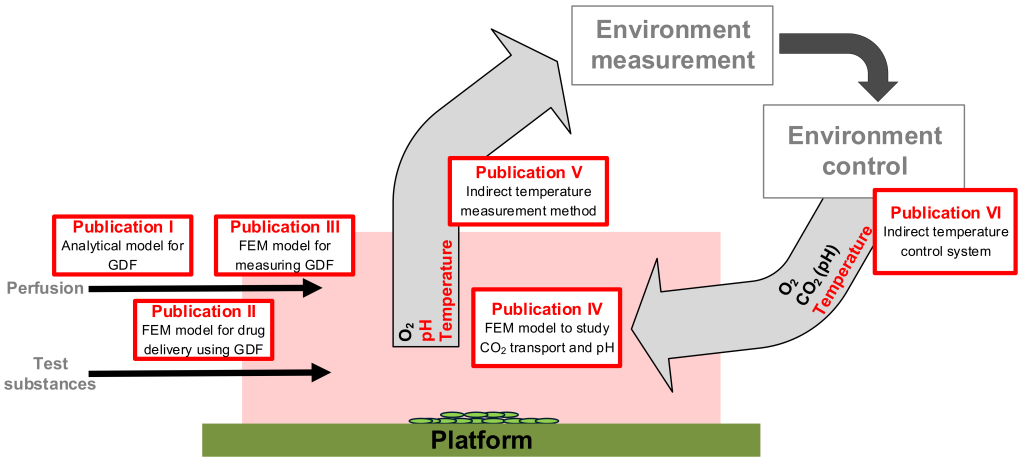

Figure 1.2: Main results from the publications of this thesis.

1.4 Outline

This thesis comprises five peer-reviewed scientific papers and one unpublished manuscript, and is divided into six chapters. Chapter 2 presents the relevant background for the study and highlights the current challenges that this thesis aims to solve. Chapter 3 explains theory related to this work. It includes all equations that are implemented in the developed models and control systems.

Chapters 4 and 5 cover research work related to this thesis. Chapter 4 presents the modeling work from Publications I – IV. Chapter 5 summarizes the developed temperature measurement and control method for cell culture microenvironments presented in Publications V and VI. Both chapters are separated by sections, each concerning one publication. The materials and methods are briefly presented before summarizing the main results. Finally, Chapter 6 concludes the main findings from this thesis and proposes the next steps that could be taken to improve microscale *in vitro* cell cultures.

Chapter 2

Background

In this chapter, a short overview of the cell culturing environment, modeling, and control issues related to this thesis are provided. The focus is on a microscale cell culturing environment that is required for successful long-term human cell culturing. The purpose is to summarize previous results from the literature and put them into context of the author's work.

2.1 Introduction

In vitro cell culturing is one of the fundamental techniques used in biotechnology, biomedical engineering, and clinical diagnostics. It refers to the cultivation of cells in a controlled, artificial environment that is outside of their biological surroundings. This complex environment may consist of extracellular matrices, cell-to-cell interactions, growth factors, essential nutrients, substrates, and physical microenvironmental conditions. A system for cell cultures that includes environmental control systems to maintain all culture conditions (such as temperature, O_2, and pH as shown in Figure 1.1) in desired values is typically called a bioreactor. For successful long-term cell culturing, it is crucial that the bioreactor maintain a stable microenvironment. On the other hand, a precisely controlled microenvironment is desirable to study cell responses to environmental changes. One of the main reasons to use human cell culture models *in vitro* in these tests is their simplicity compared to complex human pathophysiology, providing easier methods to study cellular behavior and the effects of toxic compounds or drugs (Jiang et al., 2014; Nelson et al., 2010; Pasirayi et al., 2011; Petronis et al., 2006). Obviously, an *in vitro* cell culture model should always represent the physiological phenomena of interest with reasonable accuracy, so that all experiment results are reproducible and consistent. These models are an important part of fundamental research, as they help us understand cellular and molecular biology, enable cell therapy, and can be used to study disease processes (Davis, 1994; Vickerman et al., 2008; Yum et al., 2014).

Development of new drugs is an extremely expensive process that can take more than 10 years and cost more than US$1 billion dollars. A major part of the expenses comes from candidate failures in the clinical trials. Clearly, it is vital to obtain reliable data during the pre-clinical studies to minimize the risk of failure in later stages of the development (Amir-Aslani and Mangematin, 2010; Coppeta et al., 2017; DiMasi et al., 2003; Perestrelo et al., 2015; Piccini et al., 2009; Scannell et al., 2012; Sung et al., 2010). Traditionally, animal tests and models have been used in this development process. However, there are several

drawbacks to these conventional drug-screening methods, from their slowness and ethical issues, to the fact that developed models often cannot predict human toxicity and efficacy. Because of rising production costs, the pharmaceutical industry is now looking for new ways to improve the drug development process. One promising solution is the use of cell culture models in the later stages of pre-clinical testing. The idea is to generate models that would better mimic human physiology and provide reliable human responses to drugs and other chemicals. It is even possible to predict patient-specific responses to drugs using patient-specific cell models. Studies using physiologically relevant cell culture models have significantly reduced the need for testing on living animals and humans (Christen and Andreou, 2007; Dambach et al., 2005; Jiang et al., 2014; Lahti et al., 2012; Perestrelo et al., 2015; Shuler, 2017; Trevisan et al., 2015; Yoshimitsu et al., 2014; Yum et al., 2014).

Traditional cell culturing, in which cells are typically plated in a standard vessel with media and reagents, and stored in an incubator or a bioreactor, is a widely used and well standardized technique to get reliable results. However, there are some limitations with this method. Commercial incubators usually provide uneven conditions, such as temperature, for cells stored in different parts of the devices. This is undesirable, as changes in the culture conditions can affect cell behavior, physiology and product quality, creating artifacts in the experimental data. Stem cells are particularly sensitive to their local microenvironment, as it regulates their survival and differentiation. Furthermore, continuous monitoring, tracking, imaging, and manipulation is not possible in typical culturing processes as cells must be taken out of the incubating device for observation, thereby limiting studying dynamical processes of the cells (Christen and Andreou, 2007; Discher et al., 2009; Petronis et al., 2006; Vu et al., 2017). This typically creates large, uneven environmental conditions for the cultures and reduces the usability of parallel experiments. Furthermore, uneven conditions increase in a typical laboratory environment as the incubator door is continuously opened and closed. These problems have created a need for a system that combines cell manipulation, monitoring and controlling of multiple environmental parameters, and high-resolution imaging for obtaining *in vitro* results that closely predict *in vivo* situations and improve drug development processes. One interesting solution is a miniaturized version of a bioreactor that provide better environmental control with online cell culture monitoring and manipulation (Figallo et al., 2007; Jiang et al., 2014; Oomen et al., 2016; Rodrigues et al., 2011; Titmarsh et al., 2011). These systems, called microbioreactors, combine microfluidics and microfabrication techniques, and are discussed in the next section.

2.2 Microbioreactors

Microbioreactors are downscaled version of bioreactors. Compared to conventional *in vitro* cell culturing methods, they provide, as explained in Section 1.1, a more controllable environment. This enables them also to mimic the cells' natural microenvironment more closely (such as the shear stress level), enhancing long-term cell culturing. This is very important for various biological cell studies. Microscale culture systems are not only cheaper, but they also reduce the usage of reagents, time, power and other resources, and provide better control of environmental parameters. Furthermore, it is easy to parallelize these systems to provide a high-throughput platform to simultaneously study biological processes, such as stem cell differentiation, or test different drug compounds. With microfabrication, it is possible to construct geometries and structures for the cells, such as grooves. It is also very useful that many control parameters can be varied separately, while simultaneously performing cell imaging (Bhatia and Ingber, 2014; Duffy et al., 1998;

Jiang et al., 2012; Karimi et al., 2016; Kim et al., 2007; Macown et al., 2014; Pasirayi et al., 2011; Tehranirokh et al., 2013; Vu et al., 2017; Weigl et al., 2003; Yi et al., 2006; Yoshimitsu et al., 2014; Yum et al., 2014).

Microfluidics serves as a cornerstone of microbioreactors. Microfluidics controls small amounts of fluids flowing in submillimeter geometries. Flow in small dimensions is typically laminar, such that the behavior of flow can be precisely predicted, providing opportunities for accurate flow control. Together with high surface-to-volume ratio flow, these issues make microfluidics beneficial in nutrient transport, sample handling, reagent mixing, and cell differentiation, separation, and detection. Furthermore, with microscale devices, microfluidics helps control gas concentrations (Jiang et al., 2014; Weigl et al., 2003; Yoshimitsu et al., 2014; Yum et al., 2014).

Microbioreactors scale down reaction volumes. Therefore, smaller volumes of expensive reagents are required for pharmacokinetic studies, potentially lowering drug development costs. These systems can also help researchers better understand the action mechanism of the drug. One important goal is rapid development of informative, versatile human models that correctly predict human response to compounds. Therefore, using these models in the later stages of pre-clinical testing (studying drug toxicity and efficacy) could potentially increase the success rate of drug candidates in clinical trials. In addition, physiologically relevant models could be used to study toxicological responses to products such as cosmetics and food ingredients (Coppeta et al., 2017; Jiang et al., 2014; Shuler, 2017; Sung et al., 2010).

Typically, microfluidic devices for cell applications are fabricated from silicone elastomers. Compared to silicon and glass, inexpensive material and easy fabrication processes make elastomers ideal for rapid prototyping and flexible design. Currently, probably the most commonly used material is polydimethylsiloxane (PDMS), which has been extensively used to fabricate various microfluidic devices for cell cultures, using a technique known as soft lithography. This technique replicates the structure of the master by casting PDMS over it, and then degassing and curing them, before removing the PDMS from the master. PDMS-based devices are popular in biological studies because PDMS is optically transparent, biocompatible, and permeable to gas, allowing optical microscopy and gas control, as discussed in the next section (Christen and Andreou, 2007; Duffy et al., 1998; Merkel et al., 2000; Whitesides, 2006) .

However, as with any emerging technologies, there are still some fundamental challenges to using PDMS for biological studies and drug discovery. Some problems are related to fabrication, such as a need for specialized microfabrication capabilities and problems with scaling up this manufacturing process. Another issue is that PDMS can absorb small molecules such as drugs, which alters the concentration of the investigated compound. It also adsorbs proteins, which can lead to clogging of the microchannels. There are some surface modification methods to reduce both absorption and adsorption, but these complicate the fabrication process and can lower biocompatibility of PDMS. Therefore, many microbioreactors combine PDMS and other materials (such as glass) to overcome this problem (Caballero et al., 2017; Coppeta et al., 2017; Lynn and Dandy, 2009; Merkel et al., 2000; Ngo et al., 2016; Toepke and Beebe, 2006; Tsao, 2016; Velve-Casquillas et al., 2011; Whitesides, 2006; Yi et al., 2006; Young and Beebe, 2010; Yum et al., 2014).

As presented above, microscale bioreactors are a very promising tool for drug development and study of biological systems. One major drawback compared to conventional methods is that there are no standardized cell culturing tools or analyzing methods available. To achieve widespread usage of microbioreactors within the biomedical community, it should

be possible to use standard culturing and analyzing techniques. These devices should also be user-friendly, so that people working with cells do not need extensive training to use the microbioreactors. Although scaling down has several benefits, it also provides some challenges such as maintaining precise fluid volume for long-term cell cultures (from days to weeks) without clogging microchannels and preventing liquid evaporation (Coppeta et al., 2017; Lynn and Dandy, 2009; Yum et al., 2014). To overcome the latter problem, and minimize osmolarity change of cell culture medium, we developed a system to supply dry gases (CO_2 or O_2) through a gas-permeable PDMS ring (Kreutzer et al., 2017). This method is used for several studies in this thesis.

2.3 Cell Culture Environment

Figure 1.1 shows a simplified presentation of a cell culture microenvironment. Environmental conditions for mammalian cell cultures are usually set to 37 °C, 5% CO_2, and 95% air to provide successful growth for most mammalian cells. Evaporation of liquid is minimized by setting humidity close to 100%. The next sections examine the main culture environment parameters related to this thesis, starting with fluid flow, which provides nutrients and drug compounds to cells and removes waste.

2.3.1 Fluid Flow

One of the main goals of *in vitro* cell culturing is to mimic *in vivo* cellular microenvironmental conditions, while keeping simplicity. For example, cells experience continuous flow in their natural microenvironment. Furthermore, with the use of relative small liquid volumes, the pH and osmolarity of cell media easily shift in static microscale *in vitro* cultures because of cell growth and proliferation, or medium evaporation. Therefore, perfusion systems that continuously supply fresh nutrients and remove waste for *in vitro* cell cultures are important for successful, long-term cell culturing. Furthermore, a proper shear stress level for cells can be provided, as it is possible to more precisely control the extracellular microenvironment to mimic real physiological conditions in microscale systems. These systems can also be used for delivery of drug compound to cells, and help to understand better the action mechanism of the compound. This together with smaller culture and reagent volumes requirements in microscale systems, provide a potential for higher-throughput drug screening than conventional methods (Caballero et al., 2017; Caicedo et al., 2010; Coppeta et al., 2017; Kim et al., 2007; Song et al., 2011; Yoshimitsu et al., 2014; Young and Beebe, 2010).

Liquid is typically perfused in microbioreactors using external devices, such as peristaltic or pressure-driven syringe pumps. However, passive methods, such as gravity-driven (Chen et al., 2011a; Dimov et al., 2011; Gao et al., 2012; Kim and Cho, 2011; Kim et al., 2012; Sung et al., 2010; Zhu et al., 2004) and surface-tension-driven (Berthier and Beebe, 2007; Resto et al., 2010) pumping, do not require external pumps, tubing, and interconnections. This greatly simplifies the fluidic system, so cheaper and more portable (i.e. it is easier to move the device in the laboratories) microfluidic systems could be fabricated.

Major drawbacks of using the passive pumping method include limited flow control and challenges for reconfiguration (Caballero et al., 2017; Coppeta et al., 2017; Young and Beebe, 2010). However, with careful designing, fluid flow can be controlled to stay within certain limits for a required time period. These issues are considered in Publication I, and study is further extended to cover drug delivery in Publication II. Another challenge is that microchannels can get clogged during operation, so flow rate

monitoring is desirable. However, many used flow rate sensor types cannot easily be implemented to microbioreactors, due to practical concerns and limited space. Fortunately, advanced micromachining processes allow for integrating miniaturized calorimetric flow sensors to microfluidic devices. In this non-invasive, online method, flow rate and direction is measured without the need for any moving parts, resulting in sensors with low power requirements and fast responses. For these reasons, replacing a conventional pumping system, such as a syringe pump, by a gravity-driven pump and combining it together with a calorimetric sensor provides an interesting approach for developing a cost-effective, more portable microfluidic system (Meng et al., 2008; Que and Zhu, 2014; Sun and Cheng, 2013). Publication III presents a numerical model to study this sensing method in gravity-driven microfluidic devices.

2.3.2 Gas Transport and Medium pH

Proper parameters of the cell medium, such as dissolved oxygen concentration and pH, are essential for successful cell cultures. Oxygen is not only a regulatory parameter that influences on cell differentiation and function, but is also vital for cells' energy metabolism (Oomen et al., 2016). Microfluidic devices have been developed to generate desired O_2 concentrations for cell cultures by using gas permeability properties of PDMS (Adler et al., 2010; Chang et al., 2014; Chen et al., 2011b; Funamoto et al., 2012; Lee et al., 2006; Lo et al., 2010; Oppegard et al., 2009; Peng et al., 2013; Polinkovsky et al., 2009; Shiku et al., 2006; Skolimowski et al., 2010; Thomas et al., 2011; Vollmer et al., 2005; Wang et al., 2013a; Zahorodny-Burke et al., 2011).

Cell media with mammalian cell cultures are typically formulated with a combination of $NaHCO_3$ and 5% CO_2, resulting a pH of 7.2-7.4. Proper pH value of the cell media is important, as even a small deviation (0.1 units) from the optimal pH value can have a large impact on cell growth and metabolism. Furthermore, as cells take in O_2 and release CO_2, the cell media could alter pH without a controlled environment (Eddington et al., 2001; Li et al., 2010).

Although providing a proper CO_2 concentration is a typical method to control the cell-media pH value in microscale devices (Forry and Locascio, 2011; Kim et al., 2007; Kreutzer et al., 2017; Läritz and Pagel, 2000; Li et al., 2010; Mazzei et al., 2008; Polinkovsky et al., 2009), other control strategies have also been reported. Eddington et al. (2001) presented a concept for self-regulating pH, based on a passive hydrogel to control flow, whereas Futai et al. (2006) developed a CO_2-independent cell culture medium by improving its buffering capacity. Cell media have also been maintained at proper physiological pH level by filling the surrounding area of the microfluidic device with a mixture of deionized (DI) water, Na_2CO_3, and $NaHCO_3$ (Takano et al., 2012, 2014; Yu et al., 2014). Cheng and Chang (2011), demonstrated that constant pH regulation and generation of stable pH gradients in microscale could be created using field-enhanced water dissociation. Lee et al. (2006) maintained pH by periodic injection of base. In more sophisticated systems, pH control was based on controlled dosing of two reagents (an acid and a base), together with continually measuring pH, providing a real-time control system (Funke et al., 2010; Welch and Christen, 2014).

2.3.3 Temperature

Temperature plays a vital part of successful cell culturing. For instance, small temperature variations (1-2°C) altered cardiomyocyte beating characteristics (Laurila et al., 2016),

and modulated the firing rate during up states in the cortical network (Reig et al., 2010). Furthermore, lower temperature can result in softer cells with slower activity (Picard and Donald, 2009). Density and fluid viscosity in cell culturing environments are also temperature-dependent, as is oxygen measurement to ensure stable operations. Furthermore, temperature uncertainty can be one of the main reasons for biological variability in cell cultures.

To summarize, a key component for achieving reliable data for cell culture-based modeling studies is a physiologically relevant microenvironment, in which precise temperature control plays a vital role (Chong et al., 2008; Fang et al., 2017; Gruber et al., 2017; Picard et al., 2010; Portillo-Lara and Annabi, 2016; Velve-Casquillas et al., 2010). This emphasizes the potential of microscale devices, in which localized temperature control is easier than in macroscopic systems. These devices also allow for faster temperature changes because smaller sizes decrease thermal time constants (Fang et al., 2015; Lin et al., 2011; Velve-Casquillas et al., 2011). Therefore, microscale devices allow more precise study of thermal effects on cells, as presented in Publication VI.

2.4 Modeling and Control

2.4.1 Modeling

One main focus of this thesis is on mathematical modeling of the cell culture microenvironments. In these environments, modeling is greatly needed for multiple reasons. For example, measuring the cell culture microenvironment is not always easy. Getting good measurement data is often challenging in these small dimensions, as it can difficult to properly insert the sensor. In other cases, taking measurements can be practically impossible, as there are currently no sensors with suitable size available, or the environment may be too hostile for the sensor to be used for long-term measurements. In addition, many sensors and measurements can negatively affect the cells or prevent optical inspection of the cell cultures. It is often not feasible to measure distribution in larger areas, such as the uniformity of temperature through the entire cell culture area. Luckily, modeling provides a method to overcome these issues. As numerical simulations provide insights to the underlying mechanisms in the experiments, they can provide vital information to improve future designs and devices. This can lower the amount of needed expensive prototypes by quickly simulating various designs and choosing the most optimized one (Boy et al., 2008; Caicedo et al., 2010; Christen and Andreou, 2007; Hellé et al., 2015; Kumar et al., 2013; Peng et al., 2013; Sebastian and Wiesmann, 2008; Tourlomousis and Chang, 2016; Węgrzyn et al., 2013; Weigl et al., 2003).

Partial differential equations are used to express the laws of relevant physics. They can solve both stationary and time-dependent problems in cell culturing environments. However, numerical methods are required to find solutions to more complex problems, as solving these equations using the analytical method are limited to very simple physics and geometries. One option is to create a mathematical model based on a state-space representation that uses a set of input, output, and state variables to describe the system. With this method, only one first-order matrix differential equation is required, instead of using high-order differential equations. These models are also needed for modern control methods, so the use of state-space representation is typically called the modern, or time-domain, approach (Dorf and Bishop, 2005, pp. 131 – 137). Section 3.3 provides more detailed information about state-space models.

We used FEM for the other modeling works related to this thesis, as it is suitable for solving multiphysical problems in complex geometries. FEM uses elements of finite dimensions, known as finite elements, to divide the considered system into smaller parts (also called meshing). The solution to the structure is then approximated through these elements. As partial differential equation can have several (or even infinite) solutions, boundary conditions in the model must be defined to constrain the solution. The model is solved using an appropriate numerical solver that depends on the problem (linear or nonlinear, stationary or time-dependent). The FEM simulation can be used to optimize geometry for a specific application. It should be stated that models are generally a simplified representation of the system, so any obtained data should only be used as guidelines to evaluate the effect of multiple parameters (Hellé et al., 2015; Reddy, 2006; Vozzi et al., 2010).

One of the most important issues in FEM is proper meshing. In general, denser mesh will improve model accuracy to a certain level. However, the cost is increased computation time. Solutions should also always be mesh-independent, meaning that there are only negligible changes in the solution when the mesh is refined. Therefore, it is important that the mesh is optimized for the problem to provide a computationally efficient model that provides a solution with reasonable accuracy. To ensure that modeling results are not meaningless, validating the model is always required. Ideally, this should be done with experimental investigation, whenever possible (Christen and Andreou, 2007; Jani et al., 2012; Kumar et al., 2013). Figure 2.1 shows an example of an FEM model, with a mesh and a calculated velocity distribution.

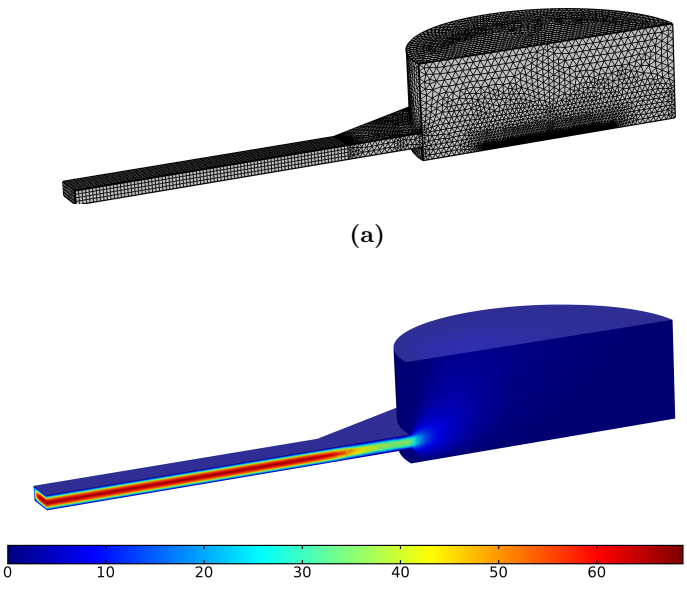

(a)

(b)

Figure 2.1: Demonstration of a FEM simulation: (a) generated mesh; and (b) the solved velocity distribution (unit µm/s).

2.4.2 Identification

A mathematical model of the system is often beneficial, as it can be used to study things such as system dynamics and control dynamics. However, determining a suitable model for these systems is not always easy, typically because of unknown parts of the system or the complexity of the studied phenomena. System identification techniques, in which measured experiment data is used to construct a model of the process, can be one solution. The idea is to select a model structure that, with certain criteria, reasonably describes the actual output of the system. The task is finding a proper model that provides acceptable output when input data is used. The selected model should be as complex as possible to fulfill its purpose, but simple enough that it still meets the requirements and reasonably describes the dynamics of the system. The purpose of starting the identification process with simpler models is to prevent overfitting the model (Barbosa et al., 2011; Ljung, 1978; Nielsen and Madsen, 2006; Shamloo et al., 2016; Sjöberg et al., 1995; Sohlberg, 2003; Worden et al., 2007).

Development of the model using system identification techniques involves an estimation measurement, creating the candidate, and validating the model. The first two techniques can be categorized into a learning state, in which a candidate model is adapted by using input-output data from the estimation measurement. Usually, there are a set of model structures that are further studied with input-output data, and then the most suitable structure is chosen. This selection is based on the comparison of the estimated and measured output data. After the learning state, it is always highly recommended to validate the candidate using a separate measurement. If an unsatisfactory response is obtained, a more suitable candidate, such as a higher order or a different model structure, is searched using the estimation measurement. When acceptable model response is obtained, this candidate is adapted for the system model (Ljung, 1978; Sjöberg et al., 1995; Sohlberg, 2003) .

One main benefit of the identification approach is that prior knowledge of the system can be limited (so-called grey-box modeling) or not needed at all. In the latter technique (black-box modeling), the model is developed purely based on input-output data, without prior knowledge of the system or physics. In Publications V and VI, we created temperature estimation, state-space models using this technique. An identification-based control system was developed in Publication VI to indirectly control the cell culture temperature. The identification approach can also automatically include fabrication tolerances and other uncertainties in practical situations in the model. Identification also provides opportunities for easier integration of modules, such as a thermal control system, onto microscale devices (Jiang et al., 2012; Kaigala et al., 2010). Furthermore, it is possible to study what type of input signals are needed for the desired output response by inverting the model (Barbosa et al., 2011; Kaigala et al., 2010; Nielsen and Madsen, 2006; Sebastian and Wiesmann, 2008; Sohlberg, 2003). In miniaturized devices, identification technique has been used to create a model-based heater controller that separates the heating elements from the microfluidic chip (Kaigala et al., 2010), analyze cellular processes (Seker et al., 2011), and develop a model that describes droplet motion in pressure-driven microfluidic channels (Wong and Ren, 2016).

2.4.3 Control

In cell culturing, environmental parameters such as pH, dissolved oxygen, temperature, and fluid flow are important (Li et al., 2010). The goal is to keep the output close to the

desired set-point value. From the control viewpoint, there are two design considerations for the controller: It should regulate around a set-point level within minimal error levels; and provide satisfactory (fast enough) responses to transient set-point level changes. The challenge is finding the optimal controller to provide the most suitable response for the system when considering design parameters such as limited input signal. A common control method is to implement a feedback control system, also known as a closed-loop control system. In these systems, measured output is compared to the desired set-point. This difference is then feed to the controller that calculates a proper signal that is fed to the system. Closed-loop control systems are widely used, as they reduce noise, increase system stability, and work with different signal types (Dorf and Bishop, 2005, p. 204; Kaigala et al., 2010; Welch and Christen, 2014). For example, closed-loop systems have been designed to control fluid flow (Huang et al., 2011), droplet movement (Wong and Ren, 2016), temperature (Christen and Andreou, 2007; Huang et al., 2011; Jiang et al., 2012; Kaigala et al., 2010; Lee et al., 2006; Yu et al., 2014), oxygen (Lee et al., 2006; Mazzei et al., 2008; Polinkovsky et al., 2009), and pH (Lee et al., 2006; Mazzei et al., 2008; Welch and Christen, 2014).

2.5 Current Challenges

This section highlights current challenges and scientific gaps in cell culturing *in vitro* related to this thesis. Problems and solutions are presented here at only a very general level. Detailed explanations of each publication are given in the following chapters.

As there are no standardized microbioreactors, culture conditions for different types of cells must be optimized. The difficulty is designing a user-friendly, simple system suitable for lab workers, while still mimicking the vital characteristics of living tissue. Therefore, standardization of design and fabrication principles is vital for widespread usage of microbioreactors. In this process, modeling the cell culture microenvironment is a valuable tool to optimize these devices. The models developed in this work are described next.

Publications I to III examine gravity-driven flow in microfluidics devices. Gravity-driven flow uses a passive pumping method to replace external devices such as syringe pumps. Publication I showed that many earlier studies concerning gravity-driven pumps and microfluidics did not consider capillary forces (Chen et al., 2011a; Dimov et al., 2011; Gao et al., 2012; Kim and Cho, 2011; Kim et al., 2012; Lam et al., 2006; Sun et al., 2008; Sung et al., 2010) or reported that these forces were cancelled out (Zhu et al., 2004). However, Publication I demonstrated that capillary forces do play an important part in typical microfluidic systems. Flow rate is overestimated in models without capillary forces, possibly leading to undesirable fluid flow. To solve this problem, we used electrical analogy to create a simple, but sufficiently precise, analytical model to estimate gravity-driven flow in these devices.

Publication I was further extended in Publication II to cover drug delivery. We developed a model to study drug distribution and shear stress in a gravity-driven microfluidic system. The major problem with conventional numerical methods is that time-dependent solutions are only at the scale of seconds at most because of computationally-intensive calculations of two-phase (gas and liquid) flows, while typical time scales of gravity-driven systems go from minutes to days. Publication II suggested combining the model presented in Publication I with FEM simulations. This approach will significantly reduce required computation time, while still providing acceptable simulation accuracy.

As microchannels can get clogged while the gravity-driven device is running, usually due to gas bubbles introduced into the channel (Bruus, 2008), it would feasible to continuously monitor fluid flow in these systems. One solution is to use miniaturized, calorimetric flow sensors. A calorimetric flow model is useful to optimize, for instance, measurement sensitivity. This sensor has been modeled in many studies (Kim et al., 2009; Palmer et al., 2013; Que and Zhu, 2014; Sazhin, 2013), but, to the best of our knowledge, there are no published models that combine calorimetric flow sensor to gravity-driven flow systems. Publication III presents this combination.

Proper O_2 and CO_2 concentrations are important for *in vitro* cell cultures. As long-term measurements of these concentrations are not easy to implement, numerical models would provide a valuable design tool to optimize the structure of the cell culturing device. It can also be very difficult to measure uniformity of gas concentration in the entire cell culturing area (Peng et al., 2013). Transport of O_2 in PDMS-based microfluidic cell culturing devices has been extensively modeled (Adler et al., 2010; Chang et al., 2014; Chen et al., 2011b; Funamoto et al., 2012; Inamdar et al., 2011; Peng et al., 2013; Polinkovsky et al., 2009; Shiku et al., 2006; Skolimowski et al., 2010; Thomas et al., 2011; Vollmer et al., 2005; Wang et al., 2013a; Zahorodny-Burke et al., 2011). However, transport of CO_2 was modeled for the first time in Publication IV.

Properly controlled temperature is important for long-term cell cultures *in vitro*. Precise temperature control typically requires that the measurement be taken directly from the cell culture, which may raise some problems. For example, the sensor can disturb cell growth and interrupt optical microscopy. One typical solution is to place the sensor next to the cells. However, this would require a larger chamber (Petronis et al., 2006; Picard et al., 2010). Therefore, temperature sensors are placed outside the chambers in many culture devices. For instance, sensors can be located close to the culture chamber or the inlet of the chip (Pennell et al., 2008; Wang et al., 2013b), in a withdrawal chamber (Vukasinovic et al., 2009), or simply next to the device (Abeille et al., 2014). Sensors can also be integrated with the heating element (Habibey et al., 2015; Jang et al., 2016; Saalfrank et al., 2015). One major problem with these solutions is that they cannot precisely control the temperature, as they do not measure temperature in the cell culturing area. To reduce this error, some studies have implemented a separate reference chamber, including a temperature measurement (Biffi et al., 2012; Lin et al., 2010; Regalia et al., 2016). However, this requires an extra space for the chamber that is only used for temperature measurement. Some solutions, in which the sensor is located outside the device but can still provide precise temperature control, have been demonstrated (Buhler et al., 2017; Regalia et al., 2016; Reig et al., 2010), but seem rather complex. A water bath surrounding the chamber is used, resulting in long settling times during the heating phase. In addition, there may be still problems with avoiding significant temperature differences in different parts of the chamber (Petronis et al., 2006). Direct temperature measurements, based on optical detection methods, have also been demonstrated (Glawdel et al., 2009; Ross et al., 2001; Samy et al., 2008). One challenge is that measurement precision (approximately 2.5 °C at 37 °C (Ross et al., 2001)) is not sufficient for cell culturing studies. For the aforementioned reasons, we proposed an indirect temperature measurement and control method in Publications V and VI, in which the desired cell culturing area temperature is controlled by outside measurement and the developed model that estimates the temperature in the cell culturing area.

Chapter 3

Theoretical Background

3.1 Microfluidic Perfusion Culture, Gravity-Driven Flow, and Drug Delivery

This section covers the theory of liquid flow, as it relates to this thesis. As we mainly deal with relatively slow, pressure-driven flows in microchannels, a few reasonable assumptions can be made to calculate and model microfluidic flow. We expect that fluid is incompressible and Newtonian, with uniform viscosity. We also assume that flow remains within the Stokes flow region, in which inertial forces are small compared to viscous forces. This can be characterized by a commonly used, dimensionless parameter, known as the Reynolds number Re. It describes the ratio of inertial to viscous forces in a fluid and is calculated using (Berthier and Silberzan, 2006, p. 11)

$$Re = \frac{inertial forces}{viscous forces} = \frac{\rho v L}{\eta} \tag{3.1}$$

where ρ and η are the density and dynamic viscosity of liquid, respectively, and v and L are flow velocity and characteristic length, respectively. The maximum Re in our studies is small (< 1), resulting in a steady-state, fully developed, laminar flow with negligible unsteady forces. In addition, any external forces, minor losses, or hydrodynamic entrance-length effects are not considered (Galvis et al., 2012; Solovitz and Mainka, 2011). It should be emphasized here that in gravity-driven flow systems considered in this thesis, gravitational forces create pressure differences that drive liquids from the inlets towards the outlets, and the resulted flows have small Reynolds numbers. Therefore, we can linearize the Navier-Stokes equations and solve the velocity field matrix $\boldsymbol{v}$, using the time-dependent Stokes equations for incompressible Newtonian fluids (p is the fluid pressure)

$$\begin{aligned} \eta \nabla^2 \boldsymbol{v} - \nabla p &= 0 \\ \nabla \boldsymbol{v} &= 0 \end{aligned} \tag{3.2}$$

Using previously mentioned assumptions, we can use the Hagen-Poiseuille law to estimate flow rate Q. The law states that the pressure difference $\Delta p(t)$ between the inlet and outlet of the channel is proportional to the $Q(t)$. The law is analogous to Ohm's law in electric circuit analysis, which states that a voltage drop over a resistive conductor is the electrical resistance multiplied by the electric current through the conductor. This hydraulic electric circuit analogy is very useful when estimating steady-state pressure

drops over microchannels and can be generalized to (Kang and Banerjee, 2011; Oh et al., 2012)

$$\Delta p(t) = R_{hyd} Q(t) \Rightarrow Q\,(t) = \Delta p(t)/R_{hyd} \tag{3.3}$$

where R_{hyd} is the hydraulic resistance of the channel. In theory, the law applies only for a pressure-driven flow in a circular, infinitely long, perfectly straight channel. However, it is also a good approximation for non-circular and finite-long channels, as long as the Re is small and the channel length (L_c) is much larger than any cross-sectional channel dimension (Oh et al., 2012; Solovitz and Mainka, 2011). Therefore, we used this approximation in our work. This method can be used to find the flow rate through a given microfluidic network, but it does not provide detailed information about the flow field. However, data about the flow rate is often sufficient information (Oh et al., 2012). To determine the hydraulic resistance of a channel with rectangular cross-section (channel width w_c and height h_c so that $w_c > h_c$) R_{hyd_rec} (Fuerstman et al., 2007)

$$R_{hyd\_rec} = \frac{12\eta L_c}{h_c^3 w_c}\left(1 - \frac{192 h_c}{w_c \pi^5}\tanh(\frac{\pi w_c}{2h_c})\right)^{-1} \tag{3.4}$$

In microchannels, capillary forces should be considered in two-phase flows. These forces are located between gas and liquid interfaces. The hydraulic radius r_h is defined as (Berthier and Silberzan, 2006, p. 20)

$$r_h = 2A/P_{wet} \tag{3.5}$$

where A and P_{wet} are the cross-sectional area and the wetted perimeter of the geometry, respectively.

A capillary pressure drop between advancing and receding fronts of liquid is due to unequal advancing and receding contact angles (θ_a and θ_r). When assuming constant contact angles and surface tension, the capillary pressure drop (Δp_{cap}) is defined by (Berthier and Silberzan, 2006, p. 43)

$$\Delta p_{cap} = 2\sigma_{lg}\left(\frac{-\cos(\theta_a)}{r_{ha}} + \frac{\cos(\theta_r)}{r_{hr}}\right) \tag{3.6}$$

where σ_{lg} is the surface tension between liquid-gas interface, and r_{ha} and r_{hr} are the hydraulic radii at the points where advancing and receding interfaces, respectively, are located. If these points have the same cross-section, such as both interfaces inside the uniform channel, we get $r_{ha} = r_{hr} = r_h$ (hydraulic radius of the geometry where liquid-gas interfaces are located). The previous equation can then be simplified to

$$\Delta p_{cap} = 2\sigma_{lg}\left(-\cos(\theta_a) + \cos(\theta_r)\right)/r_h \tag{3.7}$$

Publication I considered gravity-driven flow, in which the working pressure is created without any external pump. Instead, the height difference $\Delta h\,(t)$ between the liquid plug levels at the inlet and outlet reservoirs was used. Hydrostatic pressure for an incompressible fluid is defined as

$$p_{hyd}(t) = \rho g \Delta h(t) \tag{3.8}$$

where g is gravitational acceleration. Figure 3.1 shows the working principle of gravity-driven pumping in a microfluidic system. When the liquid plug level is higher in one

reservoir (the inlet reservoir, in this case) than in the other (the outlet reservoir), hydrostatic pressure is created (Eq. (3.8)). This pressure pushes the liquid from the inlet reservoir toward the outlet reservoir, through the microchannel between the reservoirs. While liquid is flowing, the height difference and the hydrostatic pressure are reduced, slowing flow rate. The flow rate is related to the hydrostatic pressure and the hydraulic resistance of the system.

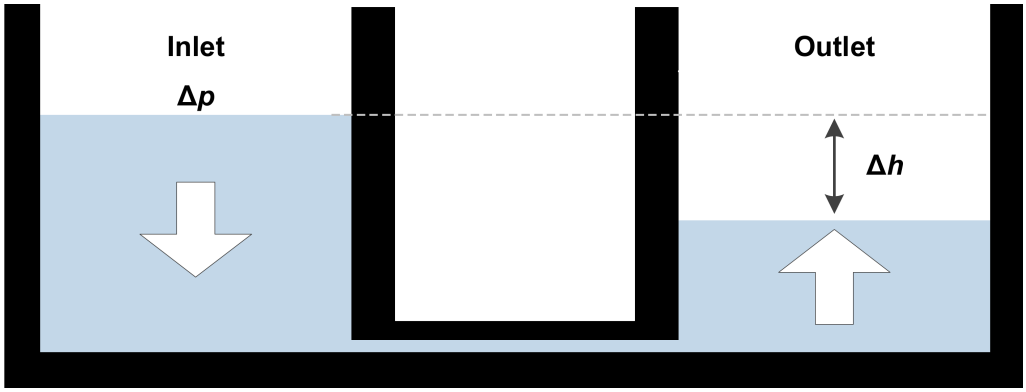

Figure 3.1: Working principle of the gravity-driven flow (not to scale). Liquid flow is driven by hydrostatic pressure created by the liquid level difference Δh between inlet and outlet reservoirs.

Low hydrostatic pressure is used in the work related to this thesis. Therefore, we assume that there is no deformation of microchannels. The hydraulic resistance of the channel can be modeled as purely resistive, without any dynamic parts. Furthermore, the model assumes a constant temperature, and constant fluid density and viscosity without evaporation or condensation of the liquid. An equal atmospheric pressure should prevail in both reservoirs, so their effects cancel each other out. If we take together these assumptions, the equations presented earlier and the fact that capillary forces oppose hydrostatic pressure for the systems in this work, the flow rate of steady-state, gravity-driven laminar flow over microchannel can be approximated when we know the total pressure drop $\Delta p(t)$. When the inlet and outlet reservoirs have identical cross-section areas, we can use the previous equations and calculate the flow rate at different time instants by

$$\begin{aligned} Q(t) &= \frac{\Delta p(t)}{R_{hyd}} = \frac{(p_{hyd}(t) - \Delta p_{cap})}{R_{hyd}} \\ &= \frac{\rho g \Delta h(t) - \frac{2\sigma_{lg}}{r_h}\left(-\cos(\theta_a) + \cos(\theta_r)\right)}{R_{hyd}} \end{aligned} \tag{3.9}$$

where R_{hyd} is now the hydraulic resistance of the whole system. The flow rate can further be converted to an average fluid velocity and a height difference change when the cross-sectional areas are known. This method is used in the analytical model developed in Publication I. The measured height difference (see Section 4.1) can be converted to flow rate using the following equation when inlet and outlet reservoirs have identical cross-section areas

$$Q(t) = -\frac{1}{2}\frac{\partial \Delta h(t)}{\partial t} A \tag{3.10}$$

where minus sign is used to convert the reducing height difference to positive flow (direction from the inlet reservoir towards the outlet reservoir) that is always the case in this thesis.

Previous equations will give steady-state, volumetric flow rates and corresponding pressure drops. However, we are often interested in the spatial distribution of flow to study, for instance, shear stresses or drug concentration profiles. This is considered in Publication II. As there were no analytical solutions available, numerical methods were implemented by using FEM. The model combines Eq. (3.9) to calculate the working pressure, and Fick's law and the mass-balance equation to find drug concentration profiles. When the consumption rate of drugs is assumed to be zero, governing equations to express drug transportation through diffusion and convection are

$$\begin{aligned} \frac{\partial c_d}{\partial t} + \nabla \cdot (-D_d \nabla c) + \boldsymbol{v} \cdot \nabla c = 0 \\ \boldsymbol{N} = -D_d \nabla c_d + \boldsymbol{v} c_d \end{aligned} \tag{3.11}$$

where c_d and D_d are the concentration and diffusion coefficient of the drug, respectively. The flux expression for the drug, $\boldsymbol{N}$, is used in boundary condition and flux computations.

Publication III presents a numerical model that combines gravity-driven flow and flow measurement. A calorimetric sensor, which is a non-invasive, fast method with low power requirements, is implemented to measure flow rate and direction. In addition, it can easily be miniaturized for microfluidic devices without any moving parts (Meng et al., 2008; Que and Zhu, 2014; Sun and Cheng, 2013). The measurement system, which is placed in a fluidic channel, includes two temperature sensors and a heating element, symmetrically located between the sensors. Generated heat is transported via convective heat transfer to the fluid, and both sensors monitor temperature T. When fluid flows over the heater, forced convection transfers the generated heat downstream. This generates a difference between downstream (T_{down}) and upstream (T_{up}) temperatures ($\Delta T = T_{down} - T_{up}$). For this reason, a relationship between the temperature difference and fluid flow can be used to measure fluid mass flow rate Q in a known channel (Kim et al., 2009; Palmer et al., 2013). Figure 3.2 shows the simplified working principle of the flow sensor.

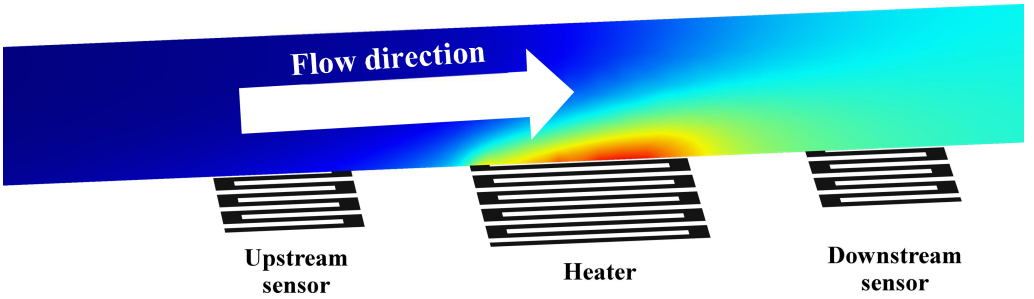

Figure 3.2: Working principle of the calorimetric flow sensor. Heat induced by the heater results in a higher temperature in the downstream sensor.

The sensitivity of the calorimetric sensor (S_{TQ}) is an important parameter. Higher sensitivity provides lower measurable flow rates. This is determined by comparing the change in the measured temperature difference (ΔT) to the change in flow rate (Sazhin, 2013)

$$S_{TQ} = \frac{\partial \Delta T}{\partial Q} \tag{3.12}$$

Sensors used in this work have positive temperature coefficients of resistance, and it is assumed that they have a constant temperature coefficient α in the measurement

range used in this study. Therefore, a linear approximation is used to determine their temperature-dependent resistances $R(T)$:

$$R(T) = R(T_0)(1 + \alpha(T - T_0)) \tag{3.13}$$

where $R(T_0)$ is the sensor reference resistance at a reference temperature T_0.

In this thesis, we consider gravity-driven microfluidic systems that include two reservoirs connected through a microchannel, with a flow sensor to measure flow rate. In these systems, the flow rate can be calculated using Eq. (3.4), (3.6), (3.8), (3.9), and (3.10).

3.2 Gas Contents and Liquid pH

This section covers equations required for the model developed in Publication IV. In a PDMS cell culturing device, CO_2 can be stored in gas, liquid, and solid phases. In this case, the solid phase refers to the CO_2 concentration within the PDMS parts. To model the entire system, CO_2 transportation mechanisms in and between these three phases must be described. CO_2 is transported by both diffusion and convection in the gas and liquid phases, whereas there is no convection in the solid phase. Transportation of CO_2 in PDMS is only diffusion-driven, and CO_2 diffuses through material due to concentration differences. Equations (3.14) to (3.17) concern mass balance, CO_2 concentration, and flux in different phases (Forry and Locascio, 2011; Polinkovsky et al., 2009; Stoian et al., 2012). If we assume no material consumption, three different mass transportation equations describes a mass balance in the system

$$\begin{aligned} \frac{\partial c_g}{\partial t} + \nabla\left(-D_g \nabla c_g\right) + \boldsymbol{v_g} \nabla c_g &= 0 \\ \frac{\partial c_l}{\partial t} + \nabla\left(-D_l \nabla c_l\right) + \boldsymbol{v_l} \nabla c_l &= 0 \\ \frac{\partial c_p}{\partial t} + \nabla\left(-D_p \nabla c_p\right) &= 0 \end{aligned} \tag{3.14}$$

where subscripts g, l, and p denote the CO_2 concentration, diffusion coefficient, and velocity field in the gas, liquid, and solid phases, respectively.

Equation (3.15) describes the equilibrium of the CO_2 concentration between (i) gas and liquid, (ii) gas and PDMS, and (iii) liquid and PDMS

$$c_g \underset{k_{lg}}{\overset{k_{gl}}{\rightleftharpoons}} c_l, \; c_g \underset{k_{pg}}{\overset{k_{gp}}{\rightleftharpoons}} c_p, \; c_l \underset{k_{pl}}{\overset{k_{lp}}{\rightleftharpoons}} c_p \tag{3.15}$$

where k represents the mass transport coefficient at the specific surface, and the subscript indicates the direction. In other words, k_{gl} provides the mass transport coefficient from the gas phase to the liquid phase at the interface between these two phases.

A dimensionless partition coefficient between two phases, Kp, is calculated using the saturated concentration values (Shiku et al., 2006; Skolimowski et al., 2010)

$$Kp_{lg} = \frac{k_{lg}}{k_{gl}} = \frac{c_{gsat}}{c_{lsat}}, \; Kp_{pg} = \frac{k_{pg}}{k_{gp}} = \frac{c_{gsat}}{c_{psat}}, \; Kp_{pl} = \frac{k_{pl}}{k_{lp}} = \frac{c_{lsat}}{c_{psat}} \tag{3.16}$$

where c_{gsat}, c_{lsat}, and c_{psat} are saturated CO_2 concentrations in the gas, liquid, and PDMS phases, respectively.

Based on the previous equations, mass transport at the interface between two different phases is modeled using mass transport coefficients and CO_2 concentrations in both sides of the interface. These fluxes between two phases are modeled using the following equations (Shiku et al., 2006; Skolimowski et al., 2010)

$$\begin{aligned} Fl_{lg} &= k_{lg}c_l - k_{gl}c_g = k_{gl}(Kp_{lg}c_l - c_g) \\ Fl_{pg} &= k_{pg}c_p - k_{gp}c_g = k_{gp}(Kp_{pg}c_p - c_g) \\ Fl_{pl} &= k_{pl}c_p - k_{lp}c_p = k_{lp}(Kp_{pl}c_p - c_l) \end{aligned} \tag{3.17}$$

where Fl_{lg}, Fl_{pg}, and Fl_{pl} denote the CO_2 flux toward the gas phase at the liquid/gas interface, the flux toward the gas phase at the PDMS/gas interface, and the flux toward the liquid phase at the PDMS/liquid interface, respectively. For the opposite flux direction, a negative sign is used.

Saturated concentrations of CO_2 in different phases can be calculated by the following equations. The saturated CO_2 concentration in the gas phase, when assuming that the ideal gas law is valid, is estimated by

$$p_{CO2}V = nRT,\ c_{gsat} = \frac{n}{V} \Rightarrow c_{gsat} = \frac{p_{CO2}}{RT} = \frac{Fv_{CO2}p_{ch}}{RT} \tag{3.18}$$

where p_{CO2}, V, n, R, Fv_{CO2}, and p_{ch} are CO_2 partial pressure, volume, amount of substance, the ideal gas constant, volume fraction of CO_2 gas component, and total pressure in the chamber, respectively.

If CO_2 is assumed to be an ideal gas, Henry's law, which describes the equilibrium between vapor and liquid, defines CO_2 concentration in the liquid phase. Henry's law as a function of temperature can be then used to calculate the dissolved CO_2 concentration in the liquid phase (Sander, 2015)

$$\begin{aligned} kh_{H(T)} &= kh_{H(0)} \exp\left[-H\left(\frac{1}{T} - \frac{1}{T_{SATP}}\right)\right] \\ c_{lsat(T)} &= \frac{p_{CO2}}{kh_{H(T)}} \end{aligned} \tag{3.19}$$

where $kh_{H(T)}$, $kh_{H(0)}$, T_{SATP}, and H are Henry's law constant at experiment temperature T, Henry's law constant at standard ambient temperature T_{SATP} (298.15 K), and a constant used to calculate temperature-dependent Henry's law constant (in K), and $c_{lsat(T)}$ is saturated CO_2 concentration in the liquid phase at experiment temperature T and CO_2 partial pressure p_{CO2}, respectively.

The saturated CO_2 concentration in PDMS is calculated, based on the solubility of CO_2 in PDMS (Merkel et al., 2000)

$$\begin{aligned} S_{CO2} &= S_{inf}\left(1 + p_{ch}n_p\right) \\ c_{psat} &= S_{CO2} \times c_{gsat} \end{aligned} \tag{3.20}$$

where S_{CO2}, S_{inf}, and n_p are the solubility of CO_2 in PDMS, the infinite dilution solubility, and the pressure dependence of solubility, respectively.

When solubility and permeability properties are known, diffusion coefficient of CO_2 in PDMS, D_p, is estimated using (Charati and Stern, 1998)

$$D_p = \frac{P}{S_{co2}} \tag{3.21}$$

where P is the permeability coefficient of CO_2 in PDMS. Using this equation, the mean diffusion coefficient can be calculated when the solubility is known, and the permeability coefficient is determined with experiments. This approach was used in Publication IV.

In Publication IV, the model was verified using water, where pH is changed by dissolved CO_2. The overall carbonate reaction in water is (Forry and Locascio, 2011)

$$\begin{aligned} CO_{2(gas)} &\Leftrightarrow CO_{2(aq)} \\ CO_{2(aq)} + H_2O &\Leftrightarrow H_2CO_3 \Leftrightarrow HCO_3^- \\ HCO_3^- &\Leftrightarrow H^+ + CO_3^{2-} \end{aligned} \tag{3.22}$$

where $CO_{2(aq)}$, H_2CO_3, HCO_3^-, H^+, and CO_3^{2-} are the dissolved CO_2 in liquid, carbonic acid, bicarbonate ion, hydrogen ion, and carbonate ion, respectively. Next, brackets are used to describe the concentration of the compound. For example, the concentration of the dissolved CO_2 in liquid ($[CO_{2(aq)}]$) equals to c_l in Eq. (3.14) to (3.17). As the hydration equilibrium constant, K_{hyd} ($[H_2CO_3]/[CO_{2(aq)}]$), is approximately 1.7×10^{-3} (Forry and Locascio, 2011), less than 0.2 percent of $CO_{2(aq)}$ molecules are converted to H_2CO_3, so the majority of the dissolved CO_2 exists as $CO_{2(aq)}$. Similarly, as $[CO_3^{2-}]$ is significantly smaller than $[HCO_3^-]$ at the pH level used in these studies (Liu et al., 2012), it was not included in the analysis. Using these assumptions, water pH can be approximated very precisely in the experimental conditions using the following equation

$$\mathrm{pH} = -\log_{10}([H^+]) \approx \log_{10}(\sqrt{K_w + c_l K_c}) \tag{3.23}$$

where K_w and K_c are the ion product of water ($\sim 10^{-14}$ at room temperature) and the thermodynamic constant for the dissociation of H_2CO_3, respectively. The latter can be approximated at a certain temperature between 0 °C and 50 °C using constants p_1, p_2, and p_3 (Millero and Pierrot, 1998)

$$K_c = \exp\left(p_1 + \frac{p_2}{T} - p_3 \ln(T)\right) \tag{3.24}$$

where $p_1 = 290.9097$, $p_2 = -14554.21$, $p_3 = -45.0575$ for H_2CO_3. In the equation, the unitless value of T (in Kelvins) is used. With these parameters, the calculated K_c is approximately 4.4×10^{-3} at 24°C.

Previous equations concerned pH of water (H_2O) solution. The cell culture medium used in this thesis includes $NaHCO_3$ as a buffer to maintain a proper pH. It is again assumed that the majority of the dissolved CO_2 exists as $CO_{2(aq)}$ (Forry and Locascio, 2011), and that $NaHCO_3$ dissociates to the medium with the following equation, so that its concentration ($[NaHCO_3]$) equals to the initial concentration of HCO_3^- ($[HCO_3^-]$) (Hochfeld, 2006, p. 106; Harrison and Rae, 1997, p. 36)

$$\begin{aligned} NaHCO_3 + H_2O &\Leftrightarrow Na^+ + HCO_3^- + H_2O \Leftrightarrow \\ Na^+ + H_2CO_3 + OH^- &\Leftrightarrow Na^+ + OH^- + H_2O + CO_{2(aq)} \end{aligned} \tag{3.25}$$

where Na^+ and OH^- are sodium and hydroxide ions, respectively. The relationship between $NaHCO_3$ and CO_2 in the culture medium can the be expressed by the Henderson-Hasselbalch equation to determine pH (Hu, 2012, p. 114; Quinn and Cooke, 2004)

$$\begin{aligned} \mathrm{pH} = \mathrm{pKa} + \log_{10}\left(\frac{\mathrm{base}}{\mathrm{acid}}\right) &= \mathrm{pKa} + \log_{10}\left(\frac{[HCO_3^-]}{[CO_{2(aq)}]}\right) \\ &= \mathrm{pKa} + \log_{10}\left(\frac{[NaHCO_3]}{[CO_{2(aq)}]}\right) \end{aligned} \tag{3.26}$$

where pKa is a negative, common logarithm of the acid dissociation constant of $NaHCO_3$.

3.3 Identification

In this thesis, we have developed temperature estimation models using the system identification techniques. Our approach was to estimate the model parameters using measured input and output data, and fit the model to the measured data without prior information about the physical system. Therefore, we used a black-box modeling technique (Kaigala et al., 2010; Sohlberg, 2003; van Schijndel, 2007).

Explicit, discrete, time-invariant, state-space models include the state vector $\boldsymbol{x}(k)$, the input vector $\boldsymbol{u}(k)$, the output vector $\boldsymbol{y}(k)$, and parameter matrices $\boldsymbol{A}$, $\boldsymbol{B}$, $\boldsymbol{C}$, and $\boldsymbol{D}$. These state-space models have the following structure (Ljung, 2016)

$$\begin{aligned} \boldsymbol{x}(k+1) &= \boldsymbol{A}\boldsymbol{x}(k) + \boldsymbol{B}\boldsymbol{u}(k) \\ \boldsymbol{y}(k) &= \boldsymbol{C}\boldsymbol{x}(k) + \boldsymbol{D}\boldsymbol{u}(k) \end{aligned} \tag{3.27}$$

where matrices $\boldsymbol{A}$, $\boldsymbol{B}$, $\boldsymbol{C}$, and $\boldsymbol{D}$ are a state matrix, an input-to-state matrix, a state-to-output matrix, and a feedthrough matrix, respectively. As time-invariant systems are considered, these matrices are constant and not time-dependent. We initially tested second-order models, but obtained unsatisfactory results. We then implemented models with three state variables. Our third-order models have the following form

$$\begin{gathered} \boldsymbol{A} = \begin{bmatrix} a_{11} & a_{12} & 0 \\ 1 & 0 & 0 \\ 0 & 1 & 0 \end{bmatrix}, \boldsymbol{B} = \begin{bmatrix} b_1 \\ 0 \\ 0 \end{bmatrix} \\ \boldsymbol{C} = \begin{bmatrix} c_1 & c_2 & c_3 \end{bmatrix}, \boldsymbol{D} = \begin{bmatrix} 0 \end{bmatrix} \end{gathered} \tag{3.28}$$

where a_{11}, a_{12}, b_1, c_1, c_2, and c_3 are constants for each of the developed models. They are discussed in Chapter 5. The coefficient of matrix $\boldsymbol{D} = 0$, so no direct or linear relationship between the input and the output was detected.

To compare and choose the most suitable models, we used a prediction error method. In this method, a model in which the outcome is as close as possible to the true system, if known, is chosen (Ljung, 1978). We used a fit number to compare our models. It is based on a normalized root mean square error criterion and can be calculated (as a percentage) using (Ljung, 2016)

$$fit = 100\left(1 - \frac{|y_m - \hat{y}|}{|y_m - \bar{y}|}\right) \tag{3.29}$$

where y_m and $\hat{y}$ are the measured and the estimated output, respectively, and $\bar{y}$ is the mean of y_m.

3.4 Closed-Loop Control System

In this section, we provide a general presentation of the closed-loop control system that is used in this work (Dorf and Bishop, 2005, pp. 3, 7, 10, 391). The feedback controller system includes a set-point value $r(t)$; an output value $y(t)$; an error signal $e(t)$ that compares these two signals ($e(t) = r(t) - y(t)$); and a control variable $u(t)$ that is the output from the controller. Here, $r(t)$, the value at which we want our process to settle (for instance, temperature at 37°C), is compared to the measured process value

$y_m(t)$ (which ideally equals to $y(t)$). The resulting $e(t)$ is then fed to a controller that continuously tries to minimize this error over time by adjusting $u(t)$. As the controller is the fundamental part of the control system, it must be properly designed. The widely used proportional-integral-derivative (PID) controller can be implemented to develop stable, closed-loop systems. Figure 3.3 presents a block-diagram model of the negative feedback system using the PID controller. This figure is a simplified presentation without noise term, filtering, and so on.

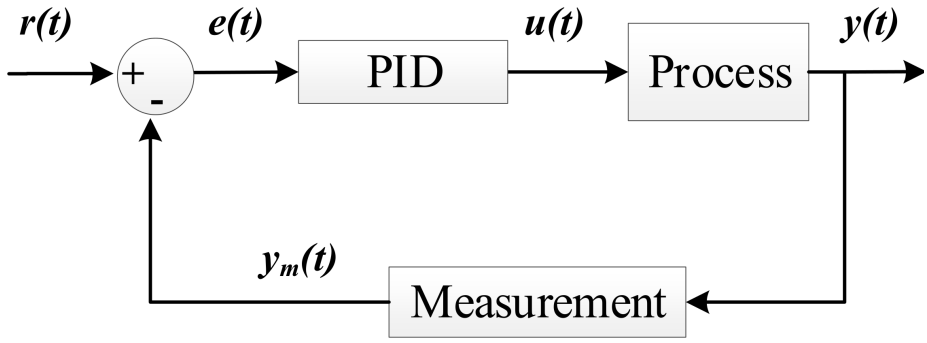

Figure 3.3: Simplified block diagram of a negative feedback control system using the PID controller.

A PID controller in time domain can be mathematically presented as

$$u(t) = K_p e(t) + K_i \int_0^t e(\tau)d\tau + K_d \frac{de(t)}{dt} \tag{3.30}$$

where K_p, K_i and K_d are non-negative coefficients of proportional, integral, and derivative terms, respectively. These terms concern the error in different time scales: K_p deals with present values, K_i calculates past values, and K_d predicts future trends of the error. The benefits of the PID controller are its simplicity and that it is only based on the measured $y_m(t)$, so it does not need the knowledge of the underlying process. Therefore, it can be used for a wide range of applications. In this study, we excluded the derivate term, implemented a discrete-time proportional-integral (PI) controller, and initialized the controller so that initial values before the measurement are zero. The so-called position form of the discrete-time PI controller is

$$\begin{aligned} s(k) &= s(k-1) + \frac{e(k) + e(k-1)}{2} t_s \\ u(k) &= K_p e(k) + K_i s(k) \end{aligned} \tag{3.31}$$

where t_s is sample time of the discrete-time controller, and $s(k)$ is the calculated integral value of the error using trapezoidal approximation.

One issue with this type of controllers is integral windup. When the error signal is significantly large and/or continues for a long period, the integral term can grow very large. The problem is that there are always limitations of physical systems (controllers and other devices), so controller output will saturate at some point. However, overshooting will occur as the integral term continues growing. For this reason, we implemented an anti-windup method, which resets the initial value of the integrator to a certain value that is chosen in advance of when saturation occurs (Kaigala et al., 2010).

Chapter 4

Modeling the Microscale Cell Culture Environment

The main parts of Publications I to IV are summarized in this chapter. It is divided into four sections, with each presenting one publication. Each section includes two subsections. The first subsection presents materials and methods, while the second subsection summarizes the main results.

4.1 Gravity-Driven Flow Model

4.1.1 Materials and Methods

The goal of Publication I was to developed a simple, effective analytical model to study gravity-driven pumping. Figure 3.1 presents the working principle of the gravity-driven flow, and Eq. (3.1) to (3.9) are used in the model. We fabricated four different devices made of PDMS to develop and verify the model, including two identical reservoirs, connected by 10-mm long and 50-µm high microchannels. Four channel widths (50 µm, 100 µm, 250 µm, and 500 µm) were studied. We imaged these fabricated channels along the channel length using microcomputing tomography (Xradia MicroXCT-400). Based on the image analysis using MATLAB (Version R2014a, The MathWorks, Inc., Natick, MA, USA), average respective channel heights and widths were 47.8 µm and 51.9 µm; 47.6 µm and 103.7 µm; 48.0 µm and 251.8 µm; and 47.1 µm and 497.3 µm, with targeted widths of 50, 100, 250, and 500 µm, respectively. Targeted and measured channel dimensions were used in three models, as presented in Section 4.1.2. During the experiments, we recorded liquid levels in the reservoirs using a digital camera (Sony XCD-X710) with a frame rate of one image per minute, and then calculated height differences between the inlet and the outlet reservoirs using image analysis. Figure 4.1 shows one of the devices and an example of the image-based analysis. As shown in the figure, we fabricated three similar devices for each channel type (targeted widths of 50, 100, 250, and 500 µm) to perform parallel experiments. Before the experiments, each inlet reservoir was first filled with DI water before pushing liquid through the microchannel, resulting in approximately 48-mm and 1-mm to 2-mm high initial plugs in the inlet and outlet reservoirs, respectively. Furthermore, an image-based contact angle estimation for θ_a and θ_r was separately performed from a few images during the experiments. Based on the measured contact angles, 110° and 60° for θ_a and θ_r, respectively, resulted in Δp_{cap} of approximately 80.8 Pa, using Eq. (3.7).

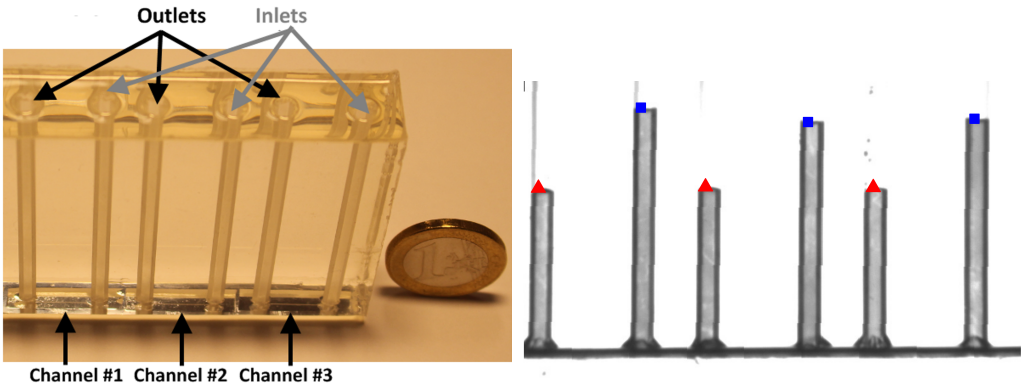

Figure 4.1: Gravity-driven flow experiment: (a) fabricated device, and (b) a snapshot of the image-based analysis, presenting estimated inlet (squares) and outlet (triangles) reservoir plug heights. Adapted from Publication I.

In the models, the hydraulic resistance of the whole system, R_{hyd}, consisted of two reservoirs, the microchannel and other connection parts. However, with the dimensions and geometries used in this study, the hydraulic resistance of the rectangular microchannel R_{hyd_rec} was several orders higher than the resistance of the rest of the system. Therefore, the total hydraulic resistance of the system R_{hyd} was approximated as R_{hyd_rec}. Three different analytical models (named Model 1, Model 2, and Model 3) were then developed. The differences between models depended upon which channel dimensions were used in Eq. (3.4) to calculate R_{hyd_rec} and which contact angles were used for capillary forces in Eq. (3.7). In Model 1, capillary forces were assumed to be zero, whereas Δp_{cap} was set to 80.8 Pa in other models, based on the measured contact angles. Furthermore, Models 1 and 2 used the targeted channel dimensions, whereas measured channel dimension were used in Model 3 to calculate R_{hyd_rec}. Finally, the three analytical models were numerically solved at different time instants using Simulink (The MathWorks, Inc.). More detailed information about the fabrication process, dimensions of the fabricated devices, simulation parameters, and details of the experimental setup can be found in Section 3 in Publication I.

4.1.2 Results and Discussion

This section summarizes the main results from Publication I. Six measurements (from two separate experiments with three parallel microchannels) were used to calculate average plug height differences of $\Delta h\,(t)$, together with their standard deviations. After the experiments, measured data were compared to data received from the three models presented in the previous section. Figure 4.2 shows the comparison. To clarify the images, measurement values with only selected time points are plotted. It can be noted that results from Model 3 have a very close relationship to experimental data. The results presented here were similar to other studies (Oh et al., 2012; Song et al., 2011). This emphasizes that the developed model can be used to determine pressure drops and flow rates in microfluidic system networks. Gravity-driven flow models, including capillary forces, produce remarkably better estimates of real flow rates than models without them. This assumption has typically been used in the previous studies. Furthermore, more precise

results were obtained from the model using the measured channel dimension. It was noticed from the imaged channels, that fabricated microchannels had trapezoidal cross-sections with rounded corners (see Figure 5 in Publication I). The hydraulic resistances of these channels can be approximated reasonably well with Eq. (3.4), that is used for channels with rectangular cross-sections. The effect of fabrication tolerances and microchannel inaccuracies on the results can also be studied from Figure 4.2. Models 2 and 3 provided very similar results with the smallest channel (Figure 4.2(a)). Therefore, using targeted channel dimensions in the model provided reliable results. In comparison, results with the largest channel (Figure 4.2(d)) showed noticeable difference between these models.

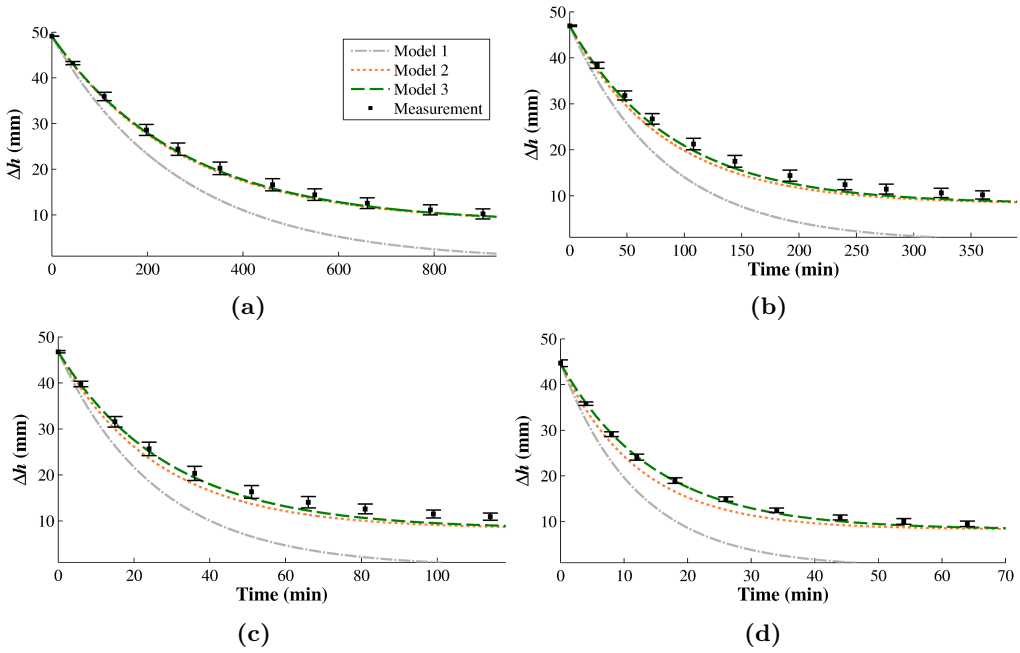

Figure 4.2: Comparison of the experimental data and the analytical model. Plug height difference Δh is plotted as a function of time when targeted microchannel width is (a) 50 µm, (b) 100 µm, (c) 250 µm, and (d) 500 µm. Adapted from Publication I.

The achieved flow rate is very important when designing gravity-driven flow systems. For this reason, Model 3 is compared to measured flow rate to evaluate how well the model can predict the flow rate of the system using Eq. (3.9). The experimental flow rate was calculated from the change of the measured height difference with the known reservoir areas (approximately 7.8 mm^2 from Publication I) using Eq. (3.10) and the Euler method. This comparison in Figure 4.3 shows that the model can approximate flow rates reasonably well.

Based on the results from this section, it is clear that gravity-driven flow has some limitations. For example, flow rate is not constant and will eventually stop unless more liquid is added to the inlet reservoir. Even though some methods to provide a constant flow rate have been presented (Kim and Cho, 2011), this is a typical challenge of the gravity-driven systems and should be taken into account in long-term cell culture experiments.

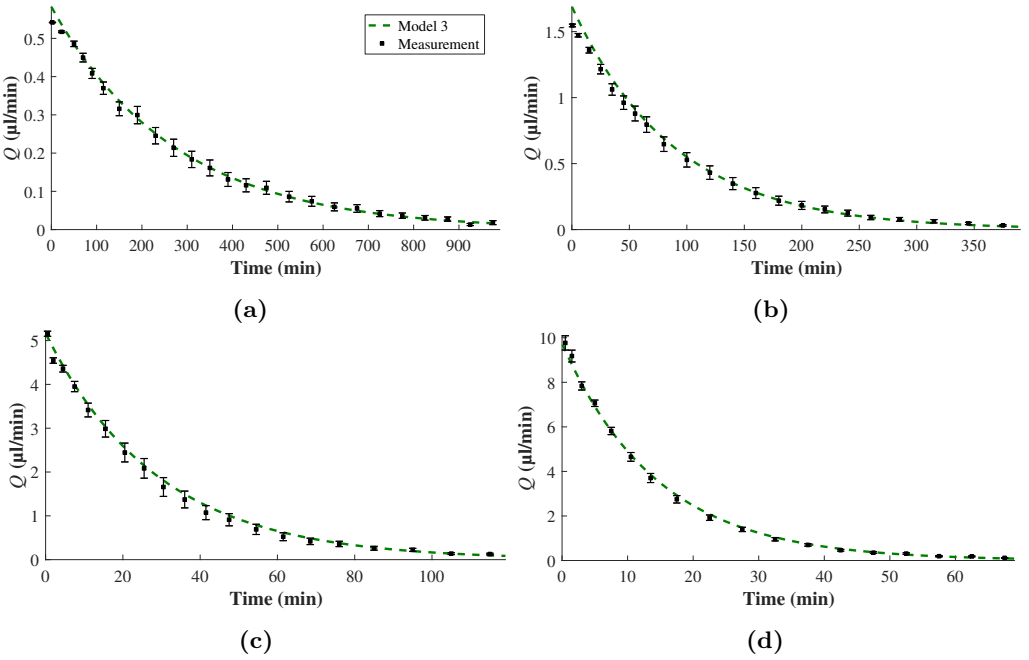

Figure 4.3: Flow rate comparison of the experimental data and Model 3. Flow rate Q is plotted as a function of time when targeted microchannel width is (a) 50 µm, (b) 100 µm, (c) 250 µm, and (d) 500 µm.

The developed model was compared to measurements performed at room temperature. As liquid properties (density, viscosity, and surface tension) are temperature-dependent, also flow rate would change in a typical cell culture temperature (37 °C). In the developed model, temperature-dependent liquid properties are included. However, as validation experiments were only performed at room temperature, the developed model was not simulated at 37 °C.

4.2 Drug Delivery Model in Microfluidic Devices Using Gravity-Driven Flow

4.2.1 Materials and Methods

In Publication II, a gravity-driven drug delivery model in a microfluidic cell culture system was studied using FEM. The paper presented a modeling approach that can simulate a time-dependent drug concentration profile in a gravity-driven, microfluidic cell culturing environment. The method was based on combining calculation of the working pressure (using model presented in Publication I) together with FEM simulations to characterize flow patterns and drug concentration profiles. Simulations were solved using COMSOL Multiphysics (Version 4.3b, COMSOL, Inc., Burlington, MA, USA), hereafter referred to as COMSOL. We combined the model with FEM simulations because the model in Publication I can only describe the average flow rate and pressure drop along the geometry, without the capability of providing information on the spatial distribution of flow velocity and drug concentration (Oh et al., 2012). Furthermore, simulations of two-phase flows (gas and liquid phases in this study) are computationally heavy and cannot be directly

used in a time-scale of several minutes, or even days, that are typical in gravity-driven flow systems.

The steps required for analyzing the distribution of drug compounds in the system were: designing and building the model geometry; calculating the working pressure $\Delta p(t)$, using the method presented in Publication I; and solving the three-dimensional (3D) velocity profile and drug concentration using FEM. With the calculated 3D velocity profile, a shear stress study was also implemented to ensure that the fluid flow would not harm the cultured cells.

The geometry for the simulation in Publication II was similar to a design presented by Kreutzer et al. (2012) that enhanced long-term culturing capabilities and electrical activity of human embryonic stem cell-derived neuronal cells. There, a reservoir (the outlet reservoir in this study) was designed to maintain stable culture conditions in three-day medium exchange periods. Open access to a cell cultivation area (hereafter referred to as a cell area) enabled easier coating and cell plating. The cell area was restricted to enhance neuronal network development. As the goal in this study was to implement drug delivery to this static cell culturing device, another reservoir (the inlet reservoir in this study) and a microchannel connecting the two reservoirs were designed. Figure 4.4 shows the geometry.

Channel dimensions were chosen to provide a desired drug delivery rate, with a maximum flow rate of 25 µl/min. We designed a channel extension connecting the cell area and the channel (shown in Figure 4.4(b)) to provide a more uniform spatial drug concentration profile over the cells. Furthermore, to minimize shear stress on cells, we placed the cell area so that the cells grew 100 µm lower than the bottom of the channel, marked as h_1 in Figure 4.4. In addition, height difference between the top of the channel and the outlet, h_2, was set to 500 µm as shown in Figure 4.4(c).

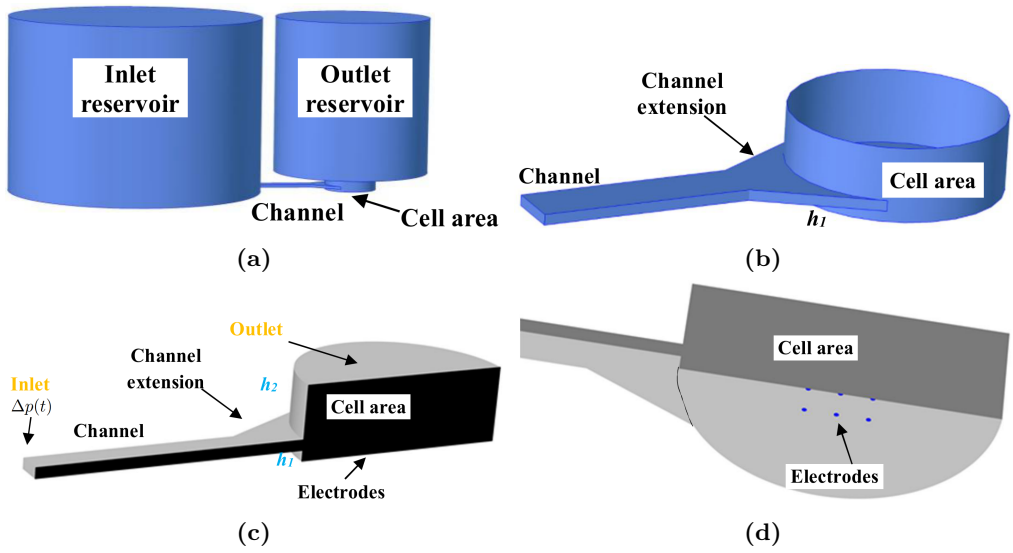

Figure 4.4: Simulation of gravity-driven, drug delivery model: (a) designed geometry, (b) an enlarged scheme of the designed geometry, (c) geometry used in the simulation (symmetry boundaries are marked in black), and (d) an enlarged scheme of the geometry showing the electrode array on the bottom of the cell area. Adapted from Publication II.

We used caffeine, a commonly used, low-concentration neurotoxin (Fernández et al., 2003), in the simulations to study drug delivery. In the model, liquid was modeled as water at 37 °C. Table 1 in Publication II provides the simulation parameters. Using these values, the working pressure was first calculated using Eq. (3.9). The calculated time-dependent, working pressure $\Delta p(t)$ (Figure 2 in Publication II) was then set to the inlet of the FEM model (Figure 4.4(c)). To calculate drug distribution in the system, Eq. (3.11) was solved by combining two interfaces, the Single-Phase Flow and the Transport of Diluted Species, in COMSOL.

In some drug tests, immediate response of the cells to the drug is studied. For this, electrical activity of the cultured cells is commonly measured using a microelectrode array. To measure the instant effect of the drug on neuronal activity, the drug concentration should be as uniform as possible over every electrode. This means that the maximum concentration difference (difference between maximum and minimum concentrations over the electrodes at each time point) should be as small as possible. To study how uniformly the drug concentration is delivered over these electrodes, the model also represents a 3x3 array of electrodes on the bottom of the cell area (Figure 4.4(d)). In addition, the model was used to redesign the device to reduce this maximum concentration difference. In the next section, we will study drug delivery over these electrodes.

4.2.2 Results and Discussion

Here, we summarize the main results from Publication II. Figure 4.5 shows the initial simulated velocity field and pressure distribution. Using the model, we calculated that shear stress in the cell area was below 0.03 Pa (see Figure 5 in Publication II), a chosen maximum level that shear stress should not to exceed. For example, shear stress larger than 0.03 Pa has been reported to have an effect on mesenchymal stem cells (Inamdar et al., 2011). However, it should be emphasized that undesirable shear stress level is very cell-type dependent.

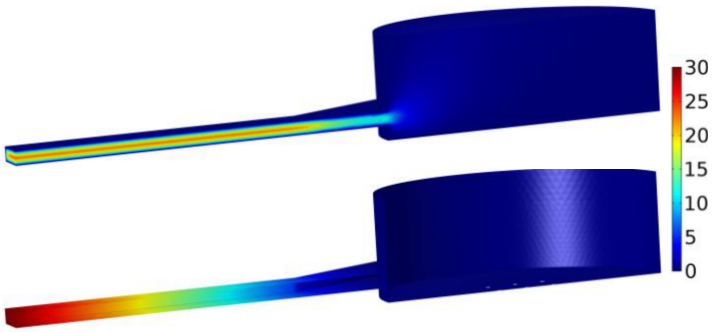

Figure 4.5: Initial velocity field (above, unit mm/s) and pressure distribution (below, unit Pa). Adapted from Publication II.

Using the calculated velocity and pressure fields, we solved for a time-dependent drug concentration profile over the geometry. From the solution, the maximum concentration difference between the electrodes was calculated. Figure 4.6 shows these results.

Based on the simulation results with the original geometry, marked as G_1 in Table 4.1, we obtained remarkably large concentration differences between electrodes. Furthermore, rise time t_r, or the time that it took the drug concentration to rise to 90 percent of

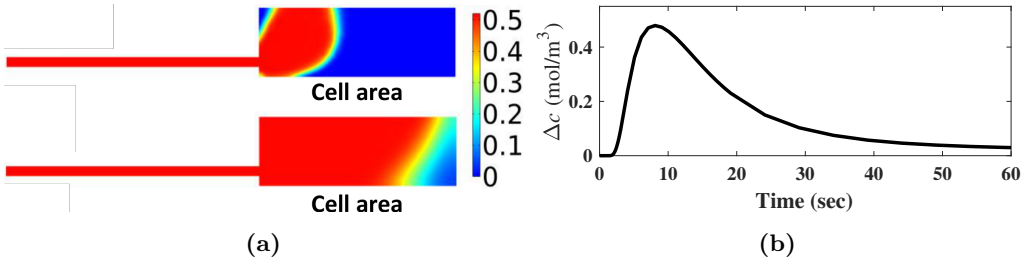

(a) (b)

Figure 4.6: Drug delivery simulation: (a) two-dimensional concentration profiles (unit mol/m^3) in the middle of the channel at times 1 sec (above) and 50 sec (below); and (b) the maximum concentration difference over the electrodes as a function of time in the designed geometry. Adapted from Publication II.

the final concentration value, was significantly different between areas over electrodes. Maximum and average concentration differences and rise time differences are marked as Δc_{max}, Δc_{avg} and Δt_r, respectively, in Table 4.1. To reduce these undesired concentration differences, three additional geometries, marked as G_2, G_3, and G_4, were designed and simulated. These three different geometries were chosen so that the effects of geometrical parameters could be studied and to demonstrate how the model-based design can improve the uniformity of the drug delivery. Simulation results are compared in Table 4.1 and in Figure 4.7.

Table 4.1: Comparison of the designed geometries.

Parameter	Unit	G_1	G_2	G_3	G_4
h_1	µm	100	100	200	500
h_2	µm	500	100	100	100
Δc_{max}	mol/m^3	0.48	0.42	0.37	0.21
Δc_{avg}	mol/m^3	0.15	0.07	0.06	0.07
Δt_r	sec	34.8	13.4	11.8	13.9

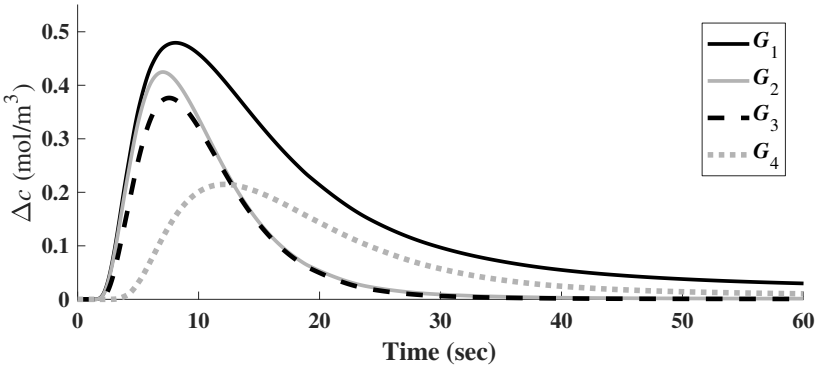

Figure 4.7: Comparison of the concentration differences over the electrodes as a function of time in different geometries. Adapted from Publication II.

Based on the simulation results, new designs provided more uniform drug concentration profiles over the measurement electrodes, which was the main goal in this study. This would ensure more desirable concentration profiles for drug testing. Based on Table 4.1 and

Figure 4.7, the most promising results were geometries G_3 and G_4. Even though Δc_{max} was larger in G_3 than in G_4, G_3 had faster response time and lower Δc_{avg}. Therefore, we concluded that G_3 provided the best average performance. This result highlights the potential usage of the model as a designing tool; intuitively, it would be easy to think that G_2 provides the most suitable result since it has the smallest chamber volume. However, in that geometry, drug distribution over the electrodes is not as uniform as in G_3 (see Table 3 and Figure 7(a) in Publication II). Therefore, as the uniformity of drug delivery was the most important design parameter, G_3 was chosen to be used in future studies. On the other hand, other geometry could have been chosen with different criteria of selection. Finally, it should be emphasized that the presented numerical model was not validated with experiments.

4.3 Flow Sensor Model in Gravity-Driven Microfluidic Devices

4.3.1 Materials and Methods

Simpler microfluidic systems could be developed using gravity-driven flow. However, as microchannels can get clogged during operation, continuously monitoring liquid flow is important. Publication III considered this problem. It presented a FEM model that integrated a calorimetric flow sensor and a gravity-driven system. Section 3.1 presented the working principle of this sensor. We fabricated the calorimetric flow sensor on a 25 mm × 25 mm × 0.9 mm glass plate. The structure (Figure 4.8) was designed such that measurable temperature differences can achieved at flow rates that are typical for gravity-driven flow systems (between 0 and 10 µl/min, as shown in Fig. 4.3). It consisted of a 275-nm thick titanium layer, coated with a 50-nm thick platinum layer and a 500-nm thick silicon nitride insulation layer. Resistor width was 20 µm, and resistor lengths were 4.78 mm and 2.22 mm for the heater and the sensors, respectively. Sensor height h_s, shown in Figure 4.8(a), was 540 µm. Center-to-center distance d_{cc} between the sensor and the heater (Figure 4.8(a)) was 300 µm, and downstream and upstream sensors were used to measure T_{down} and T_{up}, respectively. Their temperature difference $\Delta T = T_{down} - T_{up}$ can be used to estimate the flow rate when a relationship between ΔT and fluid flow in the channel is known (Kim et al., 2009; Palmer et al., 2013).

We used COMSOL (Version 4.4) to solve 3D, time-dependent, temperature distribution in the system. Three different physics were coupled together by combining the Electric Currents, Shell, the Single-Phase Flow, and the Heat Transfer in Solids interfaces in COMSOL. We used the properties of water for the liquid phase and set a typical heat transfer coefficient for air (30 $\mathrm{W{\cdot}(m^2{\cdot}K)^{-1}}$) on the outer boundaries of the model. This was done to approximate the convective heat flux on the boundaries, which were in contact with the ambient air. The model also included the heater and the sensors. Constant currents (approximately 5.9 mA and 0.2 mA) were used for warming the heater and powering the temperature sensors, respectively.

Rather than using gravity-driven flow, the FEM model was validated using a system in which a syringe pump was used to create three different flow rates (Figure 2 in Publication III); no flow (first ∼150 sec), 1 µl/min (between 150 and 275 sec), and 10 µl/min (after 275 sec). The material parameters used in the model are given in Table I in Publication III. A comparison of the measured and simulated upstream and downstream temperatures in Figure 4.9 shows that the model can estimate both temperatures sufficiently well; the largest temperature difference is during the initial heating phase (first ∼20 sec), but temperature differences in different flow rates are

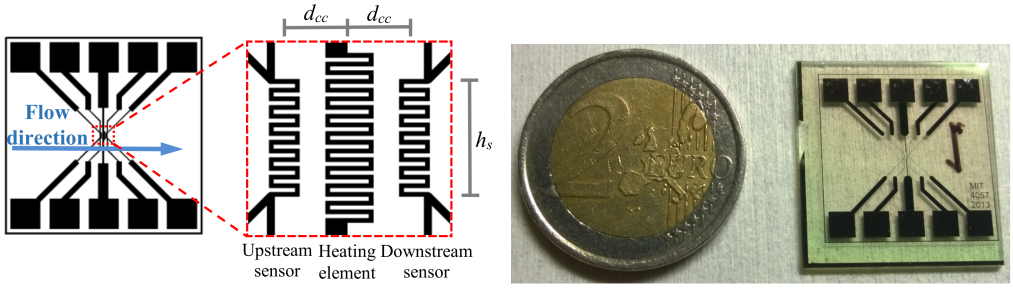

Figure 4.8: Calorimetric flow sensor: (a) designed and (b) fabricated sensor plate. Adapted from Publication III.

reasonably accurate. Therefore, the model could be used as a part of a gravity-driven flow model. From this validation measurement, we found that a minimum detectable temperature difference of ΔT_{min} with our system was approximately 0.1 °C. A reliable flow rate measurement cannot be performed if ΔT is below this. Therefore, we define the symbol Q_{min} to represent a minimum flow rate that is needed to achieve ΔT_{min} for the following simulation studies.

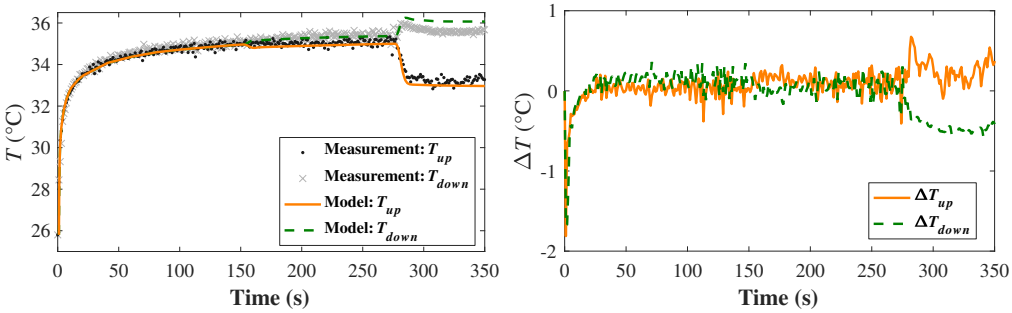

Figure 4.9: Model validation results: (a) measured and simulated temperatures (adapted from Publication III) and (b) upstream and downstream temperature differences between the measurement and simulation.

After model validation, we developed a gravity-driven model, including inlet and outlet reservoirs, a microchannel and a calorimetric flow sensor (Figure 4.10), based on four design goals. We first defined that flow rate should be larger than 0.1 µl/min for more than 10 hours to ensure a continuous flow of fresh culture medium to cells. The maximum flow rate should also not exceed 10 µl/min to ensure low shear stress on cells attached to the substrate. In addition, liquid temperature warmed by the heater should not exceed 42 °C to avoid unnecessary heating, and the temperature in the outlet of the channel should not be higher than 37 °C because cell culture was located after that, as shown in Figure 4.10. With these boundaries, we designed a system where an initial liquid plug height difference between the inlet and outlet reservoirs (radius: 8 mm) was 15 mm. This initial state is illustrated as blue in Figure 4.10. Using measured contact angles of liquid in PDMS (from Publication I), Δp_{cap} was approximately 15 Pa. Finally, we designed a 16-mm long microchannel with a rectangular cross-section ($h_c \times w_c$: 50 µm × 1000 µm)

to fulfill the design goals.

Because the simulation case presents typical cell culturing inside an incubator, the ambient temperature in the model was set to 37 °C. With these parameters, the analytical model presented in Publication I was used to determine a time-dependent pressure profile $\Delta p(t)$. We used one simplification by assuming that the liquid temperature was 37 °C everywhere, even though the heater warms some of the liquid. The solution from the model was then used as an inlet boundary condition in the FEM model, as shown in Figure 4.10. We also included the calorimetric flow sensor in the model. To ensure that the temperature of the liquid at the channel outlet did not exceed 37 °C, and that the heater would not warm liquid more than 42 °C, the distance between the center of the heater and the channel inlet was set to 2 mm, and a 3 mA heater current was used in the simulation. After the simulation, T_{down}, T_{up}, and Q were obtained, and ΔT and S_{TQ} were calculated.

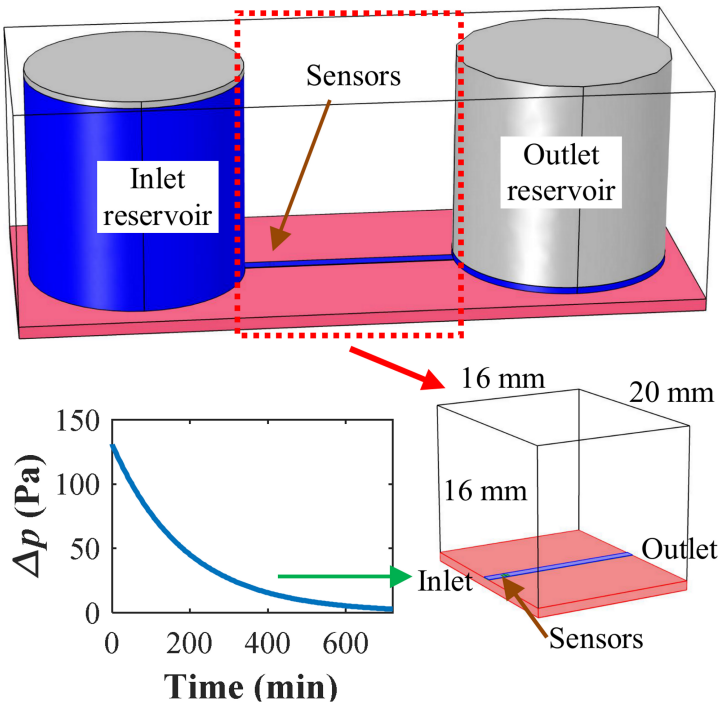

Figure 4.10: A modeled gravity-driven system. Schematic of the gravity-driven microfluidic device. Here, the blue color shows the liquid phase and the gray color shows the air phase at the beginning (above), and a modeled geometry used in the simulation, together with a calculated pressure profile, set to the model inlet (below). Adapted from Publication III.

4.3.2 Results and Discussion

From the simulation-based study of the flow behavior in a gravity-driven system, we noticed that the maximum flow rate, Q_{max}, was approximately 7 µl/min at the beginning of the simulation. We detected approximate 0.9 °C and 0.12 K·(µl/min)$^{-1}$ maximum temperature difference of ΔT_{max} and sensitivity of the sensor, respectively. Furthermore, Q_{min} was almost 1 µl/min in this design. As we would like to measure lower flow rates with higher sensor sensitivity, we made several changes to the original geometry (marked

as *G1* in Table 4.2 and Figure 4.11). First, we narrowed the microchannel. As we wanted R_{hyd_rec} and the working pressure to be approximately the same in both designs, the height of the microchannel was increased based on Eq. (3.4). In addition, the length of the sensors was reduced, and they were placed closer to the heater.

A comparison of the original and new design, *G2*, is given in Table 4.2 and Figure 4.11 As planned, almost equal flow rates were achieved with both designs. Higher upstream and downstream temperatures, and a larger ΔT resulted with the new design. It should be noted that the heater did not warm liquid over 42 °C with the new design, which was one of our design goals. Based on these simulation results, we achieved lower Q_{min} and over 20 percent greater sensitivity with *G2* compared to the original geometry.

Table 4.2: Comparison of two designs. Adapted from Publication III.

	G1	*G2*
Model parameters		
h_c (µm)	50	55
l_c (mm)	16	16
w_c (µm)	1000	790
d_{cc} (µm)	300	230
h_s (µm)	540	380
l_s (mm)	2.22	1.58
Performance measures		
Q_{max} (µl/min)	7.3	7.5
ΔT_{max} (K)	0.87	1.10
S (K·(µl/min)$^{-1}$)	0.12	0.15
Q_{min} (µl/min)	0.96	0.71

It should be noted that the developed FEM model was only validated with measurements using a syringe pump as explained in Section 4.3.1. Therefore, experiments using gravity-driven flow are to be performed in the future to verify the presented model.

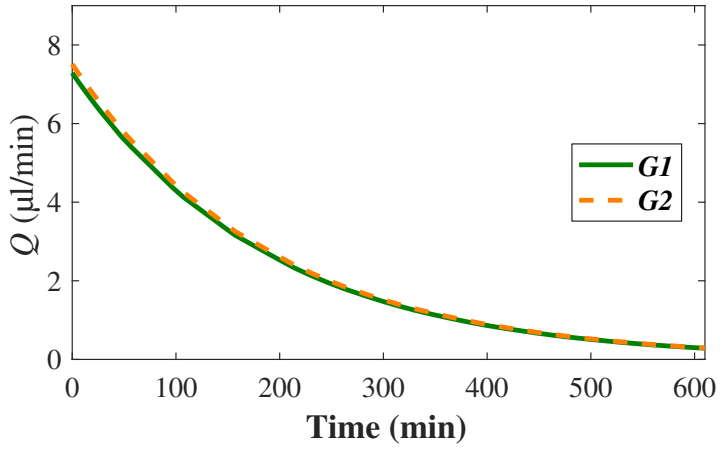

(a)

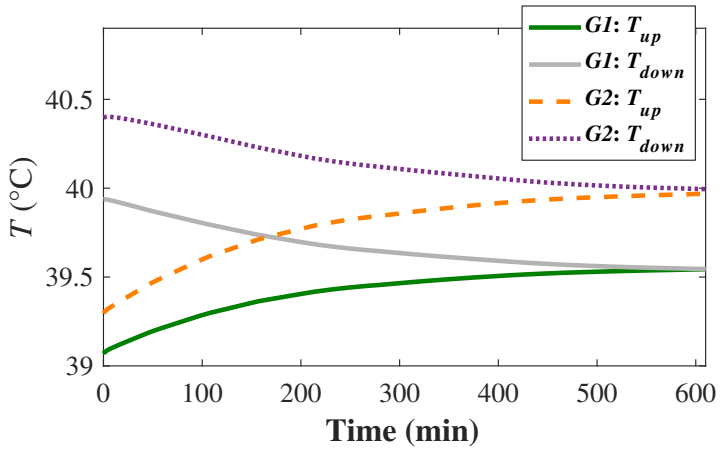

(b)

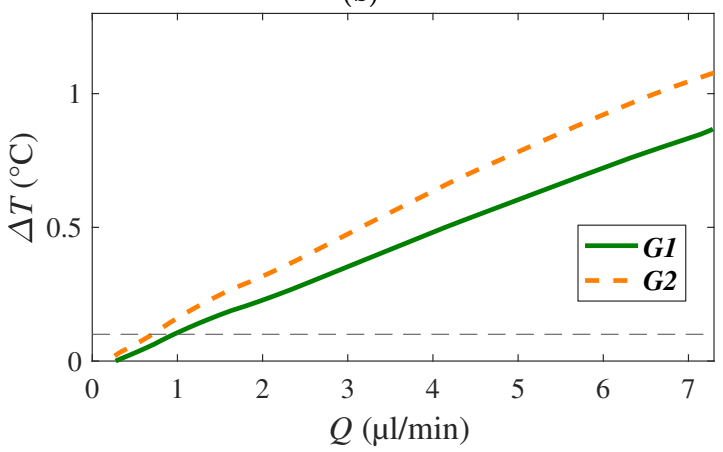

(c)

Figure 4.11: Comparison of two gravity-driven designs *G1* and *G2*: (a) flow rates; (b) upstream and downstream temperatures as a function of time; and (c) temperature differences as a function of flow rates. The dashed horizontal line represents a minimum, detectable, temperature difference level Q_{min}, based on the validation measurement. Adapted from Publication III.

4.4 CO_2 Transport and Liquid pH in PDMS-Based Devices

This section summarizes Publication IV. We also compared the model to measurements reported by Kreutzer et al. (2017) to show that the model can also be used with cell culture media. This study is included at the end of Section 4.4.2.

4.4.1 Materials and Methods

Maintaining a suitable pH level is important for successful, long-term cell culturing, as even small pH deviations can affect cell growth. Typically, cell culture media contain $NaHCO_3$ as a buffering agent, and CO_2 is used for controlling pH (Kim et al., 2007; Li et al., 2010). The gas permeability of PDMS has shown that pH can be controlled by feeding CO_2 to the cell culture through a PDMS membrane instead of directly to medium. This reduces medium evaporation and osmolarity changes (Blau et al., 2009; Kreutzer et al., 2017). Because it is very challenging to control and measure local CO_2 or pH levels in long-term cell cultures, a computational model to estimate CO_2 transport (and pH) in PDMS-based devices would be desirable. Although O_2 transport in PDMS-based microfluidic cell culturing devices has been extensively modeled (Adler et al., 2010; Chang et al., 2014; Chen et al., 2011b; Funamoto et al., 2012; Inamdar et al., 2011; Peng et al., 2013; Polinkovsky et al., 2009; Shiku et al., 2006; Skolimowski et al., 2010; Thomas et al., 2011; Vollmer et al., 2005; Wang et al., 2013a; Zahorodny-Burke et al., 2011), a comprehensive model of CO_2 transport had not been presented before Publication IV. Therefore, we developed a CO_2-transportation FEM model including Eq. (3.14) to (3.24), using COMSOL (Version 4.4). First, a large set of measurements were performed to determine the required parameters for the FEM model. In this work, we determined D_l, D_p, k_{gl}, k_{gp}, and k_{pl}. Other parameters were taken from the literature. This process is explained in Section 3 in Publication IV. Figures 1 and 3, and Table 1 summarize the measurements and models. Publication IV also compares the validation measurements and simulations in Figures 5 and 6. In these experiments, we used a non-dispersive CO_2 sensor based on infrared detection (COZIR Wide Range GC-0006, CO2Meter, Inc., Ormond Beach, FL, USA). The results clearly demonstrated that the model successfully predicted CO_2 transportation. Therefore, the parameters presented in Table 2 in Publication IV were used in the following studies (solubility of CO_2 is marked as S in Table 2, instead of S_{CO2} in this thesis).

To test and validate the computational model, we fabricated and tested a structure consisting of a culture well made from PDMS and a connection cap. The culture well was reversibly bonded on top of a glass plate. The connection cap was used to close the system to minimize liquid evaporation and supply gas to the culture well. The schematic of the device is presented in Figure 4.12(a). The culture well was filled with 600 µl of DI water, and the connection cap was placed on the top of the culture well. A dry gas mixture (95% air and 5% CO_2) was supplied from the inlet port (shown in Figure 4.12(a)) at a flow rate of 1 ml/min. In the experiment, pH was measured at a selected time interval by removing the connection cap and taking a 200 µl sample from the bottom of the culture well to a pipette tip. These were end-point measurements, leading to a single measurement per test. We measured pH using a small field-effect transistor type pH probe (MicroFET, Sentron Europe BV, The Netherlands) at several time points (0, 10, 25, 40, 60, and 75 minutes). In addition, we performed four long-term (two one-day and two five-day) measurements to determine the equilibrium pH value of the device. For FEM simulation, we used a simplified structure (Figure 4.12(b)) that only concerned the part between the upper and bottom glass plates shown in Figure 4.12(a). To compare

the simulation with the experiment, an average, simulated volume concentration of c_l was converted to pH using Eq. (3.23). The results are discussed in the next section.

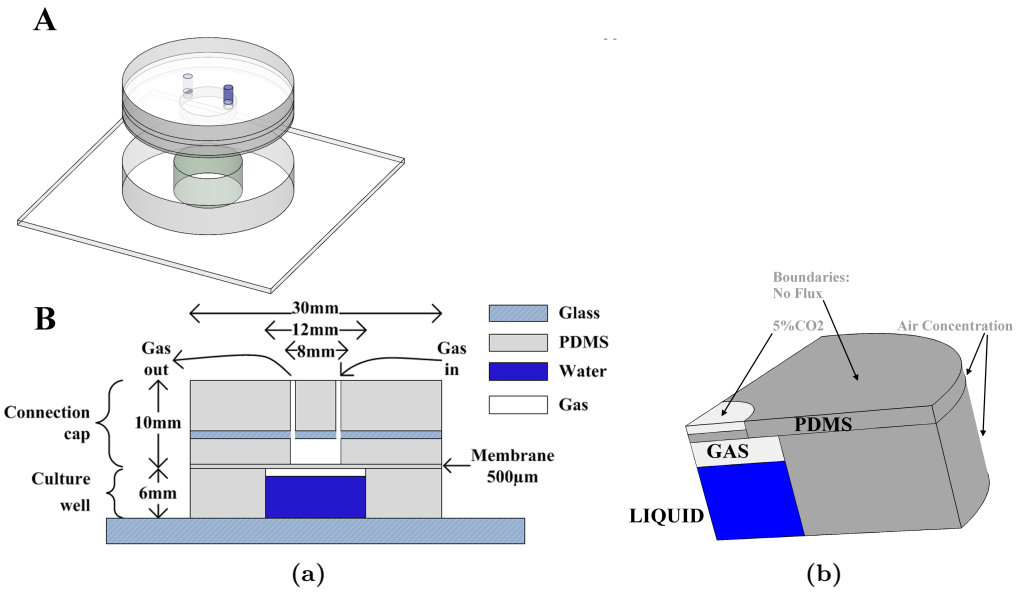

Figure 4.12: Cell cultivation device: (a) the schematic, including a 3D view (A) and the cross-sectional view (B); and (b) a model geometry used in the simulation, also showing the phases and boundaries used in the model. The bottom boundaries were set to the No Flux condition in COMSOL. Adapted from Publication IV.

4.4.2 Results and Discussion

Figure 4.13 shows a comparison of the model and measured pH (at time points 0, 10, 25, 40, 60, and 75 minutes) in the cell cultivation device presented in previous section. To clarify, this experimental data included two and three separate end-point measurements at time points 10 minutes and 25 minutes, respectively, whereas other time points were measured only once. The model predicted the dynamics of the experimental pH values remarkably well. During the first 75 minutes, we noticed only a maximum 0.1 pH difference between the simulation and the experiment. In addition, the simulated saturation value (pH = 4.72) was close to the measured values (pH = 4.73 to 4.85) obtained from the four long-term experiments explained in the previous section. To conclude, the model can be used to study the dynamics of CO_2 transportation in PDMS devices.

The validated model was used in two simulated cases to study how CO_2 is transported to the bottom of the chamber (where cells would be located) in different setups. The goal was always to provide a uniform 5% CO_2 to the bottom of the chamber. In the first case, we studied how two different CO_2 concentrations (0.04% and 5%) in the outer boundaries of the device (right side borders, marked as air concentration in Figure 4.12(b)) affect CO_2 concentration in the bottom of the chamber. These two concentrations represent cases in which the device would be in a standard laboratory environment (0.04% CO_2), or a typical incubator (5% CO_2 to maintain proper cell medium pH). The results are presented in Figure 4.14(a).

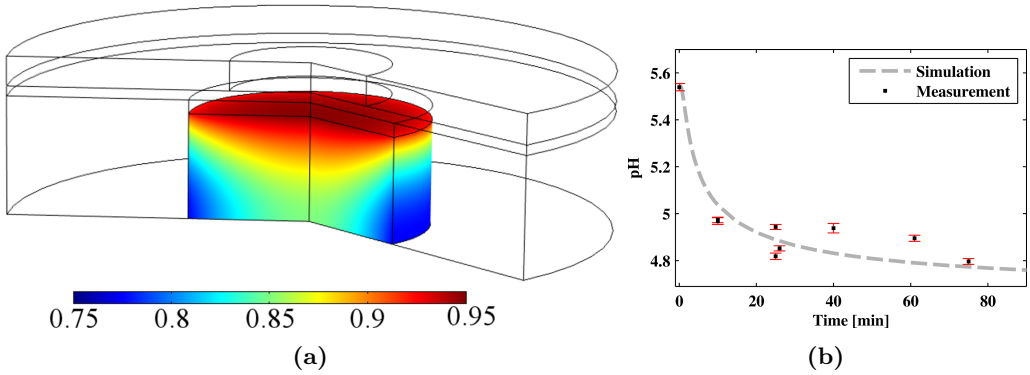

Figure 4.13: Model validation using pH measurements: (a) simulated CO_2 concentration (unit mol/dm^3) in liquid phase at time 500 min; and (b) simulated versus experimental pH. Adapted from Publication IV.

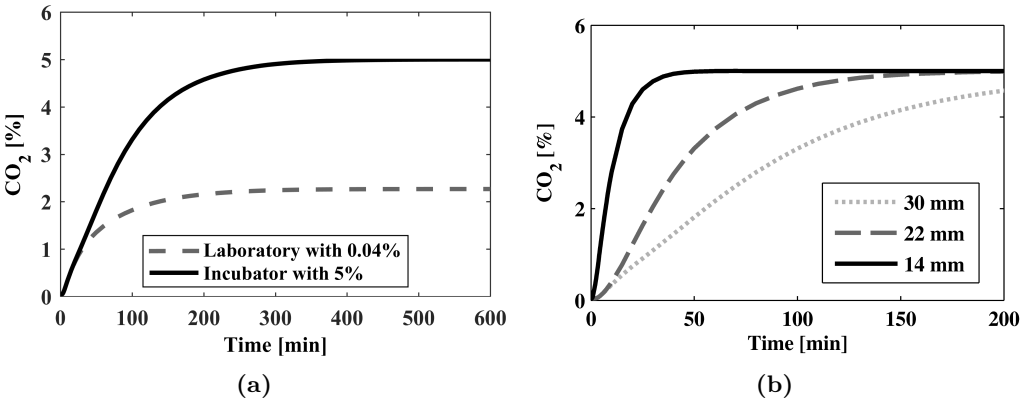

Figure 4.14: Simulation-based study of average CO_2 concentration in the bottom of the cell culture chamber when (a) outer boundaries are set to air (0.04% CO_2 concentration) and 5% CO_2 concentration; and (b) three different outer PDMS ring diameters are used and the outer boundary is set to 5% CO_2 concentration. Adapted from Publication IV.

The results from the first simulation case clearly show that the desired CO_2 concentration in the bottom of the device cannot be reached if the outer boundaries of the device have a low CO_2 concentration. Since PDMS is gas-permeable, these boundaries act as sinks. Significant amounts of gas fed through the membrane do not reach the bottom of the chamber (Figure 4.14(a)). Additionally, when 5% CO_2 concentration was set to the outer boundaries, it took more than seven hours before 5% CO_2 concentration was reached at the bottom of the chamber, which is too slow for many cases. The diameter of the outer PDMS was 30 mm, as presented in Figure 4.12(a). To improve the response, we also studied how this diameter affects the results by simulating three different outer diameters (30, 22, and 14 mm). Results are compared in Figure 4.14(b). As expected, with smaller outer rings 5% CO_2 reached the bottom of the chamber faster. The time was reduced to one hour with the 14-mm outer diameter.

In Publication IV, DI water was used as the liquid. However, for cell culturing purposes, it would be important to know how the pH of the cell medium changes, based on CO_2

transportation into the device. Therefore, it would be desirable to use a numerical model to estimate pH in the studies using cell culture media. To validate that the simulation can be used with cell culture media in different geometries, we compared previously published measurement results from Kreutzer et al. (2017) to our model. The basic principle of the simulation is as follows: CO_2 transport in the medium is first simulated as previously, using DI water. From the simulation, we get the time-dependent amount of dissolved CO_2 in the liquid. When we know the medium that was used (DMEM/F-12, including 14.29 mM $NaHCO_3$ concentration (Kreutzer et al., 2017)), we can use Eq. (3.26) to calculate the pH of the cell culture medium. The pKa of $NaHCO_3$, 6.3, was taken as an average of the reported pKa values (between 6.28 and 6.35) at 37 °C (Hu, 2012, p. 115; Harrison and Rae, 1997, p. 36; Hochfeld, 2006, p. 106; Will et al., 2011; Magnusson et al., 2013).

Figure 4.15(a) presents three different structures that were simulated. Kreutzer et al. (2017) named these Structures 1, 2, and 4. We excluded Structure 3 from this simulation study because it had a high evaporation rate of medium (Kreutzer et al., 2017); an issue that is not considered in our model. Here, Structure 2 was the same one that was used in the pH measurement with water (Section 5.2 in Publication IV, presented in Figure 4.12). In Structure 1, the gas flow was set between two PDMS rings in a cell culture chamber, and its model is very similar to the simulation case presented in Section 5.3 in Publication IV. Compared to the others, Structure 4 does not include an external CO_2 supply. In the experiments, these structures were initially inside an incubator (37 °C and 5% CO_2), before being brought outside. Therefore, their initial condition was assumed to be stabilized to the incubator environment. From the modeling point of view, outside boundaries were set to the CO_2 concentration in air.

After 72 h, measured pH values were 7.43 ± 0.03, 7.65 ± 0.06, and 8.80 ± 0.04 for Structures 1, 2, and 4, respectively (Kreutzer et al., 2017), whereas steady-state simulation results for the same structures were 7.36, 7.67, and 9.54. There was a significant difference between measurement and simulation results in Structure 4. However, no external CO_2 was supplied after the device was taken away from the incubator in this structure, so the outside CO_2 concentration in air significantly affected the results. In this first steady-state simulation, a typical CO_2 concentration in outdoor air, 0.04%, was used. However, it is not uncommon to have multiple times higher CO_2 concentrations in indoor laboratory air. For example concentrations of 0.15% CO_2 or even higher have been measured (Höppe and Martinac, 1998; Hussin et al., 2017; Seppänen and Fisk, 2004; Seppänen et al., 1999). Furthermore, different structures were measured closely to each other (Kreutzer et al., 2017). Therefore, CO_2 gas coming out from Structures 1-3 could raise CO_2 levels in the air near these devices. Based on these issues, it could be reasonable to assume that higher CO_2 concentrations surround these devices, so higher CO_2 levels should be set to the outer boundaries in the model. We tested this hypothesis by changing the boundary CO_2 level from 0.04% to 0.15%, and simulated the structures again. As Structures 1 and 2 have external CO_2 supplies, their pH levels were not significantly affected. However, steady-state pH was lowered to 8.88 in Structure 4. Based on this observation, we set a higher CO_2 concentration in the outer boundaries for the following simulations and studied pH change in these three structures. From the simulated CO_2 transportation, we calculated an average $[CO_{2(aq)}]$ in the cell area, which was then converted to pH, using Eq. (3.26). Figure 4.15(b) shows the results.

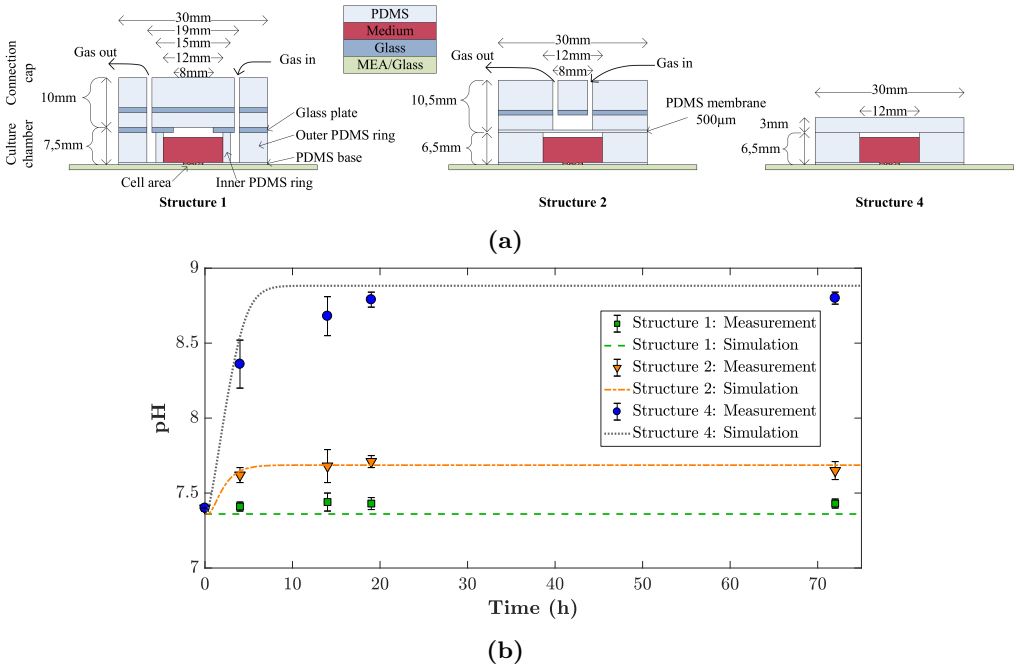

Figure 4.15: Testing CO_2 transport model with measurements using cell culture medium: (a) Structures 1, 2 and 4 (adapted from Kreutzer et al. (2017)); and (b) a comparison of measured and simulated pH values.

To summarize, this section presented a computational model to simulate CO_2 transportation in the cell culture applications. Several experiments were performed to validate the model presented in Publication IV. We demonstrated that the model can estimate CO_2 transport in silicone-based devices, and that pH values from the numerical simulations are similar to experimental data. Using the validated models, simulation-based studies demonstrated how modeling could improve the cell culturing environment. In addition, the model predicted pH change reasonably well, not only with water, but also with cell media as shown in Figure 4.15(b). Therefore, using this model, we could study CO_2 transportation and design structures that enhance pH control of the cell culture media. For the future research, a simulation-based design optimization could be possible, for example, by integrating the Optimization Module package from COMSOL together with the developed COMSOL model.

Chapter 5

Indirect Cell Culture Temperature Measurement and Control

Indirect temperature measurement and control were studied in Publications V and VI, which are summarized in this chapter. These studies present a novel method to precisely monitor and control the cell culture temperature without using a sensor in the area. The method was based on temperature estimation models that were created using system identification techniques. Reasons for this approach were discussed in Section 2.5. The concept of the indirect cell culture temperature measurement is given in Figure 5.1, where a temperature sensor located outside is used to estimate the desired cell culture temperature. This concept was used for indirect temperature measurement and control experiments presented in Publications V and VI, where a sensor located in the cell culture area was only used for monitoring purposes.

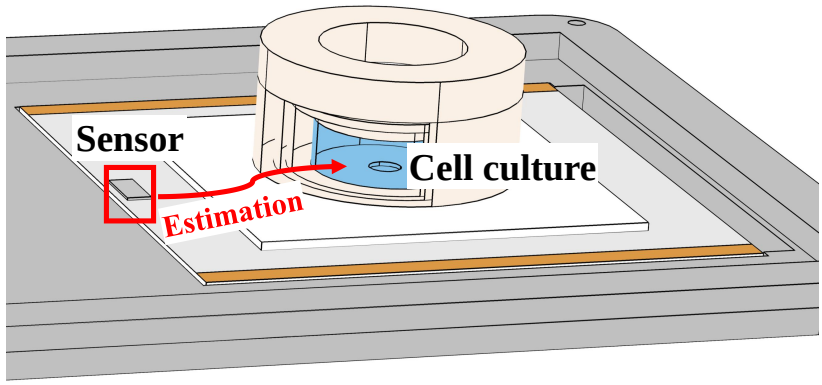

Figure 5.1: The concept of indirect cell culture temperature measurement. An outside sensor, marked with a rectangle, is used to indirectly estimate the cell culture temperature.

5.1 Indirect Temperature Measurement

5.1.1 Materials and Methods

Publication V presented an indirect, temperature measurement method that was implemented using a commercial heating device MEA1060-Inv together with a PI ($K_p = 6, K_i = 0.9$) temperature controller TC02 (Multi Channel Systems MCS GmbH, Germany). The experimental setup (Figure 5.2) included the heating device, a custom-made PDMS device and a temperature sensor plate (TSP), which included 14 sensors. The layout of the TSP was designed so that temperatures in different part of the plate could be measured. The TSP was fabricated on a cleaned 49 mm × 49 mm × 1 mm microscope slide. First, a photoresist was patterned on it with µPG501 maskless exposure system (Heidelberg Instruments, Germany). A 275 nm of copper was e-beam evaporated followed by a lift-off with acetone in an ultrasonic bath. Then, plasma-enhanced chemical vapor deposition (Oxford Instruments, UK) was used to deposit an insulator layer (approximately 500 nm of silicon nitride). See Section II-A in Publication V for more detailed description of the fabrication process. Typical resistance of the sensor was between 100 Ω and 110 Ω at room temperature, and a linear temperature dependency of the resistivity was obtained (Figure 4 in Publication V). We only used two of the sensors in this study, presented in Figure 5.2, to measure the temperature inside (T_Ri) and outside (T_Ro) the PDMS device. With the experimental setup, we developed two temperature models to estimate T_Ri using system identification techniques. We created these models using the System Identification Toolbox in MATLAB.

In Model 1, the temperature estimation was based on the measured heating device temperature T_heater, whereas Model 2 used T_Ro for the estimation. The input and output signals were T_heater and T_Ri for Model 1, and T_Ro and T_Ri for Model 2 (Figure 5.3). For the simulations, we used Simulink. Two temperature models were developed because of their use in different applications. Model 1 was easier to implement. In principle, no TSP was needed after model development, as the control was purely based on the measured T_heater, simplifying the required setup. Model 2 provided clear advantages in some cases, such as when the cooled TSP was placed on a preheated heating device. This might happen during routine cell culturing, when the TSP is moved between the heater and a microscope. In this case, Model 1 would not have worked very well, as it would have overestimated T_Ri and resulted in too low heating power. Another case in which Model 2 works better is liquid change, which is considered in Publication VI.

In this study, and the one in Section 5.2, we developed third-order, discrete-time, state-space models using a prediction error method (Section 3.3) and implemented an anti-windup method (Section 3.4) in our controllers. We also typically estimated initial state values $x(0)$ from the first 10 sec of each measurement data using MATLAB. The sample time of the models was always 1 sec.

5.1.2 Results and Discussion

Model 1 was developed and studied with an estimation measurement and four validation measurements, respectively. In addition, the same estimation measurement and two validation measurements were used to identify Model 2. These experiments are shown in Figure 5.4. Detailed model parameters (used in Eq. (3.28)) are given in Table I in Publication V.

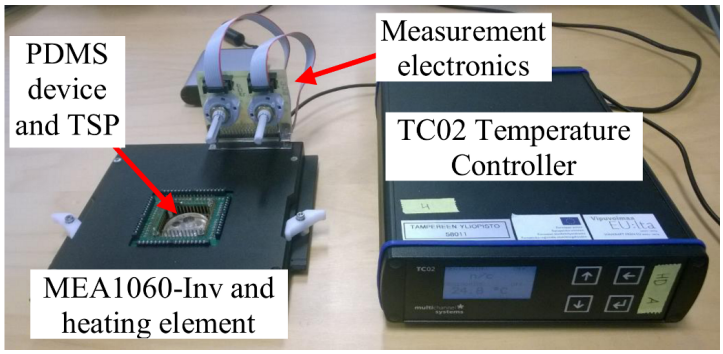

(a)

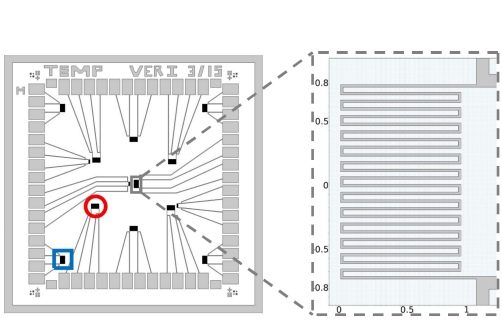

(b)

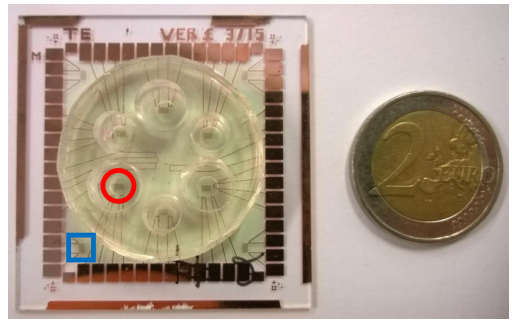

(c)

Figure 5.2: Indirect temperature measurement: (a) experimental setup; (b) a designed TSP; and (c) a fabricated PDMS device on top of the TSP. Resistors used in the experiments are marked with a circle and a square to measure *T_Ri* and *T_Ro*, respectively. Adapted from Publication V.

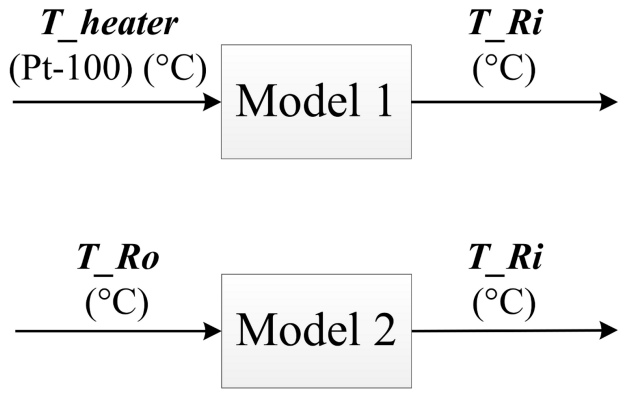

Figure 5.3: Block diagrams of the developed models. Adapted from Publication V.

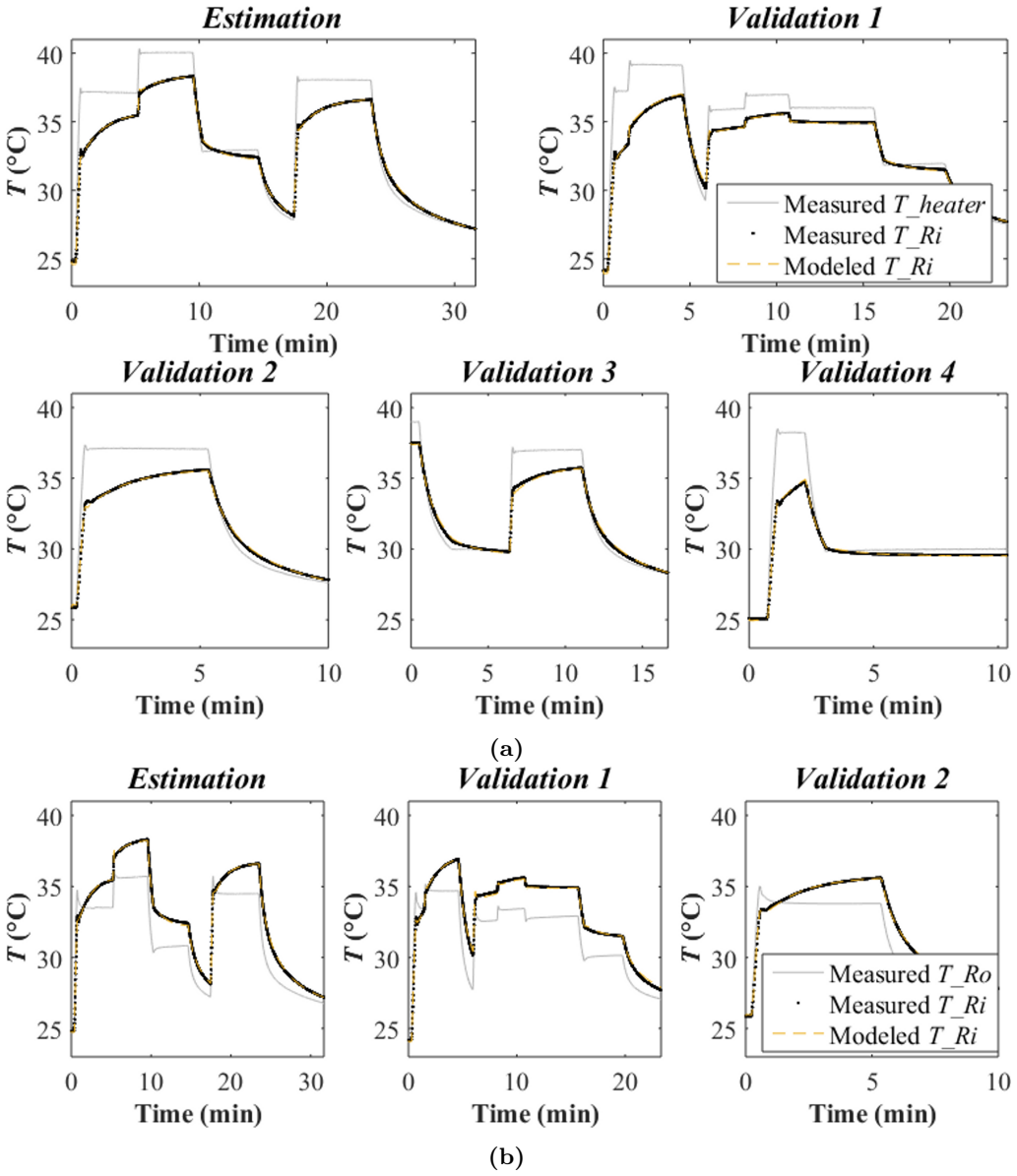

Figure 5.4: Measurement and modeled data from: (a) Model 1, in which the input signal is *T_heater* and (b) Model 2, in which *T_Ro* is an input signal. Adapted from Publication V.

Both models provided acceptable estimations of T_Ri. The average difference between measured and simulated temperatures was 0.1 °C or below in every validation measurement, summarized in Table II in Publication V. Figure 5.5 compares the models and shows the difference between measured and simulated temperatures.

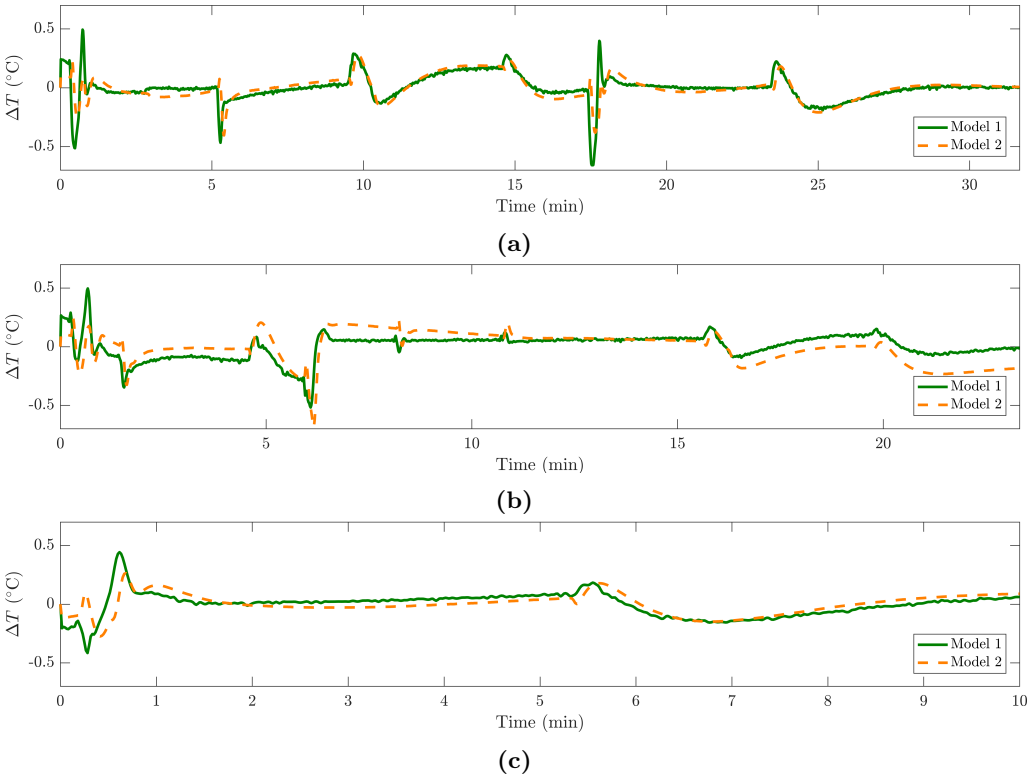

Figure 5.5: Difference between the measured and simulated temperatures when experiment is: (a) Estimation; (b) Validation 1; and (c) Validation 2. Adapted from Publication V.

As slightly better performance was obtained with Model 1, as its sensitivity for liquid volume changes was tested. The goal was to study how typical experimental changes, such as liquid evaporation during long-term cell culturing, would affect the accuracy of temperature estimation. In this case, liquid volume was increased and decreased by 50 µl compared to the original liquid volume of 200 µl. We should emphasize that this large volume change (25 percent) is more than typically seen. The purpose was to show that if the temperature estimation worked with this large a volume change, it should also work with smaller volume changes. Figure 5.6 shows the results. Acceptable results were obtained even with remarkably large volume changes. This means that the indirect temperature measurement can be used with long-term cell experiments, even though liquid volume can be changed because of, for example, evaporation.

Finally, in Publication V, closed-loop simulations were performed to study how indirect temperature control would work. These simulations are presented in Section IV-D of Publication V. Figure 5.7 shows one comparison of a closed-loop system response of measurement and simulation.

Simulation results indicated that the indirect temperature control system works well,

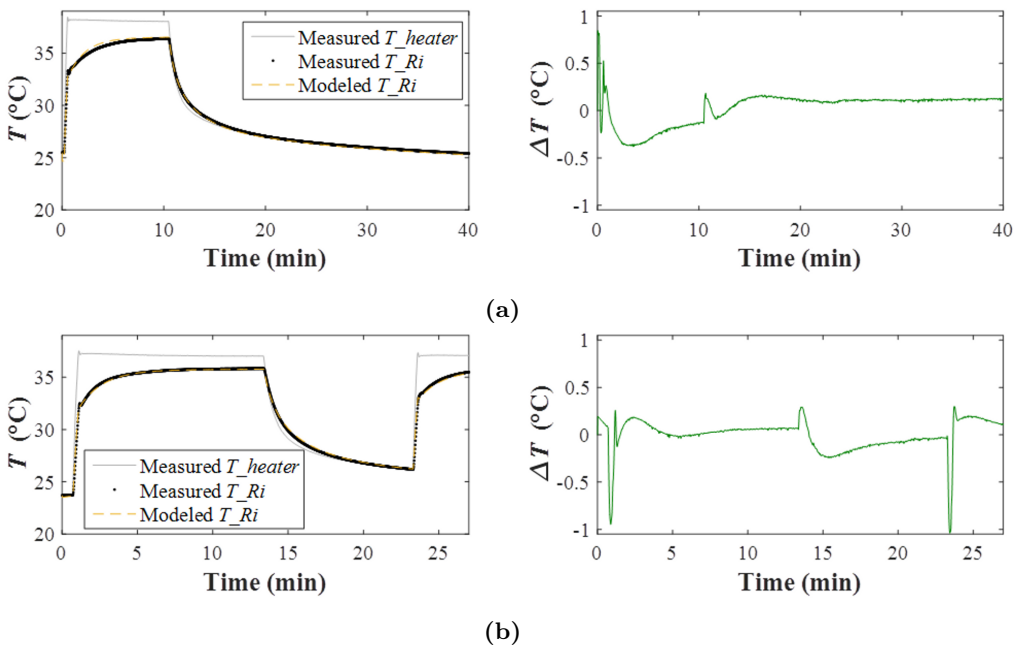

Figure 5.6: Model 1 sensitivity tests for liquid volume change. Measurement and modeled data (left figure) and difference between measured and modeled T_Ri (right) when liquid volume is (a) 250 µl and (b) 150 µl. Adapted from Publication V.

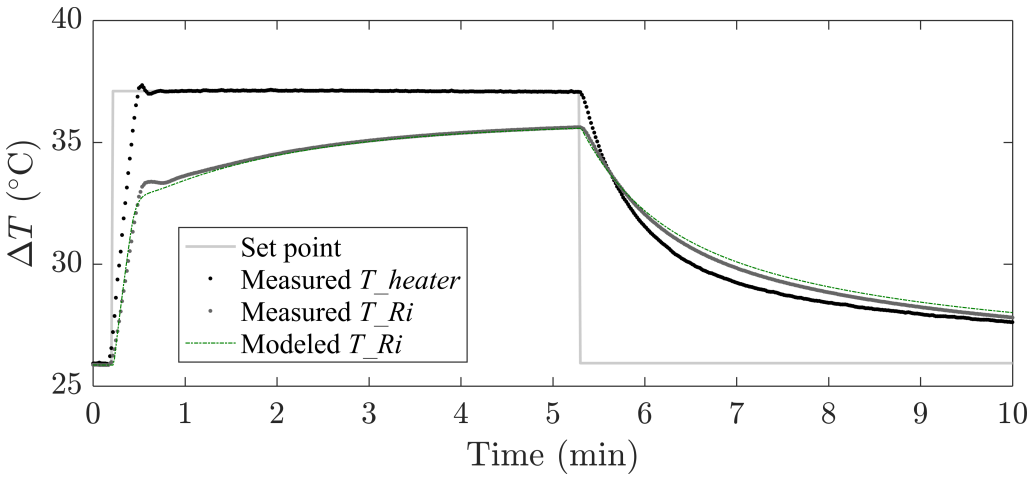

Figure 5.7: A comparison of the closed-loop system responses of measurement and simulation. Adapted from Publication V.

such as when ambient room temperatures vary. Therefore, we designed and fabricated our own indirect temperature control system in Publication VI, which will be presented in the next section.

5.2 Indirect Temperature Control

5.2.1 Materials and Methods

Publication VI presented a portable cell culture system, in which a temperature control system was based on temperature estimation. The main components of the system are presented in Figure 5.8. In our device, an indium tin oxide (ITO) plate was used as a heating element. This allowed us to design and implement an indirect temperature control system. We also designed and fabricated a new, more suitable TSP to measure two temperatures; one on the cell-culturing area (T_{cell}), and one close to it (T_{TSP}). These temperatures are similar, but not exactly the same, as T_Ri and T_Ro, respectively, presented in Section 5.1. The system also included a cell culture device to keep the cell cultures alive for several days and enable on-line microscopy. The cell culture device had three main parts: a cell culture chamber (from PDMS), a lid (from polycarbonate), and a 3D printed cover. This setup prevented contaminants from entering the chamber and enabled us to supply dry gas without much evaporation of the culture medium (Kreutzer et al., 2017). In the experiments, the cell culture chamber was reversibly bonded on the TSP. With the cover placed atop the lid and the chamber, the gas supply pipe was connected to provide the desired gas environment (CO_2 and O_2 concentrations) inside the chamber. Furthermore, a motorized, inverted microscopy system was used for imaging during cell experiments.

Figure 5.9 shows the working principle of the temperature control setup. Control was based on estimates of outside temperature ($T_{outside}$) measured using either the Pt100 sensor on the ITO plate or the resistor on TSP. These are highlighted with a rectangle in Figure 5.8(c) and a circle in Figure 5.8(e), respectively. Measured $T_{outside}$ was then inputted to the mathematical model, which calculated temperature estimation $T_{cell-est}$, which was then compared to the set-point temperature (T_{set}) to complete the closed-loop feedback system. We implemented a PI controller with parameters ($K_p = 1.7, K_i = 0.03$) to which the control system had a close-to-critically damped response, with only a minor overshoot. The controller's maximum power was 2 W. Since there was no active cooling element, the temperature was only decreased due to heat dissipation. We also monitored the ambient room temperature, T_{room}, and the real cell culture temperature, T_{cell}, that was only used for model development and analysis.

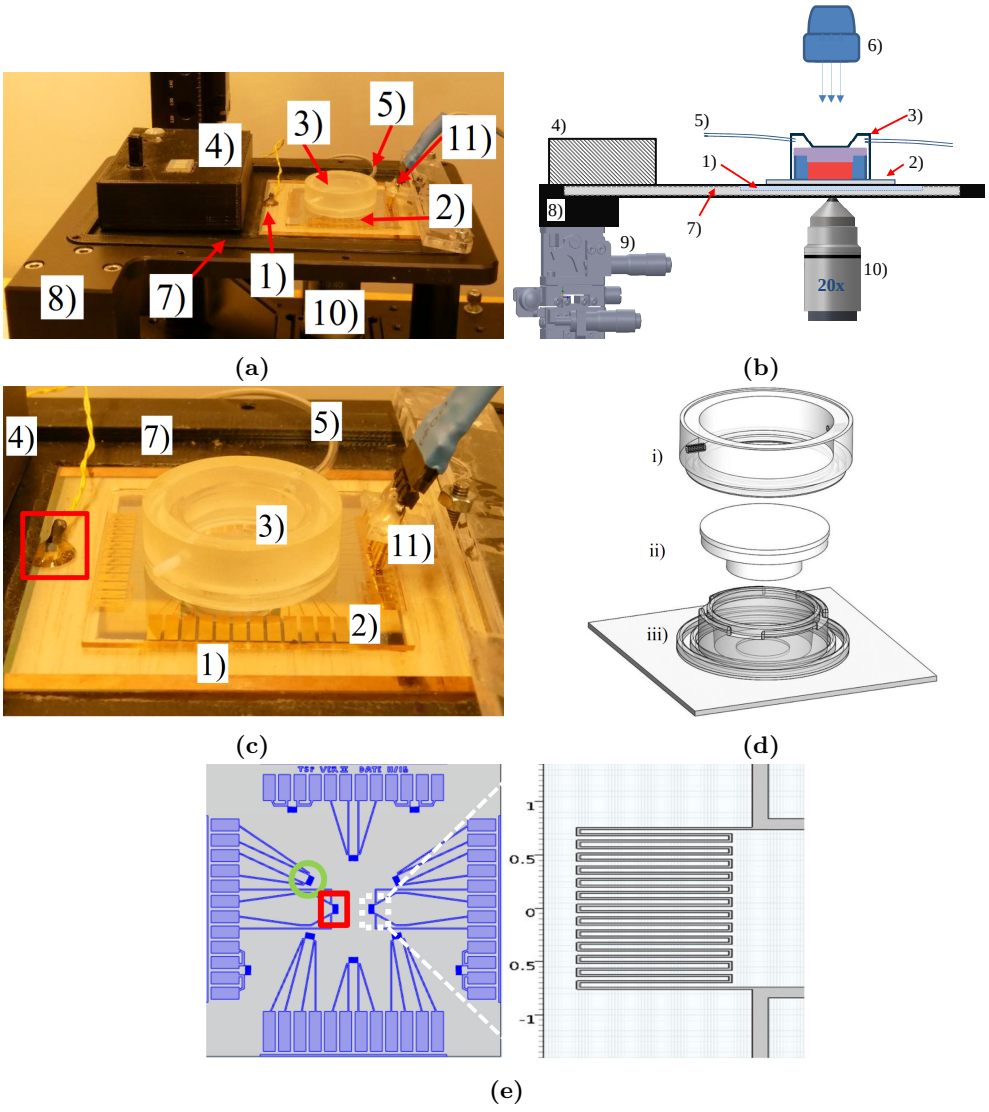

Figure 5.8: Indirect temperature control setup. System overview: (a) Experimental setup; (b) the schematic of the optical system tailored for cell culturing. Numbers show the 1) ITO heater, 2) TSP, 3) cell culture device, 4) electronics, 5) gas supply, 6) illumination unit using a white light-emitting diode, 7) ITO frame, 8) aluminum frame 9) xyz stage, 10) motorized inverted microscopy with 20x objective, and 11) connection pins to read resistances of TSP sensors; and (c) an enlarged image of the main components. The Pt100 sensor measuring temperature of the ITO plate (T_{ITO}) is marked with a rectangle. (d) Expanded view of the cell culture device: i) cover, ii) lid, and iii) cell culture chamber. (e) Designed temperature sensor layout, where resistors marked with a rectangle and a circle are used to measure T_{cell} and T_{TSP}, respectively. Adapted from Publication VI.

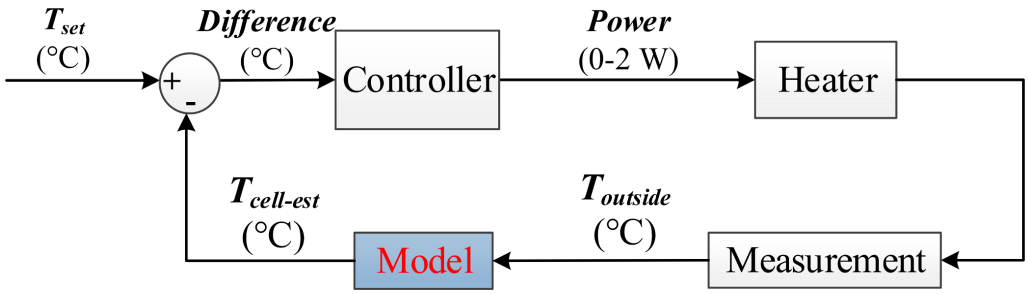

Figure 5.9: The working principle of indirect cell culture temperature measurement and control. Adapted from Publication VI.

Two different temperature estimation models were developed. In Model 1, $T_{cell-est}$ was calculated from T_{ITO}, whereas T_{TSP} was used in Model 2. In each test, 1 ml DI water was added to the cell culture chamber. As in the previous study, these temperature estimation models we created using the System Identification Toolbox.

5.2.2 Results and Discussion

We created two temperature estimation models from experiments in which temperature was controlled using $T_{outside}$. In these experiments, T_{set} was randomly changed, and both $T_{outside}$ and T_{cell} were recorded. Third-order, discrete-time, state-space models with structures presented in Eq. (3.28) were developed. Section III-A in Publication VI provides the model parameters and shows that acceptable results were obtained. Model fit numbers using Eq. (3.29) were 94.2 percent and 94.8 percent for Model 1 and Model 2, respectively.

After model development, we compared four different control strategies to maintain T_{cell} at 37 °C (in other words, T_{set} was 37 °C). The purpose of this experiment was to show how variations in the ambient room temperature (T_{room}) can produce undesired changes in T_{cell}, if an improper control system is used, thus demonstrating the benefits of the indirect control system. Here, we implemented one open-loop system and three closed-loop control systems. In the open-loop system, heating power was constant. Three closed-loop systems used the same PI controller, but the control was based on different signals in the feedback loop. In the first closed-loop system, temperature was regulated based on T_{ITO} (using the Pt100 sensor marked with a rectangle in Figure 5.8(c)). The control of the second closed-loop system was based on T_{TSP}, marked with a green circle in Figure 5.8(e). The last control system used Model 2. The control was based on the estimated $T_{cell-est}$, as explained in the previous section. Figure 5.10 shows a comparison of the different control strategies.

Results in Figure 5.10 clearly indicated significant difference between control strategies. Although the controller worked in each closed-loop system (with the controlled temperature maintained at 37 °C), T_{cell}, which is important for cell culturing, was not stable. For example, the maximum variations in the measured T_{cell} during the experiment were 1.5 °C (open-loop), 1.1 °C (closed-loop using T_{ITO}), and 0.2 °C (closed-loop using T_{TSP} or $T_{cell-est}$). The two latter methods provided significantly better control results compared to other methods. Using these two latter methods, it is significantly easier to maintain the cell culture temperature at the desired level.

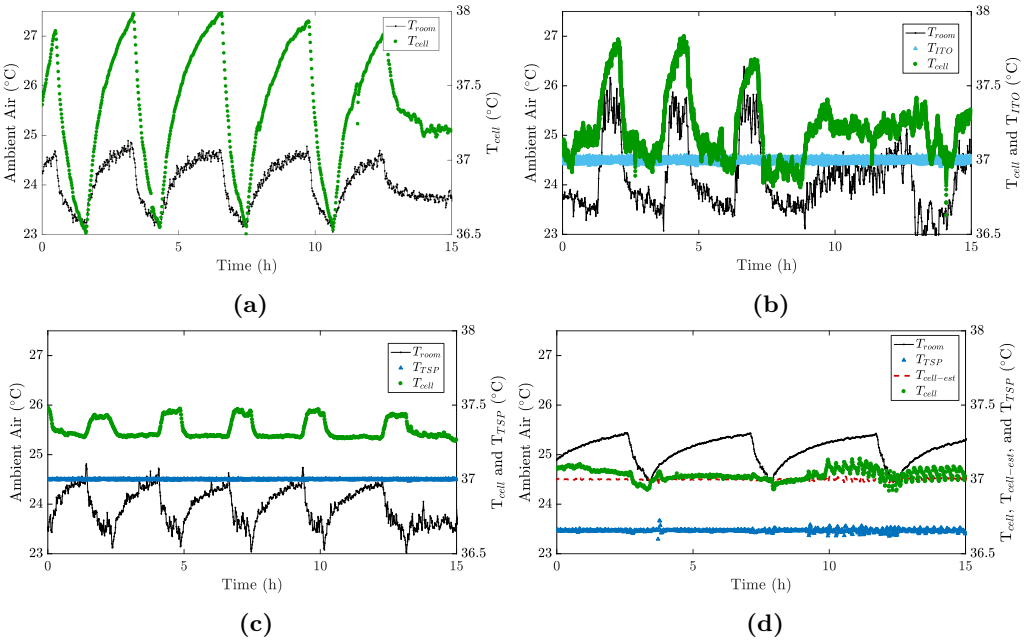

Figure 5.10: Comparison of different temperature controller strategies: (a) An open-loop control system with constant power, closed-loop control systems, in which temperature is controlled by (b) T_{ITO}, (c) T_{TSP}, and (d) $T_{cell-est}$ using Model 2. Adapted from Publication VI.

As the indirect control system provided very good results, a long-term temperature control test was performed. Proper temperature control is important, as long-term (from days to even weeks) cell cultures are used. The goal of this experiment was to regulate the cell culture temperature to 37 °C. Temperature control was based on $T_{cell-est}$ using Model 2. After experiment, variations in T_{cell} were studied. Indirect control maintained T_{cell} at 37 °C $\pm$ 0.3 °C for more than 100 hours, as presented in Figure 11 in Publication VI. This is an acceptable result for cell cultures studies, as previously reported suitable temperature variations are between $\pm$ 0.3 °C and 1 °C (Cheng et al., 2008; Lin et al., 2010, 2011; Petronis et al., 2006; Regalia et al., 2016; Reig et al., 2010; Witte et al., 2011). Environmental variations (T_{room} varied between 22.6 °C and 25.9 °C) were successfully compensated for by the control system.

When T_{cell} is precisely controlled, temperature-dependent cell behavior can be studied, such as defining a temperature threshold in which the ion channels are activated (Bridle et al., 2008). Therefore, we studied how well the indirect temperature control works when T_{set} is changed. Figure 5.11 shows an example of the experiment with Model 2. The resulting average temperature estimation error, 0.21 °C, was acceptable. In addition to these experiments, we demonstrated temperature control during a liquid change, and the portability of the control: battery-operated system to maintain temperature for more than an hour at 37 °C. These experiments are presented in Sections III-E and III-F in Publication VI.

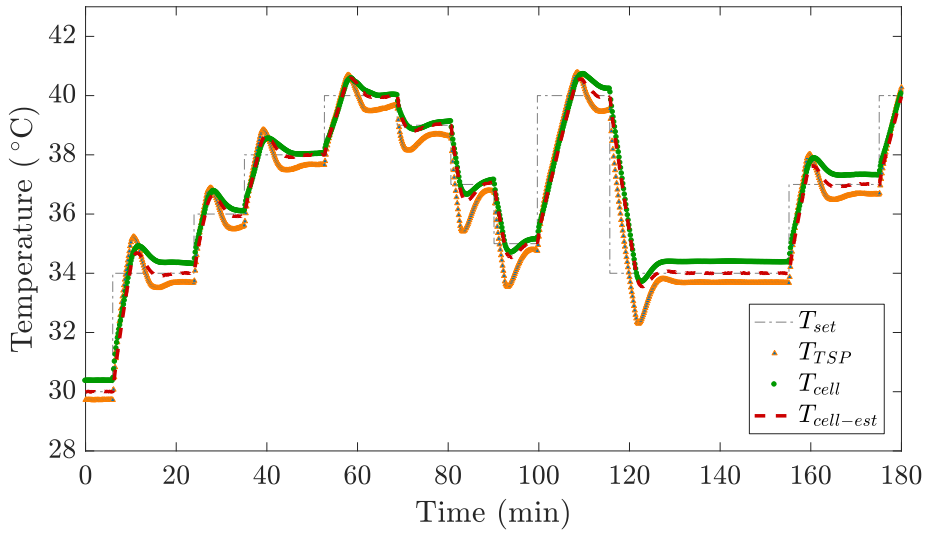

(a)

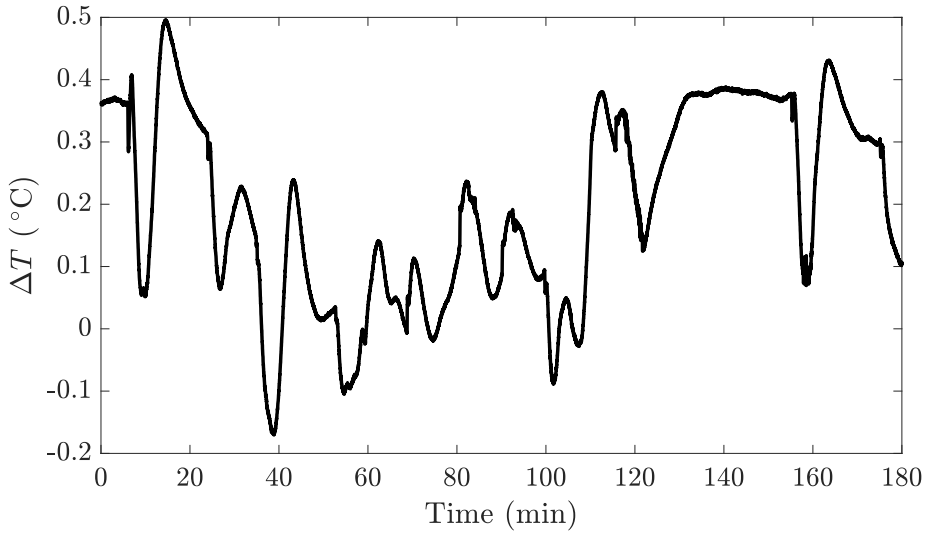

(b)

Figure 5.11: Transient temperature control using Model 2: (a) results and (b) difference between measured T_{cell} and $T_{cell-est}$. Adapted from Publication VI.

We also studied how the device would operate when cells are included. There were two goals in these cell experiments; to demonstrate a successful long-term *in vitro* culturing of beating cardiomyocytes in the system, and to show how their beating rate varied in different temperatures. In these studies, a non-invasive video image-based method presented earlier (Ahola et al., 2014) was used to analyze the mechanical beating behavior of cardiomyocytes.

First, we cultured cardiomyocytes *in vitro* over 100 hours, and recorded 60-sec videos with a frame-rate of 50 frames per second, once a day starting 24 h after the cells were initially plated to the device. Analyzed average beating rates were 44 and 36 beats per minute

(BPM) on the first day of culturing and 110 h later, respectively, demonstrating successful long-term cell culturing. Figure 5.12 shows the snapshot images of the recorded initial and final videos. We used a cell cluster on the left to analyze the beating rate.

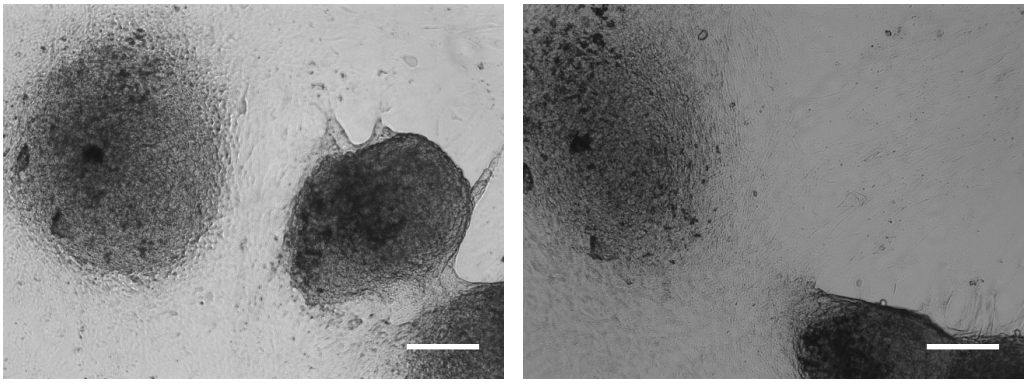

(a) **(b)**

Figure 5.12: Snapshot images of beating cardiomyocytes (a) two days after plating cells on the device, and (b) 110 h later. Scale bar represents 100 µm (Mäki et al., 2018).

In the second experiments, several different temperature values between 25 °C and 37 °C were applied to cell culture. After each temperature change, we waited 25 minutes before a video recording. After the experiment, the video image-based method was used to calculate the beating rates in different temperatures. Results are presented in Figure 5.13, where Measurement number represent the analyzed beating rate a certain temperature point. For example, Measurement number 1 represent the first measured beating rate at 37 °C, Measurement number 2 is the following measurement event at 35 °C 25 min after the set-point temperature was changed from 37 °C to 35 °C, and so on.

Figure 5.13 shows that we were able to not only change the beating rate of the cardiomyocytes, but also recover the beating rate when the temperature was returned to 37 °C. The average beating rate was 54.8 BPM ± 3.2 BPM at 37 °C, based on 11 measurements points shown in Figure 5.13(b). Interestingly, average beating rates at 35 °C and 34 °C were 44.5 BPM and 36.0 BPM, respectively. We estimated that the beating rate dropped roughly 10 percent in every °C when the temperature changed from 37 °C to 34 °C. Although these results were only from four measurement points and further studies are required, they highlight the importance of proper temperature control in the cell area to minimize undesired temperature stimulations to the cells.

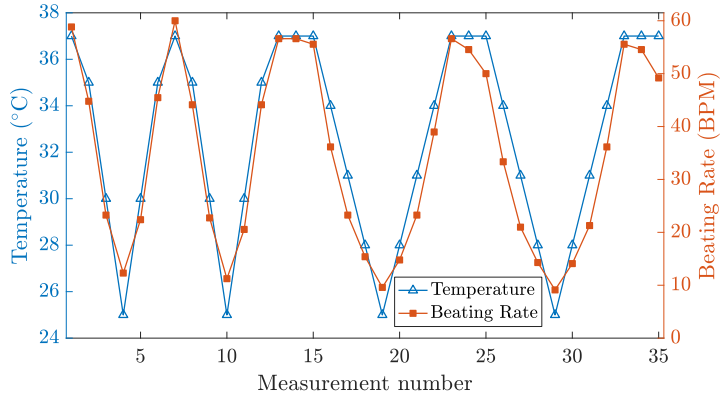

(a)

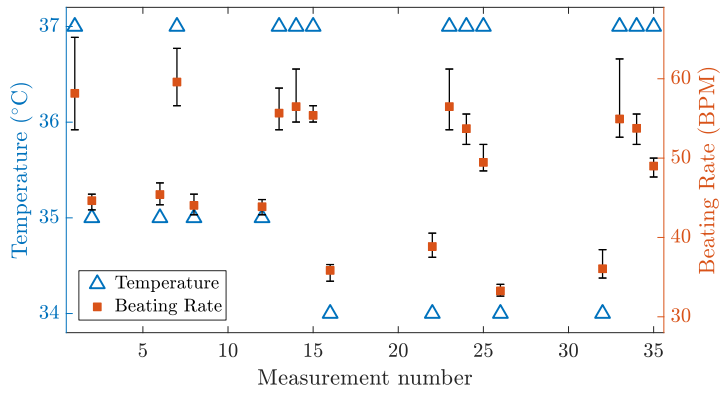

(b)

Figure 5.13: Beating rate of cardiomyocytes at different temperatures: (a) full measurement data; (b) a zoomed-in image showing the average beating rates at temperatures between 34 °C and 37 °C. Error bars represent the minimum and maximum values calculated from each 60-sec video (Mäki et al., 2018).

To summarize, Publication VI presented a combination of a microscale cell culture device and a novel, indirect temperature control method, which allowed for maintaining and regulating cell culture temperature without direct measurement from the culture area. We first demonstrated long-term temperature control by maintaining the cell culture temperature at 37 °C ± 0.3 °C for more than four days in the system. This temperature variation was comparable with other studies (Cheng et al., 2008; Fang et al., 2017; Hsieh et al., 2009; Huang et al., 2013; Lin et al., 2010, 2011; Nieto et al., 2017; Petronis et al., 2006; Regalia et al., 2016; Vukasinovic et al., 2009; Witte et al., 2011; Yamamoto et al., 2002). In addition, we were able to precisely monitor and control temperature during temperature transients, which has typically not been possible without placing the sensor to the cell culturing area. We also showed that our temperature control compensated for disturbances origin from: i) ambient room temperature variations; ii) system movements; iii) opening the cell-culture device; and iv) liquid change. Finally, we cultured beating cardiomyocytes and showed that the system can be used for studying temperature-dependent cell behavior.

Chapter 6

Conclusions

This chapter summarizes the results of this thesis, provides answers to the research questions in Section 1.2, considers the limitations of the study, concludes the thesis, and provides recommendations for future work.

6.1 Summary of the Results

There were two main goals in this thesis. The first was to develop mathematical models for microscale cell culturing environments. The aim is for these models to be used to study, design, and improve cell culture environments. These models are design tools that can also be used to develop control strategies for gravity-driven flow, drug distribution, pH, and temperature in microscale cell culturing environments. The second goal was to study indirect measurement methods to control environmental parameters. This study focused on developing indirect temperature control strategies.

The mathematical models were presented in Publications I to IV. First, gravity-driven flow was studied in Publications I to III. In Publication I, we developed an analytical model to estimate the flow rate in gravity-driven flow systems. We showed by mathematical simulations and experiments that if capillary pressures are not included in the model, it is highly likely to overestimate the flow rate of the system. This may prevent proper design of a microfluidics device using gravity-driven flow. This could cause inefficient nutrient supply and waste removal in the system, resulting in undesirable culture conditions. The model provided results with good accuracy compared to experimental data. Publication II presented a mathematical model to study gravity-driven drug delivery in a microfluidics device. Our method was to combine the analytical model presented in Publication I and a numerical model to avoid computationally-intensive calculations. Therefore, we could extended simulation times to scales that are relevant to systems using gravity-driven flow. These types of simulations have not been presented before. With the simulations, we demonstrated how drug-concentration profiles could be improved by geometry modifications. In Publication III, we developed a numerical model that combined gravity-driven flow and calorimetric flow sensors. We showed that the sensitivity of this non-invasive flow measurement can be improved using our model.

In Publication IV, we developed a numerical model to study CO_2 transportation in silicone-based microfluidic devices. The paper demonstrated that the model including transportation in and between gas, liquid, and solid phases could estimate CO_2-concentration profiles in the device. Mathematical simulations can also estimate the pH

of cell media, and model-based studies can improve pH control. This was the first time that CO_2 transportation in silicone-based devices was mathematically modeled.

The second part of the thesis considered indirect measurement and control methods. Could these methods improve the performance of *in vitro* cell cultures? In this thesis, we demonstrated indirect temperature measurement and control methods in Publications V and VI. System identification techniques were implemented to create required temperature estimation models. In Publication V, we showed that indirect temperature measurement provides excellent accuracy for cell cultures *in vitro*. Simulation-based study showed that indirect temperature measurements could also be used in feedback control. For this reason, a portable, microscale cell culturing device including indirect temperature measurement and control was implemented in Publication VI. We demonstrated that remarkably more accurate culture temperature was obtained with this novel control method. Other benefits of the developed device, such as portability and possibility to study the effect of temperature stress on cell behavior, were also presented.

6.2 Answering the Research Questions

We deduce from this thesis that the research questions presented in Section 1.2 are answered in this section. The first research question in the thesis concerned gravity-driven flow.

> *Can numerical modeling tools be used to study gravity-driven flow and drug concentration profiles in microscale systems, without the need for extensive computation time?*

This research objective was discussed in Sections 4.1 to 4.3. The combination of analytical and numerical models provides a method to study gravity-driven flow in complex geometries, without extensive usage of computation power. Using the method, we can analyze flow, shear stress, and drug concentration profiles in microscale devices based on gravity-driven flow, even in 3D-simulations.

The second research question was on CO_2 transportation.

> *Can CO_2 transportation and medium pH, be estimated using numerical methods in silicone-based microscale cell culturing devices, as only O_2 transportation models in these devices have previously been reported?*

Section 4.4 focused on this question. A large set of experiments was performed to verify that the mathematical model could estimate CO_2 transportation and liquid pH in cell culturing devices. We showed that the model could also approximate the pH of the cell culture when we know the properties of the cell medium.

The final research question dealt with the indirect measurement and control methods for the cell culturing environment by focusing on temperature in this thesis.

> *Is an indirect temperature measurement method acceptably accurate to successfully monitor and control temperature for long-term cell culturing purposes?*

This question was covered in Chapter 5. The sufficiently accurate results indicated that the indirect measurement could be used for measuring and controlling temperature in cell cultures. The indirect control method provided superb results for maintaining temperatures for long-term cell culturing and a novel method to control temperature while performing temperature-dependent cell studies.

6.3 Limitations of the Study

This section summarizes limitations related to the thesis. First, there is no comprehensive model that integrated all the presented models. Instead, models were studied separately. The models to study gravity-driven flow assume constant temperature. Furthermore, they do not consider liquid filling in a microchannel, which is a complex phenomenon. The numerical models related to drug delivery and calorimetric flow sensors were not validated with gravity-driven experiments. The mathematical model describing CO_2 transportation also assumed a constant temperature. In addition, liquid flow (demonstrating medium perfusion) was not included in this model. This same limitation concerns studies with indirect temperature measurement and control. Temperature controller parameters were also not optimized in these studies.

6.4 Discussion and Future Outlook

This thesis studied how modeling tools and indirect control methods can improve the cell cultivating environment of *in vitro* cell culturing devices. Based on the results, it is clear that there are still many issues to be examined. The challenges presented in previous sections should be studied to provide better design and control tools. One suggestion for further work, based on the thesis, is to integrate our model to one 3D-model that includes gravity-driven flow, temperature, and gas (both CO_2 and O_2) transportation. This should be possible with the tools presented here (such as COMSOL). However, it can be challenging not only to implement all the required physics in the same model, but also to solve this model without the help of very large computation power and time. It would also be desirable to build and test a more advanced system, including medium perfusion. This could be used to study, for instance, how the CO_2 transport model or the indirect temperature control model would work when perfusion is included. Future studies could also examine how to integrate more microfluidic components, cell imaging and analysis, and sensors to a single, microscale culture device that is fully controlled using a user-friendly computer interface. To goal could be to develop a modular platform that does not only provide a stable and cell-friendly environment for long-term cell culturing, but can also adjust this environment. For example, it could create hypoxia conditions to the cell cultures to meet the requirements of the physiological study. In this development task, mathematical models will provide a valuable design tool.

In conclusion, the results of this thesis show that modeling can provide valuable insight to the cell culturing environment and can be used as design tools when developing cell culturing devices. While cell experiments were not used to validate all the developed models, these models can provide beneficial information that typical single-point measurements can not provide. For example, simulation can illustrate the spatial distribution of the gas transport inside the culture area. In addition, the indirect control system using system identification techniques could improve microscale cell culturing environmental control and be further studied to examine other environmental parameters.

Bibliography

Abeille, F., Mittler, F., Obeid, P., Huet, M., Kermarrec, F., Dolega, M. E., Navarro, F., Pouteau, P., Icard, B., Gidrol, X., Agache, V., and Picollet-D'hahan, N., "Continuous microcarrier-based cell culture in a benchtop microfluidic bioreactor," *Lab on a Chip*, vol. 14, no. 18, pp. 3510 – 3518, 2014.

Adler, M., Polinkovsky, M., Gutierrez, E., and Groisman, A., "Generation of oxygen gradients with arbitrary shapes in a microfluidic device," *Lab on a Chip*, vol. 10, no. 3, pp. 388 – 391, 2010.

Ahola, A., Kiviaho, A. L., Larsson, K., Honkanen, M., Aalto-Setälä, K., and Hyttinen, J., "Video image-based analysis of single human induced pluripotent stem cell derived cardiomyocyte beating dynamics using digital image correlation." *BioMedical Engineering OnLine*, vol. 13, no. 1, p. 39, 2014.

Amir-Aslani, A. and Mangematin, V., "The future of drug discovery and development: Shifting emphasis towards personalized medicine," *Technological Forecasting and Social Change*, vol. 77, no. 2, pp. 203 – 217, 2010.

Barbosa, B. H. G., Aguirre, L. A., Martinez, C. B., and Braga, A. P., "Black and gray-box identification of a hydraulic pumping system," *IEEE Transactions on Control Systems Technology*, vol. 19, no. 2, pp. 398 – 406, 2011.

Berthier, E. and Beebe, D. J., "Flow rate analysis of a surface tension driven passive micropump," *Lab on a Chip*, vol. 7, no. 11, pp. 1475 – 1478, 2007.

Berthier, J. and Silberzan, P., *Microfluidics for Biotechnology*, 1st ed. Artech House, Inc., 2006.

Bhatia, S. N. and Ingber, D. E., "Microfluidic organs-on-chips," *Nature Biotechnology*, vol. 32, no. 8, pp. 760 – 772, 2014.

Biffi, E., Regalia, G., Ghezzi, D., De Ceglia, R., Menegon, A., Ferrigno, G., Fiore, G. B., and Pedrocchi, A., "A novel environmental chamber for neuronal network multisite recordings," *Biotechnology and Bioengineering*, vol. 109, no. 10, pp. 2553 – 2566, 2012.

Blau, A., Neumann, T., Ziegler, C., and Benfenati, F., "Replica-moulded polydimethylsiloxane culture vessel lids attenuate osmotic drift in long-term cell cultures," *Journal of Biosciences*, vol. 34, no. 1, pp. 59 – 69, 2009.

Boy, D. A., Gibou, F., and Pennathur, S., "Simulation tools for lab on a chip research: advantages, challenges, and thoughts for the future," *Lab on a Chip*, vol. 8, no. 9, pp. 1424 – 1431, 2008.

Bridle, H., Millingen, M., and Jesorka, A., "On-chip fabrication to add temperature control to a microfluidic solution exchange system," *Lab on a Chip*, vol. 8, no. 3, pp. 480 – 483, 2008.

Bruus, H., *Theoretical Microfluidics*, 1st ed. Oxford University Press, 2008.

Buhler, H., Adamietz, R., Abeln, T., Diaz-Carballo, D., Nguemgo-Kouam, P., Hero, T., and Adamietz, I. A., "Automated multichamber time-lapse videography for long-term in vivo observation of migrating cells," *In Vivo*, vol. 31, no. 3, pp. 329 – 334, 2017.

Caballero, D., Blackburn, S. M., de Pablo, M., Samitier, J., and Albertazzi, L., "Tumour-vessel-on-a-chip models for drug delivery," *Lab on a Chip*, vol. 17, no. 22, pp. 3760 – 3771, 2017.

Caicedo, H. H., Hernandez, M., Fall, C. P., and Eddington, D. T., "Multiphysics simulation of a microfluidic perfusion chamber for brain slice physiology," *Biomedical Microdevices*, vol. 12, no. 5, pp. 761 – 767, 2010.

Chang, C.-W., Cheng, Y.-J., Tu, M., Chen, Y.-H., Peng, C.-C., Liao, W.-H., and Tung, Y.-C., "A polydimethylsiloxane-polycarbonate hybrid microfluidic device capable of generating perpendicular chemical and oxygen gradients for cell culture studies," *Lab on a Chip*, vol. 14, no. 19, pp. 3762 – 3772, 2014.

Charati, S. and Stern, S., "Diffusion of gases in silicone polymers: molecular dynamics simulations," *Macromolecules*, vol. 31, no. 16, pp. 5529 – 5535, 1998.

Chen, S.-Y. C., Hung, P. J., and Lee, P. J., "Microfluidic array for three-dimensional perfusion culture of human mammary epithelial cells." *Biomedical Microdevices*, vol. 13, no. 4, pp. 753 – 758, 2011a.

Chen, Y.-A., King, A. D., Shih, H.-C., Peng, C.-C., Wu, C.-Y., Liao, W.-H., and Tung, Y.-C., "Generation of oxygen gradients in microfluidic devices for cell culture using spatially confined chemical reactions," *Lab on a Chip*, vol. 11, no. 21, pp. 3626 – 3633, 2011b.

Cheng, J.-Y., Yen, M.-H., Kuo, C.-T., and Young, T.-H., "A transparent cell-culture microchamber with a variably controlled concentration gradient generator and flow field rectifier," *Biomicrofluidics*, vol. 2, no. 2, p. 024105, 2008.

Cheng, L.-J. and Chang, H.-C., "Microscale pH regulation by splitting water," *Biomicrofluidics*, vol. 5, no. 4, p. 046502, 2011.

Chong, S. L., Mou, D. G., Ali, A. M., Lim, S. H., and Tey, B. T., "Cell growth, cell-cycle progress, and antibody production in hybridoma cells cultivated under mild hypothermic conditions," *Hybridoma*, vol. 27, no. 2, pp. 107 – 111, 2008.

Christen, J. B. and Andreou, A. G., "Design, fabrication, and testing of a hybrid CMOS/PDMS microsystem for cell culture and incubation," *IEEE Transactions on Biomedical Circuits and Systems*, vol. 1, no. 1, pp. 3 – 18, 2007.

Coppeta, J. R., Mescher, M. J., Isenberg, B. C., Spencer, A. J., Kim, E. S., Lever, A. R., Mulhern, T. J., Prantil-Baun, R., Comolli, J. C., and Borenstein, J. T., "A portable and reconfigurable multi-organ platform for drug development with onboard microfluidic flow control," *Lab on a Chip*, vol. 17, no. 1, pp. 134 – 144, 2017.

Dambach, D. M., Andrews, B. A., and Moulin, F., "New technologies and screening strategies for hepatotoxicity: use of in vitro models," *Toxicologic Pathology*, vol. 33, no. 1, pp. 17–26, 2005.

Davis, J. M., *Basic Cell Culture: A Practical Approach*, 1st ed., Davis, J. M., Ed. Oxford University Press, 1994.

DiMasi, J. A., Hansen, R. W., and Grabowski, H. G., "The price of innovation: new estimates of drug development costs," *Journal of Health Economics*, vol. 22, no. 2, pp. 151–185, 2003.

Dimov, I. K., Kijanka, G., Park, Y., Ducrée, J., Kang, T., and Lee, L. P., "Integrated microfluidic array plate (iMAP) for cellular and molecular analysis," *Lab on a Chip*, vol. 11, no. 16, pp. 2701–2710, 2011.

Discher, D. E., Mooney, D. J., and Zandstra, P. W., "Growth Factors, Matrices, and Forces Combine and Control Stem Cells," *Science*, vol. 324, no. 5935, pp. 1673–1677, 2009.

Dorf, R. C. and Bishop, R. H., *Modern Control Systems*, 10th ed. Prentice Hall, 2005.

Duffy, D. C., McDonald, J. C., Schueller, O. J., and Whitesides, G. M., "Rapid Prototyping of Microfluidic Systems in Poly(dimethylsiloxane)," *Analytical Chemistry*, vol. 70, no. 23, pp. 4974–4984, 1998.

Eddington, D. T., Liu, R. H., Moore, J. S., and Beebe, D. J., "An organic self-regulating microfluidic system," *Lab on a Chip*, vol. 1, no. 2, pp. 96–99, 2001.

Fang, C., Lee, D., Stober, B., Fuller, G. G., and Shen, A. Q., "Integrated microfluidic platform for instantaneous flow and localized temperature control," *RSC Advances*, vol. 5, no. 104, pp. 85 620–85 629, 2015.

Fang, C., Ji, F., Shu, Z., and Gao, D., "Determination of the temperature-dependent cell membrane permeabilities using microfluidics with integrated flow and temperature control," *Lab on a Chip*, vol. 17, no. 5, pp. 951–960, 2017.

Fernández, M. J., López, A., and Santa-Maria, A., "Apoptosis induced by different doses of caffeine on Chinese hamster ovary cells," *Journal of Applied Toxicology*, vol. 23, no. 4, pp. 221–224, 2003.

Figallo, E., Cannizzaro, C., Gerecht, S., Burdick, J. A., Langer, R., Elvassore, N., and Vunjak-Novakovic, G., "Micro-bioreactor array for controlling cellular microenvironments," *Lab on a Chip*, vol. 7, no. 6, pp. 710–719, 2007.

Forry, S. P. and Locascio, L. E., "On-chip CO_2 control for microfluidic cell culture," *Lab on a Chip*, vol. 11, no. 23, pp. 4041–4046, 2011.

Fuerstman, M. J., Lai, A., Thurlow, M. E., Shevkoplyas, S. S., Stone, H. A., and Whitesides, G. M., "The pressure drop along rectangular microchannels containing bubbles," *Lab on a Chip*, vol. 7, no. 11, pp. 1479–1489, 2007.

Funamoto, K., Zervantonakis, I. K., Liu, Y., Ochs, C. J., Kim, C., and Kamm, R. D., "A novel microfluidic platform for high-resolution imaging of a three-dimensional cell culture under a controlled hypoxic environment," *Lab on a Chip*, vol. 12, no. 22, pp. 4855–4863, 2012.

Funke, M., Buchenauer, A., Schnakenberg, U., Mokwa, W., Diederichs, S., Mertens, A., Müller, C., Kensy, F., and Büchs, J., "Microfluidic BioLector—microfluidic bioprocess control in microtiter plates," *Biotechnology and Bioengineering*, vol. 107, no. 3, pp. 497 – 505, 2010.

Futai, N., Gu, W., Song, J. W., and Takayama, S., "Handheld recirculation system and customized media for microfluidic cell culture." *Lab on a Chip*, vol. 6, no. 1, pp. 149 – 154, 2006.

Galvis, E., Yarusevych, S., and Culham, J. R., "Incompressible laminar developing flow in microchannels," *Journal of Fluids Engineering*, vol. 134, no. 1, p. 014503, 2012.

Gao, Y., Sun, J., Lin, W.-H., Webb, D. J., and Li, D., "A compact microfluidic gradient generator using passive pumping," *Microfluidics and Nanofluidics*, vol. 12, no. 6, pp. 887 – 895, 2012.

Glawdel, T., Almutairi, Z., Wang, S., and Ren, C., "Photobleaching absorbed Rhodamine B to improve temperature measurements in PDMS microchannels," *Lab on a Chip*, vol. 9, no. 1, pp. 171 – 174, 2009.

Gruber, P., Marques, M. P. C., Szita, N., and Mayr, T., "Integration and application of optical chemical sensors in microbioreactors," *Lab on a Chip*, vol. 17, no. 16, pp. 2693 – 2712, 2017.

Habibey, R., Golabchi, A., Latifi, S., Difato, F., and Blau, A., "A microchannel device tailored to laser axotomy and long-term microelectrode array electrophysiology of functional regeneration," *Lab on a Chip*, vol. 15, no. 24, pp. 4578 – 4590, 2015.

Harrison, M. A. and Rae, I. F., *General Techniques of Cell Culture*, 1st ed. Cambridge University Press, 1997.

Hellé, G., Roberston, S., Cavadias, S., Mariet, C., and Cote, G., "Toward numerical prototyping of labs-on-chip: modeling for liquid – liquid microfluidic devices for radionuclide extraction," *Microfluidics and Nanofluidics*, vol. 19, no. 5, pp. 1245 – 1257, 2015.

Hochfeld, W. L., *Producing Biomolecular Substances with Fermenters, Bioreactors, and Biomolecular Synthesizers*, 1st ed. CRC Press, 2006.

Höppe, P. and Martinac, I., "Indoor climate and air quality. Review of current and future topics in the field of ISB study group 10," *International Journal of Biometeorology*, vol. 42, no. 1, pp. 1 – 7, 1998.

Hsieh, C.-C., Huang, S.-B., Wu, P.-C., Shieh, D.-B., and Lee, G.-B., "A microfluidic cell culture platform for real-time cellular imaging," *Biomedical Microdevices*, vol. 11, no. 4, pp. 903 – 913, 2009.

Hu, W.-S., *Cell Culture Bioprocess Engineering*, 1st ed. Wei-Shou Hu, 2012.

Huang, S.-B., Wu, M.-H., Wang, S.-S., and Lee, G.-B., "Microfluidic cell culture chip with multiplexed medium delivery and efficient cell/scaffold loading mechanisms for high-throughput perfusion 3-dimensional cell culture-based assays." *Biomedical Microdevices*, vol. 13, no. 3, pp. 415 – 430, 2011.

Huang, S.-B., Wang, S.-S., Hsieh, C.-H., Lin, Y. C., Lai, C.-S., and Wu, M.-H., "An integrated microfluidic cell culture system for high-throughput perfusion three-dimensional cell culture-based assays: effect of cell culture model on the results of chemosensitivity assays," *Lab on a Chip*, vol. 13, no. 6, pp. 1133 – 1143, 2013.

Hussin, M., Ismail, M. R., and Ahmad, M. S., "Air-conditioned university laboratories: Comparing CO_2 measurement for centralized and split-unit systems," *Journal of King Saud University - Engineering Sciences*, vol. 29, no. 2, pp. 191 – 201, 2017.

Inamdar, N. K., Griffith, L. G., and Borenstein, J. T., "Transport and shear in a microfluidic membrane bilayer device for cell culture," *Biomicrofluidics*, vol. 5, no. 2, p. 022213, 2011.

Jang, J. M., Lee, J., Kim, H., Jeon, N. L., and Jung, W., "One-photon and two-photon stimulation of neurons in a microfluidic culture system," *Lab on a Chip*, vol. 16, no. 9, pp. 1684 – 1690, 2016.

Jani, J. M., Can Aran, H., Wessling, M., and Lammertink, R. G., "Modeling of gas – liquid reactions in porous membrane microreactors," *Journal of Membrane Science*, vol. 419-420, pp. 57 – 64, 2012.

Jiang, B., Zheng, W., Zhang, W., and Jiang, X., "Organs on microfluidic chips: A mini review," *Science China Chemistry*, vol. 57, no. 3, pp. 356 – 364, 2014.

Jiang, J., Kaigala, G. V., Marquez, H. J., and Backhouse, C. J., "Nonlinear controller designs for thermal management in PCR amplification," *IEEE Transactions on Control Systems Technology*, vol. 20, no. 1, pp. 11 – 30, 2012.

Kaigala, G. V., Jiang, J., Backhouse, C. J., and Marquez, H. J., "System design and modeling of a time-varying, nonlinear temperature controller for microfluidics," *IEEE Transactions on Control Systems Technology*, vol. 18, no. 2, pp. 521 – 530, 2010.

Kang, S.-W. and Banerjee, D., "Modeling and Simulation of Capillary Microfluidic Networks Based on Electrical Analogies," *Journal of Fluids Engineering*, vol. 133, no. 5, p. 054502, 2011.

Karimi, M., Bahrami, S., Mirshekari, H., Basri, S. M. M., Nik, A. B., Aref, A. R., Akbari, M., and Hamblin, M. R., "Microfluidic systems for stem cell-based neural tissue engineering," *Lab on a Chip*, vol. 16, no. 14, pp. 2551 – 2571, 2016.

Kim, L., Toh, Y.-C., Voldman, J., and Yu, H., "A practical guide to microfluidic perfusion culture of adherent mammalian cells," *Lab on a Chip*, vol. 7, no. 6, pp. 681 – 694, 2007.

Kim, T. H., Kim, D.-K., and Kim, S. J., "Study of the sensitivity of a thermal flow sensor," *International Journal of Heat and Mass Transfer*, vol. 52, no. 7-8, pp. 2140 – 2144, 2009.

Kim, T. and Cho, Y.-H., "A pumpless cell culture chip with the constant medium perfusion-rate maintained by balanced droplet dispensing," *Lab on a Chip*, vol. 11, no. 10, pp. 1825 – 1830, 2011.

Kim, T., Doh, I., and Cho, Y.-H., "On-chip three-dimensional tumor spheroid formation and pump-less perfusion culture using gravity-driven cell aggregation and balanced droplet dispensing," *Biomicrofluidics*, vol. 6, no. 3, p. 034107, 2012.

Kreutzer, J., Ylä-Outinen, L., Kärnä, P., Kaarela, T., Mikkonen, J., Skottman, H., Narkilahti, S., and Kallio, P., "Structured PDMS Chambers for Enhanced Human Neuronal Cell Activity on MEA Platforms," *Journal of Bionic Engineering*, vol. 9, no. 1, pp. 1 – 10, 2012.

Kreutzer, J., Ylä-Outinen, L., Mäki, A.-J., Ristola, M., Narkilahti, S., and Kallio, P., "Cell Culture Chamber with Gas Supply for Prolonged Recording of Human Neuronal Cells on Microelectrode Array," *Journal of Neuroscience Methods*, vol. 280, pp. 27 – 35, 2017.

Kumar, S., Cartas-Ayala, M. A., and Thorsen, T., "Thermal modeling and design analysis of a continuous flow microfluidic chip," *International Journal of Thermal Sciences*, vol. 67, pp. 72 – 86, 2013.

Lahti, A. L., Kujala, V. J., Chapman, H., Koivisto, A.-P., Pekkanen-Mattila, M., Kerkelä, E., Hyttinen, J., Kontula, K., Swan, H., Conklin, B. R., Yamanaka, S., Silvennoinen, O., and Aalto-Setälä, K., "Model for long QT syndrome type 2 using human iPS cells demonstrates arrhythmogenic characteristics in cell culture," *Disease Models & Mechanisms*, vol. 5, no. 2, pp. 220 – 230, 2012.

Lam, E. W., Cooksey, G. A., Finlayson, B. A., and Folch, A., "Microfluidic circuits with tunable flow resistances," *Applied Physics Letters*, vol. 89, no. 16, p. 164105, 2006.

Läritz, C. and Pagel, L., "Microfluidic pH-regulation system based on printed circuit board technology," *Sensors and Actuators A: Physical*, vol. 84, no. 3, pp. 230 – 235, 2000.

Laurila, E., Ahola, A., Hyttinen, J., and Aalto-Setälä, K., "Methods for in vitro functional analysis of iPSC derived cardiomyocytes - Special focus on analyzing the mechanical beating behavior," *Biochimica et Biophysica Acta*, vol. 1863, no. 7, pp. 1864 – 1872, 2016.

Lee, H. L. T., Boccazzi, P., Ram, R. J., and Sinskey, A. J., "Microbioreactor arrays with integrated mixers and fluid injectors for high-throughput experimentation with pH and dissolved oxygen control," *Lab on a Chip*, vol. 6, no. 9, pp. 1229 – 1235, 2006.

Li, F., Vijayasankaran, N., Shen, A., Kiss, R., and Amanullah, A., "Cell culture processes for monoclonal antibody production," *mAbs*, vol. 2, no. 5, pp. 466 – 477, 2010.

Lin, J.-L., Wu, M.-H., Kuo, C.-Y., Lee, K.-D., and Shen, Y.-L., "Application of indium tin oxide (ITO)-based microheater chip with uniform thermal distribution for perfusion cell culture outside a cell incubator," *Biomedical Microdevices*, vol. 12, no. 3, pp. 389 – 398, 2010.

Lin, J.-L., Wang, S.-S., Wu, M.-H., and Oh-Yang, C.-C., "Development of an integrated microfluidic perfusion cell culture system for real-time microscopic observation of biological cells," *Sensors*, vol. 11, no. 9, pp. 8395 – 8411, 2011.

Liu, N., Aymonier, C., Lecoutre, C., Garrabos, Y., and Marre, S., "Microfluidic approach for studying CO_2 solubility in water and brine using confocal Raman spectroscopy," *Chemical Physics Letters*, vol. 551, pp. 139 – 143, 2012.

Ljung, L., "Convergence analysis of parametric identification methods," *IEEE Transactions on Automatic Control*, vol. 23, no. 5, pp. 770 – 783, 1978.

Ljung, L., *System Identification Toolbox User's Guide*, 9th ed. The MathWorks, Inc., 2016.

Lo, J. F., Sinkala, E., and Eddington, D. T., "Oxygen gradients for open well cellular cultures via microfluidic substrates," *Lab on a Chip*, vol. 10, no. 18, pp. 2394–2401, 2010.

Lynn, N. S. and Dandy, D. S., "Passive microfluidic pumping using coupled capillary/evaporation effects," *Lab on a Chip*, vol. 9, no. 23, pp. 3422–3429, 2009.

Macown, R. J., Veraitch, F. S., and Szita, N., "Robust, microfabricated culture devices with improved control over the soluble microenvironment for the culture of embryonic stem cells," *Biotechnology Journal*, vol. 9, no. 6, pp. 805–813, 2014.

Magnusson, E. B., Halldorsson, S., Fleming, R. M. T., and Leosson, K., "Real-time optical pH measurement in a standard microfluidic cell culture system," *Biomedical Optics Express*, vol. 4, no. 9, pp. 1749–1758, 2013.

Mäki, A.-J., Verho, J., Kreutzer, J., Ryynänen, T., Rajan, D., Pekkanen-Mattila, M., Ahola, A., Hyttinen, J., Aalto-Setälä, K., Lekkala, J., and Kallio, P., "A Portable Microscale Cell Culture System with Indirect Temperature Control," *SLAS TECHNOLOGY: Translating Life Sciences Innovation*, May 3, 2018, DOI: 10.1177/2472630318768710.

Mazzei, D., Vozzi, F., Cisternino, A., Vozzi, G., and Ahluwalia, A., "A high-throughput bioreactor system for simulating physiological environments," *IEEE Transactions on Industrial Electronics*, vol. 55, no. 9, pp. 3273–3280, 2008.

Meng, E., Li, P.-Y., and Tai, Y.-C., "A biocompatible Parylene thermal flow sensing array," *Sensors and Actuators A: Physical*, vol. 144, no. 1, pp. 18–28, 2008.

Merkel, T. C., Bondar, V. I., Nagai, K., Freeman, B. D., and Pinnau, I., "Gas sorption, diffusion, and permeation in poly(dimethylsiloxane)," *Journal of Polymer Science Part B: Polymer Physics*, vol. 38, no. 3, pp. 415–434, 2000.

Millero, F. J. and Pierrot, D., "A Chemical Equilibrium Model for Natural Waters," *Aquatic Geochemistry*, vol. 4, no. 1, pp. 153–199, 1998.

Nelson, T. J., Martinez-Fernandez, A., Yamada, S., Ikeda, Y., Perez-Terzic, C., and Terzic, A., "Induced pluripotent stem cells: advances to applications," *Stem Cells and Cloning: Advances and Applications*, vol. 3, pp. 29–37, 2010.

Ngo, I.-L., Jeon, S., and Byon, C., "Thermal conductivity of transparent and flexible polymers containing fillers: A literature review," *International Journal of Heat and Mass Transfer*, vol. 98, pp. 219–226, 2016.

Nielsen, H. A. and Madsen, H., "Modelling the heat consumption in district heating systems using a grey-box approach," *Energy and Buildings*, vol. 38, no. 1, pp. 63–71, 2006.

Nieto, D., McGlynn, P., de la Fuente, M., Lopez-Lopez, R., and O'connor, G. M., "Laser microfabrication of a microheater chip for cell culture outside a cell incubator," *Colloids and Surfaces B: Biointerfaces*, vol. 154, pp. 263–269, 2017.

Oh, K. W., Lee, K., Ahn, B., and Furlani, E. P., "Design of pressure-driven microfluidic networks using electric circuit analogy," *Lab on a Chip*, vol. 12, no. 3, pp. 515 – 545, 2012.

Oomen, P. E., Skolimowski, M. D., and Verpoorte, E., "Implementing oxygen control in chip-based cell and tissue culture systems," *Lab on a Chip*, vol. 16, no. 18, pp. 3394 – 3414, 2016.

Oppegard, S. C., Nam, K.-H., Carr, J. R., Skaalure, S. C., and Eddington, D. T., "Modulating Temporal and Spatial Oxygenation over Adherent Cellular Cultures," *PLOS ONE*, vol. 4, no. 9, p. e6891, 2009.

Palmer, K., Nguyen, H., and Thornell, G., "Finite element analysis of the effect on employing thermal through vias and heat fingers to increase heat transfer to fluid in calorimetric flow sensors," *Sensors and Actuators A: Physical*, vol. 201, pp. 49 – 57, 2013.

Pasirayi, G., Auger, V., Scott, S. M., Rahman, P. K. S. M., Islam, M., O'Hare, L., and Ali, Z., "Microfluidic Bioreactors for Cell Culturing: A Review," *Micro and Nanosystems*, vol. 3, no. 2, pp. 137 – 160, 2011.

Peng, C.-C., Liao, W.-H., Chen, Y.-H., Wu, C.-Y., and Tung, Y.-C., "A microfluidic cell culture array with various oxygen tensions," *Lab on a Chip*, vol. 13, no. 16, pp. 3239 – 3245, 2013.

Pennell, T., Suchyna, T., Wang, J., Heo, J., Felske, J. D., Sachs, F., and Hua, S. Z., "Microfluidic chip to produce temperature jumps for electrophysiology," *Analytical Chemistry*, vol. 80, no. 7, pp. 2447 – 2451, 2008.

Perestrelo, A. R., Águas, A. C., Rainer, A., and Forte, G., "Microfluidic organ/body-on-a-chip devices at the convergence of biology and microengineering," *Sensors*, vol. 15, no. 12, pp. 31 142 – 31 170, 2015.

Petronis, S., Stangegaard, M., Christensen, C. B. V., and Dufva, M., "Transparent polymeric cell culture chip with integrated temperature control and uniform media perfusion," *BioTechniques*, vol. 40, no. 3, pp. 368 – 376, 2006.

Picard, C. and Donald, A., "The impact of environmental changes upon the microrheological response of adherent cells," *The European Physical Journal E*, vol. 30, no. 2, pp. 127 – 134, 2009.

Picard, C., Hearnden, V., Massignani, M., Achouri, S., Battaglia, G., MacNeil, S., and Donald, A., "A micro-incubator for cell and tissue imaging," *BioTechniques*, vol. 48, no. 2, pp. 135 – 138, 2010.

Piccini, J. P., Whellan, D. J., Berridge, B. R., Finkle, J. K., Pettit, S. D., Stockbridge, N., Valentin, J.-P., Vargas, H. M., and Krucoff, M. W., "Current challenges in the evaluation of cardiac safety during drug development: translational medicine meets the Critical Path Initiative," *American Heart Journal*, vol. 158, no. 3, pp. 317 – 326, 2009.

Polinkovsky, M., Gutierrez, E., Levchenko, A., and Groisman, A., "Fine temporal control of the medium gas content and acidity and on-chip generation of series of oxygen concentrations for cell cultures," *Lab on a Chip*, vol. 9, no. 8, pp. 1073 – 1084, 2009.

Portillo-Lara, R. and Annabi, N., "Microengineered Cancer-on-a-chip Platforms to Study the Metastatic Microenvironment," *Lab on a Chip*, vol. 16, no. 21, pp. 4063 – 4081, 2016.

Que, R. and Zhu, R., "A two-dimensional flow sensor with integrated micro thermal sensing elements and a back propagation neural network." *Sensors*, vol. 14, no. 1, pp. 564 – 574, 2014.

Quinn, P. and Cooke, S., "Equivalency of culture media for human in vitro fertilization formulated to have the same pH under an atmosphere containing 5% or 6% carbon dioxide," *Fertility and Sterility*, vol. 81, no. 6, pp. 1502 – 1506, 2004.

Reddy, J. N., *An Introduction to The Finite Element Method*, 3rd ed. McGraw-Hill Education, 2006.

Regalia, G., Biffi, E., Achilli, S., Ferrigno, G., Menegon, A., and Pedrocchi, A., "Development of a bench-top device for parallel climate-controlled recordings of neuronal cultures activity with microelectrode arrays," *Biotechnology and Bioengineering*, vol. 113, no. 2, pp. 403 – 413, 2016.

Reig, R., Mattia, M., Compte, A., Belmonte, C., and Sanchez-Vives, M. V., "Temperature modulation of slow and fast cortical rhythms," *Journal of Neurophysiology*, vol. 103, no. 3, pp. 1253 – 1261, 2010.

Resto, P. J., Mogen, B. J., Berthier, E., and Williams, J. C., "An automated microdroplet passive pumping platform for high-speed and packeted microfluidic flow applications." *Lab on a Chip*, vol. 10, no. 1, pp. 23 – 26, 2010.

Rodrigues, C. A. V., Fernandes, T. G., Diogo, M. M., da Silva, C. L., and Cabral, J. M. S., "Stem cell cultivation in bioreactors," *Biotechnology Advances*, vol. 29, no. 6, pp. 815 – 829, 2011.

Ross, D., Gaitan, M., and Locascio, L. E., "Temperature Measurement in Microfluidic Systems Using a Temperature-Dependent Fluorescent Dye," *Analytical Chemistry*, vol. 73, no. 17, pp. 4117 – 4123, 2001.

Saalfrank, D., Konduri, A. K., Latifi, S., Habibey, R., Golabchi, A., Martiniuc, A. V., Knoll, A., Ingebrandt, S., and Blau, A., "Incubator-independent cell-culture perfusion platform for continuous long-term microelectrode array electrophysiology and time-lapse imaging," *Royal Society Open Science*, vol. 2, no. 6, p. 150031, 2015.

Samy, R., Glawdel, T., and Ren, C. L., "Method for Microfluidic Whole-Chip Temperature Measurement Using Thin-Film Poly (dimethylsiloxane)/Rhodamine B," *Analytical Chemistry*, vol. 80, no. 2, pp. 369 – 375, 2008.

Sander, R., "Compilation of Henry's law constants (version 4.0) for water as solvent," *Atmospheric Chemistry and Physics*, vol. 15, no. 8, pp. 4399 – 4981, 2015.

Sazhin, O., "Novel mass air flow meter for automobile industry based on thermal flow microsensor. I. Analytical model and microsensor," *Flow Measurement and Instrumentation*, vol. 30, pp. 60 – 65, 2013.

Scannell, J. W., Blanckley, A., Boldon, H., and Warrington, B., "Diagnosing the decline in pharmaceutical R&D efficiency," *Nature Reviews Drug Discovery*, vol. 11, no. 3, pp. 191 – 200, 2012.

Sebastian, A. and Wiesmann, D., "Modeling and experimental identification of silicon microheater dynamics: A systems approach," *Journal of Microelectromechanical Systems*, vol. 17, no. 4, pp. 911 – 920, 2008.

Seker, E., Sung, J. H., Shuler, M. L., and Yarmush, M. L., "Solving Medical Problems with BioMEMS," *IEEE Pulse*, vol. 2, no. 6, pp. 51 – 59, 2011.

Seppänen, O. A. and Fisk, W. J., "Summary of human responses to ventilation," *Indoor Air*, vol. 14, pp. 102 – 118, 2004.

Seppänen, O. A., Fisk, W. J., and Mendell, M. J., "Association of Ventilation Rates and CO_2 Concentrations with Health and Other Responses in Commercial and Institutional Buildings," *Indoor Air*, vol. 9, no. 4, pp. 226 – 252, 1999.

Shamloo, A., Pedram, M. Z., Heidari, H., and Alasty, A., "Computing the blood brain barrier (BBB) diffusion coefficient: A molecular dynamics approach," *Journal of Magnetism and Magnetic Materials*, vol. 410, pp. 187 – 197, 2016.

Shiku, H., Saito, T., Wu, C.-C., Yasukawa, T., Yokoo, M., Abe, H., Matsue, T., and Yamada, H., "Oxygen Permeability of Surface-modified Poly(dimethylsiloxane) Characterized by Scanning Electrochemical Microscopy," *Chemistry Letters*, vol. 35, no. 2, pp. 234 – 235, 2006.

Shuler, M. L., "Organ-, body- and disease-on-a-chip systems," *Lab on a Chip*, vol. 17, no. 14, pp. 2345 – 2346, 2017.

Sjöberg, J., Zhang, Q., Ljung, L., Benveniste, A., Delyon, B., Glorennec, P.-Y., Hjalmarsson, H., and Juditsky, A., "Nonlinear black-box modeling in system identification: a unified overview," *Automatica*, vol. 31, no. 12, pp. 1691 – 1724, 1995.

Skolimowski, M., Nielsen, M. W., Emnéus, J., Molin, S., Taboryski, R., Sternberg, C., Dufva, M., and Geschke, O., "Microfluidic dissolved oxygen gradient generator biochip as a useful tool in bacterial biofilm studies," *Lab on a Chip*, vol. 10, no. 16, pp. 2162 – 2169, 2010.

Sohlberg, B., "Grey box modelling for model predictive control of a heating process," *Journal of Process Control*, vol. 13, no. 3, pp. 225 – 238, 2003.

Solovitz, S. A. and Mainka, J., "Manifold Design for Micro-Channel Cooling With Uniform Flow Distribution," *Journal of Fluids Engineering*, vol. 133, no. 5, p. 051103, 2011.

Song, H., Wang, Y., and Pant, K., "System-level simulation of liquid filling in microfluidic chips," *Biomicrofluidics*, vol. 5, no. 2, p. 024107, 2011.

Stoian, A. V., Druon-Bocquet, S., Groux, H., and Sanchez, J., "Modeling and simulation of the mass transfer of volatile compounds in a membrane device for toxicity tests," *Chemical Engineering Science*, vol. 80, pp. 160 – 172, 2012.

Sun, K., Wang, Z., and Jiang, X., "Modular microfluidics for gradient generation," *Lab on a Chip*, vol. 8, no. 9, pp. 1536 – 1543, 2008.

Sun, Y.-S. and Cheng, J.-Y., "Cell Culture in Microfluidic Systems," *Micro and Nanosystems*, vol. 5, no. 2, pp. 82 – 96, 2013.

Sung, J. H., Kam, C., and Shuler, M. L., "A microfluidic device for a pharmacokinetic-pharmacodynamic (PK-PD) model on a chip," *Lab on a Chip*, vol. 10, no. 4, pp. 446 – 455, 2010.

Takano, A., Tanaka, M., and Futai, N., "On-chip CO_2 incubation for pocket-sized microfluidic cell culture," *Microfluidics and Nanofluidics*, vol. 12, no. 6, pp. 907 – 915, 2012.

Takano, A., Tanaka, M., and Futai, N., "On-chip multi-gas incubation for microfluidic cell cultures under hypoxia," *Biomicrofluidics*, vol. 8, no. 6, p. 061101, 2014.

Tehranirokh, M., Kouzani, A. Z., Francis, P. S., and Kanwar, J. R., "Microfluidic devices for cell cultivation and proliferation," *Biomicrofluidics*, vol. 7, no. 5, p. 051502, 2013.

Thomas, P. C., Raghavan, S. R., and Forry, S. P., "Regulating oxygen levels in a microfluidic device," *Analytical Chemistry*, vol. 83, no. 22, pp. 8821 – 8824, 2011.

Titmarsh, D., Hidalgo, A., Turner, J., Wolvetang, E., and Cooper-White, J., "Optimization of flowrate for expansion of human embryonic stem cells in perfusion microbioreactors." *Biotechnology and Bioengineering*, vol. 108, no. 12, pp. 2894 – 2904, 2011.

Toepke, M. W. and Beebe, D. J., "PDMS absorption of small molecules and consequences in microfluidic applications," *Lab on a Chip*, vol. 6, no. 12, pp. 1484 – 1486, 2006.

Tourlomousis, F. and Chang, R. C., "Numerical investigation of dynamic microorgan devices as drug screening platforms. Part I: Macroscale modeling approach & validation," *Biotechnology and Bioengineering*, vol. 113, no. 3, pp. 612 – 622, 2016.

Trevisan, M., Sinigaglia, A., Desole, G., Berto, A., Pacenti, M., Palù, G., and Barzon, L., "Modeling Viral Infectious Diseases and Development of Antiviral Therapies Using Human Induced Pluripotent Stem Cell-Derived Systems," *Viruses*, vol. 7, no. 7, pp. 3835 – 3856, 2015.

Tsao, C.-W., "Polymer microfluidics: Simple, low-cost fabrication process bridging academic lab research to commercialized production," *Micromachines*, vol. 7, no. 12:255, 2016.

van Schijndel, A. W. M., "Integrated Heat Air and Moisture Modeling and Simulation," Ph.D. Thesis, Technische Universiteit Eindhoven, 2007.

Velve-Casquillas, G., Le Berre, M., Piel, M., and Tran, P. T., "Microfluidic tools for cell biological research," *Nano Today*, vol. 5, no. 1, pp. 28 – 47, 2010.

Velve-Casquillas, G., Fu, C., Le Berre, M., Cramer, J., Meance, S., Plecis, A., Baigl, D., Greffet, J.-J., Chen, Y., Piel, M., and Tran, P. T., "Fast microfluidic temperature control for high resolution live cell imaging," *Lab on a Chip*, vol. 11, no. 3, pp. 484 – 489, 2011.

Vickerman, V., Blundo, J., Chung, S., and Kamm, R., "Design, fabrication and implementation of a novel multi-parameter control microfluidic platform for three-dimensional cell culture and real-time imaging," *Lab on a Chip*, vol. 8, no. 9, pp. 1468 – 1477, 2008.

Vollmer, A. P., Probstein, R. F., Gilbert, R., and Thorsen, T., "Development of an integrated microfluidic platform for dynamic oxygen sensing and delivery in a flowing medium." *Lab on a Chip*, vol. 5, no. 10, pp. 1059 – 1066, 2005.

Vozzi, G., Mazzei, D., Tirella, A., Vozzi, F., and Ahluwalia, A., "Finite element modelling and design of a concentration gradient generating bioreactor: Application to biological pattern formation and toxicology," *Toxicology in Vitro*, vol. 24, no. 6, pp. 1828 – 1837, 2010.

Vu, T. Q., de Castro, R. M. B., and Qin, L., "Bridging the gap: microfluidic devices for short and long distance cell-cell communication," *Lab on a Chip*, vol. 17, no. 6, pp. 1009 – 1023, 2017.

Vukasinovic, J., Cullen, D. K., LaPlaca, M. C., and Glezer, A., "A microperfused incubator for tissue mimetic 3D cultures," *Biomedical Microdevices*, vol. 11, no. 6, pp. 1155 – 1165, 2009.

Wang, K. I.-K., Salcic, Z., Yeh, J., Akagi, J., Zhu, F., Hall, C. J., Crosier, K. E., Crosier, P. S., and Wlodkowic, D., "Toward embedded laboratory automation for smart Lab-on-a-Chip embryo arrays," *Biosensors and Bioelectronics*, vol. 48, pp. 188 – 196, 2013b.

Wang, L., Liu, W., Wang, Y., Wang, J.-c., Tu, Q., Liu, R., and Wang, J., "Construction of oxygen and chemical concentration gradients in a single microfluidic device for studying tumor cell-drug interactions in a dynamic hypoxia microenvironment," *Lab on a Chip*, vol. 13, no. 4, pp. 695 – 705, 2013a.

Węgrzyn, I., Ainla, A., Jeffries, G. D. M., and Jesorka, A., "An Optofluidic Temperature Probe," *Sensors*, vol. 13, no. 4, pp. 4289 – 4302, 2013.

Weigl, B. H., Bardell, R. L., and Cabrera, C. R., "Lab-on-a-chip for drug development," *Advanced Drug Delivery Reviews*, vol. 55, no. 3, pp. 349 – 377, 2003.

Welch, D. and Christen, J. B., "Real-time feedback control of pH within microfluidics using integrated sensing and actuation." *Lab on a Chip*, vol. 14, no. 6, pp. 1191 – 1197, 2014.

Whitesides, G. M., "The origins and the future of microfluidics," *Nature*, vol. 442, no. 7101, pp. 368 – 373, 2006.

Will, M. A., Clark, N. A., and Swain, J. E., "Biological pH buffers in IVF: help or hindrance to success," *Journal of Assisted Reproduction and Genetics*, vol. 28, no. 8, pp. 711 – 724, 2011.

Witte, H., Stubenrauch, M., Fröber, U., Fischer, R., Voges, D., and Hoffmann, M., "Integration of 3-D cell cultures in fluidic microsystems for biological screenings," *Engineering in Life Sciences*, vol. 11, no. 2, pp. 140 – 147, 2011.

Wong, D. and Ren, C. L., "Microfluidic droplet trapping, splitting and merging with feedback controls and state space modelling," *Lab on a Chip*, vol. 16, no. 17, pp. 3317 – 3329, 2016.

Worden, K., Wong, C. X., Parlitz, U., Hornstein, A., Engster, D., Tjahjowidodo, T., Al-Bender, F., Rizos, D. D., and Fassois, S. D., "Identification of pre-sliding and sliding friction dynamics: Grey box and black-box models," *Mechanical Systems and Signal Processing*, vol. 21, no. 1, pp. 514 – 534, 2007.

Yamamoto, T., Nojima, T., and Fujii, T., "PDMS – glass hybrid microreactor array with embedded temperature control device. Application to cell-free protein synthesis," *Lab on a Chip*, vol. 2, no. 4, pp. 197 – 202, 2002.

Yi, C., Li, C.-W., Ji, S., and Yang, M., "Microfluidics technology for manipulation and analysis of biological cells," *Analytica Chimica Acta*, vol. 560, no. 1-2, pp. 1 – 23, 2006.

Yoshimitsu, R., Hattori, K., Sugiura, S., Kondo, Y., Yamada, R., Tachikawa, S., Satoh, T., Kurisaki, A., Ohnuma, K., Asashima, M., and Kanamori, T., "Microfluidic perfusion culture of human induced pluripotent stem cells under fully defined culture conditions," *Biotechnology and Bioengineering*, vol. 111, no. 5, pp. 937 – 947, 2014.

Young, E. W. K. and Beebe, D. J., "Fundamentals of microfluidic cell culture in controlled microenvironments," *Chemical Society Reviews*, vol. 39, no. 3, pp. 1036 – 1048, 2010.

Yu, I.-F. F., Yu, Y.-H. H., Chen, L.-Y. Y., Fan, S.-K. K., Chou, H.-Y. Y. E., and Yang, J.-T. T., "A portable microfluidic device for rapid diagnosis of cancer metastatic potential with programmable modules of temperature and CO_2," *Lab on a Chip*, vol. 14, no. 18, pp. 3621 – 3628, 2014.

Yum, K., Hong, S. G., and Lee, L. P., "Physiologically relevant organs on chips," *Biotechnology Journal*, vol. 9, no. 1, pp. 16 – 27, 2014.

Zahorodny-Burke, M., Nearingburg, B., and Elias, A. L., "Finite element analysis of oxygen transport in microfluidic cell culture devices with varying channel architectures, perfusion rates, and materials," *Chemical Engineering Science*, vol. 66, no. 23, pp. 6244 – 6253, 2011.

Zhu, X., Chu, L. Y., Chueh, B.-h., Shen, M., Hazarika, B., Phadke, N., and Takayama, S., "Arrays of horizontally-oriented mini-reservoirs generate steady microfluidic flows for continuous perfusion cell culture and gradient generation," *The Analyst*, vol. 129, no. 11, pp. 1026 – 1031, 2004.

Publications

Publication I

Mäki, A.-J., Hemmilä, S., Hirvonen, J., Girish, N.N., Kreutzer, J., Hyttinen, J., and Kallio, P., "Modeling and Experimental Characterization of Pressure Drop in Gravity-Driven Microfluidic Systems," *Journal of Fluids Engineering*, vol. 137, no. 2, art. no. 021105, 2015.

Publication II

Mäki, A.-J., Kreutzer, J., and Kallio, P., "Modeling Drug Delivery in Gravity-Driven Microfluidic System," in *Proceedings of the ASME 2014 12th International Conference on Nanochannels, Microchannels, and Minichannels (ICNMM2014)*, paper no. ICNMM2014-21183, p. V001T02A003, Aug. 2014.

Publication III

Mäki, A.-J., Kontunen, A., Ryynänen, T., Verho, J., Kreutzer, J., Lekkala, J., and Kallio, P., "Design and Simulation of a Thermal Flow Sensor for Gravity-Driven Microfluidic Applications", in *Proceedings of the 11th IEEE Annual International Conference on Nano/Micro Engineered and Molecular Systems (NEMS)*, pp. 125 – 129, Apr. 2016.

Design and Simulation of a Thermal Flow Sensor for Gravity-Driven Microfluidic Applications

Antti-Juhana Mäki[†*], Anton Kontunen[†], Tomi Ryynänen[†], Jarmo Verho[†],
Joose Kreutzer[†], Jukka Lekkala[†], and Pasi Kallio[†]
[†]Department of Automation Science and Engineering, BioMediTech
Tampere University of Technology, Korkeakoulunkatu 3, 33720 Tampere, Finland
[*]Email: antti-juhana.maki@tut.fi

***Abstract*—Gravity-driven flow is an attractive approach to develop simpler microfluidic systems. Because clogged microchannels could easily lead to fatal operational failures, it is crucial to monitor flow rate in these systems. Therefore, we propose here for the first time a numerical model that combines a calorimetric flow sensor and a gravity-driven system. With the validated model, we studied the flow behavior in a gravity-driven system. Furthermore, we were able to improve the sensitivity of the measurement based on simulation results. This demonstrates, how the model could be used as an effective optimization tool in the gravity-driven system including calorimetric flow measurement.**

***Index Terms*—calorimetric flow sensor, gravity-driven flow, modeling, numerical simulation**

I. Introduction

A calorimetric flow sensor is a non-invasive method to measure flow rate and flow direction. It can easily be miniaturized for microfluidic devices using micromachining processes. Without any moving parts, these sensors provide fast response with low power consumption. [1]–[3] Typically, working principle of the sensor relies on temperature changes near a heating element because of fluid flow. Therefore, the flow rate in the system is determined by measuring temperature difference between two temperature sensors located symmetrically upstream and downstream from the heating element. [4] While several previous studies have modeled this principle, they have not considered microfluidic systems using gravity-driven flow. [1], [4]–[6]

In gravity-driven microfluidic systems, flow is usually generated using hydrostatic and capillary pressures [7], without using an external pump. However, especially in biological applications microchannels can get clogged during the operation, and therefore, it would be desirable to continuously monitor liquid flow to ensure that the system is working as expected. Thus, integrating a calorimetric flow sensor to a gravity-driven pump is an attractive approach to develop cost-effective and mobile microfluidic systems including on-line flow rate measurement. Because, to the best of our knowledge, this combination has not been presented previously, we propose a modeling approach that can be used to study and design gravity-driven systems including flow rate measurements. We also demonstrate, how the sensitivity of the measurement was improved using the developed model.

II. Working Principle

A typical calorimetric flow measurement system, placed in a fluidic channel, includes two temperature sensors and a heating element located symmetrically between the sensors. Heat generated in a heater is transported via convective heat transfer to liquid, and temperature T is monitored with both sensors. When fluid flows over the heater, forced convection transfers generated heat downstream. Thus, a temperature difference between downstream (T_{down}), and upstream (T_{up}) is generated ($\Delta T = T_{down} - T_{up}$). For this reason, a relationship between temperature difference and liquid flow can be used to measure liquid mass flow rate Q in a known channel. [5], [6] An important parameter of the measurement is the sensitivity S of the calorimetric sensor, as higher sensitivity provides lower measurable flow rates. Sensitivity can be determined using [4]:

$$S = \frac{\Delta T}{\Delta Q} \tag{1}$$

Sensors used in this study have positive temperature coefficients of resistance, and it is assumed that they have a constant temperature coefficient α in the measurement range used in this study. Therefore, a linear approximation is used to determine their temperature-dependent resistances $R(T)$:

$$R(T) = R(T_0)(1 + \alpha(T - T0)) \tag{2}$$

where $R(T_0)$ is the sensor reference resistance at a reference temperature T_0 (25°C in this study).

Gravity-driven microfluidic systems include usually two reservoirs that are connected through a microchannel. In these systems, flow between inlet and outlet reservoirs is generated using hydrostatic and capillary pressures, $p_{hyd}(t)$ and p_{cap}, respectively, and therefore, there is no need for an external pump [7]. To define hydrostatic pressure, the following equation is used:

$$p_{hyd}(t) = \rho g \Delta h(t) \tag{3}$$

where ρ, g, and $\Delta h(t)$ are liquid density, gravitational acceleration, and height difference between inlet and outlet reservoirs, respectively.

Capillary pressure drops are located between gas and liquid interfaces in advancing and receding fronts. These forces can be calculated when advancing (θ_a) and receding (θ_r) contact angles, and radii of inlet and outlet reservoirs, r_{in} and r_{out},

respectively, are known. Assuming constant contact angles, pressure is defined as [8]:

$$p_{cap} = 2\sigma_{lg}\left(\frac{\cos(\theta_a)}{r_{out}} - \frac{\cos(\theta_r)}{r_{in}}\right) \quad (4)$$

where σ_{lg} is surface tension between liquid and gas. In this study, we use a typical water-air value of 0.072 Nm^{-1} for the surface tension.

When pressures in the system are known, the time-dependent flow rate $Q(t)$ in the system can be estimated using the total working pressure $\Delta p(t)$, and hydraulic resistance of the system, R_{hyd}:

$$Q(t) = \frac{\Delta p(t)}{R_{hyd}} = \frac{p_{hyd}(t) + p_{cap}}{R_{hyd}} \quad (5)$$

In a typical gravity-driven system considered in this study, the majority of R_{hyd} is caused by the microchannel in the system. Therefore, the hydraulic resistance of the microchannel is used as an approximation for R_{hyd}. For a rectangular microchannel with a height h, a length l, and a width w, and $l > w > h$, hydraulic resistance can be calculated [8], [9]:

$$R_{hyd} = \frac{12\eta l}{h^3 w}\left(1 - \frac{192h}{w\pi^5}\tanh\frac{\pi w}{2h}\right)^{-1} \quad (6)$$

In this paper, (3)–(6) were used in the analytical model to approximate pressure $\Delta p(t)$ that was set to the inlet boundary of the numerical model.

III. Materials and Methods

A. Measurement Set-up

A 25 mm × 25 mm × 0.9 mm sensor plate (SP), shown in Fig. 1, included two identical temperature sensors and a heating element. The structure built on a glass substrate consisted of a 275 nm thick titanium layer coated with a 50 nm platinum layer and a 500 nm silicon nitride insulation layer. Resistors line width was 20 μm, and line lengths l_h and l_s were 4.78 mm and 2.22 mm for the heater and the sensors, respectively. Heater and sensors heights, h_h and h_s, were 780 μm and 540 μm, respectively, and the center-to-center distance between the sensor and the heater, d_{cc}, was 300 μm. Furthermore, widths of the heater and the sensors, w_h and h_s, were 220 μm and 140 μm, respectively.

The measurement system to validate the developed finite element method (FEM) model included SP, electronics for 4-wire measurement method, a polydimethylsiloxane (PDMS) microchannel, and a syringe pump as shown in Fig. 2(a). Measured microchannel dimensions ($l \times w \times h$) were 16 mm × 1020 μm × 140 μm. Only a part of the system was modeled as shown in Fig. 2(b). Constant currents (0.2 mA and ∼5.9 mA) were used for powering the temperature sensors and to warm the heater, respectively. De-ionized water was moved using the syringe pump instead of a gravity-driven method using three different flow rates as will be explained in Section IV-A.

Before experiments, temperature sensors were calibrated in a temperature-controlled oven at nine different temperature between 24.6°C and 40°C. At 25°C, measured resistances of the

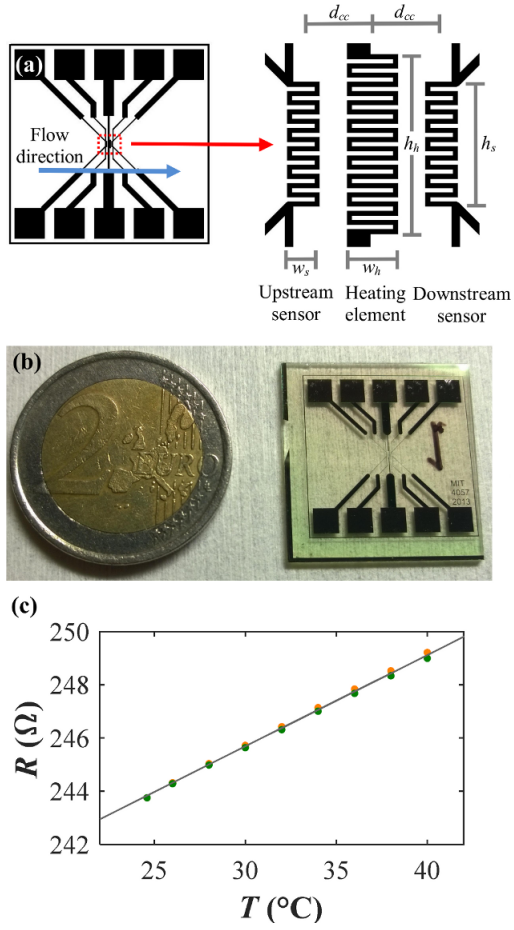

Fig. 1. Calorimetric flow sensor: (a) designed, and (b) fabricated sensor plate used in the experiments, and (c) sensor calibration curve. The line is plotted with equation: $R = 0.343 \times T + 235.38$.

sensors were approximately 244 Ω. Therefore, we estimated that resistivity of the fabricated layer (a combination of 275 nm thick titanium layer coated with 50 nm platinum layer) was approximately $6.8{\cdot}10^{-7}\Omega{\cdot}$m. This is approximately 1.6 times larger compared to typically reported titanium bulk resistivity, $4.2{\cdot}10^{-7}\Omega{\cdot}$m [10]. In addition, temperature coefficient of resistance, α, was determined from the calibration results presented in Fig. 1(c). Using (2), the coefficient was calculated to be approximately $1.4{\cdot}10^{-3}$ K^{-1} for both sensors, which is almost three times smaller than the reported earlier value of $3.8{\cdot}10^{-3}$ K^{-1} for bulk titanium [10]. These differences in electrical properties were expected as the resistivity of a thin film is always larger than that of the bulk material. [11] In addition, as the sensors showed highly linear relationships with temperatures in the measurement range, a linear temperature

conversion was used to convert measurement readings to temperature as shown in Fig. 1(c).

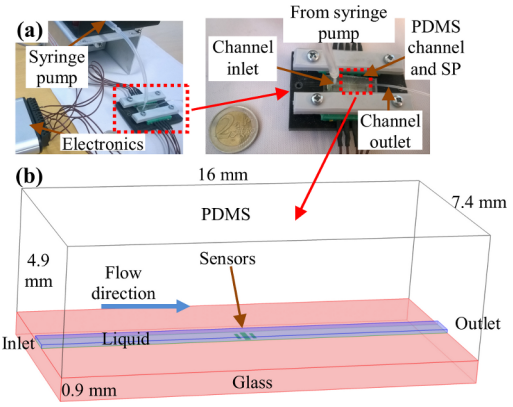

Fig. 2. Model validation measurement: (a) used measurement set-up, and (b) geometry used in the model.

B. Modeling Approach

Time-scale in gravity-driven microfluidics is typically up to hours. However, FEM simulations of two-phase flows are really time-consuming, and simulation studies are usually limited to seconds. Therefore, we propose a model composed of two parts; a previously presented analytical method [8] to calculate an average inlet pressure in a gravity-driven system using (5), and a one-phase flow FEM model to simulate temperature difference between upstream and downstream sensors. We have previously used a similar approach to model drug delivery in a gravity-driven microfluidic system [12].

Three-dimensional time-dependent fluid velocity and temperature distribution were solved using a commercial finite-element software COMSOL Multiphysics 4.4 (COMSOL, Inc.). First, the model geometry was simplified to only concern to the middle part of the measurement set-up as shown in Fig. 2(b). Three different physics were coupled together to solve the temperature distribution within the geometry. 'Laminar Flow' interface was used for solving the time-dependent velocity and pressure fields inside the microchannel using Navier-Stokes equation. The time-dependent flow rate was set to the channel inlet boundary, and zero pressure to the outlet boundary. For thin layers of the sensors and the heater, 'Electric Currents, Shell' interface was used to enable effective meshing of a thin layer present over a much thicker glass and PDMS substrates. In the model, resistors were simplified to include only 275 nm thick titanium layer without connections pads or tracks. Also, the insulator layer was neglected in the model. Same constant currents as used in the experiment, 0.2 mA and ∼5.9 mA, were set for the sensors and the heater, respectively. Measured electrical properties of the resistors, resistivity and temperature coefficient of resistance, were also included in the model. 'Heat transfer in Solids' interface coupled with other physics was first used for solving the amount of heat generated by the heater, and then for calculating the temperature distribution in the whole geometry. In the model, a typical heat transfer coefficient for air, 30 $\mathrm{W{\cdot}(m^2{\cdot}K)^{-1}}$, was set on the outer boundaries of the model to approximate the convective heat flux on the boundaries which are in the contact with the ambient air set to the measured temperature (25.8°C). Material properties used in the model are given in Table I.

TABLE I
MATERIAL PARAMETERS USED FOR THE SIMULATIONS.

Material	Density ($\mathrm{kg{\cdot}m^{-3}}$)	Specific heat ($\mathrm{J{\cdot}(kg{\cdot}K)^{-1}}$)	Thermal conductivity ($\mathrm{W{\cdot}(m{\cdot}K)^{-1}}$)
Water	997	4184	0.6
PDMS	970	1460	0.23
Glass	2510	820	0.97
Titanium	4500	525	11.4

The FEM model was validated by calculating average surface upstream and downstream temperatures from the simulation results and comparing them with measured upstream and downstream temperatures. Then, the validated FEM model was used in a PDMS based gravity-driven system including inlet and outlet reservoirs and a microchannel as shown in Fig. 3(a). In the model, we used the properties of water for liquid domain. The analytical model was used for determining a time-dependent pressure profile in the system. This pressure profile, calculated using (5) and presented in Fig. 3(b), was set as an inlet boundary condition in the FEM model, and the model was simulated. After simulation, the flow rate and the upstream and downstream temperatures were derived from the simulation data. Using these results, the temperature difference (ΔT) and the sensitivity of the sensor were calculated.

C. Design of Gravity-Driven Flow System

A gravity-driven system shown in Fig. 3 was designed and simulated based on four design goals. First, we wanted to assure that the maximum flow rate would not be over 10 μl/min. On the other hand, the flow rate should be larger than 0.1 μl/min for over 10h. This would ensure, for example, a continuous flow of fresh culture medium to cells. In addition, the heater should not warm liquid over 42 °C. Final requirement was that the liquid temperature in the outlet reservoir would not excess 37 °C because cell culture would be located there. Based on these requirements, we designed a system where an initial liquid plug height difference between the inlet and outlet reservoirs was set to 15 mm. This is illustrated as blue in Fig. 3(a). The radius of both reservoirs was 8 mm (r_{in} and r_{out} in (3)). Setting typical contact angles between PDMS and water, 60° and 110° [8] for θ_a and θ_r, respectively, the calculated p_{cap} using (4) was approximately -15 Pa. Therefore, a smaller microchannel with dimensions ($l \times w \times h$) 16 mm × 1000 μm × 50 μm was needed to fulfill our design goals. As this simulation case is expected to happen in a typical cell culture incubator, the ambient temperature in the model was set to 37°C. Based on the information above, the calculated pressure $\Delta p(t)$ was set to the channel inlet boundary in the model shown in Fig. 3(b). Next, a calorimetric flow sensor was

included in the model. As one of the design goal was to ensure that the heater will not warm liquid over 42 °C, a smaller 3 mA heater current was used in the simulation. Furthermore, the distance between the center of the heater and the channel inlet was set to 2 mm to ensure that liquid in the outlet reservoir is not exceeding 37 °C.

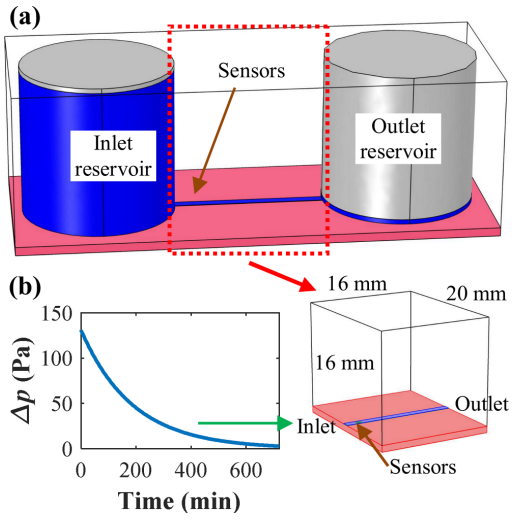

Fig. 3. (a) Schematic of the designed gravity-driven microfluidic device. Here, blue color is presenting liquid domain and gray color air domain at the begin. (b) A modeled geometry used in the simulation together with a calculated pressure profile set to inlet of the model.

IV. Results

A. Model Validation

A comparison of the measured and simulated upstream and downstream temperatures are shown in Fig. 4 with three different flow rates: no flow (first ∼150 s), 1 μl/min (between 150 and 275 s), and 10 μl/min (after 275 s). As can be seen, the model was able to estimate both temperatures sufficiently well, and therefore we conclude that it could be used as a part of gravity-driven flow model. Based on the measurement results, we approximated that a minimum detectable temperature difference, ΔT_{min}, was approximately 0.1°C in the designed system. Therefore, a reliable flow rate measurement can not be performed if the measured temperature difference is below this limit. This minimum flow rate required to achieve ΔT_{min} is marked as Q_{min}.

B. Simulation of a Gravity-Driven System

Simulation results of the model presented in Section III-C are described here. We first derived flow rate, upstream and downstream temperatures, and temperature difference from the results. We noticed that the maximum flow rate Q_{max} was approximately 7 μl/min in the begin of the simulation, and approximately 0.9 °C maximum temperature difference ΔT_{max}

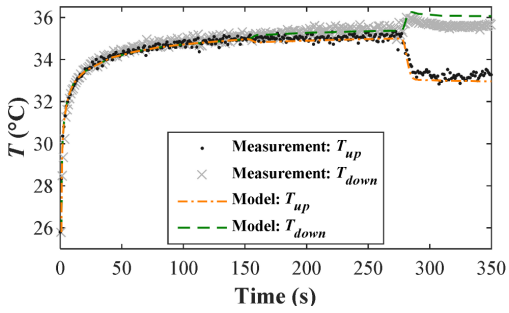

Fig. 4. Model validation results.

TABLE II
Comparison of two designs.

	G1	*G2*
Model parameters		
h (μm)	50	55
l (mm)	16	16
w (μm)	1000	790
d_{cc} (μm)	300	230
h_s (μm)	540	380
l_s (mm)	2.22	1.58
Performance measures		
Q_{max} (μl/min)	7.3	7.5
ΔT_{max} (K)	0.87	1.10
S (K·(μl/min)$^{-1}$)	0.12	0.15
Q_{min} (μl/min)	0.96	0.71

was detected. The calculated sensitivity was approximately 0.12 K·(μl/min)$^{-1}$. Furthermore, Q_{min} was almost 1 μl/min in this design. Therefore, as the results with the original geometry (marked as *G1* in Fig. 5) showed that the system should be improved, a new geometry was designed. Several issues, such as the heating power, the sensors layouts and their positions, have been reported to affect the sensitivity of the sensor [4]. For this reason, we decided first to narrow the channel. As we wanted that R_{hyd}, and thus the working pressure set to the inlet boundary in the model, would be approximately same in both designs, the height of the microchannel was increased based on (6). Furthermore, as reported in Table II, we decreased the length of the sensors (both h_s and l_s were reduced), and placed them closer to the heater to increase the sensitivity of the measurement. Results with the new design, marked as *G2*, are shown in Fig. 5. As planned, almost equal flow rates were achieved with both designs as shown in Fig. 5(a). Higher upstream and downstream temperatures, and also larger ΔT were resulted with the new design as can be seen in Fig. 5(b). It should be noted that the heater did not warm liquid over 42°C with the new design, which was one of our design goals. Finally, performances of the designs are compared in Fig. 5(c) and in Table II. Based on these results, over 20% better sensitivity and lower Q_{min} was achieved with *G2* when compared to the original geometry.

The simulation results showed that the developed FEM model can be used to design gravity-driven systems including

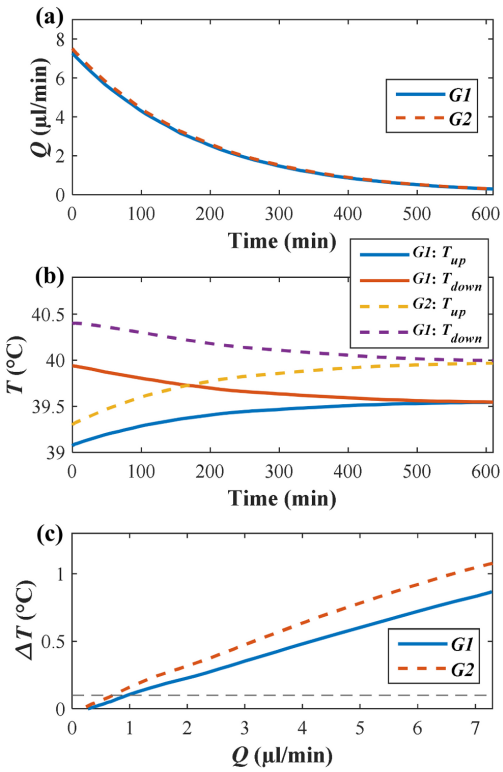

Fig. 5. Comparison of two gravity-driven designs *G1* and *G2*: (a) flow rates, and (b) upstream and downstream temperatures as a function of time, and (c) temperature differences as a function of flow rates. Dashed horizontal line represent a minimum detectable temperature difference level ΔT_{min} based on the validation measurement.

calorimetric flow sensors. We also noted that using the model, it was easy and fast to improve the system performance. A further use of the model can be the optimization of the sensor placement to achieve the highest possible detection sensitivity.

V. Conclusion

We presented a numerical model for a microfluidic system that integrates a calorimetric flow sensor measurement and gravity-driven flow. With this method, the flow rate can be measured indirectly in gravity-driven systems, thus enabling continuously monitoring flow in the system. Using the developed model, not only the flow behavior can be studied, but also the system can further be improved for better performance. We demonstrated this by improving the sensitivity of the measurement; we were able to enhance it over 20% in the second design. However, it is clear that further improvement of measured quality is possible to achieve. With the developed model, we are now able to study more complex sensor layouts and their performances. Therefore, future work includes the optimization of the sensor layout, and the implementation of the proposed gravity-driven system to verify the model design.

Acknowledgment

This work was supported by Doctoral Programme of the President of the Tampere University of Technology (TUT) and Tekes, the Finnish Funding Agency for Technology and Innovation (Decision no. 40346/11), and was carried out within the Human Spare Parts project.

References

[1] R. Que and R. Zhu, "A two-dimensional flow sensor with integrated micro thermal sensing elements and a back propagation neural network." *Sensors (Basel, Switzerland)*, vol. 14, no. 1, pp. 564–74, jan 2013.

[2] J. Sun, D. Cui, L. Zhang, X. Chen, H. Cai, and H. Li, "Fabrication and characterization of a double-heater based {MEMS} thermal flow sensor," *Sensors and Actuators A: Physical*, vol. 193, pp. 25 – 29, 2013.

[3] E. Meng, P.-Y. Li, and Y.-C. Tai, "A biocompatible parylene thermal flow sensing array," *Sensors and Actuators A: Physical*, vol. 144, no. 1, pp. 18 – 28, 2008.

[4] O. Sazhin, "Novel mass air flow meter for automobile industry based on thermal flow microsensor. I. Analytical model and microsensor," *Flow Measurement and Instrumentation*, vol. 30, pp. 60–65, 2013.

[5] T. H. Kim, D.-K. Kim, and S. J. Kim, "Study of the sensitivity of a thermal flow sensor," *International Journal of Heat and Mass Transfer*, vol. 52, no. 7-8, pp. 2140–2144, 2009.

[6] K. Palmer, H. Nguyen, and G. Thornell, "Finite element analysis of the effect on employing thermal through vias and heat fingers to increase heat transfer to fluid in calorimetric flow sensors," *Sensors and Actuators A: Physical*, vol. 201, pp. 49–57, oct 2013.

[7] X. Zhu, L. Yi Chu, B.-h. Chueh, M. Shen, B. Hazarika, N. Phadke, and S. Takayama, "Arrays of horizontally-oriented mini-reservoirs generate steady microfluidic flows for continuous perfusion cell culture and gradient generation." *The Analyst*, vol. 129, no. 11, pp. 1026–31, nov 2004.

[8] A.-J. Mäki, S. Hemmilä, J. Hirvonen, N. N. Girish, J. Kreutzer, J. Hyttinen, and P. Kallio, "Modeling and Experimental Characterization of Pressure Drop in Gravity-Driven Microfluidic Systems," *Journal of Fluids Engineering*, vol. 137, pp. 21 105–1, 2015.

[9] M. J. Fuerstman, A. Lai, M. E. Thurlow, S. S. Shevkoplyas, H. a. Stone, and G. M. Whitesides, "The pressure drop along rectangular microchannels containing bubbles." *Lab on a chip*, vol. 7, no. 11, pp. 1479–89, nov 2007.

[10] J. W. Gardner, "Thermoresistor," in *Microsensors: Principles and applications*, 1st ed. New York: Wiley, 1994, ch. 5, p. 94.

[11] S. Franssila, *Introduction to Microfabrication*. Chichester, UK: John Wiley & Sons, Ltd, sep 2010.

[12] A.-J. Mäki, J. Kreutzer, and P. Kallio, "Modeling Drug Delivery in Gravity-Driven Microfluidic System," in *Proceedings of the ASME 2014 4th Joint US-European Fluids Engineering Division Summer Meeting and 12th International Conference on Nanochannels, Microchannels, and Minichannels, FEDSM2014*, 2014, p. V001T02A003.

Publication IV

Mäki, A.-J., Peltokangas, M., Kreutzer, J., Auvinen, S., and Kallio, P., "Modeling carbon dioxide transport in PDMS-based microfluidic cell culture devices," *Chemical Engineering Science*, vol. 137, pp. 515–524, 2015.

Chemical Engineering Science 137 (2015) 515–524

Contents lists available at ScienceDirect

Chemical Engineering Science

journal homepage: www.elsevier.com/locate/ces

Modeling carbon dioxide transport in PDMS-based microfluidic cell culture devices

A.-J. Mäki [a,*], M. Peltokangas [a], J. Kreutzer [a], S. Auvinen [b], P. Kallio [a]

[a] Tampere University of Technology, Department of Automation Science and Engineering, BioMediTech, Tampere, Finland
[b] Tampere University of Technology, Department of Materials Science, Tampere, Finland

HIGHLIGHTS

- A numerical CO_2 transport model for PDMS-based microfluidic devices was developed.
- Higher CO_2 diffusion through PDMS was observed than typically reported.
- Usefulness of the model was demonstrated by comparing different device geometries.
- Based on the model predictions, an alternative CO_2 feeding strategy was proposed.

ARTICLE INFO

Article history:
Received 11 February 2015
Received in revised form
5 June 2015
Accepted 29 June 2015
Available online 17 July 2015

Keywords:
Carbon dioxide
Microfluidics cell culturing
Finite element method
Mass transport
Numerical simulation
pH

ABSTRACT

Maintaining a proper pH level is crucial for successful cell culturing. Mammalian cells are commonly cultured in incubators, where the cell culture medium is saturated with a mixture of air and 5% carbon dioxide (CO_2). Therefore, to keep cell culture medium pH in an acceptable level outside these incubators, a suitable CO_2 concentration must be dissolved in the medium. However, it can be very difficult to control and measure precisely local concentration levels. Furthermore, possible undesired concentration gradients generated during long-term cell culturing are almost impossible to detect. Therefore, we have developed a computational model to estimate CO_2 transport in silicone-based microfluidic devices. An extensive set of experiments was used to validate the finite element model. The model parameters were obtained using suitable measurement set-ups and the model was validated using a fully functional cell cultivation device. The predictions obtained by the simulations show very good responses to experiments. It is shown in this paper how the model helps to understand the dynamics of CO_2 transport in silicone-based cell culturing devices possessing different geometries, thus providing cost-effective means for studying different device designs under a variety of experimental conditions without the need of actual testing. Finally, based on the results from the computational model, an alternative strategy for feeding CO_2 is proposed to accelerate the system performance such that a faster and more uniform CO_2 concentration response is achieved in the area of interest.

1. Introduction

In recent years, cell culturing in microscale environments has become an interesting alternative to more conventional macroscale bioreactors. For example, microfluidic-based cell culture devices do not only require smaller volumes of culture medium, but also enable more precise control of the cellular microenvironments (Kim et al., 2007). In these microfluidic culture devices, poly (dimethylsiloxane) (PDMS) has become the most popular material because of its simple fabrication process, low cost, optical transparency, biocompatibility and gas permeability (Duffy et al., 1998; Gao et al., 2012). Using gas permeability properties, several PDMS-based microfluidic devices have been developed to generate desired oxygen (Adler et al., 2010; Chen et al., 2011; Inamdar et al., 2011; Polinkovsky et al., 2009; Shiku et al., 2006; Skolimowski et al., 2010; Zahorodny-Burke et al., 2011) and carbon dioxide (CO_2) (Forry and Locascio, 2011; Polinkovsky et al., 2009; Takano et al., 2012) concentrations for cell cultures.

CO_2 is typically used for controlling pH in the cell culture medium (Kim et al., 2007), and therefore it is a crucial parameter especially in long-term cell culture studies outside an incubator. There are several methods to supply the required CO_2 concentration to the medium in the

* Corresponding author. Tel.: +358 40 7364613.
E-mail address: antti-juhana.maki@tut.fi (A.-J. Mäki).

http://dx.doi.org/10.1016/j.ces.2015.06.065
0009-2509/

microfluidic cell culture devices. For example, gas permeability of PDMS allows that CO_2 can be fed to the culture medium through a PDMS-membrane instead of feeding CO_2 directly to liquid, reducing a liquid loss by evaporation and further stabilizing osmolarity (Blau et al., 2009).

While oxygen transport in PDMS-based microfluidic cell culture devices has been modeled in various studies (Adler et al., 2010; Chen et al., 2011; Inamdar et al., 2011; Polinkovsky et al., 2009; Shiku et al., 2006; Skolimowski et al., 2010; Zahorodny-Burke et al., 2011), CO_2 transport has not been comprehensively modeled. Therefore, we have developed a computational CO_2 transportation model that is based on a finite element method (FEM). The model provides a tool for designing PDMS based cell culture systems and for studying CO_2 concentration levels especially when concentration measurement is impossible or difficult.

The rest of the paper is organized as follows: first, theory required for the model is explained before presenting measurements used to validate the computational model developed in this paper. This model is presented next before comparing experimental values and results from simulations. Finally, the verified model is used for studying CO_2 transport in different devices.

2. Theory

Required equations for the numerical are described in this section. First, CO_2 transport modeling is covered before presenting equations required for estimation of liquid pH in cell culturing devices.

2.1. Carbon dioxide transport and concentration

In a PDMS cell culture device, CO_2 concentration can be in gas, liquid and solid phases (Forry and Locascio, 2011; Polinkovsky et al., 2009). In this study, the solid phase refers to the CO_2 concentration within the PDMS parts (shown as gray areas in Fig. 2B). Therefore, to model the entire system, CO_2 transport mechanisms in these three phases need to be described. In the fluidic phases (gas and liquid), CO_2 is transported by both diffusion and convection. In the solid phase there is no convection; the transport is diffusion-driven, as CO_2 diffuses through material due to concentration differences across material. When assuming no material consumption, three different mass transport equations describes a mass balance in the system (Stoian et al., 2012)

$$\frac{\partial c_g}{\partial t}+\nabla\cdot\left(-D_g\nabla c_g\right)+\boldsymbol{u_g}\cdot\nabla c_g=0\frac{\partial c_l}{\partial t}+\nabla\cdot\left(-D_l\nabla c_l\right)$$
$$+\boldsymbol{u_l}\cdot\nabla c_l=0\frac{\partial c_p}{\partial t}+\nabla\cdot\left(-D_p\nabla c_p\right)=0 \quad (1)$$

where subscripts g, l, and p denote the CO_2 concentration in gas-phase, liquid-phase, and solid-phase (PDMS), and c, D, and u are

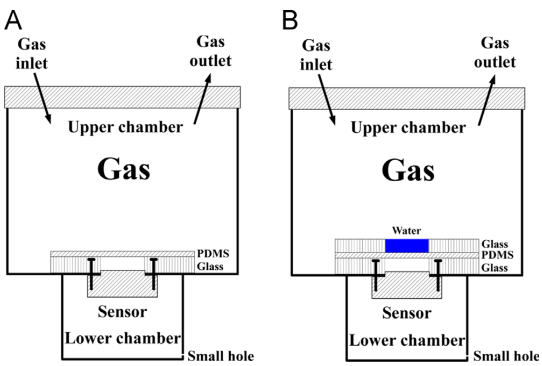

Fig. 1. Schematic of gas sensor measurements: (A) *M1*, and (B) *M2*.

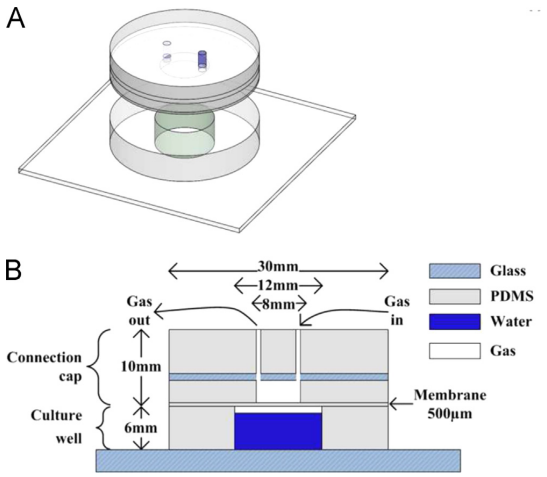

Fig. 2. The schematic of the cell cultivation device: (A) 3D view and (B) the cross-sectional view.

CO_2 concentration, diffusion coefficient, and velocity field, respectively, in each phase. Eq. (2) describes equilibrium of CO_2 concentration between (i) liquid and gas, (ii) liquid and PDMS, and (iii) PDMS and gas (Shiku et al., 2006; Skolimowski et al., 2010):

$$c_l \underset{k_{gl}}{\overset{k_{lg}}{\rightleftharpoons}} c_g,\ c_l \underset{k_{pl}}{\overset{k_{lp}}{\rightleftharpoons}} c_p,\ c_p \underset{k_{gp}}{\overset{k_{pg}}{\rightleftharpoons}} c_g \quad (2)$$

where k represents the mass transport coefficient at the specific surface, and subscript indicates the direction; e.g. k_{lp} provides the mass transport coefficient from the liquid-phase to the PDMS-phase at the interfaces between these two phases. A dimensionless partition coefficient ratio between two domains, Kp, is calculated using the saturated concentration values (Shiku et al., 2006; Skolimowski et al., 2010):

$$Kp_{lg}=\frac{k_{lg}}{k_{gl}}=\frac{c_{g\_sat}}{c_{l\_sat}},Kp_{lp}=\frac{k_{lp}}{k_{pl}}=\frac{c_{p\_sat}}{c_{l\_sat}},Kp_{pg}=\frac{k_{pg}}{k_{gp}}=\frac{c_{g\_sat}}{c_{p\_sat}} \quad (3)$$

where c_{g_sat}, c_{l_sat}, and c_{p_sat} are saturated CO_2 concentrations in gas, liquid, and PDMS domains, respectively. Based on the previous equations, mass transport at the interfaces between two different domains is modeled using mass transport coefficients and CO_2 concentrations in both sides of the interfaces. These fluxes between two phases are modeled using the following equations (separately for each interface; liquid/gas, liquid/PDMS, and PDMS/gas) (Shiku et al., 2006; Skolimowski et al., 2010):

$$Flux_{lg}=k_{lg}c_l-k_{gl}c_p=k_{gl}\left(Kp_{lg}c_l-c_g\right)$$
$$Flux_{lp}=k_{lp}c_l-k_{pl}c_g=k_{pl}\left(Kp_{lp}c_l-c_p\right)$$
$$Flux_{pg}=k_{pg}c_p-k_{gp}c_g=k_{gp}\left(Kp_{pg}c_p-c_g\right) \quad (4)$$

where $Flux_{lg}$, $Flux_{lp}$, and $Flux_{pg}$ denote the CO_2 flux towards the gas-phase at the liquid/gas interface, the flux towards the PDMS-phase at the liquid/PDMS interface, and the flux towards the gas-phase at the PDMS/gas interface, respectively. Negative sign is used for the opposite flux direction.

As the saturated concentrations in each domain are used for defining value of Kp, these are determined next. In the gas phase, the saturated CO_2 concentration is estimated by assuming that the

ideal gas law is valid, and is therefore calculated using an Eq.

$$p_{CO_2}V = nRT,\ c_{g\_sat} = \frac{n}{V}, \Rightarrow c_{g\_sat} = \frac{p_{CO_2}}{RT} = \frac{Fv_{CO_2}p_{ch}}{RT} \quad (5)$$

where p_{CO2}, V, n, R, T, Fv_{CO2}, and p_{ch} are CO_2 partial pressure, volume, amount of substance, the ideal gas constant, temperature, volume fraction of CO_2 gas component, and total pressure in the chamber, respectively.

If CO_2 is assumed as an ideal gas, Henry's law that describes the equilibrium between vapor and liquid defines CO_2 concentration in the liquid phase. Henry's law as a function of temperature can be then used to calculate dissolved CO_2 concentration in liquid (Sander, 1999)

$$kh_{H(T)} = kh_{H0}\exp\left[-H\left(\frac{1}{T}-\frac{1}{T_{SATP}}\right)\right], c_{l\_sat(T)} = \frac{p_{CO2}}{k_{H(T)}} \quad (6)$$

where $kh_{H(T)}$, kh_{H0}, T_{SATP}, H, and $c_{l\_sat(T)}$ are Henry's law constant at experiment temperature T, Henry's law constant at standard ambient temperature T_{SATP} (298.15 K), a constant used to calculate temperature dependent Henry's law constant (in K) and saturated CO_2 concentration in liquid at experiment temperature T, respectively.

Finally, the saturated CO_2 concentration in PDMS is calculated based on the solubility of CO_2 in PDMS (Merkel et al., 2000):

$$S = Sinf\,(1+p_{ch}np), c_{p\_sat} = Sc_{g\_sat} \quad (7)$$

where S, $Sinf$, and np are the solubility of CO_2 in PDMS, the infinite dilution solubility, and the pressure dependence of solubility, respectively. When solubility and permeability properties are known, diffusion coefficient of CO_2 in PDMS, D_p, is estimated using the equation (Charati and Stern, 1998)

$$D_p = \frac{P}{S} \quad (8)$$

where P is the permeability coefficient of CO_2 in PDMS. Using this equation, the mean diffusion coefficient is solved when solubility is known and the permeability coefficient is determined with experiments explained in Section 3.1.

2.2. Carbonate reaction

In the pH measurement, reaction between CO_2 and liquid (water) when CO_2 is dissolved in liquid should be considered. The overall carbonate reaction in solution (water) is following (Forry and Locascio, 2011):

$$CO_{2(gas)} \Leftrightarrow CO_{2(aq)}, CO_{2(aq)} + H_2O \Leftrightarrow H_2CO_3 \Leftrightarrow H^+ + HCO_3^-,$$
$$HCO_3^- \Leftrightarrow H^+ + CO_3^{2-} \quad (9)$$

where $[CO_{2(aq)}]$, $[H_2CO_3]$, $[HCO_3^-]$, $[H^+]$, and $[CO_3^{2-}]$, are the concentrations of the dissolved CO_2 in liquid, carbonic acid, bicarbonate ion, hydrogen ion, and carbonate ion, respectively. In this study, $[CO_{2(aq)}]$ equals c_l in Eq. (2). As the hydration equilibrium constant $Khyd$, $[H_2CO_3]/[CO_{2(aq)}]$ is around 1.7×10^{-3} (Forry and Locascio, 2011), less than 0.2 percent of $CO_{2(aq)}$ molecules are converted to $[H_2CO_3]$, thus majority of the dissolved CO_2 exists as $CO_{2(aq)}$. Similarly, as $[CO_3^{2-}]$ is not significant compared to $[HCO_3^-]$ at the pH level used in this study (smaller than 7), it will not be included in the analysis (Liu et al., 2012). Using these assumptions, liquid pH can be approximated very precisely in the experimental conditions using the following equation:

$$pH = -\log_{10}([H^+]) \approx -\log_{10}\left(\sqrt{Kw + c_l Kc}\right) \quad (10)$$

where Kw and Kc are the ion product of water ($\sim10^{-14}$ at room temperature) and the thermodynamic constant for the dissociation of $[H_2CO_3]$, respectively. The latter can be approximated at a certain temperature T between 0 and 50 °C (converted to Kelvin) using constants A, B, and C in the equation (Millero and Pierrot, 1998)

$$Kc = \exp\left(A + \frac{B}{T} - C\ln(T)\right) \quad (11)$$

where $A=290.9097$, $B=-14554.21$, $C=45.0575$ for $[H_2CO_3]$, and T is unitless in the equation. Using these, Kc is around 4.4×10^{-3} at 24 °C.

3. Experimental set-ups

The developed computational model has five unknown parameters, D_l, D_p k_{gl}, k_{gp}, and k_{pl}, which were determined experimentally in this work. To define these unknown parameters, four different measurements were performed. First, permeability coefficient of CO_2 in PDMS was measured with a commercial device, and the results were used to define the range of diffusion coefficient D_p using Eq. (8). Next, two measurement set-ups including a CO_2 gas sensor were used to determine the needed simulation parameters. It was also possible to obtain the dynamics of CO_2 transport using these measurements. Finally, pH measurement was performed to validate the developed model in the complete device.

3.1. CO_2 measurements for the model development

Three types of phase-interfaces exist in PDMS-based cell culture devices: gas–liquid, gas-solid, and liquid-solid as explained in Section 2.1. Measurements required obtaining the model parameters for each phase-interfaces and domains are described next. First, permeability of CO_2 in PDMS was measured using a carbon dioxide transmission rate testing system PERMATRAN-C Model 4/41 (MOCON, Inc., USA). In these experiments, a gas mixture containing 5% of CO_2 and 95% of N_2 (AGA, Finland) was used to measure the CO_2 transmission rate in ten different PDMS samples. The samples had a measurement area of 5 cm^2 and thicknesses between 1.72 mm and 2.92 mm. Temperature and pressure difference between sample sides were maintained at 23 °C and 1 atm (vacuum), respectively, during the experiments. The measured transmission rates (unit: $cm^3\cdot(m^2\,day\,atm)^{-1}$) were multiplied with measured sample thicknesses (unit: mm), and then the received value (unit: $(cm^3\,mm\cdot(m^2\,day\,atm)^{-1}$) was converted to Barrers (1 Barrer$=65.664\ cm^3\,mm\cdot(m^2\,day\,atm)^{-1}$ (McKeen, 2012)). Next, two sets of measurements, $M1$ and $M2$, were performed to define the required model parameters: six measurements with a gas–PDMS–gas interface ($M1a\ldots M1f$) to determine D_p, and k_{gp}, and five measurements with a gas–liquid–PDMS-gas interface ($M2a\ldots M2e$) to determine D_l, k_{gl}, and k_{pl}.

The PDMS sheets were fabricated by mixing PDMS prepolymer and curing agent (Sylgard 184, Dow Corning, USA) in a standard 10:1 ratio, poured into a 55-mm diameter Petri dish, de-gassed in a vacuum, and cured at 60 °C for three hours. After fabrication, the sheets were stored in a closed Petri-dish in normal room temperature and humidity maximum ten days before placed in the measurement system. The system consisted of two chambers separated by a PDMS sheet on a 5-mm-thick gas impermeable glass plate having a hole of 20 mm in a diameter as shown in Fig. 1. A gas mixture containing CO_2 was supplied to the upper chamber made from polypropylene, whereas a CO_2 sensor was placed inside the initially CO_2-free lower chamber. The upper chamber has a cylinder shape with a volume of 0.7 l, a diameter of 112 mm and a height of 72 mm. The lower chamber has a volume of 0.25 l with an outer height of 56 mm, an outer length of 72 mm and an outer width of 70 mm. The PDMS sheet on the glass plate covered the 20 mm hole and the glass plate entirely. In the gas–PDMS–gas

measurements, no other parts were used, whereas in the gas–liquid–PDMS–gas measurements, an additional 5-mm-thick glass plate having a hole with a diameter of 20 mm was first placed on the PDMS sheet and then the pool formed was filled with de-ionized water (Fig. 1).

The measurement range of the used non-dispersive CO_2 sensor based on infrared detection (COZIR Wide Range GC-0006, CO2Meter, USA, accuracy $\pm$ 5% of reading) was 0–20% and it was calibrated by using a gas mixture containing 5% of CO_2, 19% of O_2 and 76% of N_2 (AGA, Finland). The diameter of the active area of the sensor was 20 mm, and therefore, the sensor was tightly fixed to the hole of the glass plate. In order to prevent the pressure increase in the lower chamber while gassing the upper chamber, a small hole (diameter 0.5 mm) was drilled close to the bottom of the lower chamber (Fig. 1).

Three different PDMS thicknesses (2000 ± 10 μm, 380 ± 10 μm and 110 ± 10 μm, measured using a digital caliper before the experiments) and two different gas mixtures, 5% CO_2 and 100% CO_2, were used in the experiments. The gauge pressure of the gas mixture varied between 17 mbar and 36 mbar. Temperature was monitored during the experiments and was always between 22.8 °C and 24 °C. Detailed information on each experiment is shown in Table 1 including the average experimental temperature in every measurement.

Before each measurement, the chambers were aired in order to remove the CO_2 residues from the chambers. This was done by removing the PDMS sheet between the chambers and keeping the upper measurement chamber open. The measurement chamber was kept open for at least as long as the CO_2 sensor output agreed with the background CO_2 level. After the ventilation, the PDMS sheet was tightly placed on the glass plate. In the case of the gas–liquid–PDMS–gas experiment, the additional glass plate was placed on the PDMS sheet and the pool was filled with water as described earlier. Next, the upper chamber was closed, the gas inlet and the gas outlet were connected and recording of the CO_2 concentration was started with a sampling frequency of 1 Hz. Finally, the pressure regulators for the gas lines were opened and the gauge pressure was logged using a pressure sensor (HCXM050D6V, First Sensor AG, Germany) connected into the gas inlet. The measurement was continued until the sensor output was stabilized to 5% level (measurements with 5% CO_2) or reached the measurement range of the sensor (measurements with 100% CO_2).

Two first measurements using a 2000-μm-thick PDMS layer (labeled as *M1a* and *M1b*) were used for determining k_{gp} and the diffusion coefficient of CO_2 in PDMS, D_p. The rest of the measurements (*M1c*… *M1f* and *M2a*… *M2e*) were performed to obtain remaining parameters (D_l, k_{gl}, and k_{pl}) required for the developed CO_2 transport model.

3.2. pH measurement

A complete structure, designed for cell culture purposes (Fig. 2), was used for the validation of the proposed model. The structure consists of two parts: a culture well and a connection cap. The culture well was fabricated from a 6-mm-high PDMS ring by punching a 12 mm hole in the middle. The connection cap consists of four layers: a 6-mm-thick PDMS layer on top for tight and sealed connections for gas supply pipes, a 1 mm glass layer providing rigidity, a 3-mm-thick PDMS layer below the glass, and a 500-μm-thick PDMS membrane. The membrane seals the culture well water-tightly, but lets the gas pass through. All PDMS parts were fabricated with same process that was described in Section 3.1

The pH validation experiments were performed in typical room conditions (temperature, humidity). The culture well was filled with de-ionized water (volume 600 μl). The connection cap was placed on top of the culture well and dry gas mixture (5% CO_2) was supplied from the inlet port as shown in Fig. 2B. In these experiments, a gas flow rate of 1 ml/min was used. In a selected time interval, pH was measured by removing the connection cap and taking a 200 μl sample to a pipette tip. The sample was taken at the bottom of the culture well to obtain a pH value representative at the cell cultivation area. The pH was measured inside the pipette tip using a small field-effect transistor (FET) type pH probe (MicroFET, Sentron Europe BV, The Netherlands) that includes an integrated temperature sensor. The experimental conditions were following: an average temperature 23.7 °C and a chamber pressure 1 atm. Each measurement was recorded for two minutes continuously, and an average pH and a standard deviation (SD) were calculated. Recordings were conducted in several time-points (0, 10, 25, 40, 60, and 75 min). In addition, four long-term measurements (two one day and two five days) were performed to determine the equilibrium pH value of the device.

4. Computational model

In this section, the developed computational model is presented. Model properties are described before reporting the implementation of the model using commercial software. As mentioned in Section 3, the developed computational model had five unknown parameters (D_l, D_p, k_{gl}, k_{gp}, and k_{pl}) which were determined experimentally.

4.1. Model parameters, assumptions, geometry, and boundary conditions

This section describes the model parameters, assumptions, geometries, and boundary conditions used for simulating CO_2 concentrations in the PDMS device. Mass transport between different phases is based on the flux in the boundaries as explained in Section 2.1. Several assumptions and simplifications were included in the model. Firstly, it assumes that both the ideal gas behavior and Henry's Law are valid. Also, constant temperature and pressure conditions are used in the model. Furthermore, liquid evaporation and possible leaking are expected to be negligible. Dissolution and transportation of other molecules (for instance oxygen from air) are not considered in the model. Because only a very small amount of dissolved CO_2 concentration (c_l) converts to $[HCO_3^-]$, as discussed in Section 2.1, and c_l is the main carbonate specie in the aqueous phase; c_l is not consumed and thus,

Table 1
Experimental conditions in measurements *M*1 and *M*2.

Parameter	Measurement set 1						Measurement set 2				
	M1a	***M1b***	***M1c***	***M1d***	***M1e***	***M1f***	***M2a***	***M2b***	***M2c***	***M2d***	***M2e***
Average temperature (°C)	23	23	24	24	24	24	23	24	24	24	24
Gauge pressure (mbar)	28	28	17	17	17	19	36	34	18	18	24
Feeding CO_2 (%)	100	100	100	5	5	5	5	5	5	5	5
PDMS thickness (μm)	2000	2000	110	110	110	380	110	110	380	380	380

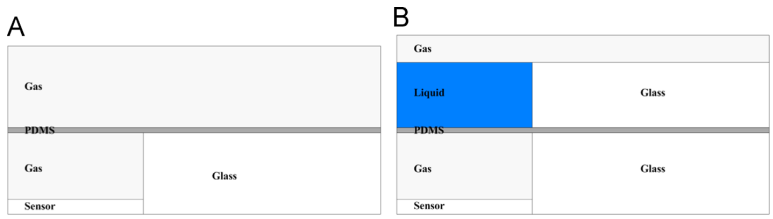

Fig. 3. Geometries used for parameter determination experiments: (A) *M*1, and (B) *M*2. Axial symmetry is set to left boundary on both models.

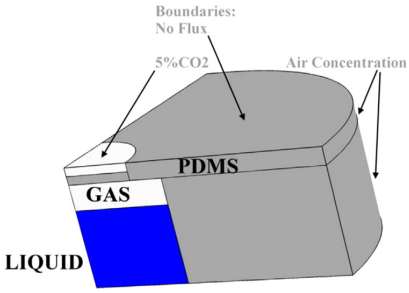

Fig. 4. pH model geometry, phases and boundaries. No flux condition was set also to the bottom boundaries (not shown).

reactions between CO_2 and liquid (water) are ignored in the model. As no perfusion is included, fluid (liquid and gas) velocities (u in Eq. (1)) are set to zero.

Two-dimensional axial-symmetric models for the parameter determination measurements sets (*M*1 and *M*2) presented in Section 3.1 were created as shown in Fig. 3. The dimensions in the models were the following (see also Section 3.1 and Fig. 1): an outer radius 27.5 mm, an inner gas chamber radius and a height: 10 mm and 4.9 mm, respectively, and a width and a height of the glass plate: 17.5 mm and 6 mm. Feeding CO_2 values (%) from Table 1, converted to concentration values using the ideal gas law, were set on the top boundary in both models. The left boundary was defined as the symmetry line and no flux condition was set on the sensor surface and the glass boundaries. The initial concentrations are based on the saturated concentrations in each phase (gas, liquid, and solid) when exposed to air, where CO_2 concentration is approximately 0.04%.

Compared to the experimental set-up used in pH measurement reported in Section 3.2, a simplified version concerning only the part below the glass plate (an outer radius 15 mm, a total height 9.5 mm, shown in Fig. 2) was used. In the simplified model, 500 μm space above the PDMS membrane was analyzed, resulting in a total height of 7 mm as shown in Fig. 4. Because of the symmetry of the device, two-dimensional axial-symmetric model was also used in this case. The left boundary was defined as the symmetry line and no flux condition was set on the bottom surface of the device and the glass boundaries in the top part. Revolution of this model is shown in Fig. 4. 5% CO_2 concentration was set to the top gas layer in the middle of the device as showing in Fig. 4.

In every model, CO_2 transport between two phases is based on the flux given in Eq. (4) using *Kp*, the partition coefficient ratio between two domains. *Kp* is calculated based on the saturated concentrations using Eqs. (5)–(7) for gas, liquid, and solid (PDMS) phases, respectively, and for each experiment conditions separately.

4.2. Model implementation

Time-dependent carbon dioxide concentrations were solved using a commercial finite-element modeling tool COMSOL Multiphysics® Version 4.4 (COMSOL, Inc., USA). In the models, "Transport of diluted species equations" using Fick's law was used as the governing equation to calculate the time-dependent CO_2 concentration profile. The used computational meshes for the models were following; for measurement set *M*1, the mesh consisted of ~3100 triangular elements for simulations of 380-μm-thick and 2000-μm-thick PDMS membranes, and ~7100 triangular elements for simulations of 110-μm-thick PDMS membranes. In the measurement set *M*2, ~3300 and ~7200 triangular elements were used for simulations of 380-μm-thick and 110-μm-thick PDMS membranes, respectively, whereas the model used for both pH measurement and simulation case study (presented in Section 5.3) consisted of ~3600 triangular elements. All the simulations were carried out using Intel i7-960 3.2 GHz processor with 24 GB of memory using direct PARDISO solver.

5. Results and discussion

This section describes first the determination of the parameters for the computational model using experiments explained in Section 3.1. Then, results from the model are compared to pH measurement presented in Section 3.2. Finally, it is demonstrated how the developed model is used for testing a variety of different experimental conditions to discover the required inlet CO_2 concentration to maintain a desired CO_2 concentration level.

5.1. Determination of the model parameters

The model parameters were determined using the measured carbon dioxide concentrations reported in Section 3. The parameters of the model and their values are shown in Table 2. As described earlier, the model had five unknown parameters, D_l, D_p, k_{gl}, k_{gp}, and k_{pl}, which were determined experimentally in this work. The infinite dilution solubility constant at 24 °C, *Sinf*, was approximated based on published values around the same temperature (Blau et al., 2009; Shah et al., 1993; Tanimura, 1993). The CO_2 diffusion coefficient in a gas-phase, D_g, was approximated based on literature (Davidson and Trumbore, 1995; Terashima et al., 2001).

The modeling process included over thirty simulation runs to determine the parameter values. First, permeability experiments presented in Section 3.1 were performed to define the diffusion coefficient D_p. The measured permeability coefficient values varied between 8000 and 10 000 Barrers ($1\ \text{Barrer} = 7.6 \times 10^{-9}\ \text{cm}^3(\text{STP}) \cdot \text{cm} \cdot (\text{cm}^2\ \text{s atm})^{-1}$). Using these values and the solubility S of CO_2 in PDMS given in Table 2, together with Eq. (8), the estimated value for D_p varies between 4.1 and $5.1 \times 10^{-9}\ \text{m}^2\ \text{s}^{-1}$. Next, as described earlier, the model was simulated with different D_p (between 2and $6 \times 10^{-9}\ \text{m}^2\ \text{s}^{-1}$) and k_{gp} values using six different experimental conditions *M*1 shown in Table 1. Measurements *M*1*a* and *M*1*b* using the 2-mm-thick PDMS membranes were used to define a more precise value for D_p and k_{gp}. During the model parameter iteration process, it was noticed that D_p must be remarkably higher than

Table 2
Used simulation parameters.

Parameter	Value	Source
Temperature, T	23–24 °C	Measured
Gauge pressure in chamber, p	17–36 mbar	Measured
Liquid density, ρ	997.5–997.3 kg m^{-3}	Water properties
Liquid dynamic viscosity, η	9.4–9.1 × 10^{-4} Pa s	Water properties
Universal gas constant, R	8.31451 J $(K\ mol)^{-1}$	
Henry's law constant for CO_2 in water at 25 °C, k_{H0}	29.41 l atm mol^{-1}	(Sander, 1999)
Constant to convert k_H to $k_{H(T)}$, H	2400 K	(Sander, 1999)
$k_{H(T)}$ for CO_2 at T, $k_{H(T)}$	27.9–28.6 l atm mol^{-1}	Calculated using Eq. (6) (Sander, 1999)
The pressure dependence of solubility constant of CO_2 in PDMS, n	5.9 × 10^{-3} atm^{-1}	(Merkel et al., 2000)
Solubility constant of CO_2 in PDMS at chamber pressure and 24 °C, S	1.5 cm^3(STP) cm^{-3} atm^{-1}	Approximated using Eq. (7) (Merkel et al., 2000)
The infinite dilution solubility constant of CO_2 in PDMS at 24 °C, $Sinf$	1.5 cm^3(STP)·cm^{-3} atm^{-1}	Approximated (Blau et al., 2009; Shah et al., 1993; Tanimura, 1993)
Diffusion coefficient for CO_2 in gas, D_g	1.6 × 10^{-5} m^2 s^{-1}	Approximated (Davidson and Trumbore, 1995; Terashima et al., 2001)
Diffusion coefficient for CO_2 in PDMS, D_p	4.2 × 10^{-9} m^2 s^{-1}	Determined using permeability and $M1$ measurements, range: 4.1-5.1 × 10^{-9} m^2 s^{-1}
Diffusion coefficient for CO_2 in liquid, D_l	(30 ± 6) × 10^{-9} m^2 s^{-1}	Determined using measurement $M2$
Dissociation constant of H_2CO_3 in water, $Khyd$	1.7 × 10^{-3}	(Forry and Locascio, 2011)
Mass transport coefficient from the gas-phase to the liquid-phase, k_{gl}	(6.0 ± 1.2) × 10^{-5} m s^{-1}	Determined using measurement $M2$
Mass transport coefficient from the gas-phase to the solid (PDMS)-phase, k_{gp}	(1.0 ± 0.2) × 10^{-5} m s^{-1}	Determined using measurement $M1$
Mass transport coefficient from the liquid-phase to the solid (PDMS)-phase, k_{pl}	(1.5 ± 0.3) × 10^{-5} m s^{-1}	Determined using measurement $M2$
Partition coefficient ratio between, liquid and solid (PDMS) domains, Kp_{lp}	1.77	Approximated using Eq. (3)
Partition coefficient ratio between liquid and gas domains, Kp_{lg}	1.17	Approximated using Eq. (3)
Partition coefficient ratio between solid (PDMS) and gas domains, Kp_{pg}	0.66	Approximated using Eq. (3)
Thermodynamic constant for the dissociation of $[H_2CO_3]$, Kc	4.4 × 10^{-3}	Approximated using Eq. (11) (Millero and Pierrot, 1998)

D_l, D_p, k_{gl}, k_{gp}, and k_{pl} were determined in this work.

typically reported in the literature, around 2–3 × 10^{-9} m^2 s^{-1} (e.g. Jawalkar and Aminabhavi, 2007). This confirmed, that the D_p values (4.1–5.1 × 10^{-9} m^2 s^{-1}) obtained in the permeability measurements were in the correct range. Next, all six $M1$ experiments ($M1a$–$M1f$) were simulated by varying D_p between 4.1 and 5.1 × 10^{-9} m^2 s^{-1}, and changing k_{gp} in the model for several orders of magnitude. Finally, comparing the model results to the experimental data $M1$, a combination of D_p and k_{gp} that gave the best overall response was chosen.

The other model parameters, k_{gl}, k_{pl}, and D_l, were determined using a similar process by comparing the model results to the data set $M2$ and using the values chosen for D_p and k_{gp}. First, to detect the lowest possible limit for D_l, measurements $M2a$ and $M2b$ were simulated so that parameters k_{gl} and k_{pl} were changed in the model for several orders of magnitude. Using this approach, it was noticed that to provide a proper simulation response, D_l must be larger than 20 × 10^{-9} m^2 s^{-1}, value that is over an order of magnitude higher than expected based on literature, around 2 × 10^{-9} m^2 s^{-1} (Sell et al., 2013; Xu et al., 2012). Next, based on literature, k_{gl} was assumed to be in the order of 10^{-5} or 10^{-4} m s^{-1} (Clark et al., 2011; Han et al., 2013; Ocampo-Torres and Donelan, 1994). Keeping k_{gl} in this range, changing k_{pl} again in several orders of magnitude (between 10^{-7} and 10^{-1} m s^{-1}), and altering D_l between 20 and 100 × 10^{-9} m^2 s^{-1}, the model was simulated with all measurements conditions $M2a$-$M2e$. It was noticed, that k_{pl} must be in the order of 10^{-5} m s^{-1}. Again, model parameters that gave the best overall response to measurement set $M2$ were chosen. Finally, the full model was validated by comparing the simulated results to the data obtained from the pH measurement presented in Section 3.2.

The final step in the model development was to study the confidence bounds of the model parameters. An important issue to consider is the measurement accuracy when determining these parameters. As noted earlier, accuracy of the CO_2 sensor was ± 5% of the reading, and the accuracy of the membrane thickness measurement was ± 10 μm. Therefore, the total measurement confidence is around ± 10%. It should be stated that this measurement inaccuracy is also the minimum uncertainty of the model. Next, the sensitivity of the chosen model parameters was analyzed. For D_p, the permeability measurement gave a result of 4.1–5.1 × 10^{-9} m^2 s^{-1}. For D_l, k_{gl}, k_{pl}, and k_{gp}, it was noted, that maximum 20% difference is possible for acceptable simulation response, therefore this was chosen as the confidence bound in Table 2.

Fig. 5 compares the simulated results using parameters chosen for D_p and k_{gp} and the experiments of data set $M1$. As can be seen, the model is able to capture the dynamics of the CO_2 transport and predicts CO_2 concentration remarkably well in six different experiments with different temperatures (between 23 °C and 24 °C), gauge pressures (from 17 mbar to 36 mbar), CO_2 feed level (5% and 100%), and PDMS thicknesses (110 μm, 380 μm, and 2 mm). Fig. 6 shows a comparison between data set $M2$ and simulation using all the model parameters shown in Table 2, and demonstrates that the model predicts accurately the CO_2 transport behavior in the device including liquid-phase.

Some of the determined values require a further discussion. Firstly, value determined for the diffusion coefficient D_p, 4.2 × 10^{-9} m^2 s^{-1} at around 24 °C is larger than values typically given in the literature (around 2.2–2.6 × 10^{-9} m^2 s^{-1}). However, as stated earlier, D_p can also be estimated based on permeability coefficient and solubility of CO_2 in PDMS using Eq. (8). As explained earlier, the measured diffusion coefficient D_p based on the permeability experiments, was between 4.1 and 5.1 × 10^{-9} m^2 s^{-1}, supporting the selected parameter value. It should also be stated that there are significant differences between values for D_p in the literature; for example Blau et al. and Kuo reported D_p values to be within 2.2–11 × 10^{-9} m^2 s^{-1} (Blau et al., 2009; Kuo, 1999) at 25 °C. On the other hand, D_p was reported to

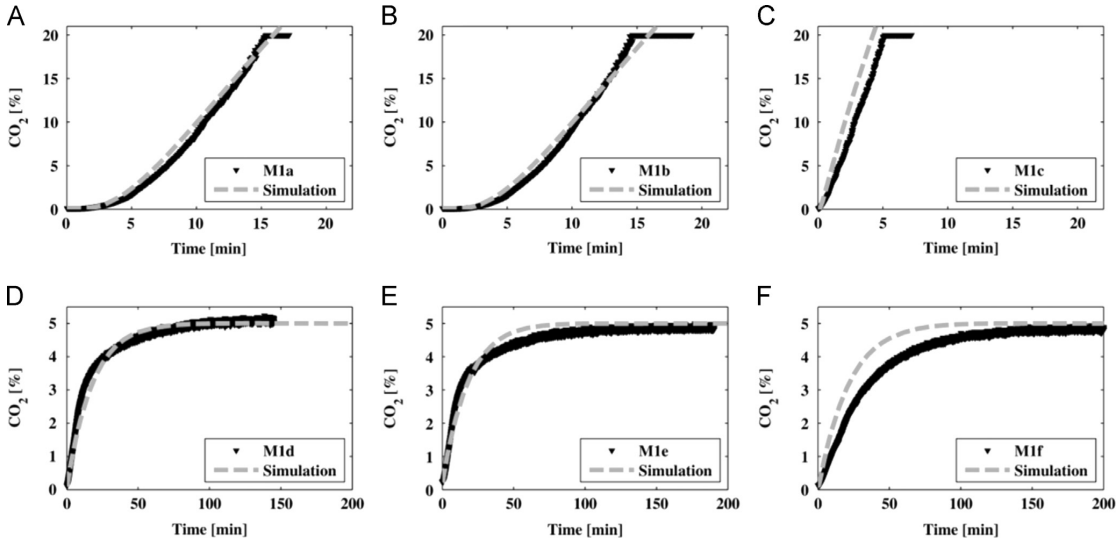

Fig. 5. Determination of model parameters D_p, and k_{gp} using measurement set *M*1: (A) *M*1*a*, (B) *M*1*b*, (C) *M*1*c*, (D) *M*1*d*, (E) *M*1*e*, and (F) *M*1*f*.

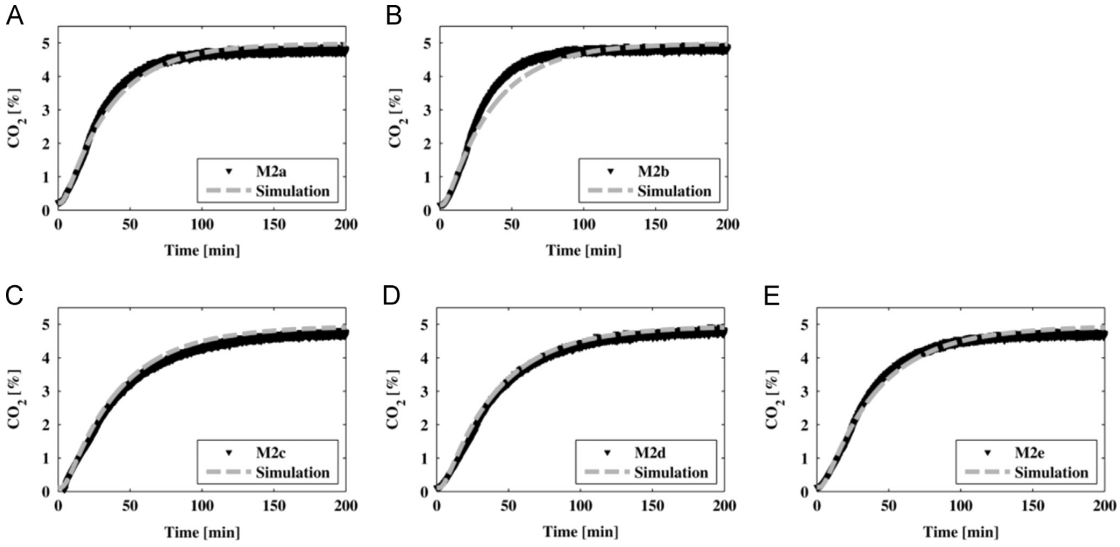

Fig. 6. Determination of the model parameters D_l, k_{gl}, and k_{pl} using measurement set *M*2: (A) *M*2*a*, (B) *M*2*b*, (C) *M*2*c*, (D) *M*2*d*, and (E) *M*2*e*.

be within $2.6–3.27 \times 10^{-9}$ m^2 s^{-1} at 25 °C (Jawalkar and Aminabhavi, 2007), 1.1×10^{-9} m^2 s^{-1} at 27 °C (Charati and Stern, 1998; Robb, 1968), around 11×10^{-9} m^2 s^{-1} at 28 °C (Tremblay et al., 2006), whereas at 35 °C D_p has been altered between 2.2×10^{-9} m^2 s^{-1} (Merkel et al., 2000), and 2.6×10^{-9} m^2 s^{-1} (Charati and Stern, 1998; Walker et al., 2002). All these results indicate that D_p is not only very sensitive to the ambient temperature and pressure, but also to the differences in the PDMS because of the different fabrication processes used. Furthermore, some variations between the experimental and simulation values could exist because of the assumptions made in the model (Jawalkar and Aminabhavi, 2007).

Another issue to be discussed is the diffusion coefficient of CO_2 in liquid (water in this work), D_l. Typically, in the literature this value is $1.6–2.8 \times 10^{-9}$ m^2 s^{-1} (Farajzadeh et al., 2007; Farajzadeh et al., 2009; Sell et al., 2013; Walker et al., 2002; Xu et al., 2012) at a standard ambient temperature and pressure, thus over one magnitude lower than determined in this work (30×10^{-9} m^2 s^{-1}). However, in our case the density-driven natural convection that enhances the mass transport of CO_2 is a possible reason for the higher value of D_l. Natural convection appears when concentration and density gradients are generated by CO_2 dissolved into water. The generated density gradient results in a remarkably faster mass transport than expected from pure Fickian diffusion (Farajzadeh et al., 2007; Farajzadeh et al., 2009, Lindeberg and Wessel-Berg, 1997). In our work, this natural convection enhanced mass transport has been taken into account by replacing the known diffusion coefficient of CO_2 in water as a larger effective diffusion coefficient value. However, natural convection could be better modeled by using two different effective diffusion coefficients values as proposed by Farajzadeh et al.

(Farajzadeh et al., 2007). They used one coefficient value in the beginning of transport process when density driven natural convection is more important, and another smaller coefficient in later stages. In their device, 43.5×10^{-9} m^2 s^{-1} was used for D_l in the early stages at 7.72 bar initial pressure, and they claimed that this value should be increased when pressure is increased. Using linear fitting based on their experimental data in three different pressures, 7.72–20.10 bar (Farajzadeh et al., 2007), approximated D_l at the early stage at atmospheric pressure is around 20×10^{-9} m^2 s^{-1}, and is similar to value determined in this work. Therefore, we believe that natural convection should be considered in the devices covered in this paper.

5.2. Model validation using pH measurements

This section reports validation of the computational model (presented in Section 3) using a complete device and pH experiments (as described in Section 3.2). A time-dependent 2D simulation was used to describe CO_2 transport and concentration distribution in the device. One simulation result showing concentration distribution in liquid phase is shown in Fig. 7.

To compare the simulated results to the pH measurement, an average volume concentration from the simulation is converted to pH using Eq. (10). Simulation results are compared to measured data in Fig. 8.

As shown in Fig. 8, the developed model predicts remarkably well the dynamics of the experimental pH values. When comparing simulation and measurement data from the first 75 minutes, only maximum 0.1 pH difference is obtained. Furthermore, the simulated saturation value (pH=4.72) is close to four measured values (pH=4.73–4.85) obtained in the long-term experiments as reported in Section 3.2. It should be remember that, as stated in Section 3.2, in the experiments pH was measured by removing the connection cap and taking a 200 μl sample, causing some variations to the measured pH values. Nevertheless, the results indicate that the developed model is able to estimate the CO_2 transportation also in a complete device.

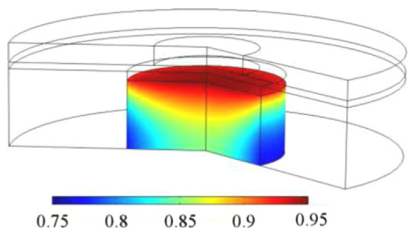

Fig. 7. Simulated CO_2 concentration [mol/dm^3] in liquid phase at time 500 min.

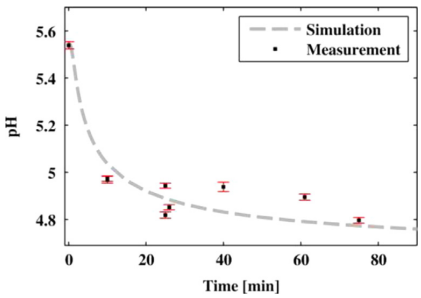

Fig. 8. pH measurement: simulated versus experimental pH. Each measurement point represents an average pH and a standard deviation value of continuous two minutes recording as described in Section 3.2.

An important issue to point out is that in this study, pH measurements were performed in water without cells or cell culture medium. It is expected, that the results with cell culture medium would differ compared to results presented in this paper because pH of culture medium is usually buffered such that the pH level is approximately 7.4 when 5% CO_2 is present. Therefore, Eq. (10) could not be used to calculate liquid pH. However, we expect that the transport of CO_2 molecules through the device is not significantly changed if water is changed to cell culture medium.

5.3. Simulation case study

The aim of the case study is to demonstrate how the developed model is used as a designing tool. In the selected simulation study, we used a time-dependent model to investigate how CO_2 is transported to the bottom of the chamber with different set-ups. The purpose here is not to fully optimize the structure, but only to demonstrate how simple geometry and set-up modifications can change the system response.

First, the model is changed to study effects of different CO_2 concentrations in the device performance. A schematic of the device is shown in Fig. 2, and the model used is shown in Fig. 4, except that now different feeding CO_2 concentrations (5–20%) were set to the top gas layer. Chamber temperature and pressure were assumed to be 24 °C and 1 atm, respectively. Initially, all the phases were assumed to be saturated to air concentration (~0.04% CO_2). Average CO_2 concentrations in the bottom of the chamber with different feeding CO_2 concentrations are presented in Fig. 9. Simulation shows that when 5% CO_2 is set to the upper gas boundary, less than 2.3% CO_2 concentration is transported to the bottom of the chamber in the first ten hours. This is not desired in cell applications, as the lack of CO_2 in cell medium results in an increase in pH. Thus, this would prevent long-term cell culturing in these types of devices (Forry and Locascio, 2011). Therefore, we investigated the required level to achieve 5% CO_2 in the bottom of the chamber by increasing the feeding CO_2 concentration from 5% up to 20%. Results indicate that by using 10% CO_2 feeding concentration, CO_2 concentration in the bottom of the chamber is approximately 4.5%, thus over 10% CO_2 feeding concentration is required to achieve the desired 5% CO_2 level.

In the model, CO_2 concentration at the outer boundaries was set to 0.04%, representing a typical amount of CO_2 in air. Next, we studied a case where the device is placed inside a conventional incubator where 5% CO_2 concentration is surrounding the device. This is modeled by changing concentration on the outer boundaries (marked as Air Concentration in Fig. 4) from 0.04% to 5%. As expected, the device performance was changed. Results from the two simulations are compared in Fig. 10. It shows how bringing CO_2 not only from the top but also from the sides of the device

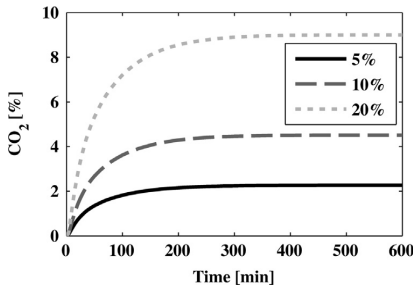

Fig. 9. Simulated average CO_2 concentration (in %) in the bottom of the chamber with different feeding concentrations.

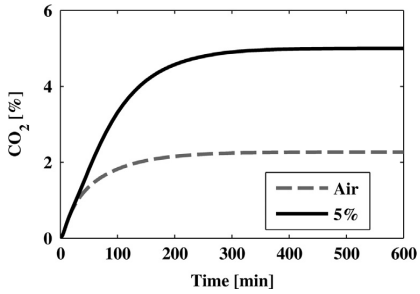

Fig. 10. Simulated average CO_2 amount (in %) in the bottom of the chamber when the CO_2 concentration at outer boundaries are set to air concentration (0.04%) and 5%.

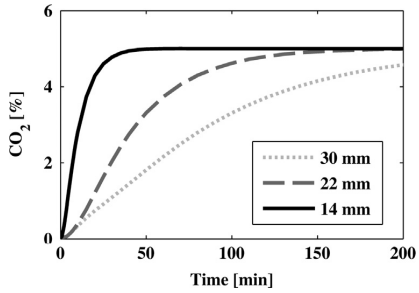

Fig. 11. Simulated average CO_2 amount (in %) in the bottom of the chamber with three different outer PDMS ring diameters. Outer boundaries are set to 5% CO_2.

guarantees the desired concentration in the bottom of the chamber.

Based on the results shown in Fig. 10, using 5% concentration at outer boundaries, over seven hours is required to achieve 5% CO_2 concentration in the bottom of the chamber. It is clear, that significantly faster response would be desirable. Therefore, we used our model to study how the diameter of the outer PDMS ring (originally 30 mm as shown in Fig. 2) affects the CO_2 transport. The results with three different outer diameters are shown in Fig. 11.

Based on simulation results shown in Fig. 11, the required time to achieve the desired 5% CO_2 concentration in the bottom of chamber is reduced from over seven hours with 30 mm to only one hour with 14 mm outer diameter, respectively. In addition, device rise time (time taken for the output to reach 90 % of steady state output value) is decreased from over 3 h with 30 mm outer diameter ring to less than 25 min when using a ring with a 14 mm outer diameter. Therefore, the simulation suggests that it is desirable to design a device where the required CO_2 concentration is brought not only from the top but also around the device. Furthermore, it is possible to achieve a faster system response by using a thinner PDMS membrane between gas and liquid. In addition, this approach can minimize or even eliminate unwanted concentration gradients, thus provide more uniform CO_2 concentration profile in the device.

6. Conclusion

Even though oxygen transport in PDMS-based microfluidic cell culture devices is extensively modeled, to the best of our knowledge, there is no comprehensive model to simulate CO_2 transport in these devices. Therefore, a new numerical model based on finite element method was developed for study CO_2 transport in PDMS-based devices. Firstly, this model was validated using experimental data from several different measurements. The results clearly demonstrated that the model predicted successfully the CO_2 concentration in different devices and geometries. Simulations allowed us for studying multiple different experimental conditions remarkably faster than that actually testing these systems, thus saving time and cost in the designing process. In addition, our aim was to demonstrate how the model and computer simulation provide a useful designing tool for microfluidic cell culture devices. For example, we studied a typical case where CO_2 is fed only from top of the device to control medium pH. Based on the simulation results, this is not necessary optimal solution for PDMS-based devices because of the gas permeable walls. Therefore, the proposed model can be effectively used to optimize the geometry of the PDMS-based microfluidic cell culture device, to study the device response with different CO_2 input concentrations, and to compare different CO_2 feeding strategies.

Nomenclature

A	parameter A used in Eq. (11) for H_2CO_3
B	parameter B used in Eq. (11) for H_2CO_3
c	molar concentration, mol m^{-3}
C	parameter C used in Eq. (11) for H_2CO_3
D	diffusion coefficient, $m^2\ s^{-1}$
F	volume force, $N\ m^{-3}$
$Flux$	flux, $mol\bullet(s\ m^3)^{-1}$
Fv	volume fraction
H	constant used to calculate kh, K
k	mass transport coefficient, $m\ s^{-1}$
Kc	thermodynamic constant for the dissociation of $[H_2CO_3]$
kh	Henry's law constant, $l\ atm\ mol^{-1}$
$Khyd$	dissociation constant of H_2CO_3 in water
Kp	partition coefficient ratio
Kw	ion product of water
$M1$	measurement set 1
$M2$	measurement set 2
n	amount of substance, mol
N	arbitrary flux expression, $mol\bullet(s\ m^2)^{-1}$
np	pressure difference of solubility, atm^{-1}
p	pressure, Pa
P	permeability coefficient, $cm^3(STP)\cdot cm\cdot(cm^2\ s\ atm)^{-1}$
R	universal gas constant, $8.31451\ J\cdot(K\ mol)^{-1}$
S	solubility, $cm^3(STP)\bullet(cm^3\ atm)^{-1}$
SD	standard deviation
$Sinf$	infinite dilution solubility, $cm^3(STP)\bullet(cm^3\ atm)^{-1}$
T	temperature, K
u	velocity field, $m\ s^{-1}$
V	volume, m^3

Greek letters

ρ	fluid density, $kg\ m^{-3}$
η	fluid dynamic viscosity, Pa s

Subscripts

$\_sat$	saturated (concentration)
ch	chamber (pressure)
CO_2	carbon dioxide (partial pressure or volume fraction)
g	gas-phase
gl	gas–liquid
gp	gas–PDMS
$H(T)$	Henry's law constant at experiment temperature T
H_0	Henry's law constant at standard ambient temperature

l	liquid-phase
lg	liquid–gas
lp	liquid–PDMS
p	solid-phase (PDMS)
pg	PDMS–gas
pl	PDMS–liquid
SATP	standard ambient temperature (298.15 K)

Acknowledgments

The authors would like to thank the financial support from the Doctoral Programme of the President of the Tampere University of Technology (TUT) and Tekes, the Finnish Funding Agency for Technology and Innovation (Decision no. 40346/11). The work was carried out within the Human Spare Parts project.

References

Adler, M., Polinkovsky, M., Gutierrez, E., Groisman, A., 2010. Generation of oxygen gradients with arbitrary shapes in a microfluidic device. Lab Chip: Miniat. Chem. Biol. 10 (3), 388–391.

Blau, A., Neumann, T., Ziegler, C., Benfenati, F., 2009. Replica-moulded polydimethylsiloxane culture vessel lids attenuate osmotic drift in long-term cell cultures. J. Biosci. 34 (1), 59–69.

Charati, S.G., Stern, S.A., 1998. Diffusion of gases in silicone polymers: molecular dynamics simulations. Macromolecules 31 (16), 5529–5535.

Chen, Y. - A., King, A.D., Shih, H. - C., Peng, C. - C., Wu, C. - Y., Liao, W. - H., Tung, Y. - C., 2011. Generation of oxygen gradients in microfluidic devices for cell culture using spatially confined chemical reactions. Lab Chip: Miniat. Chem. Biol. 11 (21), 3626–3633.

Clark, W.M., Jackson, Y.Z., Morin, M.T., Ferraro, G.P., 2011. Combining experiments and simulation of gas absorption for teaching mass transfer fundamentals: removing CO_2 from air using water and NaOH. Chem. Eng. Educ. 45 (2), 133–143.

Davidson, E.A., Trumbore, S.E., 1995. Gas diffusivity and production of CO_2 in deep soils of the eastern Amazon. Tellus Ser. B 47 B (5), 550–565.

Duffy, D.C., McDonald, J.C., Schueller, O.J.A., Whitesides, G.M., 1998. Rapid prototyping of microfluidic systems in poly(dimethylsiloxane). Anal. Chem. 70 (23), 4974–4984.

Farajzadeh, R., Barati, A., Delil, H.A., Bruining, J., Zitha, P.L.J., 2007. Mass transfer of CO_2 into water and surfactant solutions. Pet. Sci. Technol. 25 (12), 1493–1511.

Farajzadeh, R., Zitha, P.L.J., Bruining, J., 2009. Enhanced mass transfer of CO_2 into water: experiment and modeling. Ind. Eng. Chem. Res. 48 (13), 6423–6431.

Forry, S.P., Locascio, L.E., 2011. On-chip CO_2 control for microfluidic cell culture. Lab Chip: Miniat. Chem. Biol. 11 (23), 4041–4046.

Gao, Y., Sun, J., Lin, W. - H., Webb, D.J., Li, D., 2012. A compact microfluidic gradient generator using passive pumping. Microfluid. Nanofluid. 12 (6), 887–895.

Han, J., Eimer, D.A., Melaaen, M.C., 2013. Liquid phase mass transfer coefficient of carbon dioxide absorption by water droplet. Energy Procedia 37, 1728–1735.

Inamdar, N.K., Griffith, L.G., Borenstein, J.T., 2011. Transport and shear in a microfluidic membrane bilayer device for cell culture. Biomicrofluidics 5, 2.

Jawalkar, S.S., Aminabhavi, T.M., 2007. Molecular dynamics simulations to compute diffusion coefficients of gases into polydimethylsiloxane and poly{(1,5-naphthalene)-co-[1,4-durene-2,2?-bis(3,4-dicarboxyl phenyl)hexafluoropropane diimide]}. Polym. Int. 56 (7), 928–934.

Kim, L., Toh, Y. - C., Voldman, J., Yu, H., 2007. A practical guide to microfluidic perfusion culture of adherent mammalian cells. Lab Chip: Miniat. Chem. Biol. 7 (6), 681–694.

Kuo, A.C.M., 1999. Polymer Data Handbook. Oxford University Press, Oxford, UK.

Lindeberg, E., Wessel-Berg, D., 1997. Vertical convection in an aquifer column under a gas cap of CO_2. Energy Convers. Manag. 38 (Suppl. 1), S229–S234.

Liu, N., Aymonier, C., Lecoutre, C., Garrabos, Y., Marre, S., 2012. Microfluidic approach for studying CO_2 solubility in water and brine using confocal Raman spectroscopy. Chem. Phys. Lett. 551, 139–143.

Merkel, T.C., Bondar, V.I., Nagai, K., Freeman, B.D., Pinnau, I., 2000. Gas sorption, diffusion, and permeation in poly(dimethylsiloxane). J. Polym. Sci. Part B: Polym. Phys. 38 (3), 415–434.

McKeen, L.W., 2012. Permeability Properties of Plastics and Elastomers, third ed. William Andrew Applied Science, Norwich, New York, USA p. 309.

Millero, F.J., Pierrot, D., 1998. A chemical equilibrium model for natural waters. Aquat. Geochem. 4 (1), 153–199.

Ocampo-Torres, F.J., Donelan, M.A., 1994. Laboratory measurements of mass transfer of carbon dioxide and water vapour for smooth and rough flow conditions. Tellus Ser. B 46 B (1), 16–32.

Polinkovsky, M., Gutierrez, E., Levchenko, A., Groisman, A., 2009. Fine temporal control of the medium gas content and acidity and on-chip generation of series of oxygen concentrations for cell cultures. Lab Chip: Miniat. Chem. Biol. 9 (8), 1073–1084.

Robb, W.L., 1968. Thin silicone membranes – their permeation properties and some applications. Ann. NY Acad. Sci. 146 (1), 119–137.

Sander, R., 1999. Compilation of Henry's Law Constants for Inorganic and Organic Species of Potential Importance in Environmental Chemistry (Version 3). Available from: ⟨http://www.henrys-law.org⟩.

Sell, A., Fadaei, H., Kim, M., Sinton, D., 2013. Measurement of CO_2 diffusivity for carbon sequestration: a microfluidic approach for reservoir-specific analysis. Environ. Sci. Technol. 47 (1), 71–78.

Shah, V.M., Hardy, B.J., Stern, S.A., 1993. Solubility of carbon dioxide, methane, and propane in silicone polymers. Effect of polymer backbone chains. J. Polym. Sci. Part B: Polym. Phys. 31 (3), 313–317.

Shiku, H., Saito, T., Wu, C. - C., Yasukawa, T., Yokoo, M., Abe, H., Matsue, T., Yamada, H., 2006. Oxygen permeability of surface-modified poly(dimethylsiloxane) characterized by scanning electrochemical microscopy. Chem. Lett. 35 (2), 234–235.

Skolimowski, M., Nielsen, M.W., Emnéus, J., Molin, S., Taboryski, R., Sternberg, C., Dufva, M., Geschke, O., 2010. Microfluidic dissolved oxygen gradient generator biochip as a useful tool in bacterial biofilm studies. Lab Chip: Miniat. Chem. Biol. 10 (16), 2162–2169.

Stoian, A.V., Druon-Bocquet, S., Groux, H., Sanchez, J., 2012. Modeling and simulation of the mass transfer of volatile compounds in a membrane device for toxicity tests. Chem. Eng. Sci. 80, 160–172.

Takano, A., Tanaka, M., Futai, N., 2012. On-chip CO_2 incubation for pocket-sized microfluidic cell culture. Microfluid. Nanofluid. 12 (6), 907–915.

Tanimura, M., 1993. Handbook of Silicone Materials. Toray Dow Corning Silicone, Tokyo.

Terashima, I., Miyazawa, S. -I., Hanba, Y.T., 2001. Why are sun leaves thicker than shade leaves? Consideration based on analyses of CO_2 diffusion in the leaf. J. Plant Res. 114 (1113), 93–105.

Tremblay, P., Savard, M.M., Vermette, J., Paquin, R., 2006. Gas permeability, diffusivity and solubility of nitrogen, helium, methane, carbon dioxide and formaldehyde in dense polymeric membranes using a new on-line permeation apparatus. J. Membr. Sci. 282 (1–2), 245–256.

Walker, G.M., Ozers, M.S., Beebe, D.J., 2002. Insect cell culture in microfluidic channels. Biomed. Microdevices 4 (3), 161–166.

Xu, B. - Y., Hu, S. - W., Yan, X. - N., Xia, X. - H., Xu, J. - J., Chen, H. - Y., 2012. On chip steady liquid-gas phase separation for flexible generation of dissolved gas concentration gradient. Lab Chip: Miniat. Chem. Biol. 12 (7), 1281–1288.

Zahorodny-Burke, M., Nearingburg, B., Elias, A.L., 2011. Finite element analysis of oxygen transport in microfluidic cell culture devices with varying channel architectures, perfusion rates, and materials. Chem. Eng. Sci. 66 (23), 6244–6253.

Publication V

Mäki, A.-J., Ryynänen, T., Verho, J., Kreutzer, J., Lekkala, J., and Kallio, P., "Indirect Temperature Measurement and Control Method for Cell Culture Devices," *IEEE Transactions on Automation Science and Engineering*, vol. 15, no. 2, pp. 420−429, 2018.

Indirect Temperature Measurement and Control Method for Cell Culture Devices

Antti-Juhana Mäki, Tomi Ryynänen, Jarmo Verho, Joose Kreutzer, Jukka Lekkala, and Pasi Kallio, *Member, IEEE*

***Abstract*—Microfluidic devices are promising tools with which to create an environment that mimics a cell's natural microenvironment more closely than traditional macroscopic cell culture approaches. In these devices, temperature is one of the most important environmental factors to monitor and control. However, direct temperature measurement at the cell area can disturb cell growth and potentially prevent optical monitoring, and is typically difficult to implement. On the other hand, indirect measurement could overcome these challenges. Therefore, using system identification method, we have developed models to estimate the cell area temperature from external measurements without interfering cells. In order to validate the proposed models, we performed large sets of experiments. The results show that the models are able to catch the dynamics of temperature in a desired area with a high level of accuracy, which means that indirect temperature measurement using the model can be implemented in future cell culture studies. The usefulness of the model is also demonstrated by simulations that use estimated temperature as a feedback signal in a closed-loop system. We also present tuning of a model-based controller and a noise study, which shows that the tuned controller is robust for typical ambient room temperature variations.**

***Index Terms*—Control, microfluidics, numerical simulation, system identification, thermal analysis**

I. Introduction

Using microfluidic devices as a research tool for biological cell studies is attractive because of such devices have lower costs, significantly faster reaction times, and lower power and reagent consumption than conventional methods [1]. In such studies, it is crucial to properly maintain and control physiological environmental factors such as oxygen, pH, and temperature in order to support cell growth and proliferation. Microfluidic devices provide substantial benefits compared to macroscopic cell culturing solutions because they offer the possibility for more precise control of these environmental factors. In brief, their ability to mimic a cell's natural microenvironment is significantly better, which means that more realistic responses from the cultured cells can be expected. [2]-[4] The fact that these devices use much smaller volumes than conventional systems such as cell culturing in flasks makes it possible to achieve better control of environmental parameters. [5] For example, temperature control of the microenvironment of cells in microscopic devices can be much more precise, requires considerably less power, and can still provide device performance that is several times faster than macroscopic systems. Furthermore, using microsensors based on micromachining processes achieves much smaller, lighter, and easier installation and less power-consuming temperature measurements. [6]

An accurate measurement from a cell area is desirable for maintaining a physiological temperature for the cells, typically at 37°C. However, measuring temperature directly from the cell area has several drawbacks. The measurement can (negatively) affect cells and might prevent optical monitoring. Another disadvantage is that a larger cell culture chamber is needed to implement the temperature sensor inside the chamber close to cells [7]. Furthermore, in many cases it is significantly more difficult to place sensors in the region of interest than, for example, outside the cell culture chamber. Therefore, a non-destructive indirect temperature measurement is preferable compared to direct measurement from the cell area. For this reason, in many studies temperature sensors have been placed outside the cell area; for example, next to the cell culture device [8], together with the heating element [9]-[11], in the upstream and downstream of the center of the culture chamber [12], in the reference chamber [13]-[15] or on the tubing surface close to the inlet of the chip [16]. However, the problem in these cases is that usually the exact temperature on the cell area cannot be guaranteed. For example, temperature differences up to 2-3°C between the measured temperature and the temperature on the culture area have been reported [8]. One approach used for providing a uniform temperature profile is to build a complex and large insulated device where a water bath surrounds the chamber. Unfortunately, this typically leads to a longer temperature settling time during the heating phase, for example approximately 60 minutes in [15], or a minimum time of 5 min to change temperature for one degree [17].

Fluorescent labels have been used for direct temperature measurement in microfluidic devices. This method based on fluorescence intensity ratio (FIR) requires for mixing

fluorescent dyes with the working fluid. While the method typically works well with glass-based materials, it cannot be used with porous materials, such as poly(dimethylsiloxane) (PDMS), because adsorption of dye particles increases the measured fluorescence intensity, thus preventing accurate temperature measurements. Even though there are methods to overcome the adsorption problem, they still experience a decreased device performance [18]. Furthermore, error of this method is typically approximately 2.5°C at 37°C [19], which remains typically too large for cell culture studies. For example, it has been reported that the cardiomyocyte beating characteristics is altered in temperatures between 37-39°C [20].

To overcome the discussed limitations, we propose here a new method to estimate temperature in a cell culture device based on an indirect measurement signal. The idea is to estimate the temperature in the area of interest using the developed models and the temperature measured from a more suitable location. This would enable, for instance, that during cell experiments we place a temperature sensor in a suitable location outside the cell area. This prevents placing another sensor in the area where cells are located which can block optical monitoring, for example.

The method proposed in this paper is based on a system identification process. Briefly, the system identification process can be understood as a modeling process in which the model is selected on the basis of measured input and output data. The process contains three elements: data, the model, and the criteria by which the model is chosen. [21] The advantage of this approach is that the model can be identified without knowing the precise underlying physical phenomena, and can still achieve model predictions that fulfill precision requirements. [22] Therefore, we have created two system identification-based black-box models between a temperature measured outside of the device and the temperature in the cell area. These models estimate the desired temperature, and this estimated temperature in the cell area can be used as a feedback signal to a heating system to close the control loop. Simulations are provided to illustrate the closed-loop system behavior, demonstrating that the system is able to maintain temperature in the cell area using only indirect measurement data and the developed model.

The remainder of this paper is organized as follows. Section II describes details on the used experimental setup and methods. Developed models are shown in Section III. Experimental data and simulation results are presented in Section IV; the developed models are validated and their performances are compared, before closed-loop system simulations using these models are presented. Also in Section IV, a temperature controller is tuned and a noise study is performed using simulations. Conclusions and discussion of the future work are provided in Section V.

II. Experimental

This section describes the measurements required for developing and validating the identification-based temperature models. First, the experimental setup is presented, including design of a temperature measurement system and calibration of the sensors. The measurements and the models developed are also described.

A. Design and fabrication

The experimental setup was composed of three main components: (1) a heating system, (2) a temperature sensor plate, and (3) a house-made six-well PDMS chamber [23], referred to henceforth as a PDMS device. These components are shown in Fig. 1. As the heating system, we applied a commercial signal amplifier that is typically used for recording cell signaling on microelectrode array (MEA) plates. Instead of a MEA plate, we used a custom-made temperature sensor plate (TSP) to detect temperatures inside (*T_Ri*) and outside (*T_Ro*) the PDMS device, which is placed on the top of the TSP. The components are described in more detail below.

1) *Heating system*

An MEA1060-Inv amplifier system (Multi Channel Systems MCS GmbH, Germany), typically used for *in vitro* cell experiments to record electrophysiological signals and stimulate cells, was used as a platform for the temperature experiments. The heating system includes a heating element, a proportional-integral (PI) controller (Temperature Controller TC02), a temperature sensor (Pt-100, measures *T_heater* as shown in Fig. 1(b)), and contact pads for the sensor plates. It should be noted that since passive cooling is used, the ambient room temperature is always the minimum achievable temperature. For microscopic inspection, there is a hole (8 mm in diameter) in the center of the heating element. In this study, we by-passed pre-amplifiers of MEA1060-Inv, and used it only for warming the device and to provide good and stable mechanical and electrical connections between measurement electronics and TSP. During experiments, we manually changed the set-point temperature of the heating element (marked as *T_set* in Fig. 1(b)). Furthermore, the maximum heating power for the heating element was always kept at the recommended 12 W. [24], [25]

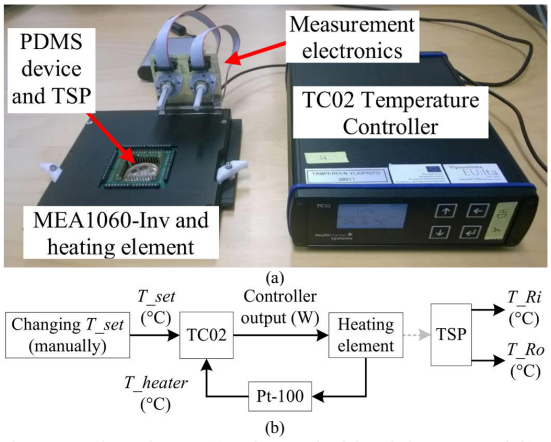

Fig. 1. Experimental setup: (a) a photograph of the whole system, and (b) a block diagram of the measurement process.

2) *Temperature sensor plate*

Fig. 2 shows the design of the TSP and the measurement electronics. A sensor layout including 14 resistors, each using a four-wire measurement, was implemented. In this paper, only

two resistors fabricated from copper, marked as *Ri* and *Ro* in Fig. 2(a), are used for measuring *T_Ri* and *T_Ro*, respectively. The layout was designed so that it can be used together with connection pins in MEA1060-Inv. In TSP, both of the used resistors (*Ri* and *Ro*) have the following dimensions: a thickness of 275 nm, a line-width of 20 µm, a total length of approximately 25.7 mm, and a total area of approximately 0.51 mm^2. The width of the tracks from the sensors to the contact pads shown in Fig. 2(a) is 100 µm. The plate was fabricated as follows: first, a custom-sized (49 mm × 49 mm × 1 mm) microscope slide (Menzel GmbH, Germany) was cleaned with acetone, isopropanol, and oxygen plasma (Vision 320 Mk II RIE, Advanced Vacuum Scandinavia AB, Sweden) before applying NR9-3000PY photoresist (Futurrex, USA) and patterning it with µPG501 maskless exposure system (Heidelberg Instruments, Germany). 275 nm of copper was e-beam evaporated 5 Å/s with a Meissner trap equipped with an Orion Series BC-3000 e-beam coater (System Control Technologies, USA) followed by a lift-off with acetone in an ultrasonic bath. The metal thickness was verified by Dektak XT contact profilometer (Bruker, USA). Next, approximately 500 nm Si_3N_4 insulator layer was deposited using Plasmalab 80+ PECVD (Oxford Instruments, UK). PR1-2000A photoresist (Futurrex, USA) was used as an etching mask when the Si_3N_4 was removed above the contact pads. Finally, the copper contact pads were polished by gently wiping them with a piece of cleanroom wipe moistened with isopropanol. An image of the fabricated plate is shown in Fig. 3.

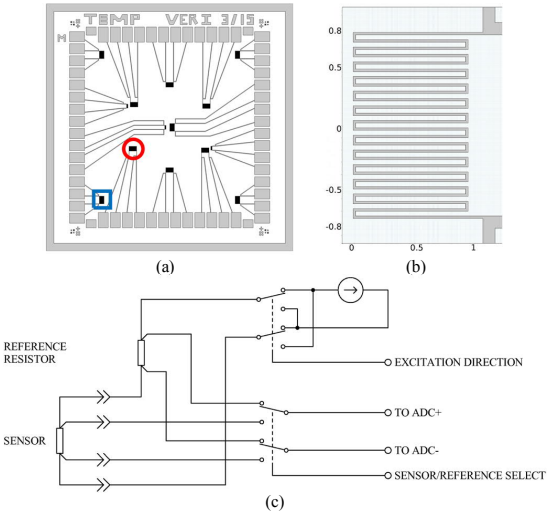

Fig. 2. Temperature sensor plate: (a) designed layout. Resistors used in this paper as temperature sensors are marked with a red circle (*Ri*) and a blue square (*Ro*). (b) A zoomed image of the used resistor (dimensions in mm), and (c) a schematic of a four-wire resistance measurement circuit.

In order to measure and log the resistances of the chosen sensors, a dual-channel four-wire resistance meter was built. In this measurement circuit, shown in Fig. 2(c), 0.59 mA constant current sources were used for sensor excitation, such that the power dissipation, and thus the heating of the actual sensing elements, were independent of the wiring resistances. However, instead of relying on the accuracy and stability of the current sources and the sensor voltage measurements, additional highly precise and stable reference resistors (PCF0805 series, TT electronics, USA) were connected in series with the sensor resistors and the current sources. A multiplexing arrangement was used to measure both the sensor resistor voltages and the reference resistor voltages using the same voltage measurement hardware. Thus, in this arrangement, the measured resistance was the ratio of the two voltages multiplied by the reference resistor's resistance. The actual voltage measurements were performed using a 24-bit A/D-converter (LTC2445, Linear Technology, USA). An additional switching arrangement was included to reverse the excitation current direction periodically so that synchronous detection could be used to remove the effects of offset voltages, noise pick-up by sensor wiring and other similar sources of error. The chosen 20.8 Hz excitation frequency was a compromise between noise rejection and ease of implementation. Next, the resistance results of 21 excitation frequency cycles were averaged, providing a measurement frequency of approximately 1 Hz. The raw measurement data were transmitted to a computer using a USB connection and stored for further processing. Initial measurements using 100Ω dummy sensors (RNC90Y series, Vishay, USA) showed 0.11 mΩ root-mean-square noise and 1.4 mΩ initial warm-up drift. Measured resistance values of the fabricated resistors were approximately 110 Ω at the room temperature. This resistance was larger than we expected based on our simulations (approximately 80 Ω) using typical electric properties of copper. Therefore, the resistivity of the fabricated copper layer was approximately 1.4 times larger than the typically reported bulk resistivity of copper (16.7 nΩ·m in [26]).

3) *PDMS device*

The PDMS device, shown in Fig. 3, was composed of two PDMS parts and a glass plate as a lid. PDMS was chosen because of its suitability for rapid prototyping, biocompatibility and optical transparency [27], [28]. The fabrication process of the similar six-well PDMS chamber was presented earlier [23]. Briefly, the device was fabricated from two PDMS parts by mixing PDMS prepolymer and curing agent (Sylgard 184, Dow Corning, USA) in a standard 10:1 ratio. The top part, which provided the walls of the containers, was punched from a bulk (thickness 6 mm) PDMS sheet using a 32 mm diameter custom-made punch. Thereafter, three 6 mm Ø holes and three 8 mm Ø holes, 8.45 mm distance from the middle of the disk, were punched through the disk for the medium reservoirs using custom-made punches. The bottom part was punched from a bulk (thickness 1 mm) PDMS sheet with the same 32 mm diameter punch. The two parts were bonded irreversibly using an oxygen plasma treatment (Vision 320 Mk II RIE, Advanced Vacuum Scandinavia AB, Sweden). The six openings for the cell cultivation areas (diameter: 3 mm) were punched through the membrane using a biopsy punch. After fabrication, the device was stored in a closed Petri dish at normal room temperature and humidity. The lid of the device, a 1-mm-thick glass plate (diameter: 32 mm), was pressed to reversibly close the system before experiments, resulting in the final PDMS

device diameter and the total height being 32 mm and 8 mm, respectively.

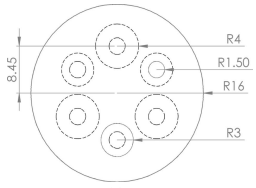

(a)

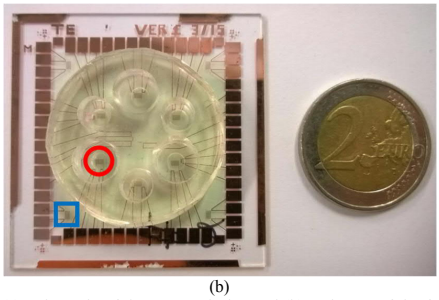

(b)

Fig. 3. (a) Schematic of the PDMS device and (b) an image of the fabricated PDMS device on the top of the TSP. Resistors used in the experiments are marked with a red circle (*Ri*) and a blue square (*Ro*).

B. Sensor calibration

Calibration of the chosen resistors was performed in a temperature-controlled oven (UN 55, Memmert GmbH, Germany). Six different temperature (*T*) points between room temperature (approximately 24°C) and 37°C were chosen. A calibrated digital thermometer (VWR 620-2000, VWR Internatiol, Belgium) was used as a reference measurement device and was placed close to the resistors. First, the temperature measurement plate was placed inside the oven. When the reference thermometer showed that the temperature was saturated, a 20-second-long resistance measurement was recorded and an average resistance (*R*) value in that temperature was calculated. When all the data points were gathered, a first-order line fitting was implemented using MATLAB (version R2015a, The MathWorks, Natick, Massachusetts, USA). A maximum difference smaller than 0.2°C and an average difference of 0.085°C between measured and fitted values were observed. Therefore, a linear calibration curve was verified to be accurate enough in the used temperature range and was used in the measurements to convert measured resistances to temperatures. The calibration results are shown in Fig. 4. The given equations are used to convert *Ri* and *Ro* to *T_Ri* and to *T_Ro*, respectively.

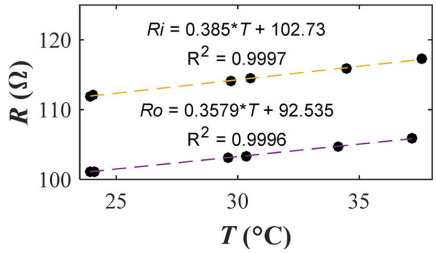

Fig. 4. Calibration curves for the selected resistors *Ri* and *Ro*: resistances as a function of temperature and their linear regression lines.

C. Measurements and developed models

In this paper, we designed three system identification-based models, as shown in Fig. 5. The first two models were developed for the indirect temperature measurement. The difference between these two models is the measured input signal that is used to estimate desired temperature. As our final goal is to implement this estimated temperature to a control-loop, and thus to be able to perform closed-loop simulations, we developed the third model. This model estimates temperature change of the heating element based on the controller output power.

We performed several measurements to estimate, validate, and test models that we had developed in this study. The entire experimental setup (see Fig. 1) was initially at room temperature and 200 µl de-ionized (DI) water was added to three 8 mm medium chambers in the PDMS device After approximately 30 s, a step change between 30°C and 40°C was manually set to the heating element using TC02. Unless otherwise stated, the recommended settings $P = 6$ W/K, and $I = 0.9$ W/(K·s) were used as the parameters of the PI temperature controller of the heating element [25].

Models 1 and 2 aim to estimate the temperature inside the PDMS device, *T_Ri,* based either on the measured heater temperature *T_heater* or the temperature measured outside the PDMS device, *T_Ro*. Therefore, the input and output signals are *T_heater* and *T_Ri* for Model 1 and *T_Ro* and *T_Ri* for Model 2. Estimation and four validation measurements were performed to identify Model 1, while the same estimation measurement and two validation measurements were used to identify Model 2.

Model 3 estimates how much the PI controller's output power (W) heats the heating element, marked as *T_heat*. A sum of this and an ambient room temperature, *T_room*, provides *T_heater*, as shown in Fig. 5. By including Model 3 in closed-loop simulations, we were able to investigate, for example, how much *T_Ri* fluctuated when measured ambient room temperature variations were included in the simulation. Furthermore, implementation of Model 3 enabled us to improve the system performance; for instance, by accelerating the system response by PI controller tuning. Only a proportional controller ($P = 1$ W/K, $I = 0$ W/(K·s)) was used when collecting the estimation data for Model 3, and the default PI controller values were used in the validation measurement.

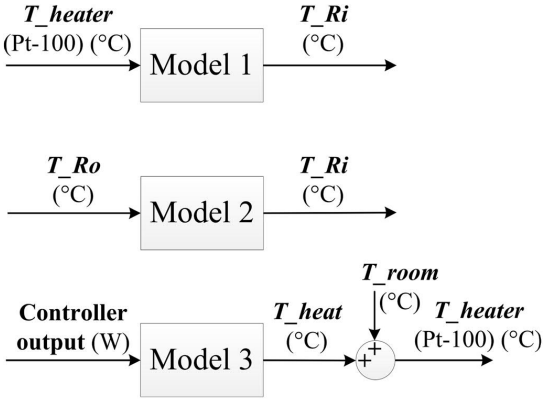

Fig. 5. Block diagrams of models.

To compare Models 1 and 2, an additional measurement was performed. The aim of this measurement was to mimic a temperature drop during visual inspection of cells, which is a routine step in cell culturing. During microscopic inspection, the TSP, together with the cells, needs to be placed from the heating system to a microscope and back after the inspection. This changes the temperature in the TSP and naturally the temperature of the cells. Therefore, we performed a test where the TSP and the PDMS device were moved from the room temperature to the pre-heated heating system. We also studied the sensitivity of Model 1 to changes in the liquid volume level in medium chambers

III. Developed Model Parameters

We used the System Identification Toolbox in MATLAB [29] to identify the models presented in Section II-C. Our objective was to estimate the system parameters using measured input and output data [30], and fit the model to the measured data regardless of the physical system; therefore, we used a black-box modeling technique. A prediction error method (PEM) was implemented to estimate the three models. This method selects models that make a prediction that is as close as possible to the true system if it was known. [21] The models were compared using a fit number, which is based on a Normalized Root Mean Square (NRMSE) criterion and can be calculated (as a percentage) using the following equation [29]:

$$fit = 100\left(1 - \frac{\|y - \hat{y}\|}{\|y - \bar{y}\|}\right) \quad (1)$$

where y, and $\hat{y}$ are the measured and estimated output, and $\bar{y}$ is the mean of y. Commonly used discrete-time state-space models include state variable vector $x(k)$, input variable vector $u(k)$, and output variable vector $y(k)$. The structure of the state-space models with three state variables used in this paper is as follows [29]:

$$\begin{aligned} x(k+1) &= Ax(k) + Bu(k) \\ y(k) &= Cx(k) + Du(k) \end{aligned} \quad (2)$$

where matrixes A, B, C, and D are state matrix, input-to-state matrix, state-to-output matrix, and feedthrough matrix, respectively. First, we tested second order state-space models and noticed that results compared to measured temperatures were not acceptable. Therefore, we chose third-order models as they provided good overall temperature estimation. Developed discrete-time models in this paper have the following form:

$$A = \begin{bmatrix} a11 & a12 & a13 \\ a21 & 0 & 0 \\ 0 & a32 & 0 \end{bmatrix}, B = \begin{bmatrix} b1 \\ 0 \\ 0 \end{bmatrix}, C^T = \begin{bmatrix} c1 \\ c2 \\ c3 \end{bmatrix}, D = d1 \quad (3)$$

The values of constants $a11$, $a12$, $a13$, $a21$, $a32$, $b1$, $c1$, $c2$, $c3$, and $d1$ in the three models are provided in Section IV-A. We estimated initial state values $x(0)$ from the first ten seconds of each measurement data using MATLAB.

IV. Simulation and Experimental Results

A. Validation of Models

Three different models were identified in this paper using the System Identification Toolbox, as described in Section III. Parameter values for the developed models are given in Table I. These state-space representations were used in simulations to compare the measured and modeled outputs. Each set of data was simulated in Simulink (The MathWorks, Inc., Natick, MA, USA) using the identified discrete state-space model with a sample time of one second.

TABLE I
MODEL PARAMETERS

Model #	*a11*	*a12*	*a13*	*a21*	*a32*	*b1*	*c1*	*c2*	*c3*	*d1*
Model 1	1.99	-0.99	0.00	1	1	2.0	0.29	-0.58	0.29	0.00
Model 2	1.99	-0.99	0.00	1	1	2.0	0.37	-0.74	0.37	0.00
Model 3	2.97	-1.47	0.48	2	1	0.5	0.15	-0.15	0.08	0.04

Model 1 was developed and validated with measurements shown in Fig. 6(a). The first measurement was used as the model estimation data, whereas four other measurements were used to study how well the model performed with different heating signals. For Model 2, we used three same experiments as for Model 1; the same estimation measurement and the first two validation measurements. The difference was that for Model 2 the measured *T_Ro* was used for the model input, as shown in Fig. 5. Measured and simulated *T_Ri* are compared in Fig. 6(b). Analysis of the results is provided in the next section.

Model 3 was identified with two measurements, as reported in Section II-C. In the estimation measurement, a proportional controller (P = 1 W/K) was used because the input signal required for Model 3 was easier to obtain when using a P-controller (error signal is simply multiplied by value of P), thus enabling a simpler identification process. In both measurements, *T_set* was first set to 37°C and, after a while (approximately five to 15 minutes), heating was switched off and the system was passively cooled down. The resulting responses of the discrete state-space model compared to the measurement data are shown in Fig. 7.

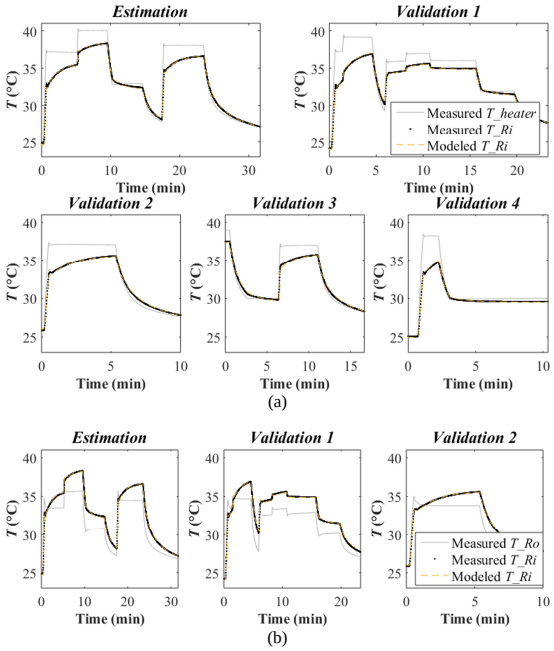

Fig. 6. Measurement and modeled data from (a) Model 1, where the input signal is *T_heater*, and (b) Model 2, where *T_Ro* is used as an input signal.

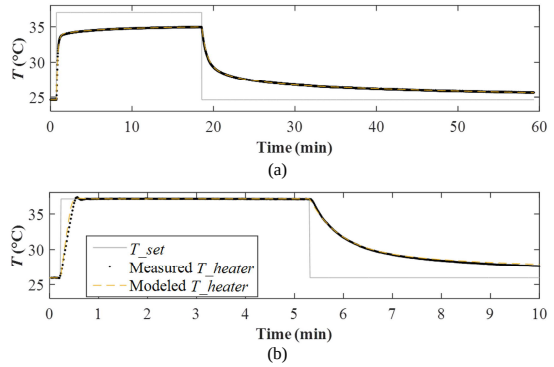

Fig. 7. Experimental and Model 3 comparison: (a) an experiment with only proportional control P = 1 W/K, and (b) an experiment with default PI controller values P = 6 W/K, and I = 0.9 W/(K·s).

As shown in Fig. 7(a), the error between the measured heater temperature and Model 3 output was negligible when proportional control was used. On the other hand, when the PI controller was implemented, Model 3 slightly overestimated the heating phase; modeled and measured rise times (time between 10% and 90% of the rise) were approximately 11 seconds and 14 seconds, respectively. However, this difference was still relatively low and insignificant compared to the response in the experiment overall, which means that the model could be used. In conclusion, based on the results reported in this section, it is clear that each of the developed models was able to estimate desired temperatures and could be used in closed-loop system simulations.

B. *Performance analysis of Model 1 and Model 2*

As Model 1 and Model 2 estimate *T_Ri*, their performance was compared. For this, two validation measurements presented in the previous section were used. The models were compared by calculating fit% (1), and average and maximum temperature differences between measured and modeled *T_Ri*, ΔT_{avg} and ΔT_{max}, respectively. The results are presented in Table II and in Fig. 8.

TABLE II
COMPARISON OF MODEL 1 AND MODEL 2 TO EXPERIMENTAL DATA

Model	**Model 1**		**Model 2**	
Measurement	*Validation 1*	*Validation 2*	*Validation 1*	*Validation 2*
Fit (%)	96.2	96.7	95.2	97.2
ΔT_{avg} (°C)	0.08	0.07	0.10	0.06
ΔT_{max} (°C)	0.52	0.44	0.69	0.27

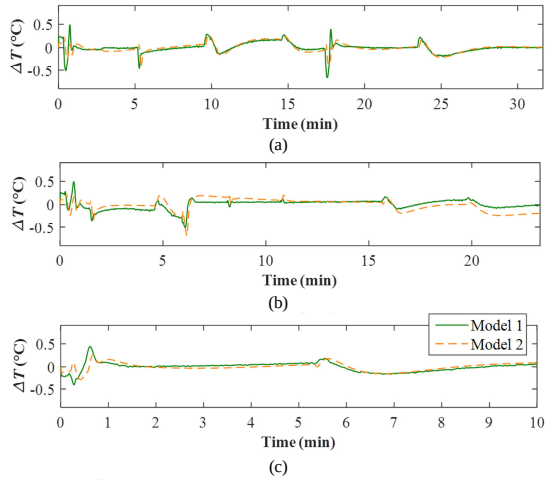

Fig. 8. Difference between measured and simulated temperatures when experiment is (a) *Estimation*, (b) *Validation 1*, and (c) *Validation 2*.

Based on the performance analysis, Model 1 performs slightly better. Therefore, it was chosen for closed-loop simulations in Section IV-D. However, Model 2 provides clear benefits in some cases, for instance, when a cooled TSP is placed on a pre-heated heating system. This is the case while moving the TSP from the heater to a microscope and back, a routine procedure performed during cell culturing. Fig. 9 shows the results of a study, where the device (at ~26.3°C) was placed on the heating system (pre-heated to 37°C) at time 30 seconds, and temperature *T_Ri* was recorded and estimated using the two models.

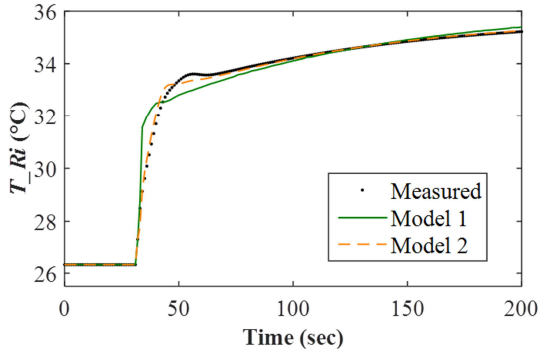

Fig. 9. Measured and simulated *T_Ri* when cooled temperature plate is brought to pre-heated heater.

In the pre-heated heater case, Model 2 estimated the output significantly more accurately than Model 1; fit% improved from 87.8% with Model 1 to 96.4% using Model 2. The reason was that now the heater and the TSP were initially in totally different temperatures, which meant that Model 1 overestimated *T_Ri* in the beginning of the measurement. To conclude, it is preferable to use Model 2 in cases where the heater and the TSP need to be separated during the study.

C. Sensitivity to liquid volume changes

Because the sensitivity of the model to environmental changes (disturbances) should be as small as possible, robustness of Model 1 to the volume in the system was studied next. The DI water volume in the three 8 mm chambers was changed ± 25% (from 200 µl to 250 µl or 150 µl). In Fig. 10 below, measurements with 250 µl and 150 µl volumes are compared to the model developed with 200 µl volume.

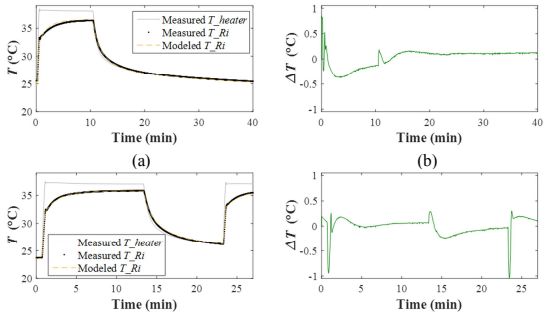

Fig. 10. Model 1 sensitivity tests for liquid volume change: (a) measurement and modeled data, (b) their difference when liquid volume is 250 µl, (c) measurement and modeled data and, (d) their difference when liquid volume is 150 µl.

As the results show, Model 1 was able to predict *T_Ri* well, which enables us to conclude that the model was not sensitive to volume changes. The difference between measurements and model predictions, ΔT_{avg} and ΔT_{max}, were now 0.14°C and 0.85°C for the liquid volume of 250 µl, and 0.11°C and 1.04°C for the liquid volume of 150 µl, respectively. It should be emphasized that reported ΔT_{max} last only very short period times, typically less than 10 seconds. One minute after the set point change, the errors are below 0.25°C in every measurement. Therefore, these results can be considered satisfactory in the planned applications, as a temperature variation of ± 0.3 to 1°C is generally still acceptable during cell cultivation [7], [14], [15], [17], [31]-[34]. As Model 1 was robust to volume changes, it is a useful temperature estimation tool in experiments with varying liquid volumes.

D. Closed-loop system simulations

The purpose of this section is to illustrate a method that can regulate *T_Ri* in the desired temperature using an indirect measurement signal. In this case, we would not need the inside sensor (*Ri*) at all. To demonstrate this approach, we present closed-loop simulations using the estimated temperature as a feedback signal by combining Models 1 and 3. First, to validate the performance of the developed closed-loop system, simulated *T_heater* was used as a feedback signal, as illustrated in Fig. 11(a). To regulate the temperature in the cell area, but not in the heater, we used *T_Ri* in the feedback loop, as shown in Fig. 11(b). Next, the performance of the default PI controller was analyzed and tuned, and a closed-loop system response with a tuned PI controller was then studied. Because of the limits of the real system (heating element power between 0 and 12 W [24]), saturation limits were also implemented in the PI controller in the model. For this reason, an integrator anti-windup design using clamping method [35] was implemented in the PI controller to stop integration when the output from the controller exceeds these saturation limits.

1) Closed-loop system validation

To validate the entire closed-loop system, shown in Fig. 11(a), Models 1 and 3 were implemented and simulated in Simulink. The same two measurements used for developing Model 3 (see Section IV-A) were also utilized here. The first measurement used proportional control (P = 1 W/K) and the second experiment was performed with the default PI controller (P = 6 W/K, and I = 0.9 W/(K·s)). Both the measurement and the simulation used *T_heater* as a feedback signal, as shown in Fig. 11(a). Modeled *T_heater* and *T_Ri* are in good agreement with the experimental data, as shown in Fig. 12; less than 0.5°C difference between the measured and modeled *T_Ri* was obtained from both experiments. This verified that a combination of Models 1 and 3 was able to estimate the desired temperature. With this control approach, the temperature in the cell area remains below the set point of 37°C.

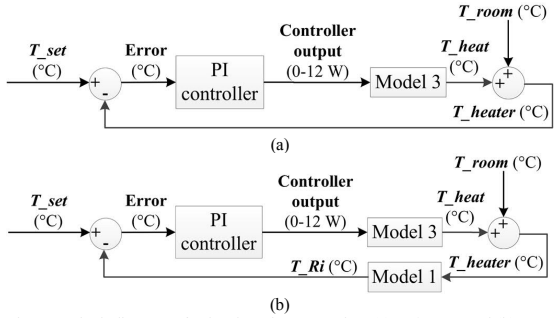

Fig. 11. Block diagram of a developed system when (a) *T_heater*, and (b) *T_Ri* is used as a feedback signal.

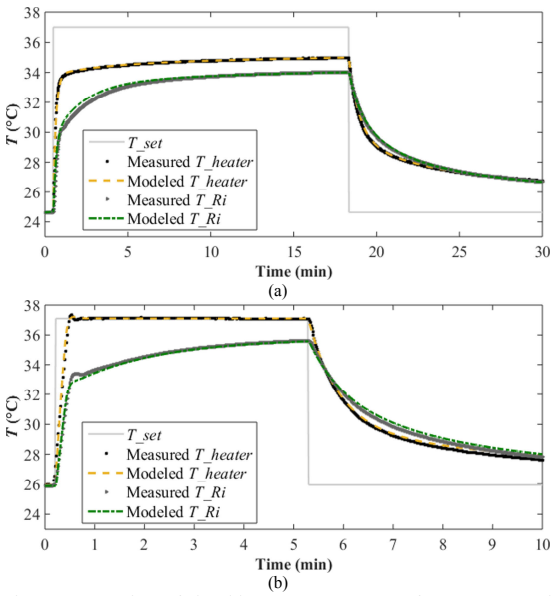

Fig. 12. Comparison of closed-loop system responses of measurement and simulation when (a) a proportional controller with P = 1 W/K, and (b) a PI controller (P = 6 W/K, and I = 0.9 W/(K·s)) was used.

2) *Controller tuning*

As stated, our goal is to develop a system that is able to control *T_Ri* using an indirect measurement signal and the developed models. Therefore, in contrast to the previous section, where we used *T_heater* as a feedback signal (Fig. 11 (a)), we first developed a model that used an output from Model 1 (*T_Ri*) as a feedback signal, as shown in Fig. 11 (b). We tuned the PI controller to improve the response of desired temperature *T_Ri*. The initial PI controller (P = 6 W/K, and I = 0.9 W/(K·s)) was simulated first and the controller parameters were then adjusted for a better performance. Our tuning goal was to decrease the overshoot and the settling time; therefore, we first increased the integral part. When an insignificant overshoot was achieved, we also increased the proportional part to accelerate the response until satisfying control results were achieved. A comparison of the system response with the default and the tuned PI (P = 9 W/K, and I = 1.2 W/(K·s)) controller is shown in Fig. 13.

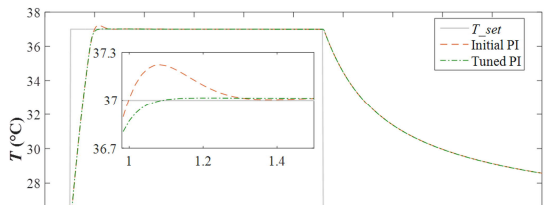

Fig. 13. Comparison of *T_Ri* with the initial (P = 6 W/K, and I = 0.9 W/(K·s)) and tuned (P = 9 W/K, and I = 1.2 W/(K·s)) controllers.

The comparison of the system responses with the default and tuned controller showed a small but improved response after tuning: overshoot was decreased from 0.22°C to a negligible 0.02°C with the same rise time of 21 seconds. The settling time (that is, the time it takes for the temperature to stay within ± 0.05°C of the set temperature 37°C) was decreased from 45 seconds to 32 seconds. To conclude, a better response with a smaller overshoot was achieved with the tuned controller.

3) *Noise study*

In the previous simulations, the ambient room temperature was approximated and was assumed to be constant. However, a more realistic situation should include temperature variations. For this reason, the developed model response with non-constant ambient room temperature was studied in this section. First, the ambient room temperature was recorded for 10 minutes, and the obtained signal was used as *T_room* value in the simulation. The measured ambient air temperature varied between 22.7°C and 22.9°C, as shown in Fig. 14.

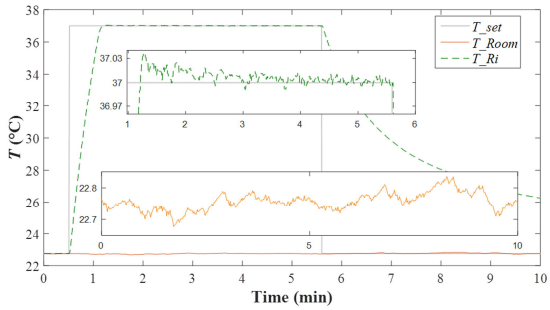

Fig. 14. Ambient air temperature variation study.

The ambient room temperature variation was included in the model and the system outcome was simulated. The results, presented in Fig. 14, showed that the controller was still able to keep *T_Ri* temperature at an acceptable level (± 0.03°C of the desired temperature of 37°C), which means that the controller is well suited for real applications where room temperature variations do exist.

V. Conclusion

This paper has presented a novel indirect temperature measurement method for microfluidic cell culture devices. The method is based on a system identification technique. The developed mathematical models make it possible to indirectly measure and control temperature in desired locations. Therefore, this method can be used as a measurement and control tool in cell culture systems without interfering cultured cells. The proposed models were validated with several measurements and we have shown that estimated temperatures correlated well with experimental results. Results also demonstrated that the developed models were capable of catching the dynamics of the system temperature. Furthermore, the models were reasonably robust to environmental changes, such as remarkably large liquid volume changes, and measured ambient air temperature variations. Finally, the parameters of the controller used were tuned using simulations and a better system response was achieved. Our future work will include

implementing the proposed identification-based closed-loop system to the cell culture experiments. To conclude, we believe that the presented method can be further extended not only to other applications in biological cell studies, but also to different areas, such as microfluidic environmental monitoring and chemical engineering.

ACKNOWLEDGMENT

The authors would like to thank Professor Matti Vilkko for helping with a system identification process, and Doctor Terho Jussila for helpful discussions related to control issues.

REFERENCES

[1] C. Yi, C. W. Li, S. Ji, and M. Yang, "Microfluidics technology for manipulation and analysis of biological cells," *Anal. Chim. Acta*, vol. 560, no. 1–2, pp. 1–23, Feb. 2006.

[2] I.-F. Yu, Y.-H. Yu, L.-Y. Chen, S.-K. Fan, H.-Y. E. Chou, and J.-T. Yang, "A portable microfluidic device for rapid diagnosis of cancer metastatic potential with programmable modules of temperature and CO2," *Lab Chip*, vol. 14, no. 18, pp. 3621–3628, 2014.

[3] E. Seker, J. H. Sung, M. L. Shuler and M. L. Yarmush, "Solving Medical Problems with BioMEMS," *IEEE Pulse*, vol. 2, no. 6, pp. 51-59, Nov.-Dec. 2011.

[4] S. Halldorsson, E. Lucumi, R. Gómez-Sjöberg, and R. M. T. Fleming, "Advantages and challenges of microfluidic cell culture in polydimethylsiloxane devices," *Biosens. Bioelectron.*, vol. 63, pp. 218–231, Jan. 2015.

[5] M. Mehling and T. Savas, "Microfluidic cell culture," *Curr. Opin. Biotechnol.*, vol. 25, pp. 95–102, Feb. 2014.

[6] R. Que and R. Zhu, "A two-dimensional flow sensor with integrated micro thermal sensing elements and a back propagation neural network," *Sensors*, vol. 14, no. 1, pp. 564–74, Jan. 2014.

[7] S. Petronis, M. Stangegaard, C. B. Christensen, and M. Dufva, "Transparent polymeric cell culture chip with integrated temperature control and uniform media perfusion," *Biotechniques*, vol. 40, no. 3, pp. 368–376, Mar. 2006.

[8] F. Abeille, F. Mittler, P. Obeid, M. Huet, F. Kermarrec, M. E. Dolega, F. Navarro, P. Pouteau, B. Icard, X. Gidrol, V. Agache, and N. Picollet-D'hahan, "Continuous microcarrier-based cell culture in a benchtop microfluidic bioreactor," *Lab Chip*, vol. 14, no. 18, pp. 3510-3518, Sep. 2014.

[9] D. Saalfrank, A. K. Konduri, S. Latifi, R. Habibey, A. Golabchi, A. V. Martiniuc, A. Knoll, S. Ingebrandt, and A. Blau, "Incubator-independent cell-culture perfusion platform for continuous long-term microelectrode array electrophysiology and time-lapse imaging," *R. Soc. Open Sci.*, vol. 2, no. 6, pp. 150031, Jun. 2015.

[10] R. Habibey, A. Golabchi, S. Latifi, F. Difato, and A. Blau, "A microchannel device tailored to laser axotomy and long-term microelectrode array electrophysiology of functional regeneration," *Lab Chip*, vol. 15, no. 24, pp. 4578–4590, Dec. 2015.

[11] J. M. Jang, J. Lee, H. Kim, N. L. Jeon, and W. Jung, "One-photon and two-photon stimulation of neurons in a microfluidic culture system," *Lab Chip*, vol. 16, no. 9, pp. 1684–1690, Apr. 2016.

[12] J. Vukasinovic, D. K. Cullen, M. C. LaPlaca, and A. Glezer, "A microperfused incubator for tissue mimetic 3D cultures," *Biomed. Microdevices*, vol. 11, no. 6, pp. 1155–1165, Dec. 2009.

[13] E. Biffi, G. Regalia, D. Ghezzi, R. De Ceglia, A. Menegon, G. Ferrigno, G. B. Fiore, and A. Pedrocchi, "A novel environmental chamber for neuronal network multisite recordings," *Biotechnol. Bioeng.*, vol. 109, no. 10, pp. 2553–2566, Oct. 2012.

[14] J.-L. Lin, M. -H. Wu, C.-Y. Kuo, K.-D. Lee, and Y.-L. Shen, "Application of indium tin oxide (ITO)-based microheater chip with uniform thermal distribution for perfusion cell culture outside a cell incubator," *Biomed. Microdevices*, vol. 12, no. 3, pp. 389–398, Jun. 2010.

[15] G. Regalia, E. Biffi, S. Achilli, G. Ferrigno, A. Menegon, and A. Pedrocchi, "Development of a bench-top device for parallel climate-controlled recordings of neuronal cultures activity with microelectrode arrays," *Biotechnol. Bioeng.*, vol. 113, no. 2, pp. 403–413, Feb. 2016.

[16] K. I.-K. Wang, Z. Salcic, J. Yeh, J. Akagi, F. Zhu, C. J. Hall, K. E. Crosier, P. S. Crosier, and D. Wlodkowic, "Toward embedded laboratory automation for smart Lab-on-a-Chip embryo arrays," *Biosens. Bioelectron.*, vol. 48, pp. 188–196, Oct. 2013.

[17] R. Reig, M. Mattia, A. Compte, C. Belmonte, and M. V Sanchez-Vives, "Temperature modulation of slow and fast cortical rhythms," *J. Neurophysiol.*, vol. 103, no. 3, pp. 1253–1261, Mar. 2010.

[18] T. Glawdel, Z. Almutairi, S. Wang, and C. Ren, "Photobleaching absorbed Rhodamine B to improve temperature measurements in PDMS microchannels," *Lab Chip*, vol. 9, no. 1, pp. 171–174, Jan. 2009.

[19] D. Ross, M. Gaitan, and L. E. Locascio, "Temperature Measurement in Microfluidic Systems Using a Temperature-Dependent Fluorescent Dye," *Anal. Chem.*, vol. 73, no. 17, pp. 4117–4123, Sep. 2001.

[20] E. Laurila, A. Ahola, J. Hyttinen, and K. Aalto-Setälä, "Methods for in vitro functional analysis of iPSC derived cardiomyocytes - Special focus on analyzing the mechanical beating behavior," *Biochim. Biophys. Acta - Mol. Cell Res.*, vol. 1863, no. 7, pp. 1864–1872, 2016.

[21] L. Ljung, "Convergence analysis of parametric identification methods," *IEEE Trans. Automat. Contr.*, vol. 23, no. 5, pp. 770-783, Oct. 1978.

[22] A. Sebastian and D. Wiesmann, "Modeling and experimental identification of silicon microheater dynamics: A systems approach," *J. Microelectromechanical Syst.*, vol. 17, no. 4, pp. 911–920, Aug. 2008.

[23] J. Kreutzer, L. Ylä-Outinen, P. Kärnä, T. Kaarela, J. Mikkonen, H. Skottman, S. Narkilahti, and P. Kallio, "Structured PDMS Chambers for Enhanced Human Neuronal Cell Activity on MEA Platforms," *J. Bionic Eng.*, vol. 9, no. 1, pp. 1–10, Mar. 2012.

[24] Multi Channel Systems MCS GmbH, Germany, "MEA Amplifier for Inverse Microscopes Manual," 2012. [Online]. Available: http://www.multichannelsystems.com/sites/multichannelsystems.com/files/documents/ manuals/MEA1060-Inv_Manual.pdf

[25] Multi Channel Systems MCS GmbH, Germany, "Temperature Controller TC01/02 Manual," 2015. [Online]. Available: http://www.multichannelsystems.com/sites/multichannelsystems.com/files/documents/manuals/TC01- TC02_Manual_RevG.pdf

[26] J. W. Gardner, "Thermoresistor," in *Microsensors: Principles and applications*, 1st ed., New York: Wiley, 1994, p. 94.

[27] D. C. Duffy, J. C. McDonald, O. J. Schueller, and G. M. Whitesides, "Rapid Prototyping of Microfluidic Systems in Poly(dimethylsiloxane)," *Anal. Chem.*, vol. 70, no. 23, pp. 4974–4984, Dec. 1998.

[28] G. Velve-Casquillas, M. Le Berre, M. Piel, and P. T. Tran, "Microfluidic tools for cell biological research," *Nano Today*, vol. 5, no. 1, pp. 28–47, Feb. 2010.

[29] L. Ljung, "System Identification Toolbox User's Guide." MathWorks Inc., USA, p. 904, 2015. [Online]. Available: http://www.mathworks.com/help/pdf_doc/ident/ident.pdf

[30] A.W.M.J. Van Schijndel, "Integrated Heat Air and Moisture Modeling and Simulation," Ph.D. dissertation, Dept. Built. Environment, Eindhoven Univ. of Tech., Eindhoven, The Netherlands, 2007.

[31] J. -Y. Cheng, M. -H. Yen, C. -T. Kuo, and T. -H. Young, "A transparent cell-culture microchamber with a variably controlled concentration gradient generator and flow field rectifier," *Biomicrofluidics*, vol. 2, no. 2, pp. 024105, Jun. 2008.

[32] L. Lin, S.-S. Wang, M.-H. Wu, and C.-C. Oh-Yang, "Development of an integrated microfluidic perfusion cell culture system for real-time microscopic observation of biological cells," *Sensors*, vol. 11, no. 9, pp. 8395–8411, Aug. 2011.

[33] M. Riley, "Instrumentation and Process Control," in *Cell Culture Technology for Pharmaceutical and Cell-Based Therapies*, CRC Press, 2005, pp. 249–297.

[34] H. Witte, M. Stubenrauch, U. Fröber, R. Fischer, D. Voges, and M. Hoffmann, "Integration of 3-D cell cultures in fluidic microsystems for biological screenings," *Eng. Life Sci.*, vol. 11, no. 2, pp. 140–147, Apr. 2011.

[35] G. V. Kaigala, J. Jiang, C. J. Backhouse, and H. J. Marquez, "System design and modeling of a time-varying, nonlinear temperature controller for microfluidics," *IEEE Trans. Control Syst. Technol.*, vol. 18, no. 2, pp. 521–530, Mar. 2010.

Antti-Juhana Mäki received the M.S. degree in automation engineering from Tampere University of Technology (TUT), Tampere, Finland, in 2010. Since 2011, he has been working toward the Ph.D. degree in automation engineering at the Department of Automation Science and Engineering, TUT, under the supervision of Prof. Kallio. Currently, he is working on the development of control system for automated human stem cell environment. His research interests include control engineering, modeling, microfluidics and autonomous systems for cell engineering.

Tomi Ryynänen received his M.Sc. degree in applied physics from University of Jyväskylä in 2000. After a couple of years in optoelectronics and software industry he has been working at Tampere University of Technology since 2005. In addition to doctoral studies he has been responsible for developing the cleanroom laboratories and microfabrication activities at the department of Automation Science and Engineering. His research is focused on microelectrode arrays (MEAs) and other microsensors for cell culturing applications. He has authored or co-authored over 20 international journal or conference papers and one patent application.

Jarmo Verho is working as a research assistant at the Department of Automation Science and Engineering, Tampere University of Technology. He is specialized in low-noise electronics design and embedded systems. His other research interests include sensor networks, radio networks, short range inductive links and capacitive sensing techniques.

Joose Kreutzer received the B.Eng. degree in Electrical and Electronic Engineering from University of Sunderland, Sunderland, England, in 2003 and M.Sc. degree in Electrical Engineering from Tampere University of Technology (TUT), Tampere, Finland, in 2005. In 2001, he joined first time the Department of Automation Science and Engineering, TUT, where he is currently a Research Scientist in the Micro- and Nanosystems Research Group. His research interests include microfabrication, microfluidics, and their applications in biomedical engineering, especially for stem cell based bioengineering.

Jukka Lekkala received the M.Sc. degree in electronics and the D.Sc. (Tech.) degree in biomedical engineering from the Tampere University of Technology (TUT), Tampere, Finland, in 1979 and 1984, respectively. Since 1991, he has been a Docent of bioelectronics at the University of Oulu, Oulu, Finland, and a Docent of biomedical engineering at TUT. Currently, he is a Professor of Automation Technology with the Department of Automation Science and Engineering, TUT. His research activities include sensors, measurement systems, and biosensing.

Pasi J. Kallio (M'03) received his M.S. degree in electrical engineering and D.Tech. degree in automation engineering from Tampere University of Technology (TUT), Tampere, Finland in 1994 and in 2002, respectively. Since 2008, he has been a Professor of Automation Engineering at TUT. He is an author of more than 120 articles, and more than 10 patent applications. His research interests include microrobotics, microfluidics and their automation in cell and tissue engineering, medical diagnostics and soft material testing applications. Prof. Kallio is a member of several societies in IEEE, he was the chair of IEEE Finland Section 2012-2013, and was a recipient of the Finnish Automation Society Award in 2009.

Publication VI

Unpublished manuscript

Mäki, A.-J., Verho, J., Kreutzer, J., Ryynänen, T., Rajan, D., Pekkanen-Mattila, M., Ahola, A., Hyttinen, J., Aalto-Setälä, K., Lekkala, J., and Kallio, P., "A Portable Microscale Cell Culture System with Indirect Temperature Control."

A peer-reviewed version of this manuscript has been published online in *SLAS TECHNOLOGY: Translating Life Sciences Innovation* on 3.5.2018.

- Mäki, A.-J., Verho, J., Kreutzer, J., Ryynänen, T., Rajan, D., Pekkanen-Mattila, M.,Ahola, A., Hyttinen, J., Aalto-Setälä, K., Lekkala, J., and Kallio, P., "A Portable Microscale Cell Culture System with Indirect Temperature Control," *SLAS TECHNOLOGY: Translating Life Sciences Innovation*, May 3, 2018, DOI: 10.1177/2472630318768710.

A Portable Microscale Cell Culture System with Indirect Temperature Control

Antti-Juhana Mäki[†*], Jarmo Verho[†], Joose Kreutzer[†], Tomi Ryynänen[†], Dhanesh Rajan[†], Mari Pekkanen-Mattila[‡], Antti Ahola[†], Jari Hyttinen[†], Katriina Aalto-Setälä[‡], Jukka Lekkala[†], and Pasi Kallio[†]

[†]BioMediTech Institute and Faculty of Biomedical Sciences and Engineering
Tampere University of Technology, Korkeakoulunkatu 3, 33720 Tampere, Finland

[‡]BioMediTech, Faculty of Medicine and Life Sciences
University of Tampere, Lääkärinkatu 1, 33014 Tampere, Finland

[*]Email: antti-juhana.maki@tut.fi

Abstract

Objective: **Physiologically relevant temperature is essential for successful long-term cell culturing *in vitro*. The present practices in cell laboratories cause undesired changes in temperature. Unfortunately, temperature measurement in the cell culture is not straightforward, as direct measurement can interfere with the cell cultures or prevent optical microscopy. Furthermore, the assessment of dynamic temperature variations in the cell culture area is challenging with typically used methods. To overcome these challenges, we integrated a microscale cell culture environment together with live-cell imaging and precise indirect temperature control.** ***Methods:*** **We developed a mathematical model for estimating temperature at the cell area using a system identification approach. The developed model and remote temperature measurement were combined in our system to control the cell culture temperature.** ***Results:*** **The system maintained temperature at $37\ ^{\circ}\mathrm{C}\ \pm 0.3\ ^{\circ}\mathrm{C}$ for over four days. The culture temperature was precisely controlled during temperature transients. Furthermore, we presented possibility to move the culture while maintaining temperature. Finally, we demonstrated successful long-term (over four days) culturing of human induced stem cell-derived cardiomyocytes, and analyzed their beating rates in different temperatures.** ***Conclusion:*** **The developed system can be used for long-term cell culturing *in vitro* and temperature-dependent cell behavior studies.** ***Significance:*** **We showed that changes in temperature alter the behavior of cells. Thus, proper temperature is required to provide an**

optimal environment for cells. With the developed method, better temperature control is obtained without implementing a sensor to the culture area, improving reliability of *in vitro* cell studies.

Index Terms

feedback control, microfluidics, modeling, system identification, temperature, cell culture, cardiomyocytes

I. Introduction

Cell culturing *in vitro* is one of the cornerstones of modern biology. It is known that mammalian cells are very sensitive to the properties of their environment; for example, temperature, oxygen concentration, and pH. Therefore, it is crucial to provide a proper microenvironment for successful long-term cell culturing. Furthermore, a physiologically relevant cell culture environment is key for achieving the reliable data required in, for example, stem cell-based disease modeling studies [1]–[4].

Compared to traditional cell culturing methods using bioreactors, the use of microfabricated microfluidic systems is a fascinating approach due to its better control over the physiological culturing conditions [5]–[7]. Other advantages of using these devices are their faster response times, lower fabrication costs and power requirements, and smaller reagent consumptions. Even though several commercial microbioreactors exist, they are typically expensive, do not provide uniform environmental conditions for cells, and have only a limited number of designs available [8]–[10]. Therefore, there have been many studies on creating cost-effective microbioreactors for cell cultures *in vitro*. Typically, these devices are fabricated from polydimethysiloxane (PDMS) using a so-called soft lithography technique, due to this being an easy, fast, and cheap fabrication method. Furthermore, because PDMS is transparent, bio-compatible, and gas permeable, it is well suited for cell culturing systems [4], [5], [11]–[15].

Proper temperature is one of the most important microenvironmental parameters in cell culturing as the intrinsic properties of fluids and cells are affected by temperature variations. Hence, temperature should be controlled carefully to provide optimal circumstances for cell growth and differentiation [16]. It has also been showed that temperature has a strong effect on the emergent network activity and membrane potential at the cellular level [17]. Precise control of the environmental temperature was required for microrheology measurements; activity of the cells slowed and they became softer when the temperature was lowered [18]. However, several

methods and techniques used in cell culturing cause temperature variations in the culture. For example cardiac cell research can include such analysis methods as patch clamp, multielectrode arrays, fluorescent imaging, impedance assays, video microscopy, and live-cell imaging, to name a few [19]. During the culturing, it is common to move the cultured cells from one measuring instrument to another; for instance, from the incubator to live-cell imaging and analysis. Unfortunately, without a proper portable heating system, these movements of the cell cultures can create significant temperature variations to the cultures, resulting unwanted stimulations to the cells. Therefore, a control system that can minimize temperature variations is very important to successfully culture cells *in vitro*. Another potential source of temperature variations is the change of the cell culture medium which is typically performed every 2-3 days. If the medium is not carefully pre-conditioned, the medium change can cause a temperature stress to the cells.

A typical problem with the accurate temperature control is that it requires a precise temperature measurement from the cell culture. This direct measurement brings some challenges; for example, the sensor can interfere with the cells and prevent microscopic inspection. In many cases, it is significantly more difficult to place sensors in the region of interest than elsewhere; for example, outside the cell culture chamber. Also, if one is placing the temperature sensor inside the chamber, close to the cells, a larger cell culture chamber is often required [2], [8]. Therefore, an indirect temperature measurement is preferable to a direct measurement in the cell area.

Temperature sensors have been placed outside the chamber in many cell culture studies. Solutions include placing sensors together with the heating element [20]–[22], close to the inlet of the chip or the culture chamber [23], [24], downstream and upstream from the culture chamber [25], or next to the device [26]. However, none of these cases can guarantee the exact temperature of the cell area. Typically reported temperature differences between the measured temperature and the temperature of the cell area have been up to $2\ ^{\circ}\mathrm{C} - 3\ ^{\circ}\mathrm{C}$ [26]. This difference is typically too large for cell culture studies [17], [19], [27]. For instance, it was shown that temperature variation between $37\ ^{\circ}\mathrm{C}$ and $39\ ^{\circ}\mathrm{C}$ altered cardiomyocyte beating characteristics [19]. Also, the firing rate during up states in the cortical network was modulated when temperatures varied between $36\ ^{\circ}\mathrm{C}$ and $38\ ^{\circ}\mathrm{C}$ [17]. To minimize temperature variations, a sensor has been placed in a separate reference chamber [28]–[30]; however, this method requires more space as one chamber is used only for temperature logging. An extremely good insulating system is required for precise temperature control using only a sensor placed outside. One

demonstrated solution to provide a uniform temperature profile has been to build a complex, large insulated device in which a water bath surrounds the chamber [17], [30], [31]. Unfortunately, this typically leads to a longer temperature settling time during the heating phase, such as approximately 60 min [30], or a minimum time of 5 min to change temperature by $1\ ^{\circ}\mathrm{C}$ [17]. Moreover, with this technique it can still be difficult to avoid excessively large temperature differences between the central part of the chamber and the surrounding parts [8].

Optical methods have also been proposed for measuring temperature locally. Measurement from the cell culture area using infrared cameras is challenging because the PDMS material shields these signals [32]. Fluorescent labels have been used for direct temperature measurement in microfluidic devices [33]–[35]. With this method, fluorescent dyes are mixed into the working fluid. Although the method can be used with glass-based materials, it presents significant problems with porous materials, such as PDMS, because accurate temperature measurements are prevented by the adsorption of dye particles into the material. Some solutions have been demonstrated to overcome this adsorption problem [33]; however, measurement performance is still reduced. Furthermore, typical temperature measurement precision (approximately $2.5\ ^{\circ}\mathrm{C}$ at $37\ ^{\circ}\mathrm{C}$ [34]) is not sufficient for cell culture studies.

To solve the aforementioned problems, we previously developed an indirect temperature measurement method to monitor temperature in the cell culture area using a system identification approach [36]. We used a commercial heater and a cell culture device made in-house, and showed that our method precisely estimated the cell culture temperature. We also presented a simulation study to demonstrate how the method could be used for temperature control purposes. In this study, we extend this approach by integrating an indirect temperature control into a developed cell culture system. The control method combines an external temperature measurement and a numerical model to calculate an approximation of the temperature at the desired location. This estimate is then compared to the desired temperature set-point, thereby providing an indirect measurement and control method for the cell culture temperature. Furthermore, the developed heating system is portable; it has a power source to maintain the desired temperature for over one hour for applications where transportation of the system is needed. The system is also suitable for a long-term microscopy and cell imaging, as it includes a gas supply for the maintenance of the proper carbon dioxide (CO_2) and oxygen (O_2) concentrations in the cell culture media.

In this study, we show how accurate temperature in the cell culture area can be performed without disturbing the cells or preventing imaging. First, we demonstrate how the heating

system compensates disturbances arising from the ambient room temperature variations. We also illustrate how the cell culture temperature is restored to the desired level after opening of the device or liquid change. Finally, we present a successful long-term cell culturing and perform a temperature-stress study of the beating cardiomyocytes with the developed system.

The rest of the paper is organized as follows. Section II explains the working principle of the system, describes details on the experimental setups used, and presents developed models. Experimental data and control results are given in Section III; the models are developed, their performances are compared to the measured data, and finally experiments with the developed closed-loop control system are presented. In Section IV, the results from this paper are discussed, before providing conclusions and possible future work in Section V.

II. METHODS

The main components of the cell culture system are an indium tin oxide plate (ITO) as a heating element (70 mm $\times$ 70 mm $\times$ 0.7 mm boro-aluminosilicate glass plate from UniversityWafer, Inc., Boston, MA, USA, with a resistivity of 8-10 Ω/sq), a temperature sensor plate (TSP) made in-house on a glass substrate (49 mm $\times$ 49 mm $\times$ 1 mm from Gerhard Menzel GmbH, Braunschweig, Germany), and a cell culture device made in-house, which is presented in Section II-B5. A Pt100 sensor attached on the ITO plate was used to measure the heater temperature (T_{ITO}), and spring contacts were used to connect the TSP pads as shown in Fig. 1.

A. Working Principle of Indirect Temperature Control

The temperature estimate is made using a mathematical model and a temperature measurement; the measured temperature outside the desired location ($T_{outside}$) is supplied as an input to the mathematical model. The model calculates an estimate of the cell culture temperature, $T_{cell-est}$, which is compared to the set-point temperature, T_{set}, to complete the closed-loop feedback system, as shown in Fig. 2. In the control system, we implemented a proportional-integral-derivative (PID) controller. In this study, however, we used only a proportional-integral (PI) controller with such parameters ($P = 1.7, I = 0.03$) that the control system had a close-to-critically damped response with only a minor overshoot. Output power of the controller was limited to values between 0 and 2 W. As there was no active cooling included, the temperature decrease was entirely based on heat dissipation. For the model development and analysis, we also monitored the ambient room temperature T_{room}, and the real cell culture temperature, T_{cell}, and

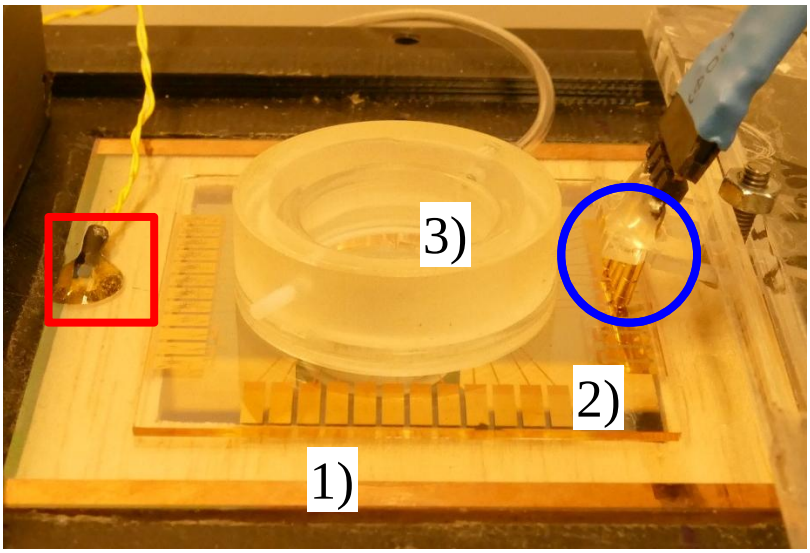

Fig. 1: The main components of the cell culture system: 1) ITO heater, 2) temperature sensor plate (TSP), and 3) cell culture device. The Pt100 sensor measuring temperature of the ITO heater (T_{ITO}) is marked with a red rectangle, and connection springs that are used to read resistances of TSP sensors is highlighted with a blue circle.

compared the estimated and measured cell culture temperatures. It should be emphasized that T_{cell} was only used to verify the temperature estimate results, and was never used for temperature control purposes.

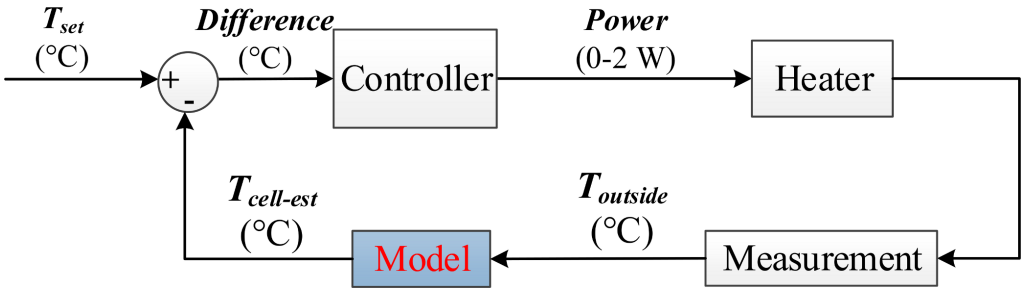

Fig. 2: Working principle of indirect cell culture temperature measurement and control.

We developed two temperature estimation models for different purposes. The difference be-

tween the models was that different measurements were used as $T_{outside}$. Model 1 was based on measured ITO heater temperature using a Pt100 sensor glued onto the ITO plate (see Fig. 1). For this reason, $T_{outside}$ is marked as T_{ITO} in Model 1. In Model 2, we measured the temperature using the TSP with a sensor located close to the cell culture area; therefore, $T_{outside}$ is marked as T_{TSP} in Model 2. The TSP will be presented in more detail in Section II-B4.

The sensor required in Model 1 is easy to place, and the location of the sensor can be chosen rather freely. Also, there is no need to use the sensor plate for temperature control. However, as this method does not measure temperature inside the cell culture chamber, the estimated temperature is less accurate. Therefore, Model 1 is not capable of fully compensating for temperature changes inside the chamber caused by, for instance, variations in the ambient room temperature. Furthermore, this approach does not work properly in cases when the temperature inside the culture chamber changes without changes in T_{ITO}. The example of opening the device and changing the liquid inside the chamber is presented in Section III-E.

For the aforementioned reasons, we also developed Model 2, which measures the temperature inside the chamber close to the cell culture area and therefore can better predict temperature changes in the cell area. Model 2 can compensate for the residual thermal disruptions caused by microscopy imaging and changes in the ambient temperature, both of which the cell culture temperature. The drawbacks of this approach are that the sensor is typically more fragile, the sensor is more difficult to position as it needs to be in a certain location, and the sensor plate is required. To summarize, the two models have their preferred applications depending on the requirements.

B. Experimental Setups

1) Overall Device Description: The measurement system included the ITO heater, TSP, PDMS-based cell culture device, gas supply, illumination and optics, frames and stages, and electronics required for temperature measurement and control. We designed all the custom-made mechanical parts in the setup using SolidWorks (SolidWorks, Cambridge, UK). The setup is shown in Fig. 3, which also presents the schematic of the optical setup used in the cell culture experiments. We used a motorized z-stage and on-line inverted microscopy together with white LED illumination, a Nikon 20x objective, and a monochrome camera (BFLY-U3-13S2M-CS, Point Grey Research, Inc., Richmond, BC, Canada) for imaging the cells. Illumination and

video recording were controlled using a MATLAB-interface made in-house (MathWorks, Inc., Natick, MA, USA).

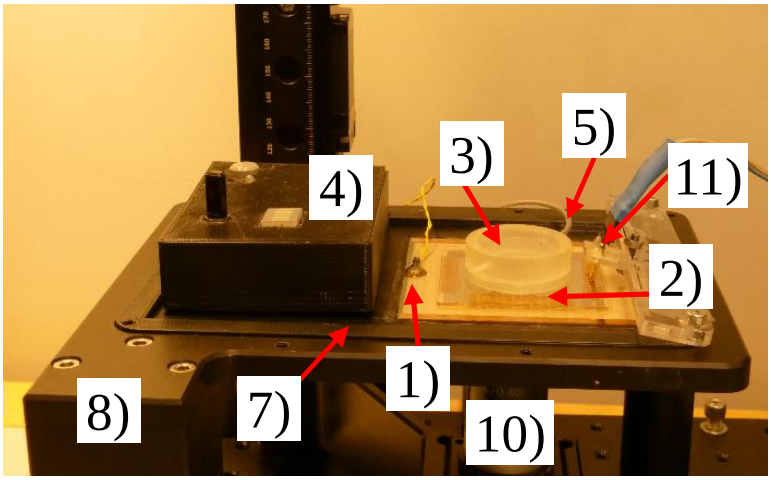

(a)

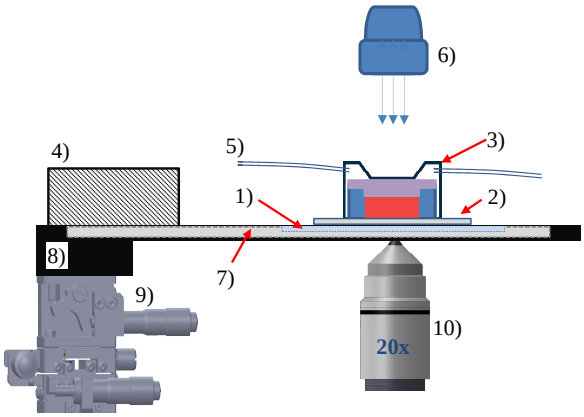

(b)

Fig. 3: System overview: (a) Experimental setup and (b) the schematic of the optical system tailored for cell culturing. Numbers show the 1) ITO heater, 2) TSP, 3) cell culture device, 4) electronics, 5) gas supply, 6) illumination unit using white LED, 7) ITO frame, 8) aluminum frame 9) xyz-stage, 10) motorized inverted microscopy with 20x objective, and 11) connection pins to read resistances of TSP sensors.

Electronic circuits made in-house, shown in Fig. 4, were designed to connect the TSP and the

heater to the computer and to the external power source, unless a battery mode was used. The main design criteria for the heating controller electronics were low cost, relatively small size, capability of running the model-based temperature control algorithms and the aforementioned option for short-term (but over an hour) battery operation. The basic measurement principle is shown in Fig. 4. Due to the low and relatively constant wiring resistances, a simple two-wire ratiometric measurement method was chosen. The rather low reference voltage (200 mV) was a compromise between sensor self-heating, resolution, noise, and the sensitivity to thermoelectric offset voltages. A 16 bit resolution of the chosen analog-to-digital converter (ADC; LTC2486 from Analog Devices, Inc., Norwood, MA, USA) results in approximately 12 mK temperature measurement resolution, which is more than sufficient and below the noise floor. Two identical 100 Ω reference resistors were used to cancel the effects of the input current of the ADC.

While the diagram shows only one channel, the device has two channels, allowing the user to easily switch between two different temperature feedback locations. This simple arrangement designed for the Pt100 sensor was not sufficient for the TSP sensors, as they can have significant and varying wiring and contact resistances. To support the use of the TSP sensors, the circuit was modified to a four-wire measurement compensating for the wiring resistance, as shown in Fig. 4. This arrangement requires the use of both ADC channels, allowing only one four-wire measurement instead of two two-wire measurements.

In order to minimize the interference caused by the heating element current, a constant current drive scheme (shown in Fig. 4) was adopted. While a fully linear driver would have been preferable from the interference point of view, the excessive power dissipation of such a driver made it impractical. Thus, a switching voltage-controlled current source (LT3477, Analog Devices, Inc.) was chosen. The control input comes in the form of a pulse-width modulated signal, which is filtered to produce a direct current (DC) control signal for the current source. While it can be assumed that some of the switching noise of the current source reaches the ITO plate, at least the amplitude is low and the frequency is well above typical biosignal frequencies.

The actual controller was built around an 8 bit microcontroller (ATMega328, Microchip Technology, Inc., Chandler, AZ, USA), which measures the sensor resistances, performs simple gain and offset compensations, and converts the results to temperatures either by using a standard (second-order) Pt100 equation or by using a user-entered, first-degree polynomial fit. This temperature reading is supplied either directly or through the identified model to the PID controller. The temperature measurement, identification and PID controller run at a 5 Hz frequency. The

device has a USB port for configuring the device and for logging temperature data. It also contains a 3.1 Ah, 18650-size lithium ion battery and an associated USB charger (LTC4098, Analog Devices, Inc.).

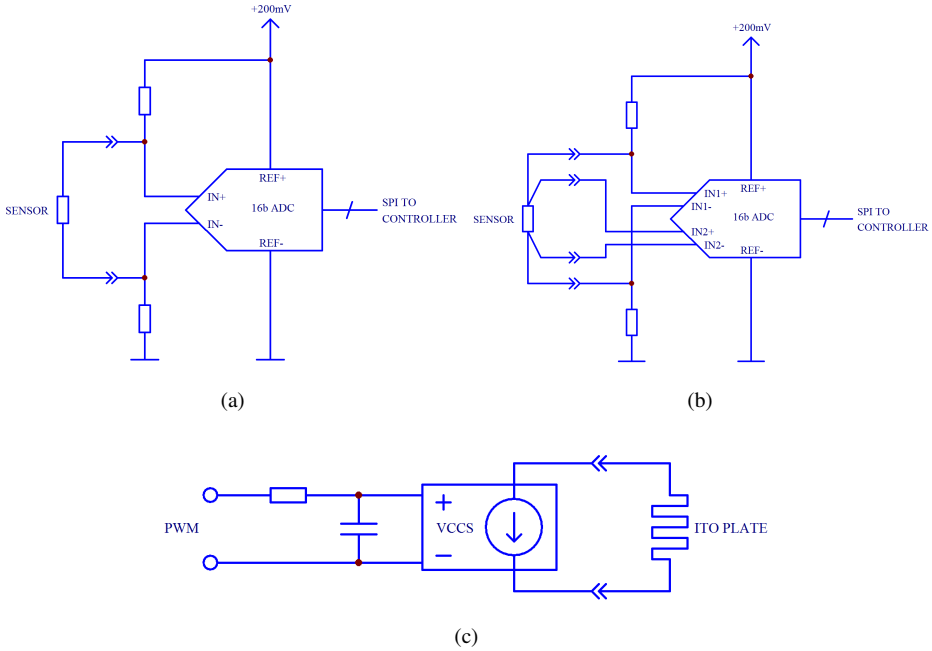

Fig. 4: Schematics of electronic circuits made in-house: (a) two-wire and (b) four-wire resistance measurement circuits for TSP, and (c) a heater control circuit.

2) Heating System: A heating system that provides a uniform temperature profile is very important for successful indirect temperature control and long-term cell culture studies. Also, optical microscopy is typically required in these studies. Therefore, an ITO plate was chosen as a heating element, as it is not only electrically conductive but also optically transparent; Joule heating can be generated when electrical power is applied, and at the same time, ITO does not obscure illumination. To supply the heating current uniformly over the ITO plate, and thus to equalize temperature on top of the plate, we e-beam evaporated copper pads 900 nm thick (3.5 mm $\times$ 70 mm) onto the ends of the ITO plate. These copper lines are shown in Fig. 1. Furthermore, a 300 nm silicon nitride (Si_3N_4) insulator layer was deposited over the ITO using a plasma-enhanced chemical vapor deposition (PECVD) process.

3) Frame Design: A proper design of the frame (see Fig. 3, item 7) for the ITO plate is important for achieving a uniform temperature profile. We tested three different frame structures. Frame 1, manufactured by Saloteam Oy (Salo, Finland), was made of aluminum and mounted to an xyz-stage, as shown in Fig. 3. However, non-uniform heating with large temperature gradients on the plate was observed with this frame. Therefore, we designed and 3D-printed a frame with the same dimensions but made from polylactic acid (PLA); this was Frame 2. We observed remarkably reduced temperature gradients with Frame 2. To further improve the uniformity of the temperature, a 3-mm-thick plate of thermally insulated material (Finnfoam plate from Finnfoam Oy, Salo, Finland) was added between the ITO glass and Frame 2. The outer dimensions of the insulation plate were 70 mm $\times$ 70 mm with a hole of approximately 62 mm $\times$ 62 mm in the middle. The combination of Frame 2 and the thermal insulator layer was Frame 3.

To compare the temperature distribution in the different frames, we used thermal imaging. As direct thermal imaging of the ITO glass was not possible due to reflection issues, we placed a glass plate (50 mm $\times$ 50 mm $\times$ 0.5 mm) on top of the ITO plate and only considered temperature measurement on this area of the plate (marked with a dashed red rectangle in Fig 5). We first heated the ITO plate such that T_{ITO} (based on the sensor reading as presented in Fig. 1) was stabilized to $34\ ^{\circ}\mathrm{C}$. Then, thermal images were taken from the three frames using a Flir One thermal camera (FLIR Systems, Inc., Seattle, WA, USA). Temperature profiles in this region were further analyzed, and the results are summarized in Table I.

It is clear from Table I that temperature gradients were significantly reduced with Frame 3 when compared to Frame 1. This is an important result, as temperature differences inside the cell culture chamber should be minimized to provide as equal temperature as possible for every cell in the culture. In the table, T_{min}, T_{max}, T_{avg}, $T_{max} - T_{min}$, and $T_{max} - T_{avg}$ are minimum, maximum, and average measured temperatures, difference between the maximum and minimum temperatures, and difference between the maximum and average temperatures, respectively.

4) Temperature Sensor Plate: We designed the TSP for logging the temperature inside the cell culture chamber. The TSP was built on a glass plate and included 14 identical temperature sensors as shown in Fig. 6. The TSP consisted of resistors, tracks, and contact pads patterned using photolithography on an e-beam evaporated copper layer that was 275 nm thick. The resistor and the track area were electrically insulated using 100 nm silicon dioxide (SiO_2) and 500 nm Si_3N_4 layers with PECVD. The width of the resistor line in the design was 20 µm.

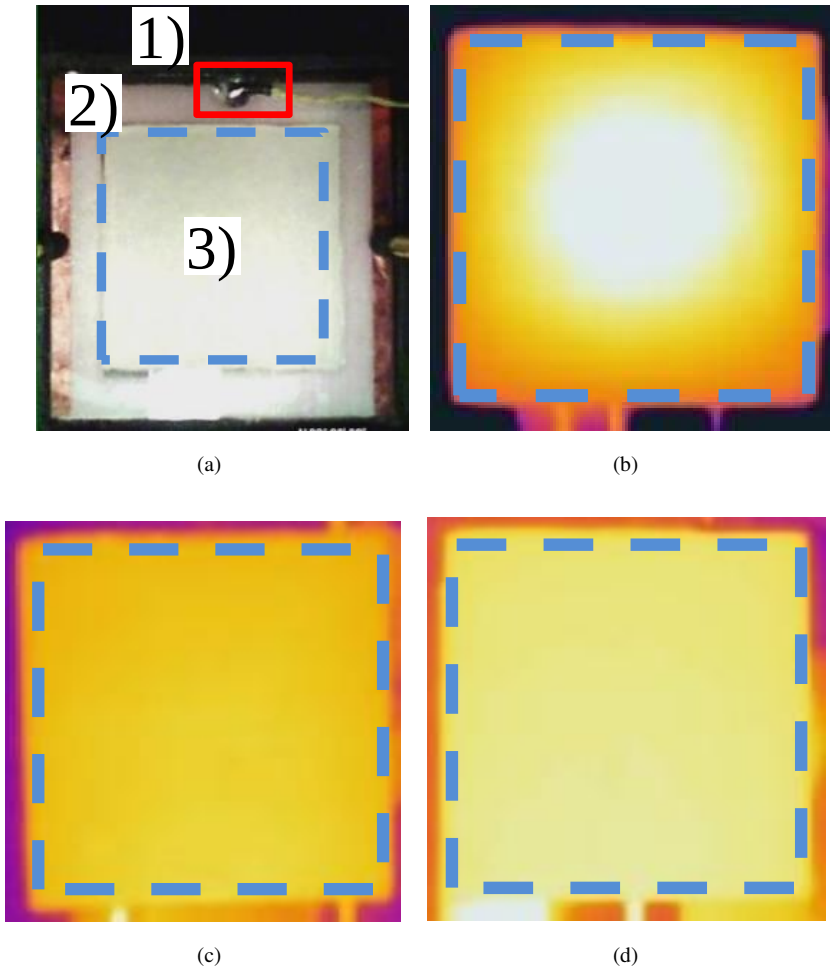

Fig. 5: Temperature distribution in different frames: (a) An image during thermal imaging, with 1) an ITO frame, 2) an ITO heater, and 3) a taped glass plate. The red rectangle highlights a sensor that is used to measure the ITO heater temperature (stabilized to 37 °C), and the blue dashed rectangle on the plate marks the area that is analyzed from each thermal image. Thermal images are analyzed for (b) Frame 1, (c) Frame 2, and (d) Frame 3.

Temperature sensors were calibrated in a temperature-controlled oven by measuring their electrical resistances using a four-wire method at several different temperatures from 24 °C to 38 °C

TABLE I: Analysis of thermal images. Here, T_{min}, T_{max}, and T_{avg}, are minimum, maximum, and average measured temperatures on the dashed region in Fig. 5, respectively, and $T_{max} - T_{min}$ and $T_{max} - T_{avg}$ are the difference between the maximum and minimum temperatures and the difference between the maximum and average temperatures, respectively. Values are presented in degrees Celsius.

	Frame 1	Frame 2	Frame 3
T_{min}	33.0	34.3	37.3
T_{max}	40.6	38.2	39.3
T_{avg}	37.6	37.0	38.9
$T_{max} - T_{min}$	7.6	3.9	2.0
$T_{max} - T_{avg}$	2.9	1.2	0.4

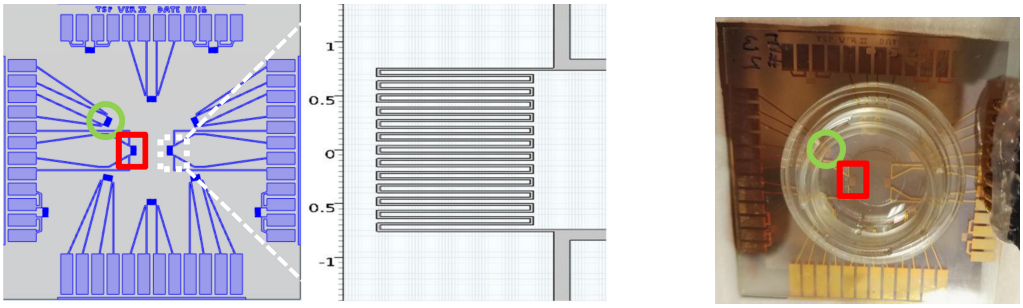

(a) (b)

Fig. 6: Temperature logging: (a) designed sensor layout and (b) temperature sensor plate together with cell culture chamber. The resistors marked with a red square and a green circle are used to measure T_{cell} and T_{TSP}, respectively.

after the plate was thermally stabilized. A typical room-temperature resistance was approximately 105 Ω. As a good linear relationship between electrical resistance and temperature was obtained, a linear interpolation was used to estimate temperature from the measured resistance.

5) Cell Culture: The cell culture device, its fabrication procedure, and the main working principle has been described previously [37]–[39]. Therefore, we present here only the main steps and details of study-specific differences. The design goals were to enable on-line microscopy (therefore, transparent materials were chosen) and to keep the cell culture alive for several days in the cell culture device.

The structure of the cell culture device is shown in Fig. 7 with three main parts: a cell culture chamber, a lid, and a cover. The lid was machined from polycarbonate (PC; Saloteam Oy), and the cover was 3D printed (from Shapeways, Eindhoven, the Netherlands). The lid made a watertight seal on the culture chamber and prevented contamination from entering the chamber. This setup also enabled the use of a dry gas supply without significant evaporation of the culture medium. The same technology has been shown to keep the cell culture alive and vivid outside an incubator over three days [37].

The cell culture chamber was cast in-house from PDMS (Sylgard 184 from Dow Corning, Auburn, MI, USA) using standard soft-lithography techniques. Cells were plated on a round opening area (diameter of 10 mm) that was punched in the bottom of the chamber. During experiments, the cell culture chamber was reversibly bonded on the TSP and filled with 1 mL deionized water or cell culture medium before the chamber lid was closed. With the cover placed atop the lid and the chamber, the gas supply pipe was connected to provide the desired gas environment (CO_2 and O_2 concentrations) inside the chamber. In cell culture studies, we used a motorized inverted microscopy system, made in-house, for cell imaging. A similar system was presented previously [39]; however, the current system used inverted microscopy as presented in Fig. 3(b).

Cardiomyocytes (CMs) derived from the human induced pluripotent stem (iPS) cell line UTA.04602WT, as described previously [40], were cultured in the developed system. For sterilization, TSPs were immersed in 70% ethanol and dried under sterilized conditions. The PDMS culture chamber was mounted directly on the sterilized TSP. The beating iPS-CM aggregates were plated at the bottom of the cell chamber, which was first hydrophilized with fetal bovine serum (FBS) and then coated with 0.1% gelatin type A (Sigma-Aldrich, St Louis, MO, USA). The iPS-CMs were cultured in KO-DMEM-media (Lonza, Basel, Switzerland) with 20% FBS (Lonza), 1% non-essential amino acids (Cambrex, East Rutherford, NJ, USA), 2 mM Glutamax (Invitrogen, Carlsbad, CA, USA), and 50 U/mL penicillin/streptomycin (Lonza). For each cell chamber, three to four iPS-CM aggregates were plated. After plating, the iPS-CM aggregates were cultured for 24 h in an incubator (37 °C, 5% CO_2, 19% O_2, 76% N_2) for initial stabilization. After that, the device was removed from the incubator, closed with the lid and the cover, and placed on the preheated (37 °C) ITO heater. The gas environment around the cell culture area was created by flushing with a gas mixture (5% CO_2, 19% O_2, 76% N_2) at a constant flow rate of 5 mL/min.

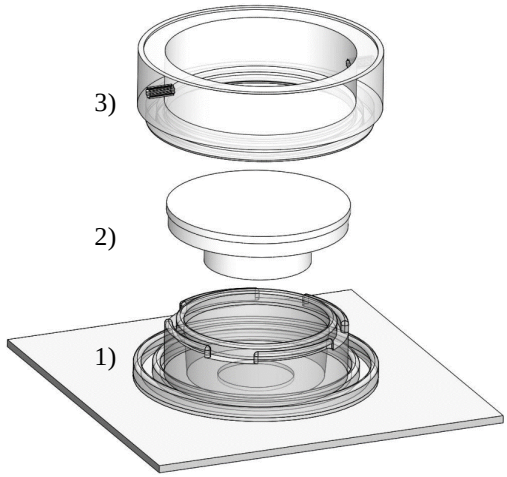

Fig. 7: Expanded view of the cell culture device: 1) the cell culture chamber, 2) the lid, and 3) the cover. The assembled device on the TSP was presented in Fig. 1.

C. Temperature Estimation Models

In the study, we used a so-called black-box technique to develop models using only input and output data, regardless of the physical system [41]. We used a prediction error [42] that made a prediction that is as close as possible to the true system if it was known, to develop our models. We compared models using a fit number, which is based on a normalized root-mean-square error criterion. It can be calculated (as a percentage) using the following equation [43]:

$$fit = 100\left(1 - \frac{|y - \hat{y}|}{|y - \bar{y}|}\right) \tag{1}$$

where y and $\hat{y}$ are the measured and the estimated output, respectively, and $\bar{y}$ is the mean of y. We used input and output data, presented in Section III-A, to develop the models. We used MATLAB R2016a together with System Identification Toolbox (the MathWorks, Inc.) to derive discrete-time, state-space models. The models include a state variable vector $x(k)$, an input variable vector $u(k)$, and an output variable vector $y(k)$, and have the following structure [43]:

$$\begin{aligned} x(k+1) &= Ax(k) + Bu(k) \\ y(k) &= Cx(k) + Du(k) \end{aligned} \tag{2}$$

where matrices A, B, C, and D represent a state matrix, an input-to-state matrix, a state-to-output matrix, and a feed-through matrix, respectively. These matrices are defined using measurements, presented in Section III-A, for both models that are developed in this study.

III. Results

A. Model Development

To develop the temperature estimation models, temperature was controlled using $T_{outside}$. In the experiments, the set-point temperature was randomly changed, and both $T_{outside}$ and T_{cell} were recorded. Fig. 8(a) presents measurements for T_{ITO} (Model 1) and Fig. 8(b) for T_{TSP} (Model 2). Initially, we tested second-order state-space models, but the accuracies of the temperature

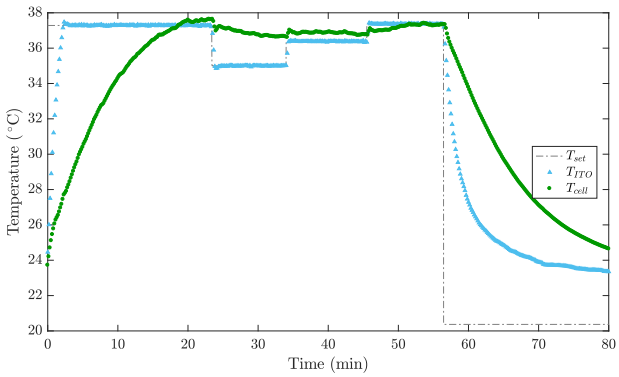

(a)

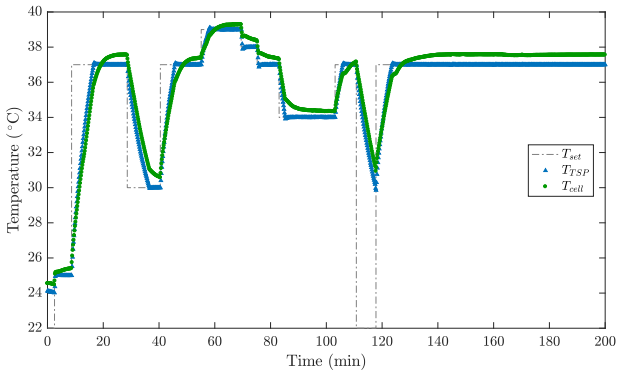

(b)

Fig. 8: Model estimation experiments for (a) Model 1 and (b) Model 2.

estimates were not acceptable, especially for Model 1; therefore, we used third-order models, with the following structure:

$$A = \begin{bmatrix} a_{11} & a_{12} & 0 \\ 1 & 0 & 0 \\ 0 & 1 & 0 \end{bmatrix}, B = \begin{bmatrix} 1 \\ 0 \\ 0 \end{bmatrix}$$
$$C = \begin{bmatrix} c_1 & c_2 & c_3 \end{bmatrix}, D = 0 \tag{3}$$

As the coefficient of the matrix D was zero, no direct or linear relation between the input and the output was detected. We determined constants a_{11}, a_{12}, c_1, c_2, and c_3 using $T_{outside}$ and T_{cell} as input and output signals, respectively, in the system identification process. We obtained the following parameter values for the models:

- Model 1: $a_{11} = 1.99$, $a_{12} = -0.99$, $c_1 = 0.33$, $c_2 = -0.66$, and $c_3 = 0.33$
- Model 2: $a_{11} = 1.19$, $a_{12} = -0.20$, $c_1 = 0.52$, $c_2 = 0.58$, and $c_3 = 0.06$

The measured temperatures and the temperatures simulated using the models with the aforementioned parameter values are compared in Fig. 9. The calculated model fit numbers were 94.2% and 94.8% for Model 1 and Model 2, respectively, indicating that the models are suitable for estimating the cell culture temperature. In the following sections, we use the outputs of these models – the estimated temperatures ($T_{cell-est}$) – for controlling the cell culture temperature. In the next section, we will illustrate the usefulness of the indirect control system.

B. Comparison of Different Control Strategies to Maintain Constant Temperature

In this section, we compare different controller strategies to illustrate the benefits of the developed indirect control system. As mentioned, to obtain optimal cell growth and differentiation, precisely controlled temperature is required. Therefore, the purpose of this experiment is to show, how variations in the ambient room (marked as T_{room}), if improper control system is used, will produce undesired changes in the cell culture temperature (T_{cell}, see Fig. 6). We implemented one open-loop and three closed-loop control systems to compare different controller strategies.

In the open-loop system, a constant heating power was used; no measurement was used to control the heating power. Three closed-loop systems used the same PI controller ($P = 1.7, I = 0.03$), but the control was based on different signals in the feedback loop (see Fig. 2). In the first closed-loop system, temperature was regulated based on the measured temperature of the ITO heater T_{ITO} (from the glued Pt100 sensor, marked with a red rectangle in Fig. 1), whereas the

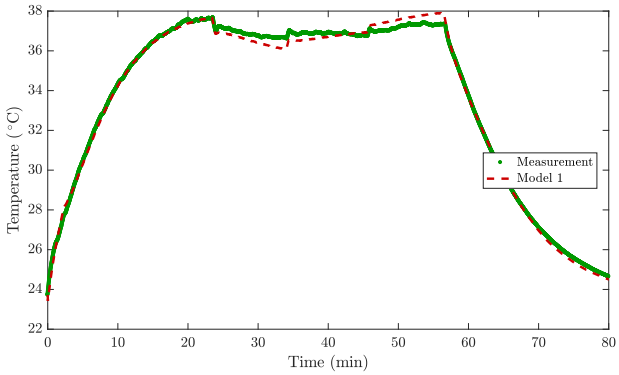

(a)

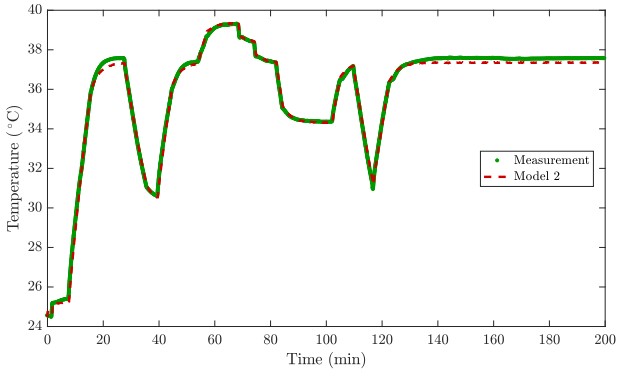

(b)

Fig. 9: Comparison of measured cell culture temperature and model estimate using (a) Model 1 and (b) Model 2

control of the second closed-loop system was based on T_{TSP}. This sensor is located on the TSP, and is marked with a green circle in Fig. 6. The last control system used the combination of T_{TSP} and Model 2; the control was based on the estimated $T_{cell-est}$ as explained in Section II-A.

In the begin of each experiment, we added 1 mL deionized water to the cell culture chamber and pre-heated the system so that T_{cell} was close to 37 °C before we started to record T_{room} and T_{cell} for 15 hours. Results using different controller strategies are shown in Fig. 10. Implemented controller strategies provided significantly different results during the 15-hour long experiments as shown in Fig. 10. Maximum variations in the measured T_{cell} during the experiment were 1.5 °C (open-loop), 1.0 °C (closed-loop using T_{ITO}), and 0.2 °C for the closed-loop systems

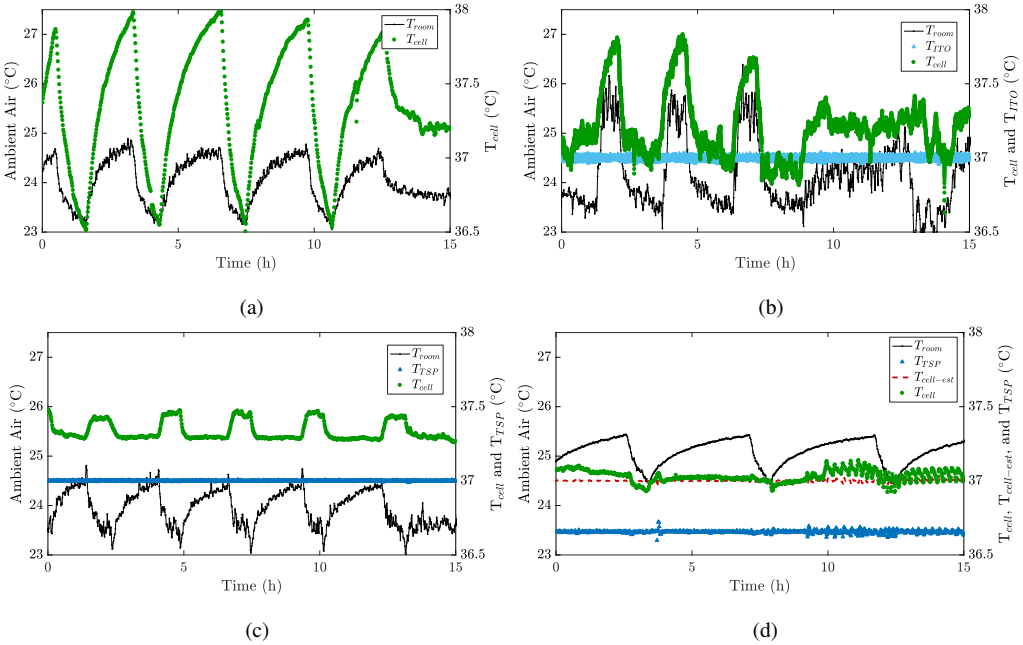

Fig. 10: Comparison of the different temperature controller strategies: (a) open-loop system with a constant power, closed-loop systems where temperature is controlled by (b) T_{ITO}, (c) T_{TSP}, and (d) $T_{cell-est}$ calculated by T_{TSP} and Model 2.

using T_{TSP} or $T_{cell-est}$. Clearly, use of the open-loop system or the first closed-loop control system based on T_{ITO} are not recommended for the temperature control as changes in the ambient air had high impact on T_{cell}. Remarkable better control results were achieved by using T_{TSP} or the developed model-based temperature estimation as a feedback signal.

C. Precise Long-Term Temperature Control

Indirect control system provided very good results as presented in the previous section. Therefore, a long-term temperature control test was performed. The purpose is to support long-term cell growth by precisely regulating the cell culture temperature was to 37 °C. We again added 1 mL deionized water to the cell culture chamber and calculated $T_{cell-est}$ using Model 2 and the measured T_{TSP}. We also monitored the real temperature, T_{cell}, and compared the estimated and measured cell culture temperatures. During the experiment, the measured ambient

room temperature, T_{room}, varied between 22.6 °C and 25.9 °C. The results in Fig. 11 show that the cell culture temperature was maintained at 37 °C ± 0.3 °C for more than four days. It should be noted that a sensor connection problem at approximately 10 h created artificial noise in the measured signal shown in Fig. 11(a). The system capability of compensating the environmental variations is demonstrated in Fig. 11(b). It presents how T_{room} and the controller output power are changed during the experiment. As mentioned, there are some variations in T_{cell} (37 °C ± 0.3 °C); however, these are more related to model inaccuracies and simplifications than environmental variations, which are compensated by the controller. This is presented in Fig. 11(b); when the measured temperature indicates a temperature change in the ambient air (T_{room}), the controller modifies the heating power to compensate this change. It should be emphasized that T_{room} was only used for the monitoring purposes, not directly in the control loop.

D. Controlled Temperature Steps

A precisely controllable cell culture temperature provides several opportunities for temperature-dependent cell behavior studies. For example, it enables one to characterize transient behaviors of the cell cultures during the heating and cooling phases around the physiological temperature [2], or to determine a temperature threshold for the activation of ion channels [44]. Our system can precisely monitor and control cell culture temperature, T_{cell}, during temperature transients, as shown here. The results using Model 1 are shown in Fig. 12. The average temperature estimation error was 0.40 °C. Fig. 13 demonstrates temperature control in temperature transients using Model 2. As this model uses T_{TSP} for $T_{cell-est}$, a temperature measured at a location that is much closer to the desired area than the location used in Model 1, the results are significantly better; the average temperature estimation error dropped to 0.21 °C. As these estimation errors are acceptable in cell culture studies, these results demonstrate that the proposed system can be used in temperature-dependent cell tests, such as cell stress tests.

E. Disturbance Compensation During Liquid Changes

The performance of the temperature control system during a liquid change, mimicking the change of a cell culture medium, is demonstrated using Model 2. Here, we changed liquid that was heated to 37 °C with liquid stabilized to the ambient air temperature (approximately 24 °C). This is an extreme case; in a typical application, the fresh cell cultivation liquid would be close to 37 °C. Therefore, this demonstration overemphasizes the effect of a typical temperature drop,

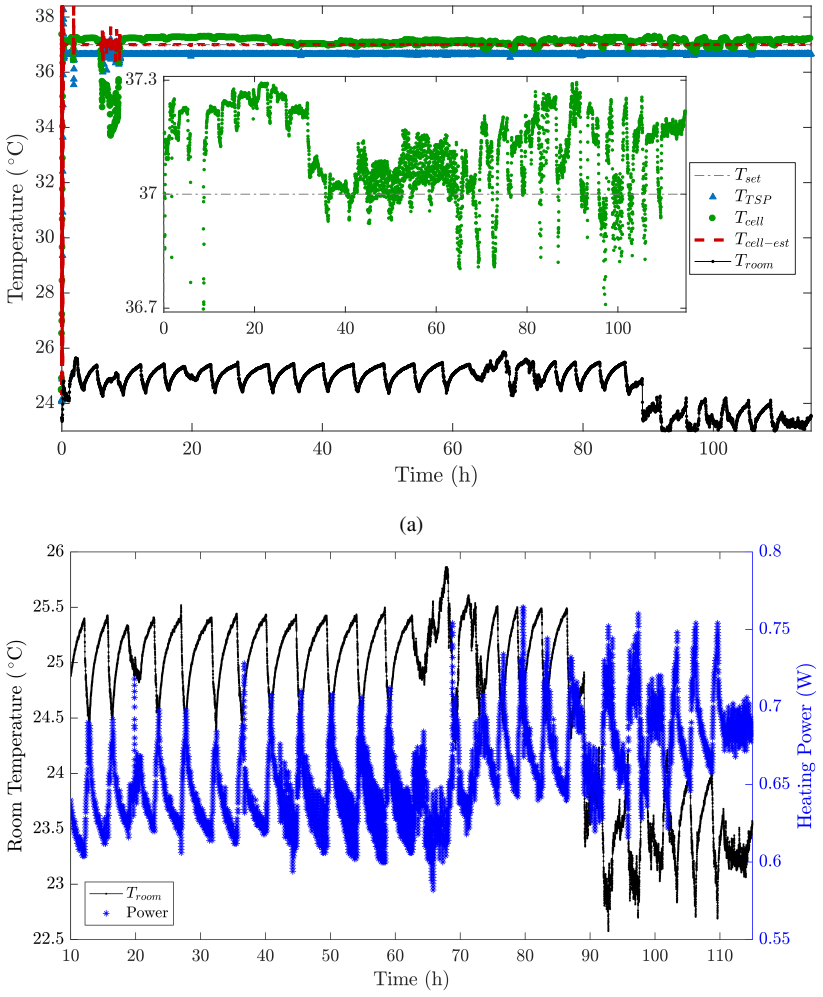

Fig. 11: Long-term temperature control using Model 2: (a) measured temperatures (inset presents only T_{cell}) and (b) controller output (blue asterisk) to compensate the ambient air (black line) changes.

thus imposing a higher requirement on the heating system. As Model 1 uses the temperature measured from the ITO heater, the result with Model 1 would not have been satisfactory, because the temperature mainly changes inside the cell culture chamber.

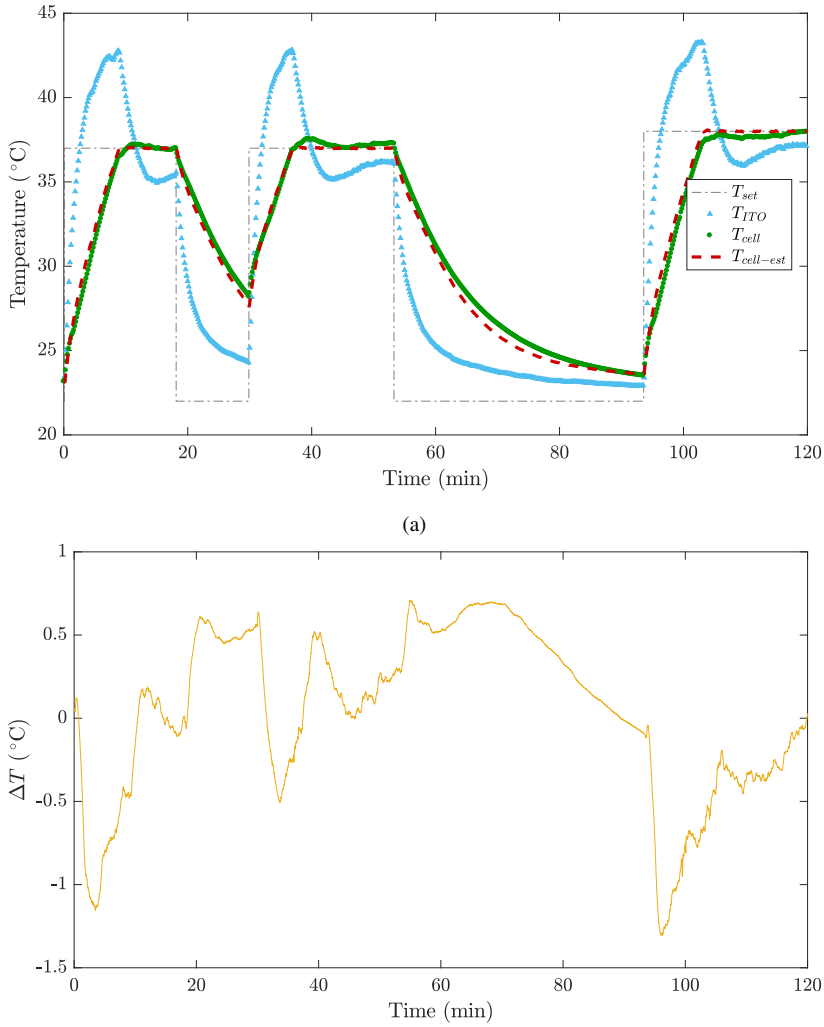

Fig. 12: Transient temperature control using Model 1: (a) results and (b) difference between measured T_{cell} and $T_{cell-est}$.

The results in Fig. 14 show how the system compensates for the temperature drop caused by changes in the liquid temperature. Fig. 14(b) shows a time period just before and after the second liquid change; the cell culture chamber was opened at approximately 53 min. Because of this, the temperature in the cell culture area started to drop, as measured by the sensor (T_{TSP}),

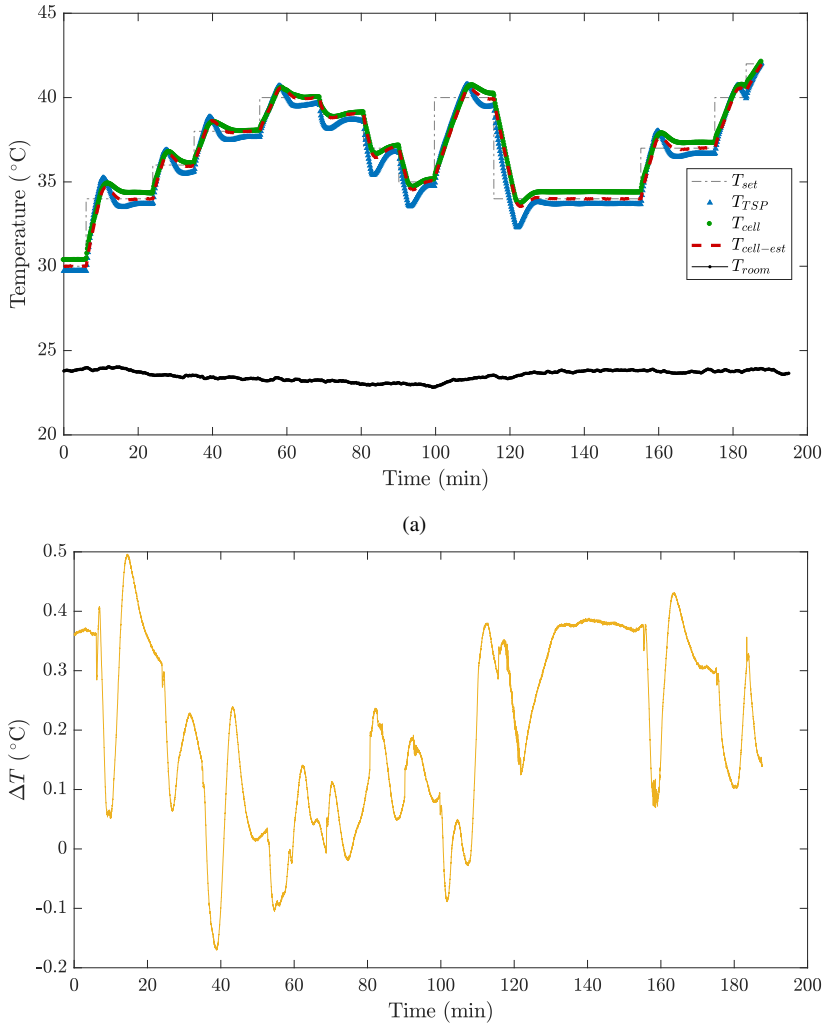

Fig. 13: Transient temperature control using Model 2: (a) results and (b) difference between measured T_{cell} and $T_{cell-est}$.

and the controller started to compensate for this drop by increasing the heating power as shown in the inset in Fig. 14(b). At 54.5 min, the system restored T_{cell} to 37 °C, before the liquid was changed at 55 min. This demonstrates that the system can maintain the temperature regardless of the typical temperature variations that occur during cell culturing.

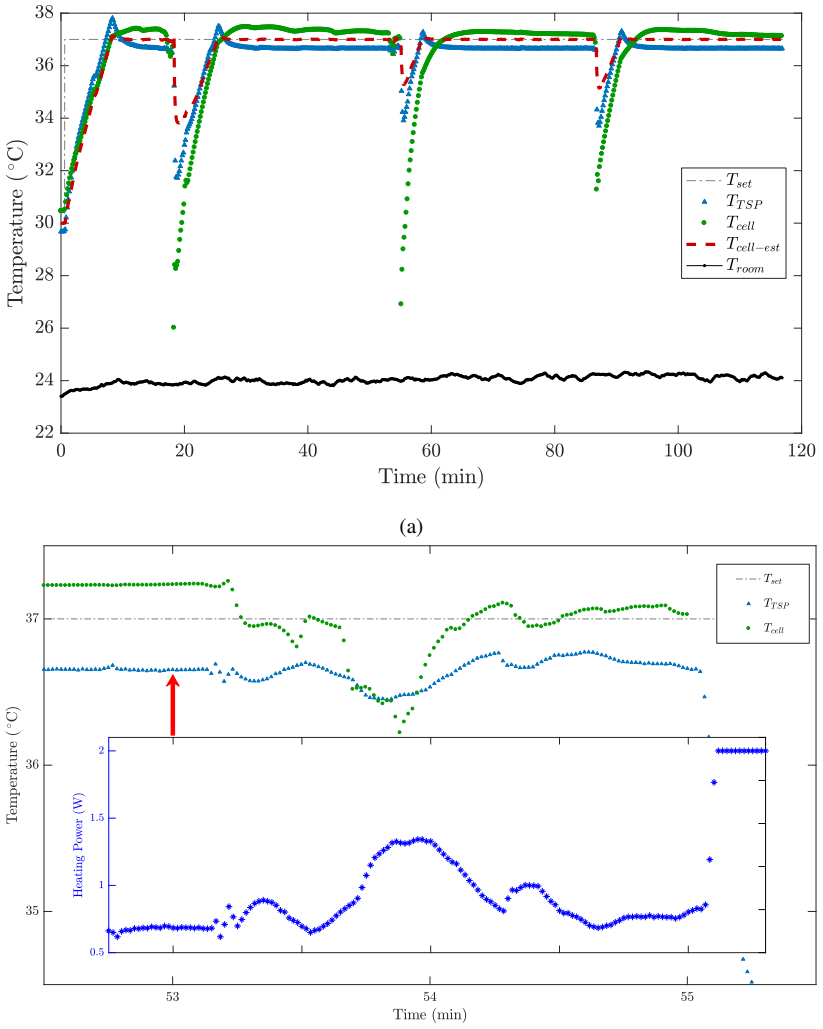

(a)

(b)

Fig. 14: Temperature measurement and control during liquid changes: (a) changing times are 18 min, 55 min, and 87 min, and (b) a zoomed-in image showing the cell culture temperature before and after the second liquid change at 55 min. After about 53 min, the cell culture chamber is opened (indicated by the red arrow), and the liquid is changed about 2 min later. Inset: the output power from the controller.

F. Portable Heating System

In the case of the portable heating system, which would be beneficial while moving the device, the temperature control was directly based on T_{ITO}. This experiment is shown in Fig. 15. Using

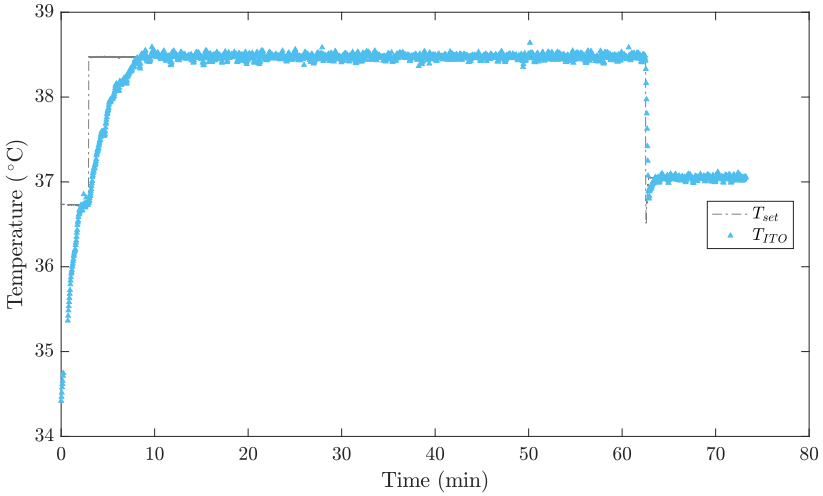

Fig. 15: Portable heating system test: heating ITO over an hour using a battery.

a battery-operated system, we maintained and precisely controlled the temperature of the ITO heater over an hour at 37 °C. Therefore, for example live-cell imaging can be performed in a constant temperature, without providing undesired temperature stimulation to the cell culture.

G. Cell Experiments

To demonstrate the capability of the system for long-term cell culturing *in vitro*, the iPS-CM aggregates were cultured in the system, and the beating behavior of the iPS-CMs was assessed for over 100 h. We used Model 1 for temperature control and the imaging system presented in Section II-B1. We recorded 60 s videos with a frame-rate of 50 frames per second, once a day starting 24 h after the cells were initially plated to the device. The iPS-CMs remained functional when cultured in the system; analyzed beating rates on the first day of culturing and 110 h later were 44 and 36 beats per minute (BPM), respectively, using a video image-based method. This non-invasive method, presented by Ahola *et al.* [45], has been proved to be a reliable and fast approach to monitor the mechanical beating behavior of cardiomyocytes [19]. Snapshot images

of the initial and final videos are presented in Fig. 16 (see supplementary material for more information). These results demonstrate the suitability of the device for a long-term cell culturing of iPS-CMs. Another set of the iPS-CM aggregates were exposed to different temperatures. We

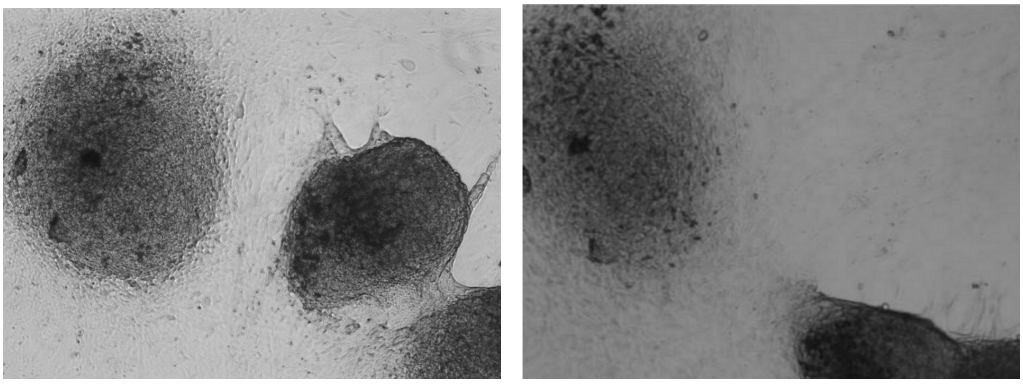

(a) (b)

Fig. 16: Cell culture experiments: snapshots of beating CMs (a) 2 days after plating cells on the device, and (b) 110 h later. See supplementary material for videos.

varied temperature between $37\ ^{\circ}\mathrm{C}$ and $25\ ^{\circ}\mathrm{C}$ in several steps. We waited 25 minutes before a video recording to stabilize the cell culture temperature. After experiment, using the same video image-based analysis [45], we calculated the beating rates in different temperatures. The results are shown in Fig. 17. As can be seen in Fig. 17, we were able not only to change the beating rate of the cardiomyocytes, but also to recover the beating rate when the temperature was returned to $37\ ^{\circ}\mathrm{C}$. The calculated average beating rate at $37\ ^{\circ}\mathrm{C}$ was 54.8 BPM $\pm$ 3.2 BPM. based on 11 measurements points presented in Fig. 17(b). Furthermore, average beating rates at $35\ ^{\circ}\mathrm{C}$ and $34\ ^{\circ}\mathrm{C}$ were 44.5 BPM and 36.0 BPM, respectively; however, it should be highlight here, that these latter results are only from four measurement points, and more comprehensive studies are required.

IV. Discussion

We demonstrated a microscale cell culture device together with a unique indirect temperature control method. To our best knowledge, this is the first time that the cell culture temperature has been precisely maintained and regulated without measuring the temperature directly from the

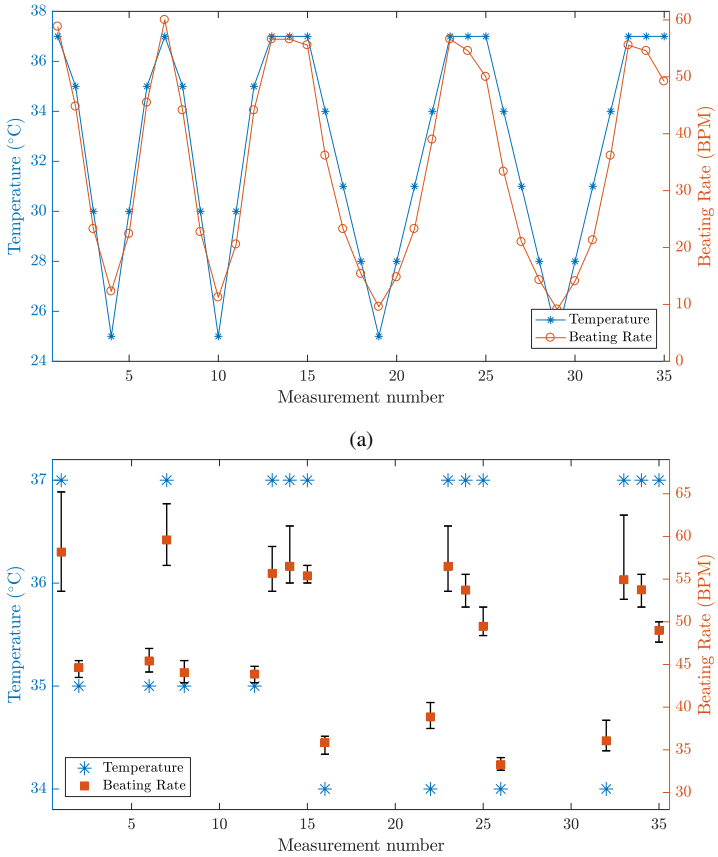

Fig. 17: Beating rate of the cardiomyocytes in different temperatures: (a) full measurement data, (b) a zoomed in image showing the average beating rates at temperatures between 34 °C and 37 °C. Error bars represent the minimum and maximum values calculated from each 60 s video.

cell culture area. Especially, our system can precisely control the cell culture during temperature transients without placing a sensor inside the cell culture area; this has typically not been possible in the systems used in previous studies. As a summary, we have demonstrated that the developed system can precisely control the cell culture temperature when i) ambient room temperature is changing, ii) the system is moved, iii) the cell culture device is opened, and iv) liquid is changed, all without direct measurement. Furthermore, the system is suitable for temperature-dependent

cell behavior studies; this was demonstrated by studying the beating iPS-CM aggregates.

Our system maintained the temperature at $37\ ^{\circ}\mathrm{C}$ for over four days. The measured temperature variation, $\pm 0.3\ ^{\circ}\mathrm{C}$ was similar to that in other studies; for instance, variations of $\pm 0.2\ ^{\circ}\mathrm{C}$ [25], [29], [30], [46], [47], $\pm 0.25\ ^{\circ}\mathrm{C}$ [16], $\pm 0.26\ ^{\circ}\mathrm{C}$ [8], $\pm 0.3\ ^{\circ}\mathrm{C}$ [48], $\pm 0.4\ ^{\circ}\mathrm{C}$ [49], $\pm 0.5\ ^{\circ}\mathrm{C}$ [50], [51], and $\pm 0.8\ ^{\circ}\mathrm{C}$ [52] have been reported. As the intrinsic properties of fluids and cells are temperature-dependent, it is highly beneficial to prevent large temperature variations in the cell studies. For this reason, it is crucial that the heating system can compensate typical temperature disturbances related to the cell cultures; for example, the variations in the ambient room temperature or the opening of the device and the change of medium. Unfortunately, this is typically not possible with the previously presented devices without direct measurement from the cell culture area, whereas we demonstrated that these disturbances can be indirectly monitored and compensated for using the developed heating system. This allow us to minimize the undesired stimulations of cells origin from the temperature variations. In addition, we presented the portability of the system. With the battery operated heating, a constant cell culture temperature can be maintained for about an hour for instance while moving the device or during live-cell imaging.

With the slight temperature variation of our heating system, a successful cell culture could be carried out. We demonstrated this by culturing the beating iPS-CM aggregates for over four days and using the video image-based beating rate analysis. We also combined this analysis and controlled temperature variations to demonstrate how the beating rate varied in different temperatures. We achieved two main results from this experiment; firstly, we were able to return the beating rate when temperature was set back to $37\ ^{\circ}\mathrm{C}$ as is shown in Fig. 10(a). Secondly, even though more tests are needed, the initial results in Fig. 17(b) clearly show the importance of the precise temperature control. For example, if we consider the closed-loop heating system based on the direct control of T_{ITO} presented in Fig. 10(b), approximately $1\ ^{\circ}\mathrm{C}$ temperature differences in the cell area were obtained only because of the variations in the ambient air temperature. This can create unwanted artificial stimulation to the cells; based on the study presented in Section III-G, the beating rate of the iPS-CM aggregates was significantly dropped when temperature was decreased from $37\ ^{\circ}\mathrm{C}$ to $34\ ^{\circ}\mathrm{C}$. From the average beating rates ($54.8\ \mathrm{BPM}$, $44.5\ \mathrm{BPM}$, and $36.0\ \mathrm{BPM}$ at $37\ ^{\circ}\mathrm{C}$, $35\ ^{\circ}\mathrm{C}$, and $34\ ^{\circ}\mathrm{C}$, respectively), we can estimate that the beating rate dropped roughly 10% in every $^{\circ}\mathrm{C}$ when temperature was decreased from $37\ ^{\circ}\mathrm{C}$ to $34\ ^{\circ}\mathrm{C}$. Even though similar results have been reported [53], [54], more studies in different temperatures are

required to verify our results. Also, for instance the measurement of electrophysiology of the cells in different temperatures using a patch clamp method could be included.

V. Conclusion

We developed a portable microscale cell culture system device including a precise heating system based on an indirect control method. The method combines a numerical model and a temperature measurement to maintain and control the temperature in the desired area, without the need of placing a sensor in that area. Using the method, we precisely maintained a constant temperature over 100 hours. We also presented accurate temperature control during temperature changes. The model-based control system was also able to compensate for temperature disturbances caused by variations in the ambient temperature, for instance, during liquid changes. Furthermore, we cultured the beating iPS-CM aggregates in the developed system for more than four days. The system was capable of providing a stable and cell-friendly environment for the cell cultures. In addition, a temperature-dependent beating rate was demonstrated with the iPS-CM aggregates.

One future step is to implement oxygen sensing in the system, similar to that presented previously [39]. Integration of a zigzag-shaped heater and a sensor on a single ITO plate could be possible through conventional photolithography methods [49], [55]. Cell cultures *in vitro* in this study were on a plane. Unfortunately, two-dimensional culture models poorly mimic tissues *in vivo* [56]. In the future, designing a three-dimensional cell culture environment would offer a biologically more relevant *in vitro* model and would better reproduce *in vivo* culturing conditions and cell-cell interactions.

Acknowledgment

This work was supported by Tekes, the Finnish Funding Agency for Technology and Innovation (Decision no. 40346/11), Finnish Culture Foundation, and was carried out within the Human Spare Parts 2 project.

References

[1] H. Chen and R. E. Nordon, “Application of Microfluidics to Study Stem Cell Dynamics,” in *Emerging Trends in Cell and Gene Therapy*, 2013, vol. 9781627034, ch. 19, pp. 435–470.

[2] C. Picard, V. Hearnden, M. Massignani, S. Achouri, G. Battaglia, S. MacNeil, and A. Donald, “A micro-incubator for cell and tissue imaging,” *BioTechniques*, vol. 48, no. 2, pp. 135–138, 2010.

[3] R. Portillo-Lara and N. Annabi, "Microengineered Cancer-on-a-chip Platforms to Study the Metastatic Microenvironment," *Lab on a Chip*, vol. 16, pp. 4063–4081, 2016.

[4] G. Velve-Casquillas, M. Le Berre, M. Piel, and P. T. Tran, "Microfluidic tools for cell biological research," *Nano Today*, vol. 5, no. 1, pp. 28–47, feb 2010.

[5] G. M. Whitesides, "The origins and the future of microfluidics." *Nature*, vol. 442, no. 7101, pp. 368–73, 2006.

[6] R. J. Macown, F. S. Veraitch, and N. Szita, "Robust, microfabricated culture devices with improved control over the soluble microenvironment for the culture of embryonic stem cells," *Biotechnology Journal*, vol. 9, no. 6, pp. 805–813, 2014.

[7] G. Velve-Casquillas, C. Fu, M. Le Berre, J. Cramer, S. Meance, A. Plecis, D. Baigl, J.-J. Greffet, Y. Chen, M. Piel, and P. T. Tran, "Fast microfluidic temperature control for high resolution live cell imaging," *Lab Chip*, vol. 11, no. 3, pp. 484–489, 2011.

[8] S. Petronis, M. Stangegaard, C. B. V. Christensen, and M. Dufva, "Transparent polymeric cell culture chip with integrated temperature control and uniform media perfusion," *BioTechniques*, vol. 40, no. 3, pp. 368–376, mar 2006.

[9] C. S. Chen, X. Jiang, and G. M. Whitesides, "Microengineering the Environment of Mammalian Cells in Culture," *MRS Bulletin*, vol. 30, no. 03, pp. 194–201, 2005.

[10] S. R. Heidemann, P. Lamoureux, K. Ngo, M. Reynolds, and R. E. Buxbaum, "Open-dish incubator for live cell imaging with an inverted microscope," *BioTechniques*, vol. 35, no. 4, pp. 708–716, 2003.

[11] D. C. Duffy, J. C. McDonald, O. J. Schueller, and G. M. Whitesides, "Rapid Prototyping of Microfluidic Systems in Poly(dimethylsiloxane)." *Analytical chemistry*, vol. 70, no. 23, pp. 4974–4984, dec 1998.

[12] T. Merkel and V. Bondar, "Gas sorption, diffusion, and permeation in poly (dimethylsiloxane)," *Journal of Polymer Science Part B: Polymer Physics*, vol. 38, no. 3, pp. 415–434, 2000.

[13] I. L. Ngo, S. Jeon, and C. Byon, "Thermal conductivity of transparent and flexible polymers containing fillers: A literature review," *International Journal of Heat and Mass Transfer*, vol. 98, pp. 219–226, 2016.

[14] E. W. K. Young and D. J. D. Beebe, "Fundamentals of microfluidic cell culture in controlled microenvironments." *Chemical Society Reviews*, vol. 39, no. 3, pp. 1036–1048, 2010.

[15] C. Yi, C. W. Li, S. Ji, and M. Yang, "Microfluidics technology for manipulation and analysis of biological cells," *Analytica Chimica Acta*, vol. 560, no. 1-2, pp. 1–23, 2006.

[16] C. Fang, F. Ji, Z. Shu, and D. Gao, "Determination of the temperature-dependent cell membrane permeabilities using microfluidics with integrated flow and temperature control," *Lab on a Chip*, vol. 17, pp. 951–960, 2017.

[17] R. Reig, M. Mattia, A. Compte, C. Belmonte, and M. V. Sanchez-Vives, "Temperature modulation of slow and fast cortical rhythms." *Journal of Neurophysiology*, vol. 103, no. 3, pp. 1253–1261, 2010.

[18] C. Picard and A. Donald, "The impact of environmental changes upon the microrheological response of adherent cells," *The European Physical Journal E*, vol. 30, no. 2, p. 127, 2009.

[19] E. Laurila, A. Ahola, J. Hyttinen, K. Aalto-Set??l??, and K. Aalto-Setälä, "Methods for in vitro functional analysis of iPSC derived cardiomyocytes - Special focus on analyzing the mechanical beating behavior," *Biochimica et Biophysica Acta - Molecular Cell Research*, vol. 1863, no. 7, pp. 1864–1872, 2016.

[20] D. Saalfrank, A. K. Konduri, S. Latifi, R. Habibey, A. Golabchi, A. V. Martiniuc, A. Knoll, S. Ingebrandt, and A. Blau, "Incubator-independent cell-culture perfusion platform for continuous long-term microelectrode array electrophysiology and time-lapse imaging," *Royal Society Open Science*, vol. 2, no. 6, p. 150031, 2015.

[21] R. Habibey, A. Golabchi, S. Latifi, F. Difato, and A. Blau, "A microchannel device tailored to laser axotomy and long-term microelectrode array electrophysiology of functional regeneration," *Lab on a Chip*, vol. 15, no. 24, pp. 4578–4590, 2015.

[22] J. M. Jang, J. Lee, H. Kim, N. L. Jeon, and W. Jung, "One-photon and two-photon stimulation of neurons in a microfluidic culture system," *Lab on a Chip*, vol. 16, no. 9, pp. 1684–1690, 2016.

[23] K. I.-K. K. Wang, Z. Salcic, J. Yeh, J. Akagi, F. Zhu, C. J. Hall, K. E. Crosier, P. S. Crosier, and D. Wlodkowic, "Toward embedded laboratory automation for smart Lab-on-a-Chip embryo arrays." *Biosensors and Bioelectronics*, vol. 48, pp. 188–196, oct 2013.

[24] T. Pennell, T. Suchyna, J. Wang, J. Heo, J. D. Felske, F. Sachs, and S. Z. Hua, "Microfluidic chip to produce temperature jumps for electrophysiology," *Analytical Chemistry*, vol. 80, no. 7, pp. 2447–2451, 2008.

[25] J. Vukasinovic, D. K. Cullen, M. C. LaPlaca, and A. Glezer, "A microperfused incubator for tissue mimetic 3D cultures." *Biomedical microdevices*, vol. 11, no. 6, pp. 1155–1165, dec 2009.

[26] F. Abeille, F. Mittler, P. Obeid, M. Huet, F. Kermarrec, M. E. Dolega, F. Navarro, P. Pouteau, B. Icard, X. Gidrol, V. Agache, and N. Picollet-D'hahan, "Continuous microcarrier-based cell culture in a benchtop microfluidic bioreactor." *Lab on a Chip*, vol. 14, no. 18, pp. 3510–3518, 2014.

[27] M. Riley, "Instrumentation and Process Control," in *Cell Culture Technology for Pharmaceutical and Cell-Based Therapies*, ser. Biotechnology and Bioprocessing. CRC Press, aug 2005, pp. 249–297.

[28] E. Biffi, G. Regalia, D. Ghezzi, R. De Ceglia, A. Menegon, G. Ferrigno, G. B. Fiore, and A. Pedrocchi, "A novel environmental chamber for neuronal network multisite recordings," *Biotechnology and Bioengineering*, vol. 109, no. 10, pp. 2553–2566, oct 2012.

[29] J.-L. Lin, M.-H. Wu, C.-Y. Kuo, K.-D. Lee, and Y.-L. Shen, "Application of indium tin oxide (ITO)-based microheater chip with uniform thermal distribution for perfusion cell culture outside a cell incubator." *Biomedical Microdevices*, vol. 12, no. 3, pp. 389–398, jun 2010.

[30] G. Regalia, E. Biffi, S. Achilli, G. Ferrigno, A. Menegon, and A. Pedrocchi, "Development of a bench-top device for parallel climate-controlled recordings of neuronal cultures activity with microelectrode arrays," *Biotechnology and Bioengineering*, vol. 113, no. 2, pp. 403–413, 2016.

[31] H. Buhler, R. Adamietz, T. Abeln, D. Diaz-Carballo, P. Nguemgo-Kouam, T. Hero, and I. A. Adamietz, "Automated multichamber time-lapse videography for long-term in vivo observation of migrating cells," *In Vivo*, vol. 31, no. 3, pp. 329–334, 2017.

[32] L. Liu, S. Peng, W. Wen, and P. Sheng, "Micro thermoindicators and optical-electronic temperature control for microfluidic applications," *Applied Physics Letters*, vol. 91, no. 9, 2007.

[33] T. Glawdel, Z. Almutairi, S. Wang, and C. Ren, "Photobleaching absorbed Rhodamine B to improve temperature measurements in PDMS microchannels," *Lab on a Chip*, vol. 9, no. 1, pp. 171–174, 2009.

[34] D. Ross, M. Gaitan, and L. E. Locascio, "Temperature Measurement in Microfluidic Systems Using a Temperature-Dependent Fluorescent Dye," *Analytical Chemistry*, vol. 73, no. 17, pp. 4117–4123, 2001.

[35] R. Samy, T. Glawdel, and C. L. Ren, "Method for Microfluidic Whole-Chip Temperature Measurement Using Thin-Film Poly (dimethylsiloxane)/ Rhodamine B," *Measurement*, vol. 80, no. 2, pp. 4117–4123, 2008.

[36] A.-J. Mäki, T. Ryynänen, J. Verho, J. Kreutzer, J. Lekkala, and P. Kallio, "Indirect Temperature Measurement and Control Method for Cell Culture Devices," *IEEE Transactions on Automation Science and Engineering*, no. 99, pp. 1–10, 2016.

[37] J. Kreutzer, L. Ylä-Outinen, P. Kärnä, T. Kaarela, J. Mikkonen, H. Skottman, S. Narkilahti, and P. Kallio, "Structured PDMS Chambers for Enhanced Human Neuronal Cell Activity on MEA Platforms," *Journal of Bionic Engineering*, vol. 9, pp. 1–10, 2012.

[38] J. Kreutzer, L. Ylä-Outinen, A.-J. Mäki, M. Ristola, S. Narkilahti, and P. Kallio, "Cell Culture Chamber with Gas Supply for Prolonged Recording of Human Neuronal Cells on Microelectrode Array," *Journal of Neuroscience Methods*, vol. 280, pp. 27–35, 2017.

[39] H. Välimäki, J. Verho, J. Kreutzer, D. K. Rajan, T. Ryynänen, M. Pekkanen-Mattila, A. Ahola, K. Tappura, P. Kallio, and

J. Lekkala, “Fluorimetric oxygen sensor with an efficient optical read-out for in vitro cell models,” *Sensors and Actuators B: Chemical*, vol. 249, pp. 738–746, 2017.

[40] A. L. Lahti, V. J. Kujala, H. Chapman, A.-P. Koivisto, M. Pekkanen-Mattila, E. Kerkelä, J. Hyttinen, K. Kontula, H. Swan, B. R. Conklin, S. Yamanaka, O. Silvennoinen, and K. Aalto-Setälä, “Model for long QT syndrome type 2 using human iPS cells demonstrates arrhythmogenic characteristics in cell culture,” *Disease Models & Mechanisms*, vol. 5, no. 2, pp. 220–230, 2012.

[41] A. W. M. van Schijndel, “Integrated Heat Air and Moisture Modeling and Simulation,” Eindhoven University Press, Eindhoven, The Netherlands, Technische Universiteit Eindhoven, 2007.

[42] L. Ljung, “Convergence analysis of parametric identification methods,” *IEEE Transactions on Automatic Control*, vol. 23, no. 5, pp. 770 – 783, 1978.

[43] ——, *System Identication Toolbox User’s Guide*, 9th ed. The MathWorks, Inc., 2016.

[44] H. Bridle, M. Millingen, and A. Jesorka, “On-chip fabrication to add temperature control to a microfluidic solution exchange system,” *Lab on a Chip*, vol. 8, no. 3, p. 480, 2008.

[45] A. Ahola, A. L. Kiviaho, K. Larsson, M. Honkanen, K. Aalto-Setälä, and J. Hyttinen, “Video image-based analysis of single human induced pluripotent stem cell derived cardiomyocyte beating dynamics using digital image correlation.” *Biomedical engineering online*, vol. 13, no. 1, p. 39, 2014.

[46] C.-C. Hsieh, S.-B. Huang, P.-C. Wu, D.-B. Shieh, and G.-B. Lee, “A microfluidic cell culture platform for real-time cellular imaging.” *Biomedical microdevices*, vol. 11, no. 4, pp. 903–13, aug 2009.

[47] S.-B. Huang, S.-S. Wang, C.-H. Hsieh, Y. C. Lin, C.-S. Lai, and M.-H. Wu, “An integrated microfluidic cell culture system for high-throughput perfusion three-dimensional cell culture-based assays: effect of cell culture model on the results of chemosensitivity assays,” *Lab on a Chip*, vol. 13, no. 6, p. 1133, 2013.

[48] L. Lin, S.-S. Wang, M.-H. Wu, and C.-C. Oh-Yang, “Development of an integrated microfluidic perfusion cell culture system for real-time microscopic observation of biological cells,” *Sensors*, vol. 11, no. 9, pp. 8395–8411, jan 2011.

[49] T. Yamamoto, T. Fujii, and T. Nojima, “PDMSglass hybrid microreactor array with embedded temperature control device. Application to cell-free protein synthesis,” *Lab on a Chip*, vol. 2, no. 4, pp. 197–202, 2002.

[50] H. Witte, M. Stubenrauch, U. Fröber, R. Fischer, D. Voges, and M. Hoffmann, “Integration of 3-D cell cultures in fluidic microsystems for biological screenings,” *Engineering in Life Sciences*, vol. 11, no. 2, pp. 140–147, apr 2011.

[51] D. Nieto, P. McGlynn, M. de la Fuente, R. Lopez-Lopez, and G. M. O’connor, “Laser microfabrication of a microheater chip for cell culture outside a cell incubator,” *Colloids and Surfaces B: Biointerfaces*, vol. 154, pp. 263–269, 2017.

[52] J. Y. Cheng, M. H. Yen, C. T. Kuo, and T. H. Young, “A transparent cell-culture microchamber with a variably controlled concentration gradient generator and flow field rectifier,” *Biomicrofluidics*, vol. 2, no. 2, p. 024105, 2008.

[53] R. Kienast, M. Stöger, M. Handler, F. Hanser, and C. Baumgartner, “Alterations of field potentials in isotropic cardiomyocyte cell layers induced by multiple endogenous pacemakers under normal and hypothermal conditions.” *American journal of physiology. Heart and circulatory physiology*, vol. 307, no. 7, pp. H1013–23, 2014.

[54] J. Weisser, J. Martin, E. Bisping, L. S. Maier, F. Beyersdorf, G. Hasenfuss, and B. Pieske, “Influence of mild hypothermia on myocardial contractility and circulatory function,” *Basic Research in Cardiology*, vol. 96, no. 2, pp. 198–205, nov 2001.

[55] S. Demming, G. Peterat, A. Llobera, H. Schmolke, A. Bruns, M. Kohlstedt, A. Al-Halhouli, C.-p. P. Klages, R. Krull, S. Bu, and S. Büttgenbach, “Vertical microbubble column-A photonic lab-on-chip for cultivation and online analysis of yeast cell cultures,” *Biomicrofluidics*, vol. 6, no. 3, p. 34106, sep 2012.

[56] M. Schindler, A. Nur-E-Kamal, I. Ahmed, J. Kamal, H.-Y. Liu, N. Amor, A. S. Ponery, D. P. Crockett, T. H. Grafe, H. Y. Chung, T. Weik, E. Jones, and S. Meiners, “Living in three dimensions,” *Cell Biochemistry and Biophysics*, vol. 45, no. 2, pp. 215–227, 2006.

Tampereen teknillinen yliopisto
PL 527
33101 Tampere

Tampere University of Technology
P.O.B. 527
FI-33101 Tampere, Finland

ISBN 978-952-15-4168-1
ISSN 1459-2045